



NTNU – Trondheim
Norwegian University of
Science and Technology

Igneous Hydrothermal Alteration and Ore-Forming Processes in the Land's End Granite, Nanjizal

Marte Eik

Geology

Submission date: May 2015

Supervisor: Bjørn Eske Sørensen, IGB

Co-supervisor: Rune Berg Larsen, IGB

Norwegian University of Science and Technology
Department of Geology and Mineral Resources Engineering

Abstract

This study addresses the hydrothermal alteration and mineralization related to a system of tourmaline-quartz veins intersecting biotite-granite in Nanjizal, in the Land's End granites of the Cornubian batholith. Nanjizal is an important site as it is one of the few locations in the southern segment of the Land's End Granite where magmatic-hydrothermal tin mineralizations have been mined. The aim is to identify the alteration-patterns and their correlation with hydrothermal ore-forming events and the formation of cassiterite ore.

Three vein-types, distinguished from their field appearance, were mapped and sampled. Petrographic studies (microscopy, SEM, EPMA) and geochemical analyses (XRD, XRF, ICP-MS) were carried out to characterize the alteration types, with focus on tourmaline and rutile as recorders of ore-forming processes and Sn (\pm W) hosts. Compositional data from tourmaline indicate both reducing and oxidizing conditions.

Three hydrothermal episodes are recognized. The first comprises tourmaline (\pm quartz)-veins, characterized by a red potassic alteration zone, consisting of newly formed K-feldspar-quartz at 400-500 °C. This episode was likely formed by hydrofracturing from high temperature reducing magmatic-hydrothermal fluid exsolved from the magma in a process of second boiling. Rutile and hematite formation and Fe³⁺ incorporated in the vein-comprising tourmaline indicate later influence of highly oxidizing fluids. It is likely that boiling and subsequent phase separation due to pressure changes yielded a high density, oxidizing fluid phase, resulting in cassiterite formation (1000 ppm Sn) and tourmalinization of the vein. The second hydrothermal event comprises tourmaline (\pm quartz)-veins, characterized by sericitic alteration of the feldspars and muscovite replacing biotite. Locally red alteration zone, similar to the first hydrothermal episode, and formation of cassiterite (100 ppm Sn) indicate initial oxidizing conditions and potassic alteration, later overprinted by sericitic alteration of the feldspars by reducing, saline magmatic-hydrothermal fluids.

The third hydrothermal episode comprises tourmaline veins and sericitic alteration, from reducing magmatic-hydrothermal fluids. Tourmaline formed during reducing conditions, likely obtaining Fe and Mg from the breakdown of biotite by muscovite-replacement. None of the three hydrothermal episodes show evidence of mixing with cooler, oxidizing meteoric fluids that otherwise yielded the greisen-associated cassiterite deposits described elsewhere in the Cornubian ore-field.

Sammendrag

Denne studien omhandler hydrotermal omvandling og mineraliseringer relatert til et system av turmalin-kvarts-årer som kutter biotitt-granitt i Nanjizal, i Land's End-granitten i den Cornubiske batolitten. Nanjizal er et viktig område som et av få steder i den sørlige delen av Lands End-granitten hvor magmatisk-hydrotermale tinn-mineraliseringer har blitt utvunnet. Målet med oppgaven er å identifisere omvandlingsmønstre og deres sammenheng med hydrotermale malmdannende hendelser og dannelsen av kassiteritt. Tre typer årer er kategorisert basert på utseende observert i felt, som ble kartlagt og prøvetatt. Petrografiske studier (mikroskopi, SEM, EPMA) og geokjemiske analyser (XRD, XRF, ICP-MS) ble utført for å karakterisere omvandlingstypene. Fokus var på turmalin og rutil, som bevarer informasjon av malmdannende prosesser og er potensielle verter for Sn (\pm W). Komposisjonelle data fra turmalin indikerer både reduserende og oksiderende forhold. Tre hydrotermale episoder er gjenkjent. Den første episoden omfatter turmalin (\pm kvarts) -årer, preget av en rød kaliumholdig omvandlingssone, bestående av nydannet K-feltspat-kvarts ved 400-500°C. Denne episoden ble trolig dannet ved hydraulisk oppsprekking av magmatisk-hydrotermale væsker med høy temperatur, frigjort fra magmaen som følge av retrograd koking. Rutil-og hematitt-dannelse og Fe^{3+} i turmalinstrukturen i selve åren indikerer senere påvirkning av sterkt oksiderende væsker. Koking og påfølgende fase-separasjon på grunn av trykkforandringer førte til en oksiderende væskefase med høy tetthet, som resulterte i utfellingen av kassiteritt (1000 ppm Sn) og turmalinisering av åren. Den andre hydrotermale episoden består av turmalin (\pm kvarts) -årer, preget av serisitt-omvandling av feltspat og muskovitt som erstatter biotitt. Lokal rød omvandlingssone, i likhet med den første hydrotermale episoden, og dannelsen av kassiteritt (100 ppm Sn) indikerer innledende oksiderende forhold og kaliumholdig omvandling. Disse teksturene ble senere overprintet av serisitt-omvandling av feltspat fra reduserte magmatisk-hydrotermale væsker med lav pH. Den tredje hydrotermale episoden består av turmalin-årer og serisitt-omvandling, fra reduserte magmatisk-hydrotermale væsker. Turmalin ble dannet under reduserende forhold, hvor en trolig kilde til Fe og Mg kom fra nedbryting av biotitt. Ingen av de tre hydrotermale episodene viser tegn innblanding med kjøligere, oksiderende meteoriske væsker som ellers ga greisen-assosierte kasserittforekomstene som er beskrevet andre steder i det Cornubiske malmfeltet.

Acknowledgement

This master thesis has been carried out at the Department of Geology and Mineral Resources Engineering (IGB) at the Norwegian University of Science and Technology (NTNU), Trondheim. The main supervisor has been Associate Professor Bjørn Eske Sørensen, and Professor Rune Berg Larsen has been the co-supervisor. I would like to express my gratitude to everyone who contributed to this project. First of all, I would like to thank Bjørn and Rune for help and guidance during the project despite their busy schedule, and PhD-candidate Kristian Drivenes for guidance and expertise during fieldwork and for providing additional samples and analyses.

I would also like to thank Trond Slagstad at the Geological Survey of Norway for enabling me to perform SEM element mapping. I am especially grateful to my fellow student Anette Utgården Granseth for lending her time to help me carry out the analyses at NGU, and for discussions, advice, help and support. I will also thank Elise Svergja for being a great field partner, and my brother Christer Eik for proofreading.

A big thanks goes to all my classmates for all the great memories. Lastly, I would like to thank my friends and family for supporting me, especially my fiancé Geir Marius Skrede for encouragements and support.

Trondheim, 15.05.2015

Marte Eik

Contents

Abstract	iii
Sammendrag	v
Acknowledgement	vii
Contents	ix
List of Figures	xi
List of Tables	xiii
Chapter 1. Introduction	1
Chapter 2. Theory	3
2.1. Granitic magmatism	3
2.1. The magmatic- hydrothermal system	4
2.2. Tourmaline	8
2.3. Alteration types	12
Chapter 3. Regional Geology	19
3.1. The Variscan Orogeny	19
3.2. The Cornubian batholith	19
3.3. Land's End Granite	21
3.4. Alteration and associated mineralizations in Cornwall	23
3.5. Previous studies of Tourmaline and Rutile associated with Sn-mineralizations in Cornwall	28
Chapter 4. Methodology	33
4.1. Sample preparation	33
4.2. Geochemical analysis	36
4.3. Petrographic analysis	38
4.4. Calculations and plotting	41
4.5. Sources of Error	42
Chapter 5. Results	47
5.1. Field investigations	47
5.2. Petrographic descriptions	56
5.3. Geochemical results	84

Chapter 6. Discussion	111
6.1. Type A: Potassic alteration and tourmalinization	112
6.2. Type B and C: Sericitization and tourmalinization	114
6.3. Insights into hydrothermal processes	115
6.4. Origin of the veins and mineralizing fluids.....	118
6.5. Formation of cassiterite	122
Chapter 7. Conclusions.....	125
7.1. Suggestions for future work	126
Chapter 8. References.....	127

Appendices

- A- Mineral abbreviations
- B- Thin section images
- C- Geochemical data
- D- Tourmaline structure calculations
- E- XRD spectra

List of Figures

Figure 2.1: Evolution of a magmatic-hydrothermal system.....	8
Figure 2.2: Major compositional groups of the tourmaline minerals.....	10
Figure 2.3 Idealized evolutionary alteration sequence.....	14
Figure 3.1: Geological map of the major and minor granite outcrops in Cornwall.....	20
Figure 3.2: Distribution of textural variations within the Land's End Pluton.....	22
Figure 3.3: Greisen vein from Cligga Head, Perranporth, Cornwall.....	27
Figure 3.4: Rose diagrams for veins at Nanjizal.....	29
Figure 3.5: Rutile in the matrix of tourmaline breccia at Wheal Remfry.....	30
Figure 3.6: Microprobe traverse from within the MQT tourmaline.....	32
Figure 4.1: Thin section placements in (a) ME02V and (b) ME04V.....	34
Figure 4.2: Flow chart of work process.....	35
Figure 5.1: The area of investigation of Nanjizal rock outcrop.....	47
Figure 5.2: Vein system superimposed on aerial photo of Nanjizal.....	49
Figure 5.3: Geological map of the vein system in Nanjizal bay.....	50
Figure 5.4: Rose diagrams.....	51
Figure 5.5: Images of the three vein types categorized in Nanjizal.....	53
Figure 5.6: Crosscutting relationships between vein type A, B and C.....	55
Figure 5.7: Thin sections of type A, B and C.....	60
Figure 5.8: ME02V with six areas (C1-C6) used in further analysis.....	60
Figure 5.9: Transition from feldspar-rich and quartz poor assemblage, Type A.....	61
Figure 5.10: Inclusions of feldspar, rutile and needle-shaped tourmaline in quartz.....	63
Figure 5.11: CL-traverse of the quartz-tourmaline vein in ME01V, type B.....	64
Figure 5.12: CL-traverse of the quartz-tourmaline vein, zoomed in.....	65
Figure 5.13: Sericitization in ME04V-B, type B and Microperthite in type C, ME05V.....	67
Figure 5.14: K- feldspar with rough pitted surface textures.....	67
Figure 5.15: K- feldspars showing varying degrees of sericitization.....	68
Figure 5.16: Alkali feldspar in type A (ME02V-A) and granite (ME03V).....	69
Figure 5.17: Biotite in granite (KDC granite and ME03V)..	70
Figure 5.18: Biotite with inclusions of rutile and monazite, type A.....	71
Figure 5.19: Altered biotite consisting of opaque aggregates in type C (ME05V).....	72

Figure 5.20: Muscovite replacing biotite in the granite	73
Figure 5.21: Altered biotite in type A (ME02V-A)	74
Figure 5.22: Altered biotite with aggregates of rutile, type A	75
Figure 5.23: Yellow Tourmaline with blue-brown overgrowths.	76
Figure 5.24: Brown and pale blue tourmaline comprising the veins	78
Figure 5.25: Blue-brown tourmaline	78
Figure 5.26: Finely zoned blue-brown tourmaline.....	79
Figure 5.27: Prismatic laths of tourmaline growing in cavities	80
Figure 5.28: Hematite as disseminations and veinlets	81
Figure 5.29: Cassiterite in rutile	83
Figure 5.30: Cassiterite associated with pale blue needle-shaped tourmaline	84
Figure 5.31: Harker diagrams of whole rock chemistry and trace element content.....	86
Figure 5.32: Distribution of elements across a vein zone in ME02V	88
Figure 5.33: Distribution of elements across a vein zone in ME02V	89
Figure 5.34: SEM-Element mapping of the polished slabs of ME02V	90
Figure 5.35: Isocon mass balance calculations, ME02V	92
Figure 5.36: Feldspar ternary diagrams.....	93
Figure 5.37: Distribution map of four different domains within rutile	95
Figure 5.38: Rutile composition diagrams	96
Figure 5.39: Legend for tourmaline plots.....	100
Figure 5.40: Binary plot of cation occupancies and tourmaline classification diagrams.....	101
Figure 5.41: Binary plots of cation occupancies in tourmaline.....	102
Figure 5.42: Binary plots of cation occupancies in tourmaline.....	104
Figure 5.43: Binary plots of cation occupancies in tourmaline.....	106
Figure 5.44: Element map of pale blue tourmaline in type C (ME05V).....	107
Figure 5.45: Microprobe traverse 1 of tourmaline in type A proximal.....	108
Figure 5.46: Microprobe traverse 2 of tourmaline in type A distal.....	109
Figure 5.47: Microprobe traverse 3 of tourmaline in type C	110

List of Tables

Table 2.2: Common substitutions within and between sites in tourmaline.....	11
Table 3.1 Petrographic summary of granite type B	21
Table 3.2: Mineralogical compositions of the main granite units.....	23
Table 3.3: Chronology of the mineralization types and metals.....	24
Table 3.4: Paragenetic sequence of vein mineralization	25
Table 3.5: The two distinct mineralization types	26
Table 4.1: Counting times and detection limits, microprobe analysis	41
Table 5.3: Summation of the identified exchange vectors in tourmalines	99

Chapter 1. Introduction

South West England is famous for its long mining history and multiple Sn-W-Cu deposits. The Land's End Granite of the Cornubian batholith is not normally associated with significant ore-deposits, and Nanjizal is an important site as it is one of the few locations in the southern segment of the Land's End Granite where magmatic-hydrothermal tin mineralizations have been worked (LeBoutillier et al., 2002). A series of veins on the cliff have been studied by LeBoutillier et al. (2002), where cassiterite mineralization were interpreted to have formed as a response to magmatic-hydrothermal fluids mixing with oxidizing meteoric fluids.

This study addresses the hydrothermal alteration and Sn-mineralizations related to a not previously studied system of tourmaline-quartz veins intersecting granite on a rock outcrop on the beach in Nanjizal. The aim of the study was to:

- Identify the alteration-patterns and their correlation with hydrothermal ore-forming events and the formation of cassiterite ore.
- Interpret a relative chronology of vein forming and ore forming events, and the physio-chemical conditions that led to cassiterite deposition.
- Account for the previously identified alteration and related cassiterite mineralization in Cornwall by literature study.

The following limitations were made. Only one sample per alteration type was sampled due to challenging conditions in the field, with untimely high tides and difficulties in finding good sampling sites in the slippery and weathered rock-face. Microprobe analysis was focused on the key alteration types only, due to time and cost restrictions.

Chapter 2. Theory

This chapter addresses the magmatic-hydrothermal continuum, from granitic magmatism and the emplacement of granitic bodies, through the exsolution of magmatic hydrothermal fluids, and the following vein formation in the roof zone of granite or in the country rock lithologies. The chemical properties of the hydrothermal fluids in terms of metal solubility, with focus on Sn, are also looked at. The chemical properties of tourmaline, a mineral associated with B-rich granites and associated magmatic-hydrothermal mineralization, are also described. Finally, there is a review of hydrothermal metasomatism and the hydrothermal alteration types, potassic, propylitic, phyllic, greisen, tourmalinization and argillic alteration.

2.1. Granitic magmatism

Granitoids are the most abundant rock in the upper continental crust, often occurring in significant volumes in areas where the crust is thickened by orogenic processes (Winter, 2010). The petrography of granitoid rocks are described by Winter (2010) as medium- to coarse-grained, with plagioclase, quartz and K- feldspar as the predominant phases. Biotite and hornblende are the dominant mafic phases. The content of minor minerals such as apatite, zircon, magnetite, ilmenite, monazite, tourmaline, plus a host of others, depend on the availability of relevant elements – often trace elements such as Zr, REE and B. Geochemically, the composition of granitoids is variable, with origins typically involving both the mantle and crust (Winter, 2010). The S-I-A-M-classification is used to classify the granitoids, where I- types and M-types are mantle derived, and S- types and A- types have a significant crustal component. S-type granites are often peraluminous and fairly reduced with low oxygen fugacity, determined by a $\text{Fe}_2\text{O}_3/\text{FeO}$ ratio less than 0.3 (Robb, 2005). Oxygen fugacity ($f\text{O}_2$) is a variable controlling oxidation potential in terms of partial pressure of oxygen, and essentially relates to the potential of Fe to occur in a more oxidised (Fe^{3+}) or reduced (Fe^{2+}) state (Pirajno, 2009).

Petford et al. (2000) states that there are four processes responsible for continental granitoid magmatism; *Partial melting, segregation, ascent and emplacement*. Partial melting of the common crustal rocks usually occurs when heat is advected into the crust by the underlying and hotter mantle by basaltic magmas, called underplating. Segregation, the small-scale

movement of melt, is dependant on the physical properties of the granitic melts, of which viscosity and density is the most important. The ascent of granitic magma normally occurs through narrow conduits, either along pre-existing fault or as self-propagating dykes (Petford et al., 2000). The ascent of magmas is caused by rheology, mostly the viscosity, and density contrasts between a magma and its surrounding rocks. The emplacement of magma at shallower depths occurs when the upward forces of buoyancy are arrested by the internal thermodynamic brake in the magma, or are balanced by the external forces of containment (Clarke, 1992). Plutons are emplaced into the crust by thickening it, displacing the Moho downward to replace the volume of melted mantle source and/or lifting the surface of the earth (Best, 2003). In batholiths (plutons or commonly groups of separately intruded plutons with volumes of more than $1 \times 10^5 \text{ km}^3$), emplacement is an episodic process involving discrete pulses of magma. The shapes of plutons are usually flat-lying to open funnel-shaped structures, with central or marginal feeder zones (Petford et al., 2000).

2.1. The magmatic- hydrothermal system

2.1.1. Formation of magmatic fluids

Most of the water present in granitic magmas is derived from the dehydration of minerals in the crust, which were melted to form the magma (Robb, 2005). Best (2003) states that magma in general consists of a mobile mixture of solid, liquid and vapour, and the nature and number of phases is dependant on pressure, temperature and concentration. Volatiles in magmas are dominated by H_2O , and to a lesser extent CO_2 . Above the *critical point* at 218 bars and $372 \text{ }^\circ\text{C}$ for H_2O , vapour and liquid states are no longer distinguishable, and are usually referred to as a supercritical volatile fluid or simply a fluid. The concentration of H_2O in silicate magmas mainly depends on pressure, and to a lesser extent temperature (Robb, 2005). As magmas rise to shallower levels and cools, the melts can become saturated with volatile fluids. The excess dissolved volatiles are released from the melt and separated into a fluid phase in a process called *exsolution* or *boiling* (Best, 2003). The process where an undersaturated melt becomes saturated by decreasing pressure is called “*first boiling*”, and happens generally in shallow, crustal, volcanic environments (Best, 2003, Robb, 2005). Saturation is also achieved as stagnant, isobaric magma is cooling as it loses heat to the environment, and crystallization of anhydrous minerals is increasing the water concentration in the residual melt. This process is called “*second boiling*”, generally occurring in more deep-seated magmatic systems (Best,

2003, Robb, 2005). The resulting fluid can have a wide compositional range, depending on the magma composition, the timing of H₂O formation (i.e. early or late), and may be enriched in incompatible elements (Yardley, 2013). The Fe content in the parent magma determines the oxidised or reduced character of magmatic fluids, controlled by the oxygen fugacity (Pirajno, 2009). The oxygen fugacity of the silicate melts will in turn determine the type of ore system, where S-type magmas will yield reduced fluids, and I-type magmas will yield oxidised fluids (Pirajno, 2009). In the presence of volatiles, the composition of the granitic melt is more alkaline than if formed under volatile-poor conditions (Pirajno, 2013). Magmas that are progressively enriched in B, F and Li during fractionation are simultaneously enriched in the Ab-component, while the fluid phase is enriched in K. When volatiles are lost from the system, during second boiling or opening of the system by fracturing, the residual melt is enriched in Or, while Na is transferred to the fluid phase (Pirajno, 2013).

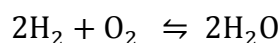
2.1.2. Metal solubility and deposition of Sn

To be effective as a mineralizing agent, hydrothermal fluids need to circulate through the crust and/or a silicate magma in order to dissolve and transport the metals needed to form hydrothermal ore deposits (Robb, 2005). Transport of metals by hydrothermal fluids occurs only if the fluid contains ligands that may form complexes with metallic cations (Robb, 2005). A metal ion joined by coordinate bonds to neutral molecules and/or negative ions (ligands) is called a complex ion (Pirajno, 2009). How metals go into solution are similar to acid-base reactions, where metals and ligands can be classified as either hard or soft. Hard metals and ligands are highly charged with small atomic radii, and are slightly polarisable. Soft metals and ligands are large, of low charge and are highly polarisable (Robb, 2005, Pirajno, 2009). In accordance to Pearson's principle, hard metals tend to bind with hard ligands, and soft metals with soft ligands. In addition, some metals that can complex readily with both hard and soft ligands (borderline), and Cl⁻ can be an effective complexing agent for both intermediate and soft metals (Robb, 2005). Temperature plays a very important role in the degree to which metals enter solution, and the existence of a metal-ligand complex in a fluid depends on oxidation state, pH, temperature and fluid composition (Robb, 2005).

Precipitation of metals from hydrothermal fluids can be a result of temperature variations, pressure changes and boiling, reactions between solution and wall rock, and chemical changes due to fluid mixing (Pirajno, 2009). In order to make an economically viable ore body, the

metal in solution must be extracted from the fluid and concentrated in a portion of the crust that is restricted and accessible, and deposited in economic quantities (Robb, 2005). A widespread manifestation of hydrothermal mineralization is the development of alteration mineral assemblages in and around the fluid conduits. The wall rock –fluid – interaction promotes metal precipitation by chemically changing the fluid properties, especially in terms of acidity (pH) and the redox state (Robb, 2005).

Phase separation/boiling is an important mechanism of precipitating metals from ore-forming solutions by dramatically modify the fluid properties (Robb, 2005). The transition from a single-phase supercritical fluid to one consisting of a fluid phase and vapour phase usually occurs as a result of decrease in fluid pressure. This boiling will effectively remove CO₂ from solution, resulting in a large pH increase (Drummond and Ohmoto, 1985, Robb, 2005). In very reduced high temperature systems, especially open boiling systems, it is likely that the mass action equation



would dominate the redox equilibria of a boiling hydrothermal fluid due to high concentrations of H₂ (Drummond and Ohmoto, 1985). Because of the extremely high volatility of H₂, this redox control would be a relatively rapid oxidizing event related to the earliest stages of boiling (Drummond and Ohmoto, 1985). This process is potentially very important as mechanisms for precipitating metals from ore-forming solution, where oxides (e.g. Fe₃O₄, SnO₂) are most likely to deposit from boiling hydrothermal solutions meeting the threshold criteria for pH- increases (Drummond and Ohmoto, 1985, Robb, 2005).

Tin (Sn) is a metal that exists both as hard acid quadrivalent (Sn⁴⁺) and borderline divalent (Sn²⁺) ions, and thus complexes readily with a number of different ligands (Robb, 2005). Under oxidising conditions, the Sn⁴⁺- hydroxychloride complex Sn(OH)₂Cl₂ is the dominant species, with a low solubility. In more reducing conditions, both Sn²⁺ and Sn⁴⁺ can complex with Cl, forming very soluble complexes (Robb, 2005). In conditions of low pH and low f_{O₂}, Sn²⁺ is transported as SnCl⁻ in more reducing conditions and at higher temperatures, with higher solubilities than the Sn⁴⁺ hydroxychloride complex (SnOHCl) that exists in more oxidised conditions (Robb, 2005, Pirajno, 2009). SnCl₂, SnOHCl and Sn(OH)₂Cl₂ are able to transport tin in concentrations of many thousands g/ton at temperatures of more than 400 °C (LeBoutillier, 2002).

Destabilisation of the transporting complexes leads to the precipitation of cassiterite (SnO_2), occurring either by f_{O_2} increase, and increase in pH, a decrease in temperature or a combination of said physio -chemical factors (Pirajno, 2009). Decrease in fluid acidity exerts a major control on cassiterite deposition, and disseminated deposits are often a result of neutralisation of fluids during greisenisation (LeBoutillier, 2002). Above 400°C and 1-2 kbar, Sn deposition are more sensitive to changes in fluid acidity than T and P, and is extracted efficiently by mixing the primary magmatic fluid with cooler, low-salinity meteoric fluids near neutral acidity (LeBoutillier, 2002). Tungsten (W) mineralization is often associated with cassiterite, and is dominantly transported as polytungstate ions (e.g. HWO_4^-) (LeBoutillier, 2002). Unlike cassiterite, wolframite (FeWO_4) deposition is unaffected by acidity and oxygen fugacity changes, and is largely temperature dependant (LeBoutillier, 2002).

2.1.3. Vein formation

The Burnham model is described in Pirajno (2009), based on the work of Burnham (1979), (1997). The model addresses the magmatic hydrothermal system generated during the cooling of a hypothetical granodiorite intrusive stock containing 3wt% water. Pirajno (2009) discusses the cooling of an intrusive body (Figure 2.1), where the initially open system has become a closed system, with the crystallization of a solidified shell (A). A H_2O -saturated shell of melt is accumulated at the top of the intrusive stock, where biotite and quartz crystallizes, leading to H_2O - saturation of the remaining interstitial melt, as second boiling (Pirajno, 2009). The volume expansion causes overpressurization of the chamber interior, leading to hydrofracturing in the surrounding brittle crystalline shell above, taking place in the direction of least principle stress (Figure 2.1B) (Robb, 2005). The stockwork zone developed becomes healed by the precipitation of silica, and continued cooling will cause the retreat of solidus and H_2O -saturated zone to deeper levels of the stocks. Further cooling of the magma then leads to a repetition of the process, where a complex fracture system is developed (Figure 2.1). This acts as a channel-way for ore-bearing fluids and heat from the underlying igneous body, where ore minerals have been concentrated in the late fluid phases. Mineralization is usually associated with late pulses of magmatic hydrothermal activity. Later influx of meteoric water will eventually dominate and collapse the hydrothermal system, as well as overprint the signatures of the preceding magmatic-hydrothermal system (Pirajno, 2009).

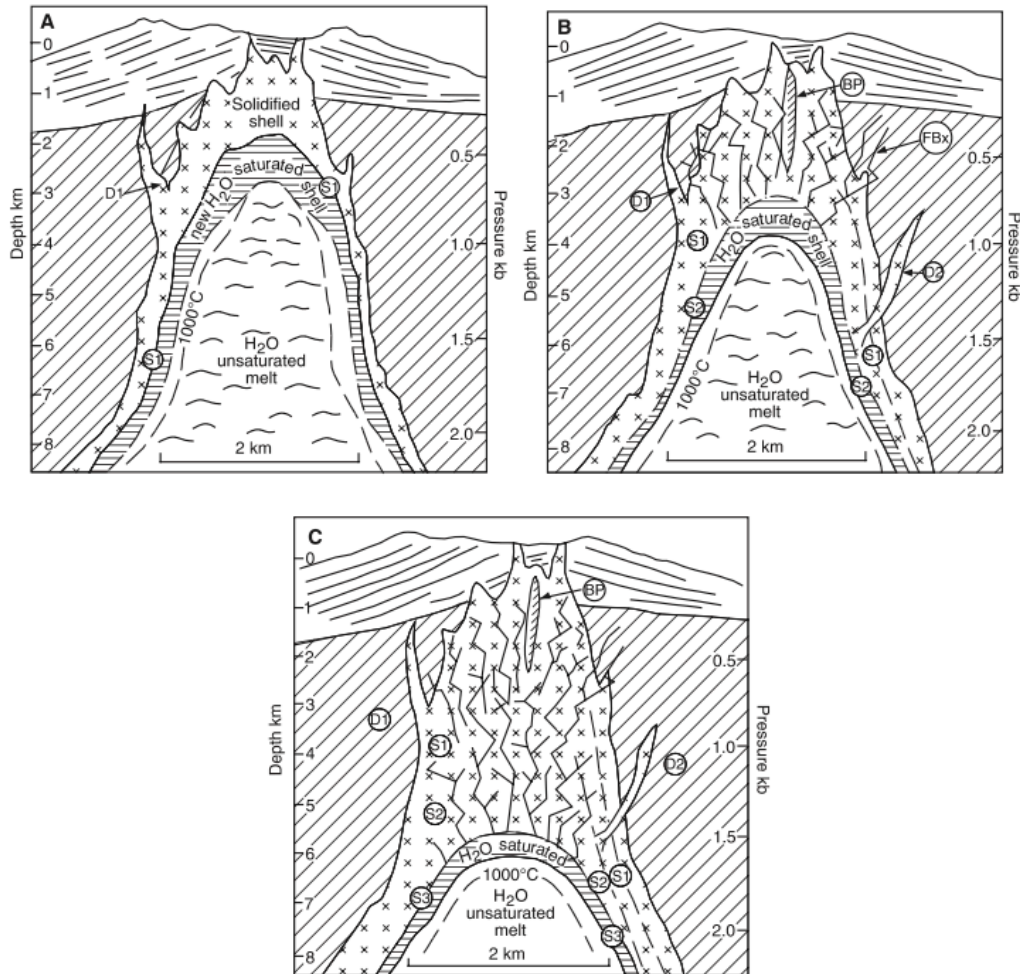
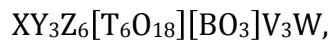
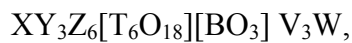


Figure 2.1: Evolution of a magmatic-hydrothermal system during cooling of a porphyry intrusion. After Burnham (1979) as cited in Pirajno (2009).

2.2. Tourmaline

Hawthorne and Henry (1999) writes the general formula for the tourmaline as:



Where common site occupancies include:

X= Ca, Na, K or □ (vacant)

Y= Li, Mg, Fe²⁺, Mn²⁺, Fe³⁺, Al, Cr³⁺, V³⁺, Fe³⁺

Z= Mg, Al, Fe³⁺, V³⁺, Cr³⁺

T= Si, Al

V= OH, O

W= OH, F

Tourmaline is known for being a complicated mineral both chemically and structurally, as the formula can include three light lithophile elements (H, Li, B) in variable amounts, and Fe can occur as both Fe^{2+} and Fe^{3+} (Hawthorne and Dirlam, 2011). These constituents are not easily analysed, and stoichiometric assumptions are often necessary in order to calculate a chemical formula (Hawthorne and Dirlam, 2011). Tourmaline has a wide range of stability from low to high temperature and pressures (<150°C to >700°C and 1 bar to <10 bar), but is strongly influenced by the composition of the fluid phase and mineral assemblage (Henry and Dutrow, 1996). Complex fine-scale zonation in tourmalines is indicative of rapid growth in a changing chemical environment (London and Manning, 1995).

Tourmaline species are defined by their chemical composition, where the primary criterion is the dominance of a particular chemical constituent at a given crystallographic site (Hawthorne and Dirlam, 2011). The resulting end-member composition for the different tourmaline species is listed in Table 2.1.

Table 2.1: Tourmaline species and their end-member compositions. After Hawthorne and Dirlam (2011)

General formula	(X)	(Y ₃)	(Z ₆)	T ₆ O ₁₈	(BO ₃) ₃	V ₃	W
Alkali Group							
Dravite	Na	Mg ₃	Al ₆	Si ₆ O ₁₈	(BO ₃) ₃	(OH) ₃	(OH)
Schorl	Na	Fe ²⁺ ₃	Al ₆	Si ₆ O ₁₈	(BO ₃) ₃	(OH) ₃	(OH)
Chromium-dravite	Na	Mg ₃	Cr ₆	Si ₆ O ₁₈	(BO ₃) ₃	(OH) ₃	(OH)
Vanadium-dravite	Na	Mg ₃	V ₆	Si ₆ O ₁₈	(BO ₃) ₃	(OH) ₃	(OH)
Fluor-dravite	Na	Mg ₃	Al ₆	Si ₆ O ₁₈	(BO ₃) ₃	(OH) ₃	F
Fluor-schorl	Na	Fe ²⁺ ₃	Al ₆	Si ₆ O ₁₈	(BO ₃) ₃	(OH) ₃	F
Elbaite	Na	Li _{1.5} Al _{1.5}	Al ₆	Si ₆ O ₁₈	(BO ₃) ₃	(OH) ₃	(OH)
Povondraite	Na	Fe ³⁺ ₃	Mg ₂ Fe ³⁺ ₄	Si ₆ O ₁₈	(BO ₃) ₃	(OH) ₃	O
Chromo-alumino-povondraite	Na	Cr ₃	Mg ₂ Al ₄	Si ₆ O ₁₈	(BO ₃) ₃	(OH) ₃	O
Fluor-buergerite	Na	Fe ³⁺ ₃	Al ₆	Si ₆ O ₁₈	(BO ₃) ₃	(O) ₃	F
Olenite	Na	Al ₃	Al ₆	Si ₆ O ₁₈	(BO ₃) ₃	(O) ₃	(OH)
Calcic Group							
Fluor-uvite	Ca	Mg ₃	MgAl ₅	Si ₆ O ₁₈	(BO ₃) ₃	(OH) ₃	F
Feruvite	Ca	Fe ²⁺ ₃	MgAl ₅	Si ₆ O ₁₈	(BO ₃) ₃	(OH) ₃	(OH)
Uvite	Ca	Mg ₃	MgAl ₅	Si ₆ O ₁₈	(BO ₃) ₃	(OH) ₃	(OH)
Fluor-liddicoatite	Ca	Li ₂ Al	Al ₆	Si ₆ O ₁₈	(BO ₃) ₃	(OH) ₃	F
Vacancy Group							
Foitite	□	Fe ²⁺ ₂ Al	Al ₆	Si ₆ O ₁₈	(BO ₃) ₃	(OH) ₃	(OH)
Magnesio-foitite	□	Mg ₂ Al	Al ₆	Si ₆ O ₁₈	(BO ₃) ₃	(OH) ₃	(OH)
Rossmannite	□	Li Al ₂	Al ₆	Si ₆ O ₁₈	(BO ₃) ₃	(OH) ₃	(OH)

The tourmaline minerals are divided into groups, based on the extensive compositional variation at the X, Y, Z and W sites, and the primary subdivision is based on variations at the X site (Figure 2.2) (Hawthorne and Dirlam, 2011). X-site vacant, alkali and calcic group are the primary tourmaline groups, where the occupancy of the Y site is considered in terms of the constituents ${}^Y\text{Fe}$, ${}^Y\text{Mg}$ and ${}^Y\text{Li}$ (Hawthorne and Dirlam, 2011). The Alkali tourmalines have Na (+ K) dominant at the X site, Al in the Z site, and at the C site, and OH at the W site (Hawthorne and Henry, 1999).

The chemical composition of tourmaline can also be represented as exchange vectors (Table 2.2) for certain specific ionic substitutions, for example the exchange vector FeMg_{-1} , which relates the compositions of schorl and dravite (London and Manning, 1995). The colour and spectroscopic properties of iron-bearing tourmalines do not correspond to iron concentration, but strong optical absorption and pleochroism can be ascribed to intervalence charge transfer between Fe^{2+} and Fe^{3+} (Mattson and Rossman, 1987). Blue to black colours associated with schorl in broad colour zones have been interpreted to be dominated by $\text{Fe}^{2+} \rightarrow \text{Fe}^{3+}$ and $\text{O}^{2-} \rightarrow \text{Fe}^{3+}$ charge-transfer processes, and the brown hues of dravite by uv-centered $\text{O}^{2-} \rightarrow \text{Fe}^{2+}$ and $\text{Fe}^{2+} \rightarrow \text{Ti}^{4+}$ processes (Taylor and Slack, 1984).

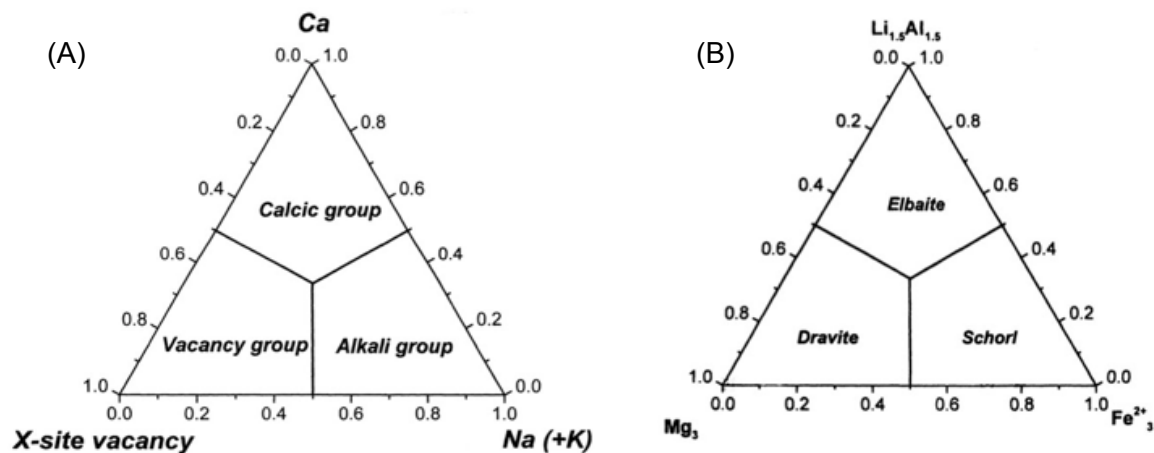


Figure 2.2: (a) Major compositional groups of the tourmaline minerals, classified according to the principal constituent at the X-site. (b) The compositional ranges of the principle tourmaline minerals in the alkali-tourmaline group.

Table 2.2: Common substitutions within and between sites including a compilation of exchange vectors after Henry and Guidotti (1985) and Henry and Dutrow (1996), as cited by Collins (2010).

Substitutions*	Exchange vectors
${}^Y\text{Mg} = {}^Y\text{Fe}^{2+}$	$\text{Fe}^{2+}\text{Mg}_{.1}$
${}^Y\text{Mn} = {}^Y\text{Fe}^{2+}$	$\text{Fe}^{2+}\text{Mn}_{.1}$
${}^Z\text{Al} = {}^Z\text{Fe}^{3+}$	$\text{Fe}^{3+}\text{Al}_{.1}$
${}^Z\text{Al} = {}^Z\text{Cr}^{3+}$	$\text{CrAl}_{.1}$
${}^{\text{O}(1)}\text{OH}^- = {}^{\text{O}(1)}\text{F}^-$	$\text{F}(\text{OH})_{.1}$
$2{}^Y\text{Fe}^{2+} = {}^Y\text{Li} + {}^Y\text{Al}$ elbaite substitution	$\text{LiAlFe}^{2+}_{.1}$
${}^X\text{Na} + 2{}^Y\text{Mg} = {}^X\text{□}^{**} + {}^Y\text{Al}$ alkali-defect substitution	$\text{□AlNa}_{.1}\text{Mg}_{.1}$
${}^X\text{Na} + {}^Y\text{Mg} + {}^{\text{O}(1)}\text{OH}^- = {}^X\text{□} + 2{}^Y\text{Al} + {}^{\text{O}(1)}\text{O}^{2-}$ aluminobuergerite substitution	$\text{□Al}_2\text{ONa}_{.1}\text{Mg}_{.2}(\text{OH})_{.1}$
${}^Y\text{Mg} + {}^{\text{O}(3)}\text{OH}^- = {}^Y\text{Al} + {}^{\text{O}(3)}\text{O}^{2-}$	$\text{AlOMg}_{.1}(\text{OH})_{.1}$
${}^Y\text{Fe}^{2+} + {}^{\text{O}(3)}\text{OH}^- = {}^Y\text{Fe}^{3+} + {}^{\text{O}(3)}\text{O}^{2-}$ buergerite substitution	$\text{Fe}^{3+}\text{OFe}^{2+}_{.1}(\text{OH})_{.1}$
${}^Y\text{Mg} + {}^{\text{T}}\text{Si} = {}^Y\text{Al} + {}^{\text{T}}\text{Al}$ Tshermaks substitution	$\text{Al}_2\text{Mg}_{.1}\text{Si}_{.1}$
$2{}^Y\text{Al} = {}^Y\text{Mg} + {}^Y\text{Ti}$	$\text{MgTiAl}_{.1}$
${}^X\text{Na} + {}^Y\text{Al} = {}^X\text{Ca} + {}^Y\text{Mg}$ uvite substitution	$\text{CaMgNa}_{.1}\text{Al}_{.1}$
${}^X\text{□} + {}^Y\text{Al} + {}^{\text{O}(1)}\text{OH}^- = {}^X\text{Ca} + {}^Y\text{Mg} + {}^{\text{O}(1)}\text{O}^{2-}$	$\text{CaMgO}(\text{OH})_{.1}\text{□}_{.1}\text{Al}_{.1}(\text{OH})_{.1}$
$2{}^Y\text{Mg} + {}^Z\text{Al} + {}^{\text{O}(1)}\text{OH}^- = 2{}^Y\text{Al} + {}^Z\text{Mg} + {}^{\text{O}(1)}\text{O}^{2-}$	$\text{CaMgO}(\text{OH})_{.1}\text{□}_{.1}\text{Al}_{.1}(\text{OH})_{.1}$

*Superscripts denote specific crystallographic sites.

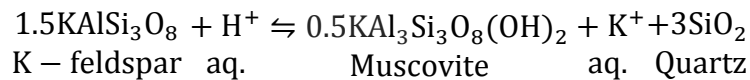
**This symbol represents an X-site vacancy

2.3. Alteration types

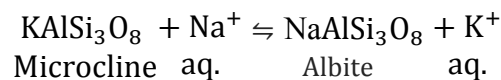
2.3.1. Metasomatism and alteration

Zharikov (2007) defines metasomatism as “a metamorphic process by which the chemical composition of a rock or rock portion is altered in a pervasive manner and which involves the introduction and/or removal of chemical components as a result of the interaction of the rock with aqueous fluids (solutions). During metasomatism the rock remains in a solid state.” The extent to which metasomatism occurs in a fluid flow pathway depends on the amount of fluid available, and the concentration of dissolved solids in the fluid. Many magmas give off acid, saline fluids as they crystallize, and may also contain volatile components derived from the melt. The magmatic brines will have a high transition metal content as well, making them potential ore-formers (Yardley, 2013).

Pirajno (2009) explains *Hydrogen Ion Metasomatism* as an alteration process that involves the ionic decomposition of H₂O into H⁺ and OH⁻, where H⁺ is consumed during reaction with the silicate minerals, thus changing the H⁺/OH⁻ ratio and releasing metal ions into the solution.



The formula displays one of the most common forms of alteration, the hydrolytic decomposition of K-feldspar to form muscovite or sericite and quartz, where the only requirement is the presence of H⁺ ions in an aqueous solution (Robb, 2005, Pirajno, 2009). If the reaction proceeds to the right, H⁺ ions will be consumed until the K-feldspar is used up, and upon further reaction with H⁺ ions in an increase in fluid/rock ratio, the muscovite would react to form kaolinite, as seen in formula 4 (Pirajno, 2009). The release of aqueous base cations in the evolving fluid from hydrogen ion metasomatism will have an effect on the nature of fluids, which may react with the wall rock in a type of alteration known as *cation metasomatism* or *base cation exchange* (Robb, 2005).



This formula depicts a chemical reaction during cation metasomatism, where microcline reacts with Na⁺, thus converting to albite and releasing K⁺ in the aqueous fluid, called albitisation (Na replaces K) (Pirajno, 2009). If the fluid phase is enriched in K, there may be a

transfer of K to the wall rocks, where albite is converted to microcline in a process called microclinisation (K replaces Na) (Pirajno, 2009).

Alteration of a rock is marked by the development of a mineral assemblage that is different from the original one, reflecting the original rock composition and the amount and concentration, activity and chemical potential of the fluid components, such as H^+ , CO_2 , O_2 , K^+ , H_2S and SO_2 (Robb, 2005, Pirajno, 2009). The stabilities of mineral assemblages are largely dictated by temperature and pressure, and the host rock composition controls which ingredients are available to make up a particular alteration assemblage. The fluid/rock ratio dictates the extent to which reactions will move to completion, and as hydrothermal fluids migrate along pathways, alteration should be viewed in a dynamic sense as a function of changing fluid/rock ratios (Robb, 2005).

The effect of the hydrothermal alteration on a wall rock is a result of variations in the activities of K^+ and H^+ ions in the system, the aK^+/aH^+ ratio. This ratio decreases as the system evolves towards lower temperatures and pressures, meaning that the alteration process would move from alkalic to argillic in a theoretically continuous system with increasing H^+ metasomatism, schematically shown in figure 4 (Pirajno, 2009). The types of alteration discussed, in order of increasing H^+ metasomatism, are potassic alteration, Propylitic, Phyllic/sericitic alteration and greisen, tourmalinization and argillic alteration.

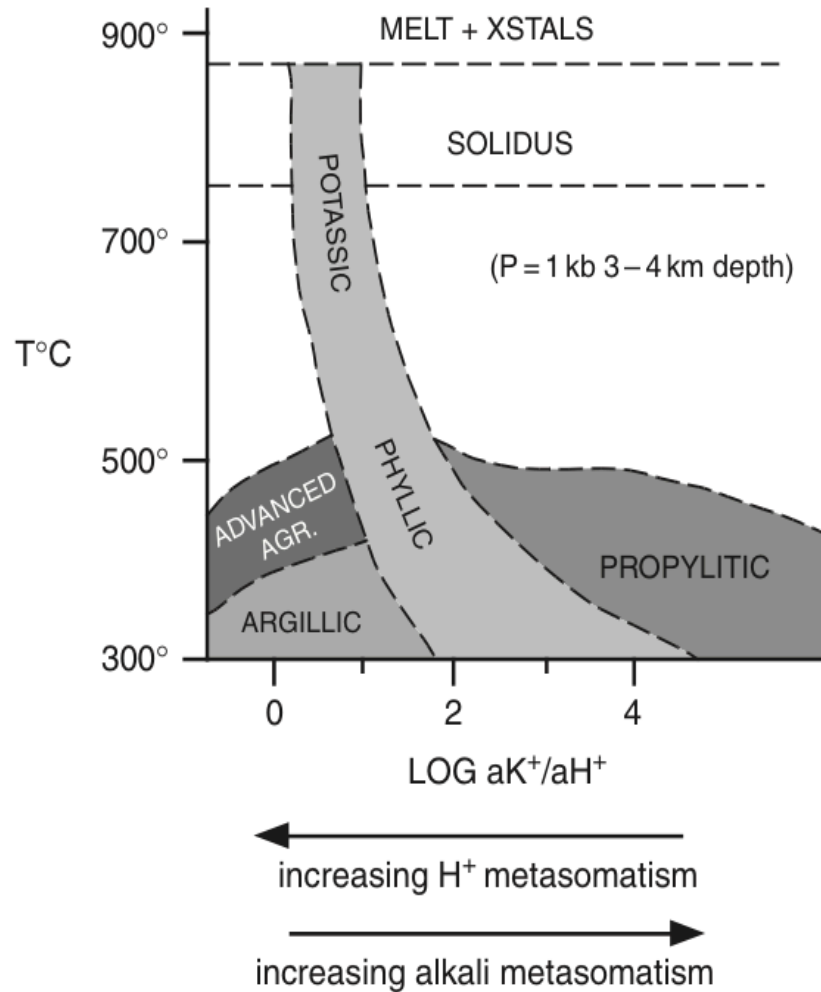


Figure 2.3 Idealized evolutionary alteration sequence as a function of temperature and activities of K^+ and H^+ (Pirajno, 2009).

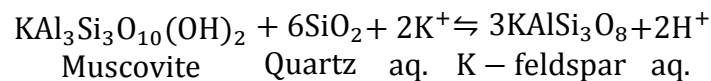
2.3.2. Potassic alteration

Potassic alteration is the highest temperature alteration, occurring at 500-600 °C in high temperature core zones in epithermal systems and porphyry systems. Common mineral assemblages are new K-feldspar and/or biotite, chlorite and quartz, as well as varying quantities of other minerals such as albite, sericite, anhydrite, apatite, hematite, magnetite and occasionally rutile, derived from the breakdown of biotite (Robb, 2005, Pirajno, 2009).

The alteration is a result of H^+ metasomatism and K^+ metasomatism, where K^+ replaces Na^+ , replacing plagioclase and mafic silicate minerals by intermediate to ordered microcline. The K-feldspars in potassic zones are characteristically reddish in colour in hand specimens, which is manifested by turbidity of feldspar crystals in thin sections (Pirajno, 2009, Pirajno, 2013). Kinnaird et al. (1985) concludes it is due to expulsion of hematite laths from the

feldspar lattice, and Meyer and Hemley (1967) also explains the colour to be exsolution of hematite, of Fe³⁺ initially present in aluminium sites, released during the K for Na exchange. A more recent theory is that the colour is due to formation of hematite within pores in K-feldspar, as a sub-solidus fluid-rock interaction depending on the iron content in the fluid (Putnis et al., 2007). According to Putnis (2002), the turbidity in K-feldspar is due to microporosity, from pseudomorphic recrystallization of plagioclase in the presence of a fluid phase.

Volatile fluids escaping from a hot two-feldspar granite into cooler rock cannot reach equilibrium with both Na-rich and K-rich feldspar until the K/Na ratio in the fluid phase is lowered, accomplished by the replacement of Na-rich feldspar by K-rich feldspar, or sericitization of plagioclase (Orville, 1962). In a rock consisting of equal volumes of muscovite, K-rich feldspar and quartz, the following chemical reaction occurs when introduced to a K-rich fluid phase (Orville, 1962):



The reaction will stop unless quartz and K⁺ is introduced from outside, and the requirement of excess quartz results in a final K-feldspar rich rock with a small amount of quartz (Orville, 1962).

2.3.3. Propylitic alteration

Propylitic alteration describes a weakly metasomatic alteration, typically of relative mafic rock types (i.e. andesite, basalt etc.), representing low to intermediate temperatures of 200-350 °C, and low fluid/rock ratios. The alteration type characterizes the margins of porphyry Cu deposits, as well as epithermal precious metal ores (Robb, 2005). The alteration type is characterized by the addition of H₂O and CO₂, and locally S, with no appreciable H⁺ metasomatism. The typical mineral assemblage consists of chlorite and epidote, with lesser amounts of clinzoisite, carbonates, albite, K-feldspar, pyrite and zoizite. In some places, sericite, Fe-oxides, montomorillonite and zeolite may also be common (Robb, 2005, Pirajno, 2009). Chloritization is a subdivision of propylitization, caused by Mg –metasomatism (Evans and Evans, 1993, Pirajno, 2009). Chlorite may be present alone with quartz or tourmaline, but usually with other propylitic minerals (Evans and Evans, 1993). Development of secondary chlorite may be a result of the alteration of mafic minerals, e.g. biotite, or from the introduction of magnesium and iron (Evans and Evans, 1993).

2.3.4. Phyllic (sericitic) alteration and greisenisation

Phyllic alteration is probably the most abundant, widespread and significant of all alteration assemblages, and is very common in a variety of hydrothermal ore deposits, especially porphyry Cu deposits (Meyer and Hemley, 1967, Robb, 2005). H^+ metasomatism of feldspars forms a typified assemblage of quartz – sericite – pyrite (QSP), with minor associated K-feldspar, kaolinite, calcite, biotite, rutile, anhydrite and apatite, over a wide temperature range (Pirajno, 2009). This alteration grades into the potassic type by increasing amounts of K-feldspar and/or biotite, and into the argillic type by increasing amounts of clay minerals (Pirajno, 2009).

Increasing amounts of topaz, coarse-grained muscovite tourmaline, quartz and zunyite (a very rare high Al silica mineral) characterize a transition to *greisen*-type alteration (Pirajno, 2009). Greisen is an old miners term, and is a common alteration type near tin and molybdenite ore bodies in granite, being most favourable in the cupola zones of S-type granites that contain Sn-W mineralization (Meyer and Hemley, 1967, Robb, 2005, Pirajno, 2009). Muscovite preferentially replaces the biotite and feldspars, and during destabilisation, metal cations locked in the mineral lattice are released. These are possibly responsible for the paragenetically later associated metallic mineralization (Pirajno, 2009).

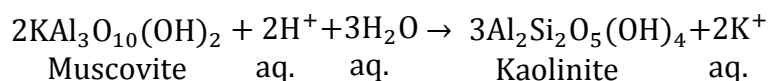
2.3.5. Tourmalinization

Quartz and muscovite greisens may be followed (or preceded) by progressive stages of B-metasomatism and thus developing tourmaline, which in excess of 15% in a rock is classified as a tourmalinite (Pirajno, 2009). The environment in which the tourmaline originated can be indicated from the composition, as tourmaline has the ability to preserve textural, chemical and isotopic features that reveal details about the hydrothermal system in which it formed (Pirajno, 2009, Slack and Trumbull, 2011). An example of this is seen in southwest England, where the schorl variety of tourmaline is a common product of alteration, especially around the zones of economic mineralization (Alderton et al., 1980). Concentric growth zoning, often rhythmic, is a result of compositional changes in the growth medium, as the tourmaline composition is governed largely by changes in the fluid and/or wall rocks, and by chemical equilibrium with coexisting phases (Slack and Trumbull, 2011).

In general, Fe-rich tourmalines are associated with Sn-W deposits of greisen affinity, and Mg-rich tourmalines are found with massive sulphide deposits and stratabound W deposits (Pirajno, 2009). Also associated with Sn-W deposits and breccia pipes are pervasive tourmalinization, often being particularly abundant in zones of fracturing in the country rocks surrounding greisenised granites. The quartz-tourmaline-dominated assemblages form pervasive replacements, as well as cross-cutting veins (Pirajno, 2009).

2.3.6. Argillic alteration

Argillic alteration is an alteration type characterized by the formation of clay minerals, due to intense H^+ metasomatism and acid leaching, and is subdivided into intermediate and advanced categories depending on the intensity of host mineral breakdown (Robb, 2005, Pirajno, 2009). Alteration occurs typically on the fringes of porphyry systems, at temperatures between 100 and 300 °C (Robb, 2005, Pirajno, 2009). Typical for Intermediate argillic alteration is the replacement of plagioclases and the mafic silicates by clay minerals kaolinite and smectite group, with a presence of illite, chlorite, montmorillonite, kaoline group clays and minor sericite, while K-feldspar may remain unaltered (Pirajno, 2009). The breakdown of muscovite to kaolinite occur as follows:



Advanced argillic alteration is due to intense acid attack, and represents an extreme form of base leaching where rocks have been entirely stripped of alkali elements, at high/fluid rock environments. For feldspars and mafic silicate, feldspar is completely destructed, and dickite, kaolinite, pyrophyllite, barite, alunite and diaspora are typical mineral phases, and quartz, topaz, tourmaline and sulphides may be present (Robb, 2005, Pirajno, 2009).

Chapter 3. Regional Geology

This chapter addresses the regional geology of the Cornwall area, starting with the variscan orogeny and the subsequent emplacement of the Cornubian Batholith. The batholith is described in terms of petrography and geochemistry, followed by a more thorough description of the Land's End pluton. The alteration and mineralizations are then described, especially in terms of tourmalinization, greisenisation and Sn-mineralizing veins. Finally, previous studies are reviewed, dealing with tourmaline-quartz mineralization at Nanjizal, Rutile as a tin-tungsten host in a tourmaline breccia at Wheal Remfry and geochemical constraints on zoned hydrothermal tourmaline at Roche rock.

3.1. The Variscan Orogeny

The variscan orogeny is directly linked to the Late Paleozoic formation of Pangea, and affected vast areas of continental crust, running from Portugal over Poland to Cornwall and the Scilly Islands in a broad, sinuous E-W trending fold belt (LeBoutillier, 2002, Kroner and Romer, 2013). In the Devonian and carboniferous periods, the Rheic ocean was in a process of closure due to the convergence of Gondwana and Laurasia. The Rheic basin was compressed and folded to form the Variscan orogen, with a crustal thickness of ~ 40 km. Orogenic collapse and extension followed soon after, accompanied by renewed rifting and the formation of sedimentary basins and volcanism (LeBoutillier, 2002).

3.2. The Cornubian batholith

The Cornubian Batholith of South England extends from Dartmoor in Devon through Cornwall to the Isles of Scilly, running in excess of 200 km (Manning, 1998, LeBoutillier, 2002). It is exposed in Cornwall in five major plutons; Land's End, Tregonning – Godolphin, Carmenellis, St Austell and Bodmin moor, as well as eleven satellite intrusions (Figure 3.1) (Manning, 1998). The batholith consists of S-type, felsic, two-mica granites, is strongly peraluminous, have high K/Na ratios, and is characterized by extreme oversaturation in Al, as well as extreme enrichments in elements such as B, P, Rb, Sn, Cs and W (Chappell and Hine, 2006). The granites also have an exceptionally high content of the radioactive elements K, Th and U, which account for the high heat production and geothermal gradient of the area (Manning, 1998).

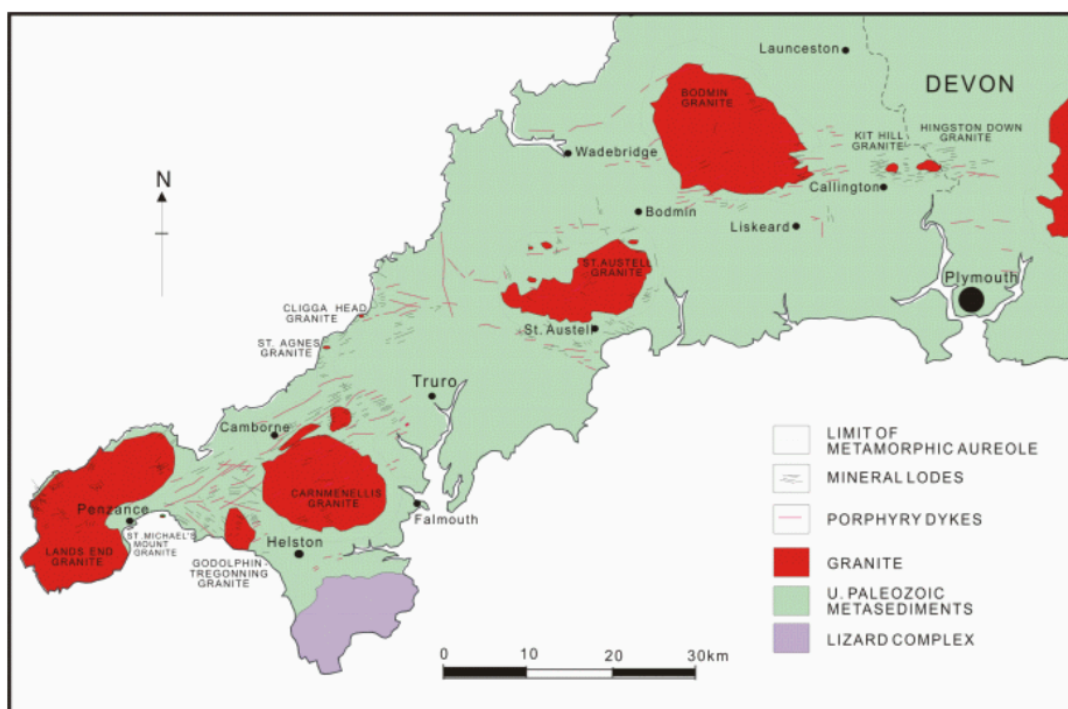


Figure 3.1: A simplified geological map of the major and minor granite outcrops in Cornwall. After LeBoutillier (2002).

The exposed granites are the cupolas of a continuous large elongated batholith, whose floor lies between 8 and 20 km below the surface (Bott et al., 1958). Rb-Sr-studies by Darbyshire and Shepherd (1985) have established that the major granites were emplaced between 290 Ma and 280 Ma.

The dominant rock type in Cornwall is a medium-to coarse-grained two mica granite, accounting for more than 90 % of the total exposure (LeBoutillier, 2002). This granite is classified by Exley et al. (1983) as Type B, and its petrographic summary can be found in Table 3.1. These granites are commonly megacrystic, with K-feldspars megacrysts varying from 2 cm up to 20 cm (Manning, 1998). These granites are characterized by the presence of biotite (6%), perthitic K-feldspar megacrysts (32%), plagioclase (22%) and quartz (24%). Muscovite (4%) occurs widely as a distinct phase or alteration product, and tourmaline (1%) is a common accessory mineral (Manning, 1998, Chappell and Hine, 2006). Fine-grained porphyritic and non-porphyritic granites make up less than 10 % of the outcrops, Lithium-enriched granites only occur to any extent in the Tregonning-Godolphin and St Austell

plutons, and topaz and fluorite granites are restricted to the western lobe of the St Austell granite (LeBoutillier, 2002).

Table 3.1 Petrographic summary of granite type B, coarse-grained megacrystic biotite granite. After Exley and Stone (1982).

Minerals (approximate mean modal amounts in parenthesis)						
Texture	K-Feldspar	Plagioclase	Quartz	Micas	Tourmaline	Other
Medium to coarse. Megacrysts max. 5-17 cm, mean about 2 cm- Hypodiorphic, granular	Eu – to subhedral, micropoerthitic (32%)	Eu- to subhedral. Often zoned. Cores An ₂₅ -An ₃₀ . Rims An ₈ -An ₁₅ .	Irregular (34%)	Biotite, often in cluster (6%). Muscovite (4%)	Eu – to anhedral. Often zoned. “Primary” (1%)	Zircon. Ore. Apatite. Andalusite Etc. (1%)

3.3. Land's End Granite

The Land's End Granite is the youngest of the major plutons which form the Cornubian batholith, emplaced between 277 to 274.5 Ma (Chen et al., 1993). In size, the pluton is the second largest of the cornubian batholith at 190 km² (Chappell and Hine, 2006). Pownall et al. (2012) proposes a laccolitic emplacement model of the Land's End granite, where successive intrusion and coalescence of dyke-fed granites seems to have formed a tabular intrusion with a flat base and domed roof. Müller et al. (2006) establishes three main stages of intrusions, in order from older to younger; (1) fine-grained biotite granites (FGG) containing K-feldspar megacrysts with an average length > 3 cm. (2) coarse-grained biotite granite containing K-feldspar megacrysts with an average length > 3 cm. (3) fine-grained porphyritic Li-siderophyllite granite containing sparse K-feldspar megacrysts with an average length > 3 cm and co-existing medium-grained equigranular Li-siderophyllite granites. The mineralogy and petrography of the main stages of intrusions are described in Table 3.2 Distributions of textural variations in the Land's End pluton are shown in Figure 3.2. In general, the granites in Land's End are strongly peraluminous, high K, calc-alkaline rocks with low phosphorus content.

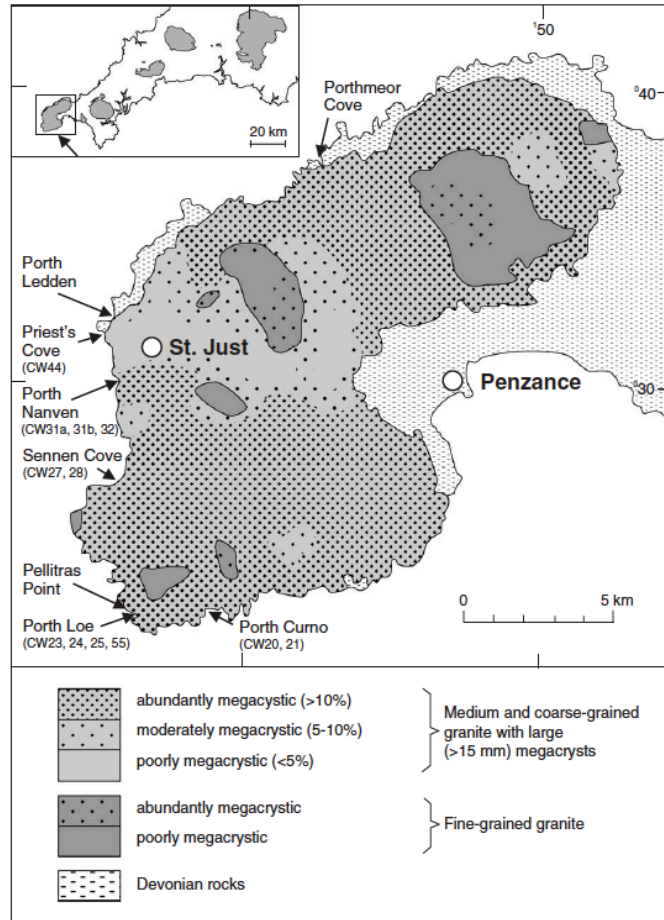


Figure 3.2: Distribution of textural variations within the Land's End Pluton. The inset shows the location of the pluton within the Cornubian batholith in SW England. after Müller et al. (2006).

Table 3.2: Mineralogical compositions and petrographic features of the main granite units of the Land's End pluton (Müller et al., 2006). The nomenclature of micas by (Tischendorf et al., 2001) is applied. ap - apatite, crd -cordierite, kfs -K-feldspar, mon - monazite, mu - muscovite, pl - plagioclase, qz –quartz, tur –tourmaline, zir – zircon.

Major granite units	Macroscopic features	Rock-forming minerals	Major accessories (dominant minerals in italics)
Fine-grained porphyritic granite (FGG)	Common kfs megacrysts (>3 cm), sparse crd (up to 1 cm), grey	qz, kfs, pl (An ₁₀₋₃₃), magnesian siderophyllite, crd, ferroan polyolithionite	<i>ap, zir, mon, tur</i> , xenotime, rutile, ilmenite
Medium- to coarse-grained porphyritic granite (CGG)	Common kfs megacrysts (>3 cm), sparse crd (up to 1 cm), whitish grey	qz, kfs, pl (An ₁₀₋₃₃), magnesian siderophyllite, crd, ferroan polyolithionite	<i>ap, zir, mon, tur</i> , xenotime, rutile, ilmenite
Albite microgranite	Fine-grained equigranular, white	qz, pl (An ₇₋₁₂), ferroan polyolithionite, kfs,	<i>ap, zir, mon, tur, ilmenite</i> , rutile, thorite
Porphyritic Li-siderophyllite granite	Fine-grained with sparse kfs phenocrysts (<3 cm), sparse crd (up to 0.5 cm), whitish grey	qz, kfs, pl (An ₈₋₁₄), lithian siderophyllite, crd, siderophyllite	<i>ap, zir, mon, tur</i> , xenotime, rutile, ilmenite, thorite, ferrocolumbite, sulphides (chalcopyrite, arsenopyrite, galena), bismuth
Equigranular Li-siderophyllite granite	Fine- to medium-grained equigranular, yellowish white	qz, kfs, tur, pl (An ₈₋₁₄), lithian siderophyllite	<i>ap, zir, mon, rutile, ab</i> , xenotime, thorite, ferrocolumbite, fluorite
Tourmaline granite (Porth Ledden)	fine-grained equigranular, pink	qz, tur, kfs, lithian muscovite, ferroan polyolithionite, pl (An ₂)	<i>ap, zir, mon</i> , niobian and tantalum rutile, cassiterite, thorite

3.4. Alteration and associated mineralizations in Cornwall

Cornwall's metal deposits come in a great variety, with a considerable production of Sn, Cu, Pb, Zn, Fe, Ag and As in historic times (Scrivener and Shepherd, 1998). Granite related hydrothermal veins carrying mineralizations of Sn, W, As, Cu and Sn are of early Permian age, 270-290 Ma (LeBoutillier, 2002). The chronologies of the different mineralization types are presented in Table 3.3. Two main structural trends are apparent: an early set of veins trending mostly between WNW-ESE and ENE- WSE (known generally as E-W) which carry Sn-Cu-As-W-minerals, and a later set trending roughly N-S (known as cross-courses) characterized by Pb- Zn-Ag ores (Scrivener and Shepherd, 1998).

Table 3.3: Chronology of the mineralization types and metals in the Cornubian orefield. After Leveridge et al. (2002), as cited in Camm and Hedley (2005).

Age	Mineralization type	Metals
Mid Triassic 230-240 Ma	Hydrothermal vein (Post-granite crosscoursure)	Pb- Ag -Zn- Cu – As- F-Ba- Ni-Co-U-Au-Pd-Se
Early Permian 270-290 Ma	Hydrothermal vein (Granite related)	Sn-W-As-Cu-Zn
Late Carboniferous 290 -300 Ma	Hydrothermal vein (Pre-granite)	Sb-Pb-Zn
Early Carboniferous 332-350 Ma	Stratiform exhalative Sedimentary diagenetic	Mn Pb-Zn
Mid to Late Devonian 367 -381 Ma	Stratiform exhalative /replacement volcanic association Stratiform Basic igneous association	Fe-Sb Sb-As-Pb-Cu-Ag-Au
Early Devonian 390 -396 Ma	Stratabound epigenetic Basic volcanic association	Fe-As

Most of the deposits are of hydrothermal origin, and the main stage mineralized veins in the province are enclosed within a zone of wall rock alteration of varying type and intensity (Scrivener and Shepherd, 1998, LeBoutillier, 2002). The temperature of the mineralizing fluids forming greisen-bordered vein systems (Sn/W) were 400-450 °C, with varying salinities (5-50 wt%) and high pH (2,4 to 4,9) (LeBoutillier, 2002, Camm and Hedley, 2005). During the early cassiterite phase, the average salinity was > 20 % (Scrivener and Shepherd, 1998). The origin of the hydrothermal fluids were hydrous saline magmatic fluids exsolved from the crystallizing granite, and were later mixed with various amounts of external meteoric fluids of meteoric origin (Scrivener and Shepherd, 1998). The Paragenetic sequence of vein mineralization is depicted in Table 3.4.

Table 3.4: Paragenetic sequence of vein mineralization in granites in Cornwall, southwest England. After (Exley et al., 1983)

Paragenetic Stages	GREISEN VEINS	HYPOTHERMAL				MESOTHERMAL		EPITHERMAL	
		1	2	3	4	5a	5b	6	7
T _h °C of fluid inclusions		500–250				350–150		150>	
Salinity of fluids Equiv. Wt% NaCl		40–8				10–0.1		-25	
Gangue Minerals	<ul style="list-style-type: none"> — Feldspar ————— — Muscovite ————— — Tourmaline ————— 		<ul style="list-style-type: none"> — Chlorite ————— — Haematite ————— 	<ul style="list-style-type: none"> — Fluorite ————— — Chalcedony ————— 	<ul style="list-style-type: none"> — Quartz ————— — Barytes, Dolomite, Calcite ————— 				
Ore Minerals		<ul style="list-style-type: none"> — Arsenopyrite ————— — Wolframite ————— — Cassiterite ————— — Molybdenite ————— — Specularite ————— — Scheelite ————— — Stannite ————— — Chalcocopyrite ————— — Pyrite ————— — Sphalerite ————— 			<ul style="list-style-type: none"> — Pitchblende ————— — Niccolite ————— — Smaltite ————— — Cobaltite ————— — Bismuthinite ————— — Argentite ————— — Galena ————— 		<ul style="list-style-type: none"> — Tetrahedrite ————— — Boumonite ————— — Siderite ————— — Haematite ————— — Marcasite ————— — Jamesonite ————— — Sibnite ————— 		
Economically important elements		<ul style="list-style-type: none"> — As ————— — W ————— — Sn ————— 	<ul style="list-style-type: none"> — Cu ————— 		<ul style="list-style-type: none"> — U ————— — Ni ————— — Co ————— — Bi ————— — Zn ————— — Ag ————— — Pb ————— — Fe ————— — Sb ————— 				
Typical form of emplacement	Sheeted veins, Stockworks, Fault-related fractures	Main Lodes, Caunter Lodes, Fault-related veins, breccias, Stockworks and Carbonas				Lodes, Caunter Lodes, Faults, Cross-Courses		Mainly Cross-Courses and Faults	
Wall-rock alteration		<ul style="list-style-type: none"> — Greisenization ————— — Tourmalinization ————— 	<ul style="list-style-type: none"> — Feldspathization ————— — Chloritization ————— — Haematization ————— 	<ul style="list-style-type: none"> — Silicification ————— 					

Scrivener and Shepherd (1998) describes two distinct styles of mineralization associated with cassiterite, caused by the early, magmatic hydrothermal fluids, which is elaborated in Table 3.5.

Table 3.5: The two distinct mineralization types of granite -related mineralization in Cornwall. After Scrivener and Shepherd (1998)

Type 1	Type 2
Veins of quartz with cassiterite and/or wolframite; minor lollingite and base metal sulphides may be present. The veins are enclosed by greisen-altered selvages to a mass of white mica and quartz, commonly with topaz.	Bodies of quartz and tourmaline with cassiterite, commonly also with hematite. Sulphides are rare. Wall rock alteration involved replacement of the host by tourmaline and secondary feldspar, and is commonly marked by intense reddening

Tourmaline-cassiterite and greisen-bordered veins (with cassiterite+ wolframite) developing adjacent to and in the roof of the granite plutons are the earliest recognized mineral deposits, from high temperature (>400°C) magmatic fluids (Scrivener and Shepherd, 1998). The difference in style between tourmaline-rich and greisen-hosted early vein mineralization have been suggested to be due to separation of a parent magmatic fluid into a denser fraction (tourmaline veins) and a lighter, CO₂-rich fractioning (greisen) (Shepherd et al., 1985). At a number of localities, early quartz-tourmaline vein complexes carry cassiterite, which may be locally rich but overall generally low of grade. An example is at Ding Dong Mine, in the centre of Land's End granite (Scrivener and Shepherd, 1998).

Greisen alteration enclosing quartz veins carrying cassiterite and/or wolframite is a result of early magmatic-hydrothermal hydraulic fracturing (Scrivener and Shepherd, 1998). The greisen veins often occur as sheeted complexes accompanied by pervasive argillic or sericitic alteration, both in the granite (endogranitic) and in the metasediments (exogranitic) (Scrivener and Shepherd, 1998, Camm and Hedley, 2005). A sample of a greisen vein from Cligga Head is shown in Figure 3.3.

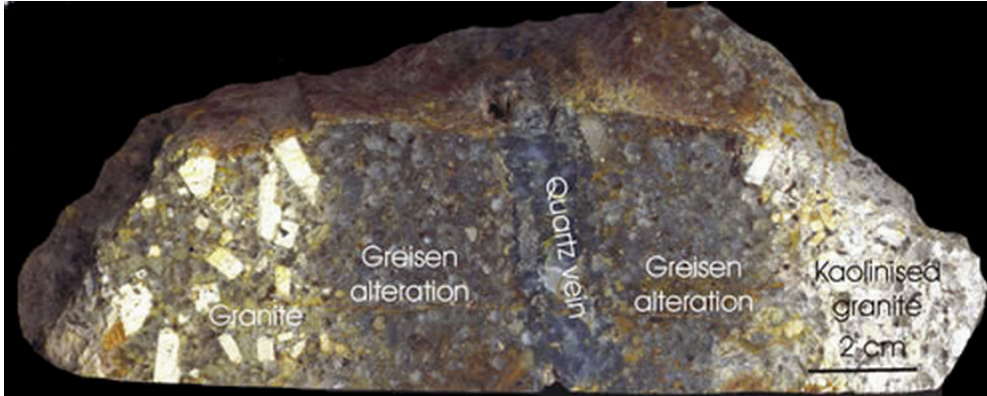


Figure 3.3: Greisen vein from Cligga Head, Perranporth, Cornwall. After Camm and Hedley (2005)

The main stage mineralization is associated with early cooling of the granite, but have a protracted history of vein formation with multiple episodes of fracturing, brecciation and mineralization (Scrivener and Shepherd, 1998). The varieties of hydrothermal alteration recognised in the cornubian orefield are tourmalinization, sericitization, chloritization, alkali metasomatism and argillization (Camm and Hedley, 2005).

Tourmaline, commonly as schorl, is a distinctive feature of the cornubian batholiths, and early quartz-tourmaline vein complexes may carry cassiterite (London and Manning, 1995, Scrivener and Shepherd, 1998). The primary tourmaline in the granites is essentially unzoned chemically, uniform in composition and consists of individually disseminated interstitial brown to yellow grains, often mantled by a later generation of green-blue prismatic, needle-shaped tourmaline of hydrothermal origin (London and Manning, 1995). The vein-associated tourmaline has a complex optical and chemical oscillatory zonation, but on average its composition overlaps the primary magmatic, and is differentiated by a larger variation of $Fe/(Fe+Mg)$ (London and Manning, 1995). The igneous tourmaline is close to schorl-dravite in composition, and is interpreted as a solid-solution phase crystallized in a closed magmatic system. The complex chemical zonation in hydrothermal tourmaline is interpreted as a reflection of changing fluid compositions, fluctuations in P and T, and possibly rapid disequilibrium growth (London and Manning, 1995).

Quartz-tourmaline veining is very abundant in and around the granites, and is commonly accompanied by wall rock alteration (London and Manning, 1995, Scrivener and Shepherd, 1998). The alteration involves replacement of primary granite by tourmaline and secondary feldspar, often showing distinct reddened or pink coloration, and biotite has been replaced by tourmaline or chlorite. Minor phases which may be present is Ti-bearing species (anatase, brookite and rutile), and secondary monazite (Scrivener and Shepherd, 1998, LeBoutillier et al., 2003). The former exhibit textures compatible with hydrothermal formation, where a likely source of titanium is from the breakdown of biotite in the granite wall rocks, releasing Fe, Mg, Al and Ti into the hydrothermal fluids at temperatures at around 400 °C (LeBoutillier et al., 2003). Such association of Ti minerals, monazite and tourmaline suggest that these phases were deposited from primarily magmatic hydrothermal fluids of high temperature, high salinity and low pH (LeBoutillier et al., 2003).

3.5. Previous studies of Tourmaline and Rutile associated with Sn-mineralizations in Cornwall

3.5.1. Tourmaline-quartz-cassiterite mineralization of the Land's End granite at Nanjizal, West Cornwall

LeBoutillier et al. (2002) has studied the tourmaline-quartz-cassiterite mineralization in Nanjizal, a cove, 2 km SE of Land' End. Tourmaline-quartz veins were mapped and the mineralogy was analysed. Three principle vein-forming episodes were recognised, illustrated in Figure 3.4 as rose diagrams. The first mineralizing episode comprises steeply dipping ENE- WSE striking tourmaline ± quartz veins. The second mineralizing episode comprises steep NNW-SSE striking schorl-cassiterite veins. The third mineralization episode is dominated by steeply dipping WNW-NW striking Quartz-limonite –chalcedony veins that are associated with wall rock hematitisation and kaolinization. The fluids were interpreted as being primarily of magmatic origin, but mark the transition from purely magmatic hydrothermal (High-Mg) to fluid with meteoric source (high Fe, oxidising).

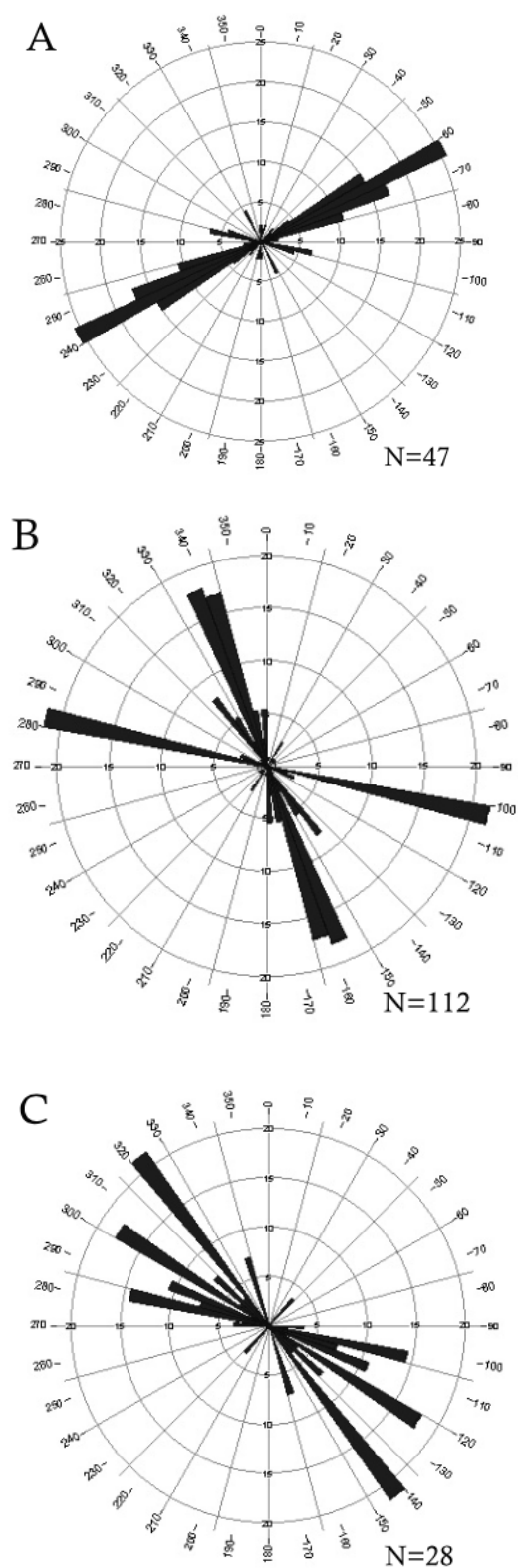


Figure 3.4: Rose diagrams for (a) Tourmaline (shorl) –quartz veins, (b) tourmaline (shorl) veins and (c) Quarts-limonite –chalcedony veins at Nanjizal. After LeBoutillier et al. (2002).

3.5.2. Rutile - the tin-tungsten host in the intrusive tourmaline breccia at Wheal Remfry, SW England

Müller and Halls (2005) have analysed trace element composition in accessory rutile from the tourmaline breccia in Wheal Remfry, Cornwall. No cassiterite was identified, and rutile is the main carrier of Sn. The rutile is dendritic, corroded and overall lath-shaped, and four different domains were distinguished from BSE images, as illustrated in Figure 3.5. Quantitative microprobe of rutile, analysing Al, Si, Ca, Zr, Nb, V, Fe, Sn and W, shows that it contains variable amounts of Fe, Nb, V, W and Sn. Tourmaline was analysed by making an analytical profile using microprobe, where the core plots in the dravite field and the outermost zone has schorl composition. The amount of Fe, W and Sn reach a maximum in the latest overgrowth, and has increased progressively during the history of crystallization. The strong increase of Fe in the last overgrowth of both rutile and tourmaline suggest an open-system behaviour, with increasing contributions from relatively oxidising formation waters. Sn^{4+} has entered the sites available in rutile, as the amount of Sn in the fluids probably was too low to deposit cassiterite.

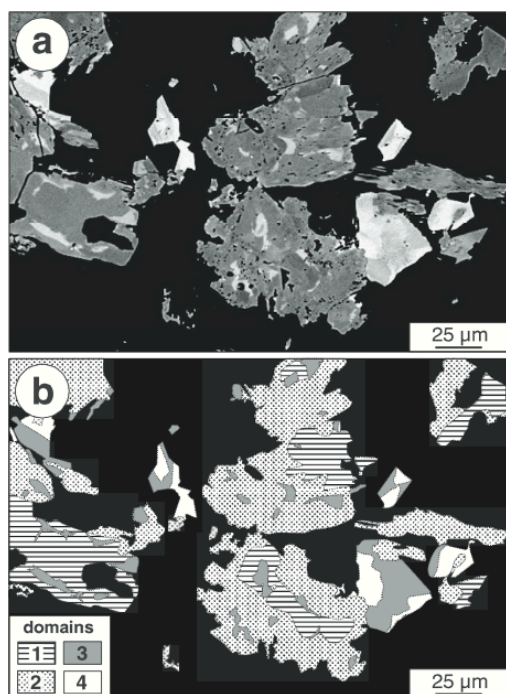


Figure 3.5: (a) BSE image of rutile in the matrix of tourmaline breccia at Wheal Remfry. (b) Distribution map of four different domains within the rutile shown in (a). After Müller and Halls (2005)

3.5.3. Geochemical constraints on zoned hydrothermal tourmalines on fluid composition and Sn Mineralization: an example from Fault Breccias at Roche, SW England

Williamson et al. (2000) studied the hydrothermal fluid evolution of the St Austell granite by geochemical analysis of tourmaline from a <2 cm wide brecciated vein within a massive quartz-tourmaline (MQT) rock at Roche. Tourmaline occurs as angular, fractured tourmaline, often with concentrically zoned hydrothermal overgrowths, as well as fine-grained needles throughout the quartz matrix. Quantitative microprobe analysis was performed making two traverses across the contact and secondary overgrowths. The overgrowths were divided into four zones, and traverses were plotted showing Fe and Mg in a.p.f.u, Al in Y-site and Sn wt.%, as shown in Figure 3.6.

Zone 1 is Mg rich, and lies within the dravite field. Zones 2, 3 and 4 fall within the schorl field. Zones 2 and 4 have high Fe (<3 a.p.f.u), and with the maximum occupancy in the Y-site of 3 a.p.f.u, the “excess” Fe is thought to enter the Z-site as Fe³⁺. Sn was found in significant levels in zone 2, and to lesser extent in zones 1 and 4. Sn is interpreted as being structurally bound in the tourmaline structure as Sn⁴⁺, rather than being contained as a discrete mineral. Substantial chemical changes in the hydrothermal fluid are reflected by variations in the tourmaline composition. The overgrowths are interpreted as having initially crystallized from relatively Mg- and Al-rich hydrothermal fluids of magmatic origin, which were progressively mixed with more oxidized, Fe-rich formation waters.

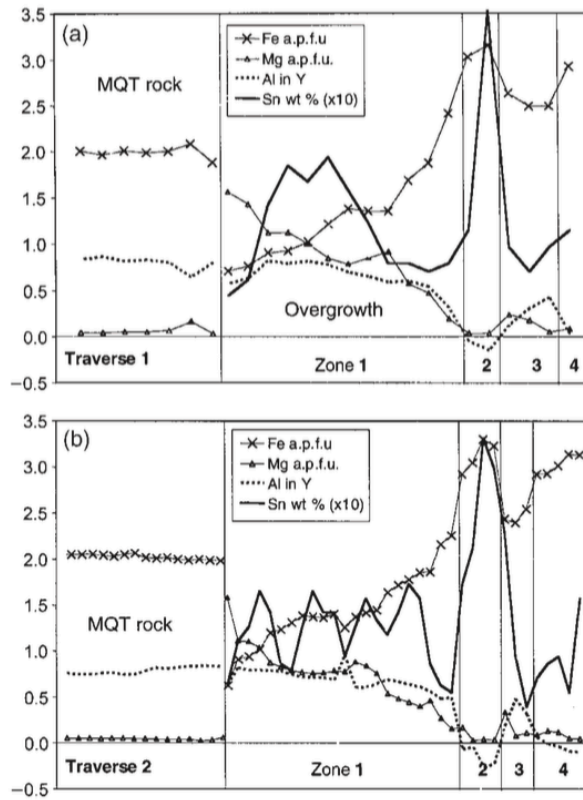


Figure 3.6: Microprobe traverse from within the MQT tourmaline and across the overgrowths. The units on the left are in a.p.f.u. Note the amount if Sn correlates with Fe increase and Mg-Al decrease. After Williamson et al. (2000)

Chapter 4. Methodology

This chapter first addresses the methods used for sample preparations, geochemical (XRD, XRF, ICP) and petrographic (microscope, SEM, EMPA) analyses. The calculations and plotting methods are also described. Finally, the sources of error associated with these methods are assessed.

4.1. Sample preparation

4.1.1. Initial splitting of hand specimens

Six samples were collected during fieldwork, consisting of the granite and the observed vein types. Each hand specimen was cut directly across the vein, which were marked for petrographic studies. Other sections of each hand sample, containing vein and representative alteration zone, were selected for geochemical studies.

4.1.2. Thin sections

Out of the six samples collected, eight polished thin sections were prepared for petrographic studies. Thin sections, 28×48mm and a standard 30 µm thick, and polished slabs were prepared at the thin section laboratory at the Department of Geology and Mineral Resources Engineering, NTNU by laboratory technicians Kjetil Eriksen and Arild Edin Monsøy. Two thin sections for each of sample ME02V and ME04V were made, one of the tourmaline-quartz vein and one of the altered area approximately 3-4 cm from the vein, respectively. The Additionally, the ME02V hand specimen was cut in a 2 cm wide slab, traversing two tourmaline veins and the surrounding red alteration zone (Figure 5.8). The bottom of the slab was cut into four separate pieces the size of a fluid inclusion section, as seen in Figure 4.1, and then polished to be analysed using SEM.

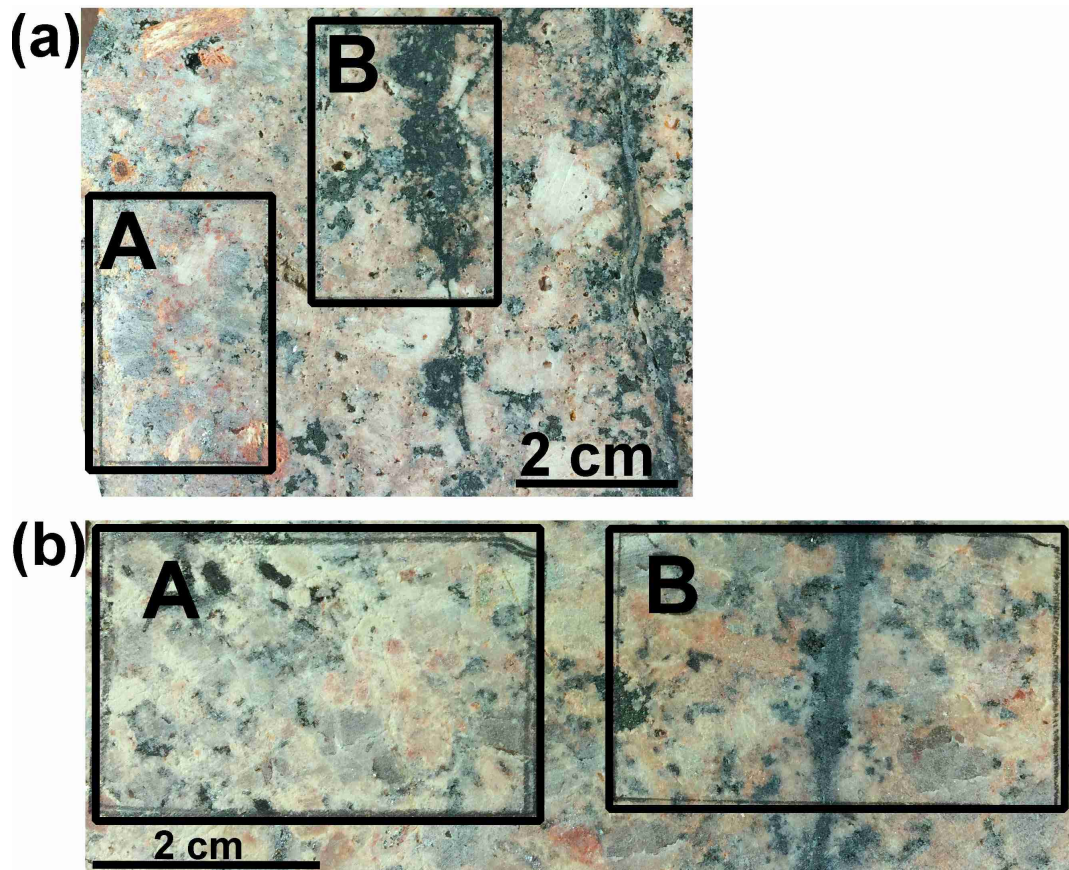


Figure 4.1: Thin section placements in (a) ME02V and (b) ME04V.

4.1.3. Milling and micronization

All the samples underwent three to four size reduction steps prior to the X-ray Diffraction (XRD) analysis, X-ray Fluorescence (XRF) analysis and Inductively Coupled Plasma Mass Spectrometry (ICP-MS). This was executed at the Mineral Processing Lab the Department of Geology and Mineral Resources Engineering, NTNU. The workflow is illustrated in Figure 4.2

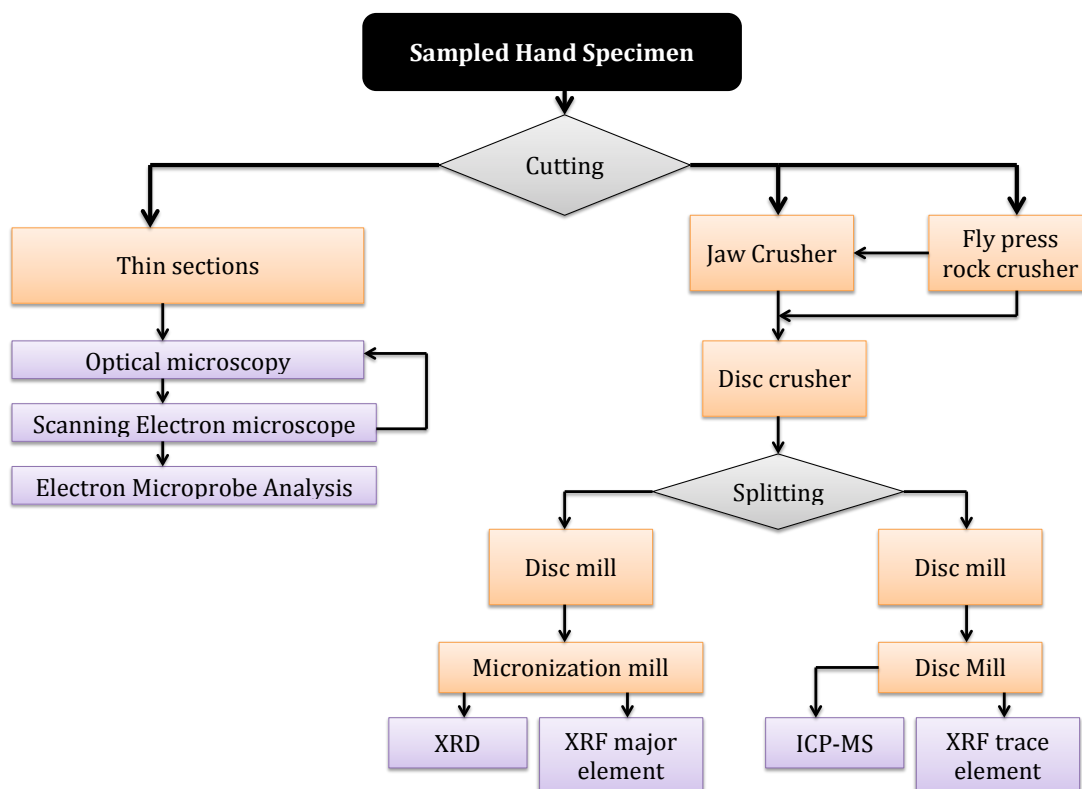


Figure 4.2: Flow chart of work process. Orange colour is preparation; purple is petrographic or geochemical analysis method, grey is dividing the material.

Large samples were broken to smaller pieces by a Fly press rock crusher, and were then crushed in a Retch Jaw crusher, reducing the size of the samples from several centimetres down to a grain size of approx. 0.5 cm. The grain size were the further reduced by crushing in a disc crusher. The samples were then split 2-3 times to obtain a representative sample when only using a portion of the crushed material for further grinding. 20-30 grams of each sample were grinded to a powder using a Siebtechnik Laboratory disc Mill with agate chamber and grinding sets in 5-6 minutes for each sample. Prior to XRF trace element and ICP-MS analysis, the sample material was grinded in the disc mill for another 5 minutes. Prior to XRD -analysis, a McCrone micronization mill was used to further reduce the grain size without destroying the crystal structure of the minerals. The micronization was carried out by stacking 42 agate pellets in a plastic container, mixing 2 heaped spoons of sample material with 10 mL ethanol. The micronization mill ran for 2 minutes for each sample. Then the sample material was collected in petri dishes and dried.

One crushed sample of biotite- granite, sampled by PhD-candidate Kristian Drivenes on Pordenack point 1.5 km from Nanjizal, was prepared to undergo XRD -analysis. It was split and further crushed in a disc crusher. It was split again, and grinded using the disc mill for 4 minutes and the micronization mill for 2 minutes. After drying, the material was homogenised before prepared for XRD analyses in standard Bruker PNMA sample holders. A thin section of the same granite was also lent and used for petrographic examinations.

One of the samples, ME02V, underwent further analysis. A slab containing two veins and the altered area around were cut into six pieces of roughly the same size, following the observed veins and colour differences in the alteration zone. The pieces were prepared to undergo XRD, XRF major element and trace element analysis, and ICP-MS. The preparations were done the same way as the other samples, with the exception of using the Fly press rock crusher instead of the Retch jaw crusher to minimize contamination.

4.1.4. Extracting minerals with a drill

An uncommon method of drilling single grains from a hand specimen to be identified with XRD was carried out with help from Arild Edin Monsøy. In order to characterize the red alteration in sample ME02V and to achieve single feldspar samples, four minerals were drilled with a Dremel moto-tool 10000-3000 with a diamond drill. The material were deposited on a greaseproof paper and transferred into individual paper bags.

4.1.5. HMS

Laboratory work was done using safety footwear and laboratory coat. When crushing and grinding, safety glasses, hearing protection and dust mask was used.

4.2. Geochemical analysis

4.2.1. X-ray Diffraction (XRD)

X-ray powder diffraction as a powerful, fast and versatile analytical method for determining chemical and physical characteristics of materials, and its application is useful in identifying the type and semi-quantifying the phases present and the crystal structure in minerals (Will, 2006). The X-ray diffraction is a result of the interaction between x-rays and electrons of atoms, the manner of diffraction is revealing the structure of the crystal (Stock and Cullity,

2001). The Rietveld method uses full pattern refinement and simultaneous crystal structure refinement, and can be used for quantitative phase analysis of the relative abundances of minerals in a sample (Will, 2006). Homogenized powder samples were put in Bruker PMMA sample holders, and the powder surface was pressed flat and finished with a carrier glass for microscopy in order to ensure flatness and planarity (Castro et al., 2012). In the single mineral XRD analysis, the samples extracted from ME02V was grinded to a fine powder using a mortar, then added a small amount of ethanol and transferred on a silicon disc using a disposable pipette. XRD data were collected using a Bruker X-ray Diffractor D8 Advance, using 40 kV, 40 mA and $\text{CuK}\alpha$ radiation of wavelength $\text{K}\alpha_1 = 1.5406 \text{ \AA}$ and $\text{K}\alpha_2 = 1.54439 \text{ \AA}$ and a $\text{K}\alpha_1/\text{K}\alpha_2$ ratio of 0.5. Diffractograms were recorded from $3\text{-}65^\circ 2\theta$, in $0.009^\circ 2\theta$ increments with 0.6 s counting time per increment, with a total analysis time of 71 minutes per sample (Cepuritis et al., In review). Further analysis was based on the XRD results, with mineral identification by best peak fit, using the minerals in the ICDD database implemented in the software Bruker EVA. TOPAS Rietveld analysis software was used for semi-quantitative mineralogy based on 2θ -intensity data. The interpretation of the results was done with the help of Bjørn Eske Sørensen. Chief engineer Laurentius Tjihuis at NTNU chemical-/mineralogical laboratory oversaw the XRD-analysis.

4.2.2. X-Ray Fluorescence (XRF)

Beckhoff et al. (2006) describes X-ray fluorescence as a well-established multi-element analysis technique, using the excitation of characteristic fluorescent x-rays to make a quantitative determination of atomic elements. Being a comparative method for analysis, standards of certified reference materials are used.

XRF major element analysis was performed on fused glass pills prepared at the guidance of Torill Sørøkk at NTNU chemical-/mineralogical laboratory. Roughly 2.5 grams of fine powder of each of the Nanjizal samples was exactly weighed into porcelain crucibles, dried in heating cabinets and subsequently heated at 1000°C for two hours. When cooled, the samples were weighed once more, and the Loss on Ignition (LOI) was calculated, which is the weight loss that occurs when volatiles, including structural volatiles (H_2O , CO_2 etc.), are released (Winter, 2010). 5.0000 g flux (Lithiumtetraborate 66%/metaborate 33%) and 0.5000 g sample was weighed exactly in metal crucibles. 60 μL lithium iodide was added to the mixture. The contents were fused together to form glass pills using a Claisse Fluxer fusion instrument.

When fusing, chemical reactions in the melt convert the mineral phases into glass-like borates, ensuring a homogenous bead ideal for direct placement in a spectrometer (Beckhoff et al., 2006). The XRF major element analysis was performed using a BRUKER S8 Tiger 4 kW x-ray spectrometer with a calibrated program for major elements.

XRF trace element analysis was performed on pressed pellets. Pelletizing is necessary to reduce surface effects and to obtain a better precision than by using loose powder (Beckhoff et al., 2006). 9.6 g of fine powder of sample and 2.4 g licowax were mixed thoroughly in a container using a FluXana MU-XRF-Mixing-Set. Pressed pills of each sample were made using a Herzog pellet press. XRF Trace element analysis was performed using a BRUKER S8 Tiger 4 kW x-ray spectrometer with GEO-QUANT trace element program. Torill Sørlokk at NTNU chemical-/mineralogical laboratory supervised the preparations and interpreted the results of the XRF-analysis.

4.2.3. Inductively coupled plasma mass spectrometry (ICP-MS)

Inductively Coupled Plasma Mass Spectrometry (ICP-MS) as a rapid trace element technique, offers extremely low detection levels (sub ppm level), as well as quantification at high ppm-levels (Thomas, 2008). The technique uses high-temperature argon plasma to generate positive ions, which travel through a plasma torch, and at the analytical zone at 6000-7000 K will exist as ground-state atoms and ions, representing the elemental composition of the sample (Thomas, 2008). 0.1 g of sample material was dissolved in 5 mL HNO₃ plus 3 mL HF in a microwave at 180 °C in 45 minutes. The solution was then diluted to 50 mL, and further diluted 100 times prior to analysis. Ramp time was 25 minutes. Laurentius Tjihuis at NTNU chemical-/mineralogical laboratory ran the ICP-MS trace element analysis using The Perkin Elmer Elan DRC II system.

4.3. Petrographic analysis

4.3.1. Microscopic analysis

Eight polished thin sections were used for petrographic studies. The main focus was to identify the minerals optically and chemically, to determine the alteration minerals and textures in the samples. The microscopic studies were done using a Leica DM 2500 P with

magnifications from 25 – 500x. Images of thin sections were captured using ProgRes speedXT core5 with ProgRes CapturePro v.2.8.0 software. The overview images of the thin sections were captured using Epson perfection V600 photo scanner with and without using polarizing filters.

4.3.2. Scanning Electron Microscope (SEM)

Scanning Electron microscope as a technique primarily used for imaging, as well as semi-quantitative analysis using Energy-dispersive x-ray spectrometry (EDS) (Reed, 2005). A focussed electron beam impinges on the specimen, electrons and X-rays signals are generated, and images are displayed (Goldstein, 2003). Topographic (Secondary electrons, SE) or compositional contrast (Backscattered electrons, BSE) is usually chosen for imaging (Goldstein, 2003). The Energy Dispersive Analysis (EDS) mode provides the x-ray spectra for elemental analysis (Mehta, 2012). Energy peaks correspond to various elements, identifying the elements as well as giving a semi-quantitative measurement of the element content (Reed, 2005). Element mapping was obtained by using a beam scan. CL images of a quartz vein in ME01V was obtained by SEM-CL, where variations in the quartz can provide useful information about the crystal defects and substitution of trace elements as well as details of cementation, recrystallization and fracture healing (Reed, 2005).

Chief engineer Morten P. Raanes coated the thin sections with carbon prior to using Scanning Electron Microscope (SEM) at The Department of Materials Science and Engineering, NTNU, The instrument used in SEM-analysis at the Department of Materials Science and Engineering at NTNU was a Hitachi SU6600 Scanning electron microscope with Bruker Quantax 800 Espirit software. A working distance of 15 mm was used, the probe current was 1-1,80 kV and the voltage was 15 eV og 51 μ A. EDS- analysis was used to identify and obtain semi-quantitative measurements, correlating to the grey levels in BSE imaging. SEM-CL was done with a CL detector, using a working distance of 20 mm, and 20.0 eV.

4.3.3. Element mapping using SEM

The four polished slabs of sample ME02V was analysed at The Geological Survey of Norway (NGU), using SEM BSE imaging and element maps stitched together to create a visualization of the distribution of elements at thin section scale. The mineral phases of interest are quartz, feldspar, mica and tourmaline and mineralizations of Sn. This is obtained by setting up an

“automate” session within the INCA software, capturing BSE images and element maps at specific coordinates, which is stitched together in the software creating a fullscale image of the section. The adjusted variables in the INCA software were image resolution of 1024x832, medium speed, data of 8 bit and one frame. The smart map setup was map resolution of 1024x832 (same as the image resolution), process time 3, spectrum range of 0-10 kV, number of frames 3, dwell time 200 and channels 2K. The program was set up and run with the help of Anette Utgård Granseth, a fellow master student at NTNU, on the suggestion and supervision of Trond Slagstad at NGU. A 1450 Variable Pressure (VP) SEM by LEO Electron Microscopy Ltd was used, using X-ray analytical system by Oxford Instruments with accompanying INCA software from Oxford Instruments, suite version 4.09.

4.3.4. Electron microprobe analysis (EMPA)

Electron microprobe analysis (EMPA) as a technique closely related to the scanning electron microscope, using x-rays excited by a focussed electron beam to chemically analyse small selected areas (Reed, 2005). Wavelength-Dispersive Spectrometer (WDS) is used for qualitative analysis, and is obtained by identifying characteristic line energies of elements from their wavelength (Goldstein, 2003). Comparing their intensities with those emitted by standard samples, quantitative concentrations are determined with accuracy approaching $\pm 1\%$ (Reed, 2005).

Four thin sections were selected for analysis using the EMPA based on the type of alteration observed and occurrence of cassiterite. Main element programs were set, as well as three different trace element programs for tourmaline, rutile and cassiterite (Table 4.1.). The Silicate programme contained the elements of feldspar, muscovite, biotite and tourmaline. An oxide program contained the elements of rutile, monazite, zircon, apatite and cassiterite. The quantitative electron microprobe analysis was performed on the JEOL JXA 8500 hyperprobe at NTNU, using wavelength dispersive detectors (WDS). Defocused beam diameter was varied, with 1 μm and 2 μm depending on the size of the grain. The beam current and acceleration was set to 20 nA and 15 kV, respectively. Counting times and detection limits (ppm) for the trace elements in different minerals are shown in Table 4.1. The reference materials used included olivine ($\text{SiK}\alpha$, $\text{FeK}\alpha$), Apatite ($\text{FK}\alpha$), Tugtupite ($\text{ClK}\alpha$), Willemite ($\text{MnK}\alpha$), Plagioclase An65 ($\text{NaK}\alpha$, $\text{AlK}\alpha$, $\text{CaK}\alpha$), Monazite ($\text{PK}\alpha$), Garnet ($\text{MgK}\alpha$, $\text{AlK}\alpha$),

Sanidine ($\text{NaK}\alpha$), Rutile ($\text{TiK}\alpha$), Barite ($\text{BaK}\alpha$), Cassiterite ($\text{SnK}\alpha$) and metal oxide standards for W, Nb and V.

Table 4.1: Counting times and detection limits for different minerals and trace elements, microprobe analysis

Mineral	Element	Counting time (seconds)	Detection limit (ppm)
Tourmaline	Sn	250	100
Rutile	Nb	60	200
	W	60	500
	Sn	60	250
	Fe	60	150
	V	60	150
Cassiterite	Fe	60	200
	W	60	600
	Ti	60	200

4.4. Calculations and plotting

The geochemical data was plotted using Microsoft excel and the graphing program Grapher from Golden Software. Tourmaline formulas and end-member classifications were calculated using an Microsoft Excel spread sheet created by Tindle et al. (2002) (10.12.2014), available at <http://www.open.ac.uk/earth-research/tindle/AGTWebPages/AGTSoft.html>. Normalization procedures and web address to the spread sheet is described by Clark (2007). Modifications to accommodate for an excess of Fe in the Y site was done manually by distributing some of the Fe as Fe^{3+} in the Z-site until both the Y and Z sites were full, resulting in a minimum Fe^{3+} estimate assuming no disordered Fe^{2+} in the Z-site.

Isocon analysis is used as a simple and effective method to quantitatively evaluate chemical gains and losses is mass transfer during hydrothermal alteration (Grant, 2005). The Excel worksheet “EASYGRESGRANT” published by López-Moro (2012) was used to carry out the isocon analysis, and immobile elements (Zr, TiO_2) were selected as reference frame for mass-balance modelling.

4.5. Sources of Error

4.5.1. Sample preparation

To minimize contamination between samples, thorough cleaning of the equipment with vacuum cleaner, compressed air and alcohol was conducted after each run of the crushing and grinding devices. When milling, agate grinding chamber sets and pellets were used, as tungsten carbide would give contamination of W. When using the micronization mill, residue of the sample used was discovered after cleaning the second sample prepared. This led to a more thorough cleaning routine of the equipment; however there might be some slight contamination from sample ME01V in sample ME02V. The amount of material left in the chamber after cleaning is less than a milligram, so it does not affect the XRD results, which are in the percent range. During preparation for XRD and XRF, all equipment was cleaned with alcohol when changing samples.

4.5.2. XRD

The XRD method is based on a fully random distribution of crystallites of equal size, and too much pressing of the sample when depositing the powder can cause a preferred orientation of the crystals and thus give inaccurate results. This was taken into consideration when preparing the samples, as well as being controlled by the laboratory staff before analysing, so this is probably not a major source of error. The first XRD interpretations did not give a perfect fit, due to wide peak with and not a best fit for especially the feldspars. Performing XRD analysis on separate feldspar grains solved this problem by selecting feldspar structures that matched the peaks of the observed feldspar diffraction patterns. The new feldspar refinements were used to make a new microcline structure with strict limits to lattice parameters. The whole rock samples were subsequently reinterpreted, resulting in a better fit for the feldspars as well as a better overall fit and better quantification of the bulk mineral quantities.

Another difficulty in the XRD method is the overlapping diffraction peaks, making correct mineral identification more difficult. To be certain of the minerals identified, optical mineral identification should be used in combination to this method. XRD does also obtain semi-quantitative results, and as such the modal percentage should be rounded to the nearest percentage, and all results that are less than 1 % should be listed as such. Because of insecurities in classifying different end-members of tourmaline, the results for schorl and

dravite are combined and listed as total tourmaline. As long as the restriction in the XRD method is taken into consideration, it is a powerful and reliable method giving reliable mineral quantities in the percent range.

4.5.3. XRF and ICP

XRF major element analysis is a reliable method, and is calibrated using certified standards. Trace element analysis was done using XRF trace element analysis and ICP-MS. There are deviations in the results, especially in the values Sn, Rb, Sr and Ba, with differences of several hundred ppms. The XRF apparatus is calibrated on standard samples on a regular basis, and is therefore a reliable method. The method is also done on pressed pills, which does not require the dissolution of the sample, unlike ICP-MS. There is a possibility in the ICP-MS method that not all Sn in Cassiterite is completely dissolved, where the resulting value could be the Sn accommodated in the tourmaline. XRF trace element analysis on the other hand will include Sn from both tourmaline and cassiterite, explaining the deviating results.

4.5.4. SEM

As some elements have overlapping photon energy range, peak overlap could cause error in interpreting EDS analysis. Guidelines when doing EDS quantitative analysis in SEM is to only use peaks that are statistically significant for identification and to keep the dead time below 30% (Goldstein, 2003). When using automatic element identification software, it is important to evaluate if the elements makes sense given the known context of the sample. This was taken into consideration when using SEM-EDS analysis. One mineral phase was wrongly identified as an Ag-phosphate on EDS, which turned out to be Th when quantifying it using microprobe analysis. Since SEM-EDS mainly was used as identification of phases at an early stage, and quantitative measurements using microprobe has been done after, one can conclude that it is not a vital source of error.

4.5.5. Electron microprobe analysis

The quantitative measurements using EMPA is done using certified standards, and is thus a precise and reliable method. When analysing cassiterite, the total percentage was close to 120 %, indicating either an error during analysing or that it was romarchite (SnO) instead of cassiterite (SnO₂). Since romarchite forms only on pewter bowls and are products of tin corrosion in an unique cold fresh water environment (Ramik et al., 2003), it was reasonable to

assume there was something wrong with the analysis result. Further investigations led to the discovery of the problem, that the cassiterite standard had a porous topography. The cassiterite analysis was redone, using another cassiterite standard, giving normal results. Sn had been analysed in tourmaline as well, and the results were recalculated using a conversion factor based on the average difference of Sn in cassiterite from the first to the second microprobe analysis. This could yield some error in measurements, as the beam will probably not analyse the exact same spot the second time. The average was calculated using results from a related master project, which analysed at the same time and with the same error in Sn. A higher number of analysis points (28 in total) gave a better approximation of the average. The average ratio between the original cassiterite analysis and the correct analysis was used to calculate the standard deviation, of 1.30. The result can be interpreted as a standard error of 1.30 % out of a total close to 100%, which lies in the same quantity as the standard error given by the EMPA method. Thus, the recalculation of Sn-values in tourmaline is reasonable.

4.5.6. Tourmaline-structure calculation

The tourmaline structure was calculated using an excel spreadsheet, which assumes normalization on 31 anions and $Y+Z+T = 15 \text{ a.p.f.u}$ (atoms per formula unit) (Clark, 2007). The $\text{Fe}^{2+}/\text{Fe}^{3+}$ ratio is unknown, and the spreadsheet assumes that all iron is Fe^{2+} and situated at the Y site. In multiple analyses, this resulted in high amounts of iron in the Y site, giving the Y site a total of more than 3 anions. To correct this, the excess Fe was distributed as Fe^{3+} in the Z-site until both the Y and Z sites were full. The amount of Fe^{3+} required was found by adding the minimum Fe^{3+} needed in each analysis to give a Z-site a sum of 6,0 and the Y-site a sum of 3,0. The resulting structural formula would then fulfil the initial assumption of $Y+Z+T=15 \text{ a.p.f.u}$. Although these adjustments are made, the spreadsheet still has flaws in terms of the large number of unknowns in the analytical data (see Clark (2007) for in depth discussion). The tourmaline end-member classification was still the same after the adjustment, and total Fe was used in tourmaline plots, so the tourmaline-calculation is assumed to be good enough, and is not a source of error.

4.5.7. Isocon diagram

The isocon method has a number of pitfalls, where any handling of the data without careful consideration could affect the result. The immobile elements do not always plot directly on the isocon line, but scatter around it due to geochemical heterogeneity, analytical errors or the

element not being completely immobile (Mukherjee and Gupta, 2008). In choosing immobile elements to plot, it is recommended to have support from geochemical and petrographic evidence, and make sure the immobile elements does not have coupled behaviour (Grant, 1986). Because of the deviating analytical results using ICP-MS and XRF trace element, the immobile elements chosen was from XRF trace element method only.

Because of the pervasive alteration in some of the samples, finding immobile elements that fit the isocon line is difficult. Another problem is that the granite sample from Nanjizal is not completely unaltered. Granseth (2015) have determined that the isocon diagram should only be used on samples that are spatially close (on the cm scale), due to the chemical variation in the host rock. Thus only the ME02V-C (1-6) samples will be analysed using this method. Given the sources of error in this method, it will be used mostly as an indicator of gains and losses, and is considered an inaccurate method in this context.

Chapter 5. Results

This chapter provides the results obtained from fieldwork, including mapping and descriptions. Further on, petrographic descriptions of the mineral assemblages are presented, as well as geochemical results. Finally, using the calculated tourmaline formulas, binary plots of cation occupancies were assessed by looking at common exchange vectors.

5.1. Field investigations

5.1.1. Geological mapping of Nanjizal tourmaline-vein system



Figure 5.1: The area of investigation of Nanjizal rock outcrop with tourmaline veins, looking NW-SW. In focus is vein-type A, comprising of a tourmaline vein with characteristic red alteration zone.

The area of investigation is an area of rock outcrop on the beach in Nanjizal bay in Land's End, Cornwall. Tourmaline-quartz veins intersecting biotite-granite was mapped in detail with a scale of 1:200 (Figure 5.3). The granite in the area is a leucocratic, coarse-grained quartz-biotite-K- feldspar granite, containing megacrysts of K- feldspar. Three vein-types are distinguished from their field appearance, and they follow three main fracture-directions (Figure 5.4). Six samples of the various vein types were sampled for further petrographic and geochemical studies. In the map (Figure 5.3), solid lines represent tourmaline – or quartz-tourmaline veins and are marked “A”, “B” and “C” based on the appearance and thickness of alteration (See 5.1.3). Dashed lines represent veins that are reactivated and contain a core zone of quartz.

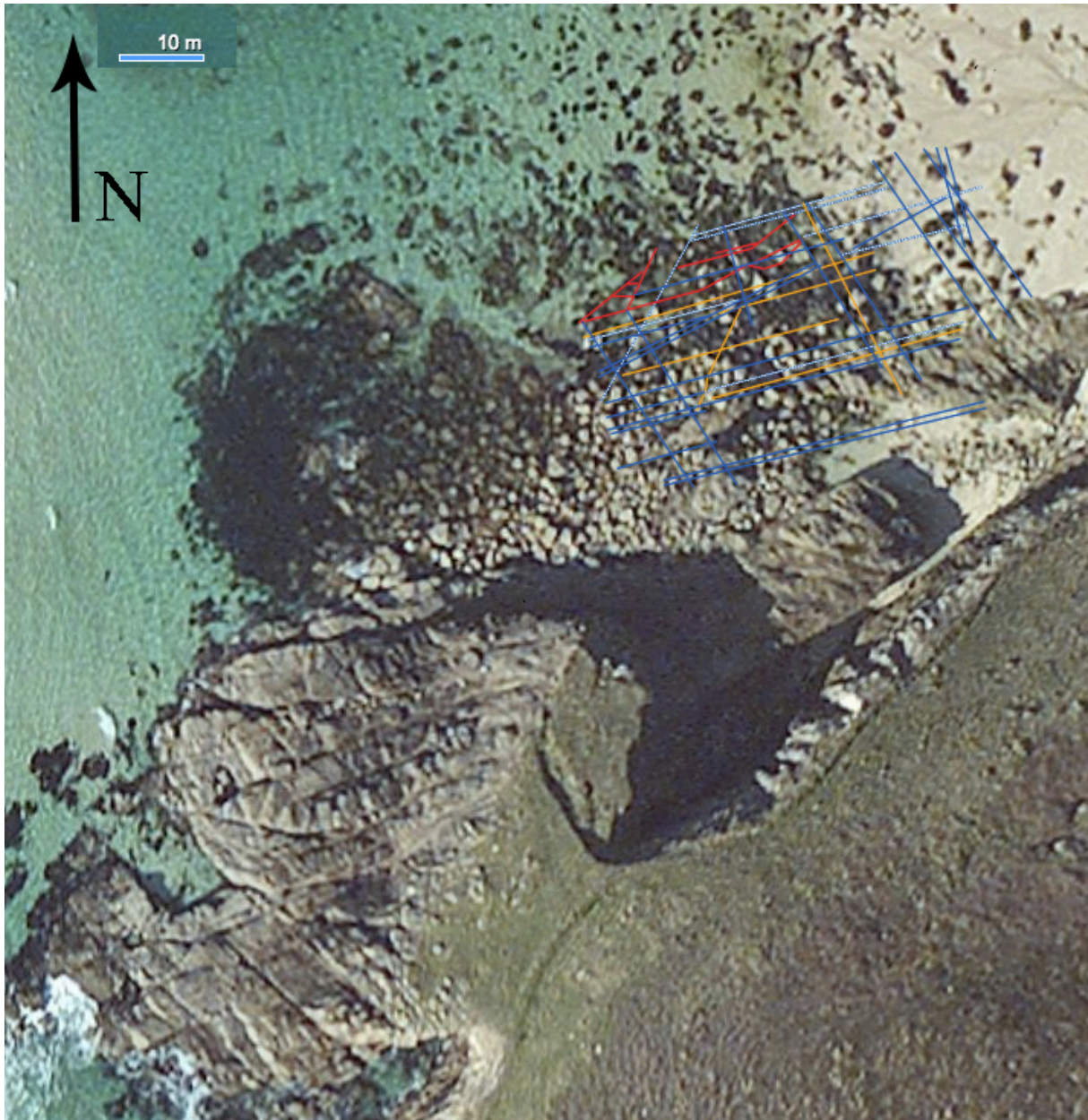


Figure 5.2: Vein system superimposed on aerial photo of Nanjizal(Bing, 2015), showing the location of the rock outcrop mapped in this study. See Figure 5.3 for legend.

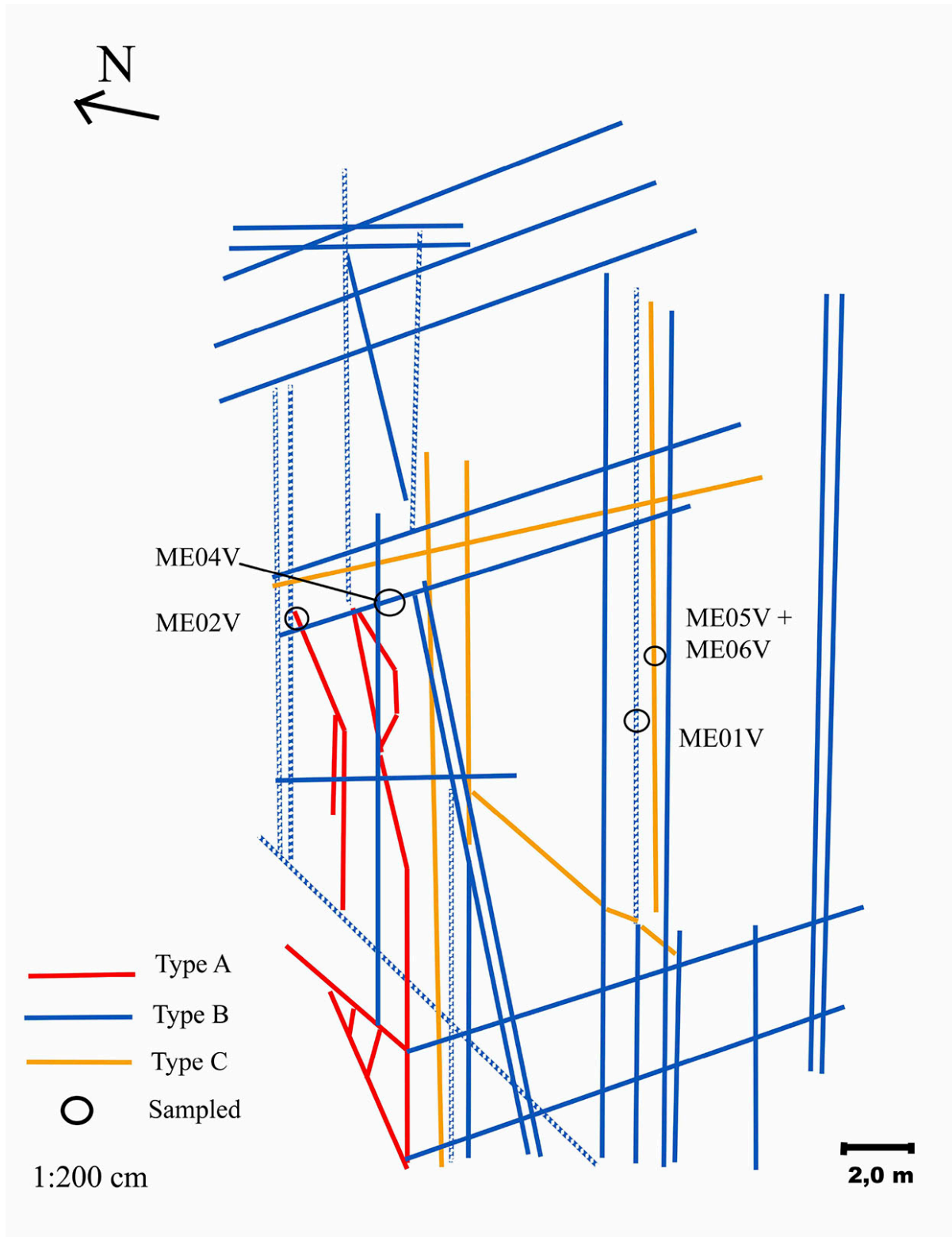


Figure 5.3: Geological map of the vein system in Nanjizal bay, Land's End, scale 1:200 cm. Type A, Type B and Type C vein styles are identified. Solid lines represent tourmaline/tourmaline-quartz veins, and dashed lines represent tourmaline veins with quartz infill. Marked are locations for the sampled hand specimens.

5.1.2. Structural measurements

Whenever possible, strike/dip measurements were made. Where dip was not possible to measure, veins were assumed vertical. The appearance of veins have been plotted and presented in rose diagrams for type A, B and C, based on the strike and frequency of the different directions (Figure 5.4). Three main directions are observed, ca. 345 °, ca. 30 ° and ca. 75 °.

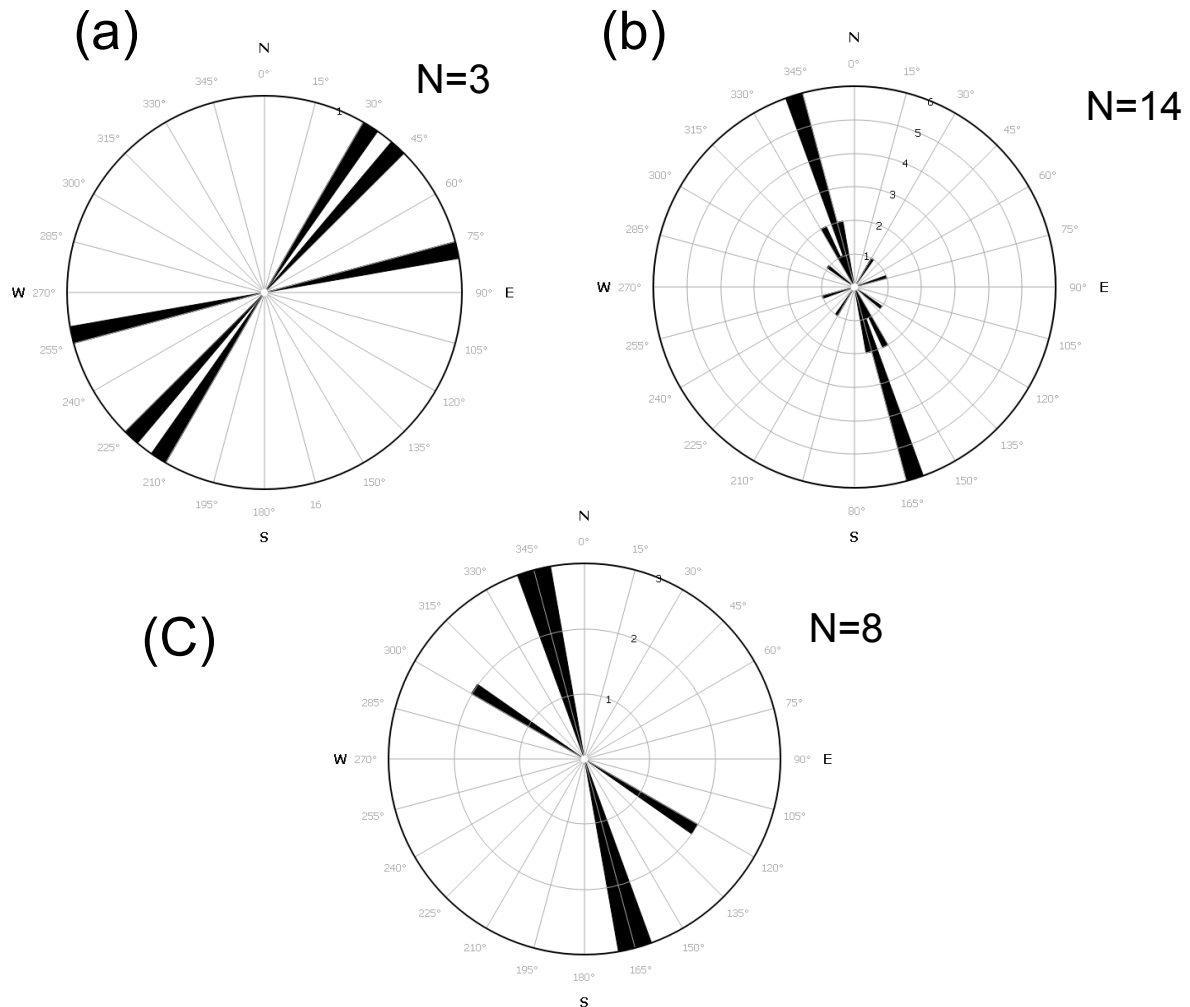


Figure 5.4: Rose diagrams based on stratigraphic measurements, showing similar main directions in type B and C. (A) Vein type A, showing NE-SW trending strike. (B) vein type B, showing N-S and NE-SW trending strike. (C) vein type C showing N-S and NW-SE trending strike.

5.1.3. Vein descriptions

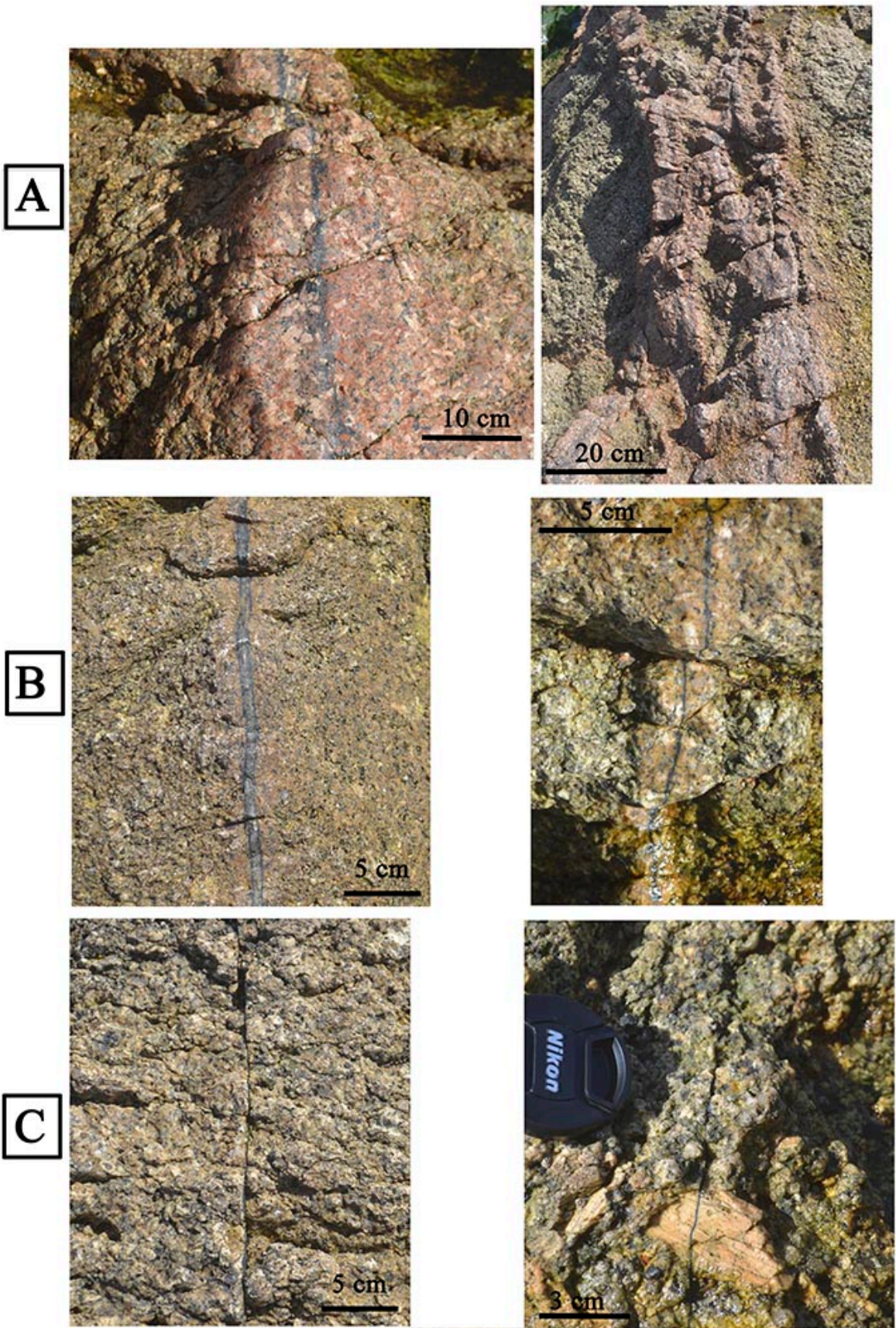


Figure 5.5: Images of the three vein types categorized in Nanjizal. (A) Type A, occurring as a single vein or clustered. Consisting of tourmaline vein, sometimes with a core-zone of quartz, characterized by intense red colouration of the alteration zone. (B) Type B, consisting of tourmaline vein and tourmaline vein with core-zone of quartz. Often comprising of a pink-reddish alteration zone. (C) Type C, consisting of a narrow tourmaline vein without any visible alteration zone.

The granite in Nanjizal bay consists of two types of granite. Medium-grained granite contains quartz, feldspar, disseminated tourmaline and sometimes biotite. The other type is leucocratic, megacrystic, with oriented euhedral feldspar megacrysts up to 6 cm and is generally more coarse-grained. The medium-grained granite cuts through the megacrystic granite in multiple locations. The granite on the rock outcrop (ME03V) is leucocratic white, phaneritic with medium-grained grey quartz and white feldspar matrix, spotted with randomly oriented fine-grained tourmaline. It contains phenocrysts of grey quartz and white feldspar. The amount of megacrystic K- feldspar varies in the area. A fresh medium-to coarse-grained, megacrystic biotite-granite granite, sampled from Pordenack point 1.5 km from Nanjizal has been analysed. It is used as an indicative comparison of the alteration in the samples, although it cannot be compared directly.

Three vein-types are distinguished from their field appearance, and categorized as Type A, Type B and Type C, pictured in Figure 5.5. Six hand sections were sampled for further analysis. ME01V (Type B, NE-SW strike), ME02V (Type A, NE-SW strike), ME03V (Granite), ME04V (Type B, E-W strike), ME05V (Type C, NE-SW strike) and ME06V (Type C NE-SW). The latter two were sampled at the same location.

Vein *type A* consists of a 1-2 mm tourmaline-vein, and 22 cm wide red alteration zone. The colouring of the alteration zone is characteristic for type A. The vein and alteration zone is weathering out, forming a crest from the surrounding biotite-granite. Is commonly split into more veins, and comprises of a core zone of quartz (Figure 5.6A). In hand section (ME02V, Figure 5.8), two parallel tourmaline veins 2 cm apart cut through a matrix consisting of grey quartz and pink feldspar. K- feldspar megacrysts are usually white, but also occurs as pink-red and cream coloured. Fine-grained black anhedral tourmaline is disseminated in the sample, and also occurs as clots surrounding the veins in a 2 cm wide zone. The red colouration is

more intense at the edge towards the granite, forming a 2 cm zone of intense red coloration with visible crystals of hematite.

Type B consists of either a tourmaline vein (ME04V) or tourmaline vein with a core-zone of quartz (ME01V), usually displaying a reddish alteration zone 4 cm across. Compared to type A, the colouring is usually less distinct, and varies from the red colour seen in type A to almost none-existent. The categorization of this type was based on the overall appearance of each vein. The vein is in some instances seen weathering out forming a crest, but not as extensive as in type A. In hand section, the alteration zone is 2-4 cm wide, where pink and red feldspar is providing the reddish colour. The samples lack the intense red edge of alteration seen in type A. Sample ME04V (Figure 4.1B) consists of a 4 mm tourmaline vein with clots of forming in 0.5 cm proximity. In ME01V, the vein is 8 mm wide, with a 1 mm black tourmaline vein with clots. The core comprises of grey quartz. An additional alteration of 1 cm is visible around the vein, where the minerals are paler, cream-coloured and more fine-grained.

Type C (ME05V and ME06V) consists of very thin tourmaline veins without any visible alteration zones. It was neither reactivated or contained quartz infill, nor weathered out from the host rock. In hand section, the tourmaline-vein is <1mm wide, with some tourmaline clots in 0,5 cm proximity. An alteration zone, 6 cm wide, is characterized by either cream or intense red coloured feldspar crystals, different from the pinkish colour in type A and B, similar to the more intense red and cream feldspars in the outer alteration zone in type A.

5.1.4. Crosscutting relationships

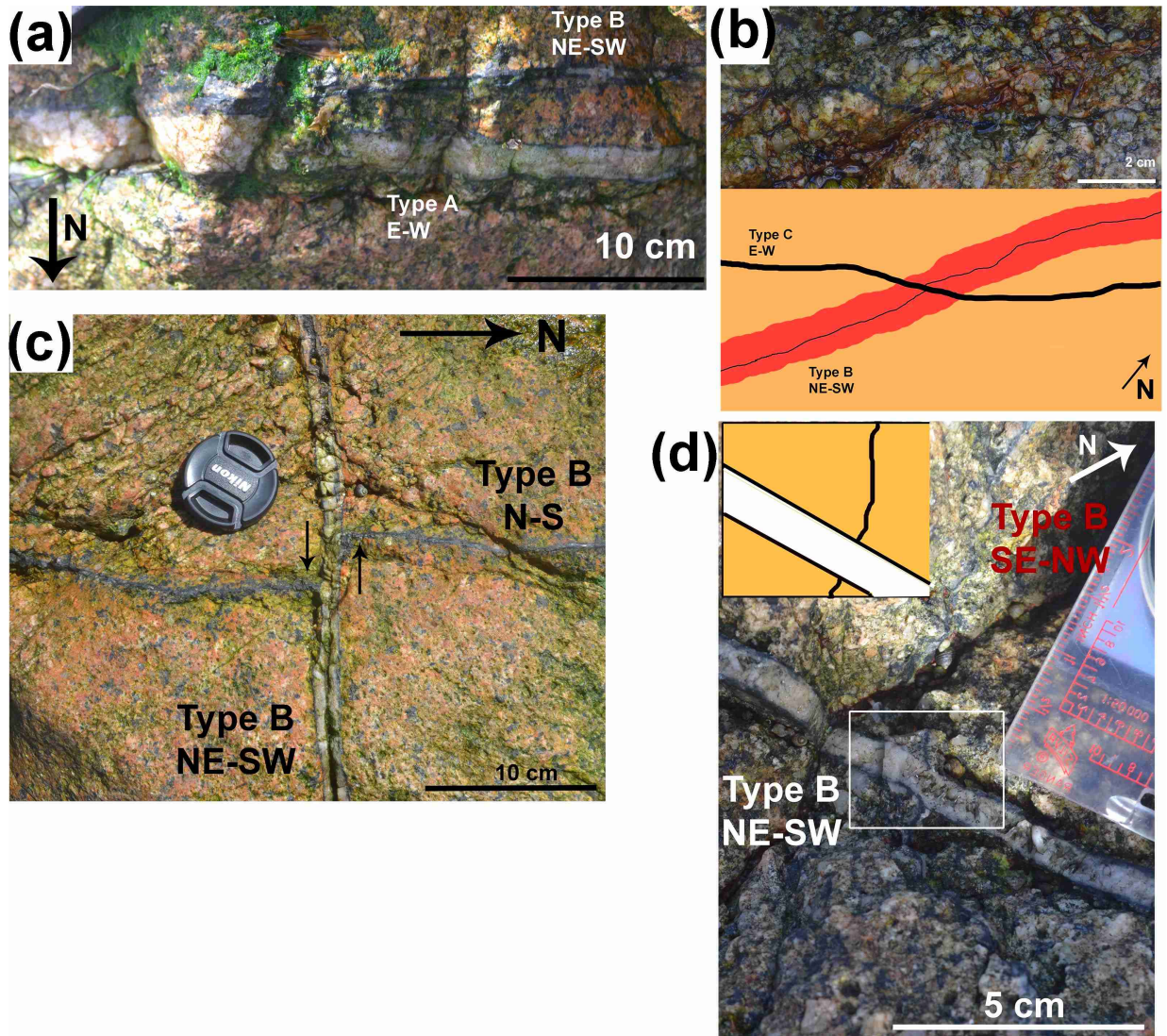


Figure 5.6: Crosscutting relationships between vein type A, B and C. (a) Type B merging with Type A, and is thus synchronous or younger. (b) Type C crosscutting Type B, and is thus younger. (c) Type B NE-SW crosscutting Type B N-S, and is thus younger. (d) Type B SE-NW crosscutting Type B NE-SW, and is thus younger.

In spite of multiple cross-cuttings, observations of relative chronology were sparse due to weathering and seaweed. Figure 5.6A depicts vein type B vein merging with type A, where type B is interpreted as younger or synchronous as type A. Figure 5.6D depicts crosscutting relations between two generations of type B vein, where NE-SW trending vein with quartz infill is the youngest of the two. Figure 5.6C depicts the same chronology, where NE-SW type B with quartz infill is youngest. Figure 5.6B depicts a type C vein crosscutting type B, thus making type C the younger of the two. Based on these observations, together with an overall look at the area, the chronology is (from oldest to youngest): Type A, quartz infill in type A, type B, quartz infill in type B, type C.

5.2. Petrographic descriptions

Eight thin sections were prepared and studied in the optical microscope. A petrographic summary is presented in Table 5.1 and Table 5.2, where the modal mineralogy and general appearance of quartz, feldspar, mica, tourmaline, accessory minerals and alteration of the different samples and vein types are summarized. Thin samples ME01V, ME02V-A, ME02V-B and ME05V were selected for further analysis using SEM and EMPA, representing the three vein types observed in field.

Sample	Vein type	Textures	Alkali feldspar	Plagioclase	Quartz	Micas	Yellow Tourmaline	Blue (-brown) tourmaline	Accessory minerals	Alteration observation
ME01V	B	Allotriomorphic, medium grained. Dustyness in Feldspars.	Microcline 11%, Microperthite 25%. Interstitial groundmass: Inequigranular, anhedral. Megacrysts: Subhedral, max 2.4 mm. carlsbad twinning, inclusions of quartz	Albite 10%. subhedral, irregular. Albite-twinning. Quartz-inclusions.	44%. In matrix: Anhedral and inequigranular. Phenoocrysts, max 2.6 mm. In quartz vein: mostly anhedral, slightly elongated.	Absent.	Sub-to Anhedral equigranular.	Dark blue to brown overgrowths on yellow tourmaline and as needle-shaped crystals.	Hematite, Rutile, apatite, zircon, cassiterite	2% muscovite as sericitization.
ME02V-A	A	Allotriomorphic, medium grained. Varying intensities of dustyness in Feldspars. Undulating extinction in quartz phenoocrysts.	Microcline 37%, Microperthite 32%. Interstitial: Inequigranular, anhedral. Megacrysts: Subhedral, Carlsbad twinning, max 6 mm. inclusions of quartz.	Absent.	17%. Matrix: Inequigranular and anhedral, phenoocrysts max 9 mm.	Biotite absent. Muscovite as inequigranular and anhedral grains.	Sub-to Anhedral, equigranular.	Pale blue-brown tourmaline overgrowths on yellow tourmaline and as needle-shaped crystals.	Hematite, rutile, apatite, monazite, zircon, cassiterite.	Sericitization. Altered biotite with rutile along the cleavage planes.
ME02V-B	A	Allotriomorphic, medium grained. Dustyness in Feldspars.	Microcline 37%, Microperthite 32%. Interstitial: Inequigranular, anhedral. Megacrysts: Subhedral, Carlsbad twinning, max 4 mm. inclusions of quartz	Absent.	17%. Matrix: Inequigranular and anhedral. Phenoocrysts max 3 mm. Inclusions of needle-shaped tourmaline.	Absent.	14% tourmaline. Sub-to Anhedral inequigranular.	Blue-brown tourmaline overgrowths and needle-shaped crystals. Very fine-grained in the vein. Zoned.	Hematite, rutile, apatite, monazite, zircon, cassiterite.	None to very little Sericitization. Altered biotite with rutile along the cleavage planes.
ME03V	Granite	Allotriomorphic, medium grained. Dustyness in Feldspars.	Microcline 6%, Microperthite 28%. Interstitial: Anhedral, inequigranular. Megacrysts: subhedral max 4 mm, carlsbad twinning.	Albite 13%. Subhedral, equigranular, albite-twinning.	45%. Matrix: Anhedral, inequigranular. Phenoocrysts max 4 mm. Slightly cloudy, undulating extinction.	3% muscovite, biotite.	4%, Sub-to-nhedral, equigranular.	Absent.	Rutile, monazite, zircon.	Kaolinite. Sericitization in feldspars. Some biotites are undergoing replacement by muscovite, and some have chloritization.

Table 5.1: Petrographic description of the thin sections. Modal percentage (%) from XRD.

Sample	Vein type	Textures	Alkali feldspar	Plagioclase	Quartz	Micas	Yellow Tourmaline	Blue (-brown) tourmaline	Accessory minerals	Alteration observation
ME04V-A	B	Allotriomorphic, medium grained. Dustyness in feldspars.	No Microcline. Microperthite 35%. Matrix: anhedral, inequigranular. Megacrysts: subhedral, max 3 mm.	Albite 12%. Subhedral, equigranular, albite-twinning.	41%. Matrix: Inequigranular and anhedral, phenocrysts max 4 mm. Cloudy.	3% muscovite, some altered biotite. Opaque inclusions along the cleavages of biotite, is brown and cloudy. Masked or abnormal interference colours.	Anhedral, equigranular.	Blue tourmaline as overgrowth on one yellow tourmaline.	Rutile, monazite, zircon.	Kaolinite. Varying intensities of Sericitization in feldspars. Rutile inclusions along the cleavages of biotite.
ME04V-B	B	Allotriomorphic, medium grained. Dustyness in feldspars.	No Microcline, Microperthite 35%. Perthitic. Matrix: Anhedral, inequigranular. Megacrysts, subhedral, max 3 mm. Carlsbad twinning.	Albite 12%. Subhedral, equigranular, albite-twinning.	41%. Matrix: Anhedral and inequigranular. Phenocrysts: max 5 mm. Dusty.	3% muscovite, biotite absent.	Matrix: Sub-to Anhedral, equigranular.	Pale blue-green tourmaline as overgrowths on yellow tourmaline as needle-shaped crystals in radiating clusters and in the vein as elongated needle-shaped crystals. Zoned.	Rutile, monazite, zircon, apatite, hematite.	Kaolinite. Coarse-grained sericitization of feldspars.
ME05V	C	Allotriomorphic, medium grained. Dustyness in feldspars.	Microcline 3%, Microperthite 33%. Interstitial: Anhedral, inequigranular, interstitial. Megacrysts, Subhedral, max 3 mm. Carlsbad twinning.	Albite 9%, Subhedral, equigranular. Albite twinning.	42%. Interstitial: Anhedral and inequigranular. Dusty. Phenocrysts: max 3 mm, undulating extinction.	3% muscovite, biotite absent.	Anhedral.	Dark to pale blue, needle-shaped and zoned, mostly located as vein. Dark blue overgrowths in yellow tourmaline close to the vein or as needle-shaped crystals in clusters.	Rutile, apatite.	Feldspars it is very textured and brown, the serizite is very small grained. Intense Sericitization in feldspars. Rutile inclusions along the cleavages of altered biotite.
ME06V	C	Allotriomorphic, medium grained. Dustyness in feldspars.	Microcline 7%, Microperthite 33%. Interstitial: Anhedral, inequigranular, interstitial. Megacrysts: Subhedral, calssbad twinning, max 2.5 mm.	Albite 9%, Subhedral, equigranular. Albite twinning.	42%. Interstitial: Anhedral and inequigranular. Dusty. Phenocrysts max 3 mm. Smaller grains does not have undulating extinction.	2% muscovite, biotite absent.	5% tourmaline. Sub-to Anhedral. Yellow to colourless pleochroism.	Dark blue- pale blue comprising the vein, zoned. As overgrowths on yellow tourmaline close to the vein.	Rutile, apatite.	Kaolinite. Sericitization in feldspars.
KDC Granite	Granite	Allotriomorphic, medium grained. Dustyness in feldspars.	Microcline 10%, Microperthite 21%. Interstitial: Anhedral and inequigranular, interstitial. More greyish-dusty than the megacrysts. Megacrysts: Subhedral, max 4 mm.	Albite 16%.	42%. Interstitial: Anhedral and inequigranular. Phenocrysts: Max 4 mm, cracked. Undulating extinction.	4% muscovite, 2% biotite, 4% chlorite.	1% Sub-to Anhedral, equigranular. Orange-brown colour.	Absent.	Rutile, ilmenite, zircon.	Sericitization in the feldspars. Chloritization in biotite.

Table 5.2: Petrographic description of the thin sections. Modal percentage (%) from XRD.

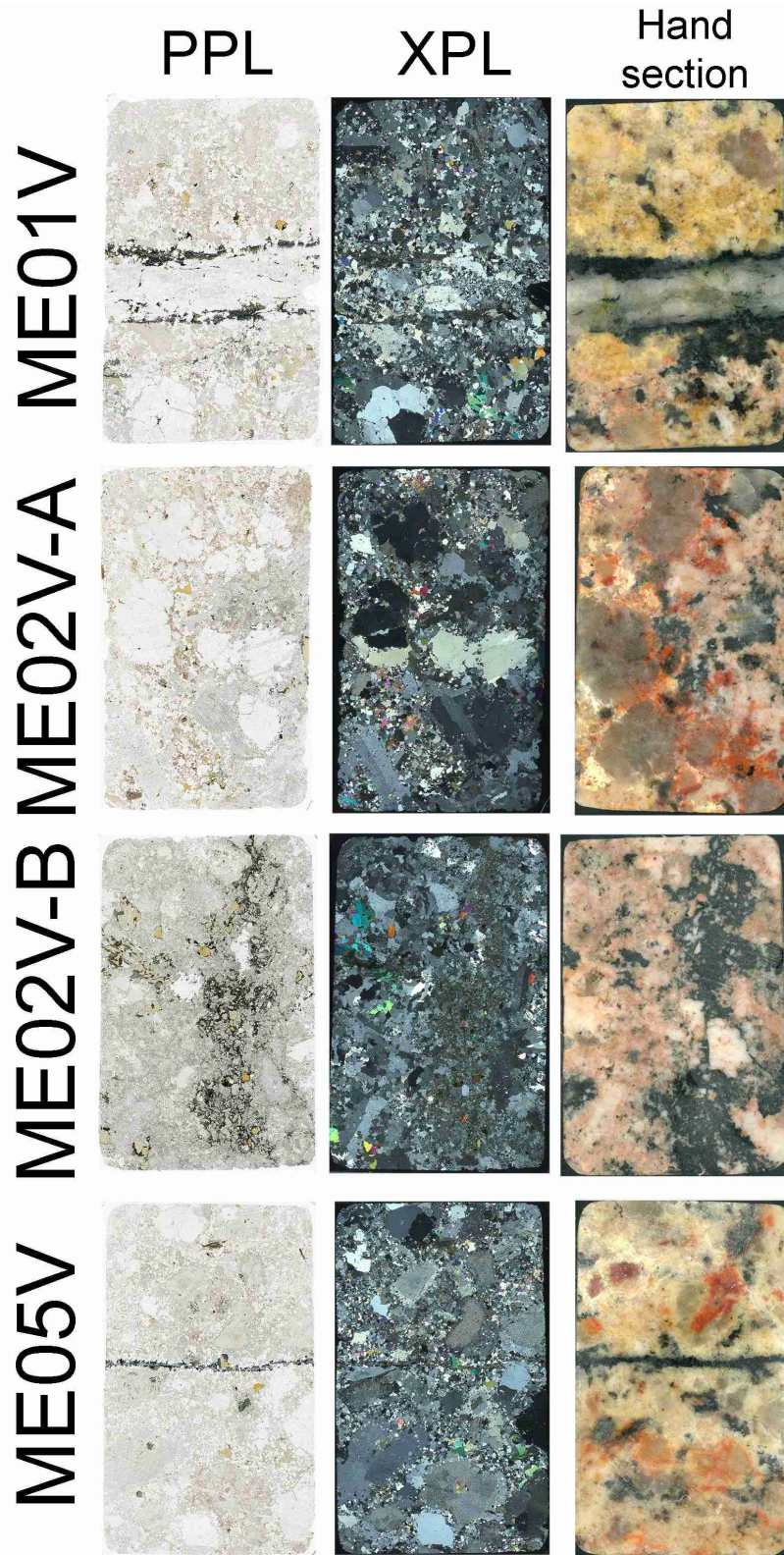


Figure 5.7: Thin sections ME01V (Type B), ME02V-A (Type A distal), ME02V-B (Type A proximal) and ME05V (Type C), shown in plane-polarized light view, crossed-polarized light view and the hand section slabs used to make the thin sections.

Based on the distinctive character of ME02V in terms of macroscopic and microscopic descriptions, as well as enrichment in Sn, it was analysed in more detail. Modal percentages, whole-rock chemistry and trace element content of various zones were analysed, and polished sections were analysed using SEM. Thin sections were not made due to limited time.

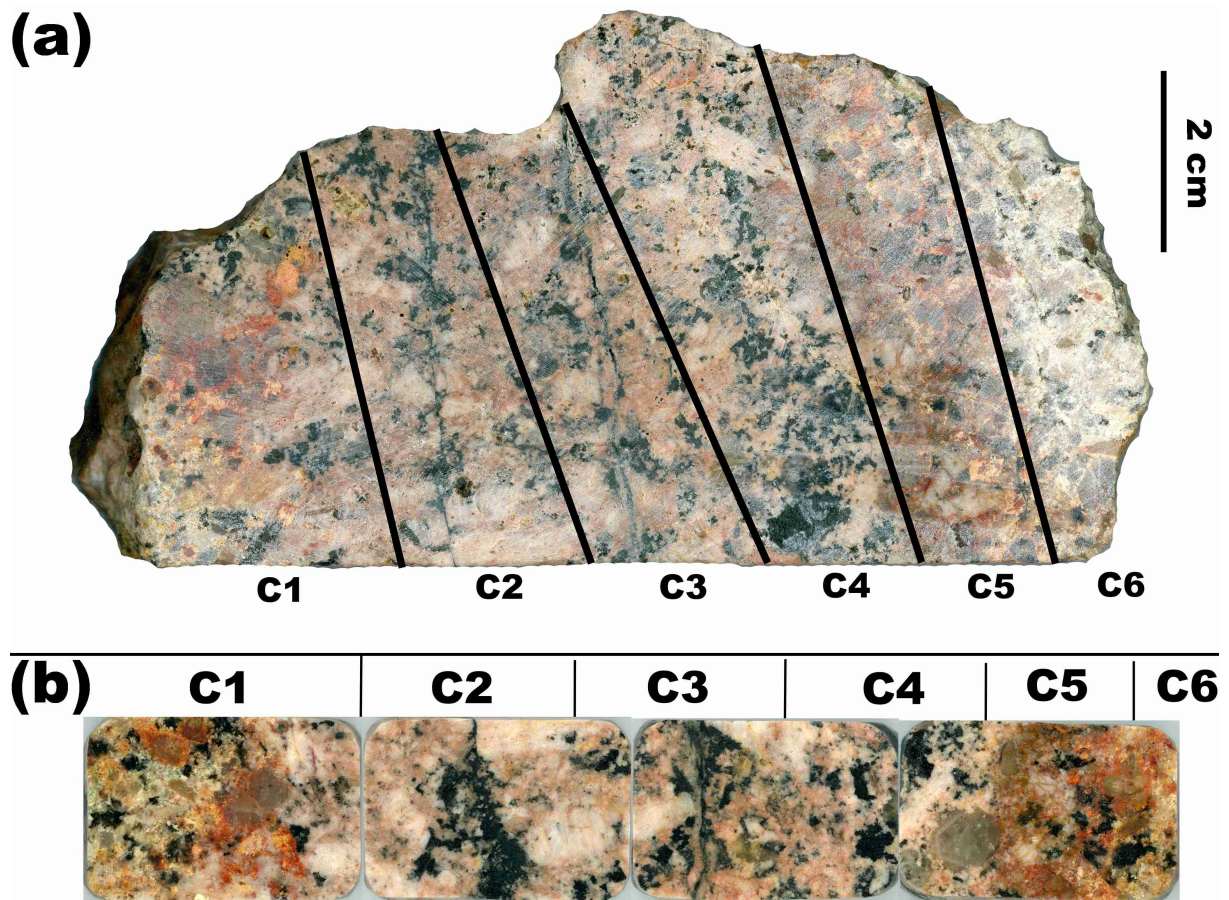


Figure 5.8: ME02V with six areas (C1-C6) used in further analysis. (a) Hand section cut and analysed using XRD, XRF and ICP-MS. The sections were cut to contain red alteration zone, each tourmaline vein and a zone of tourmalinization. (b) Four slabs that were cut from the bottom of the hand section, polished and analysed using SEM.

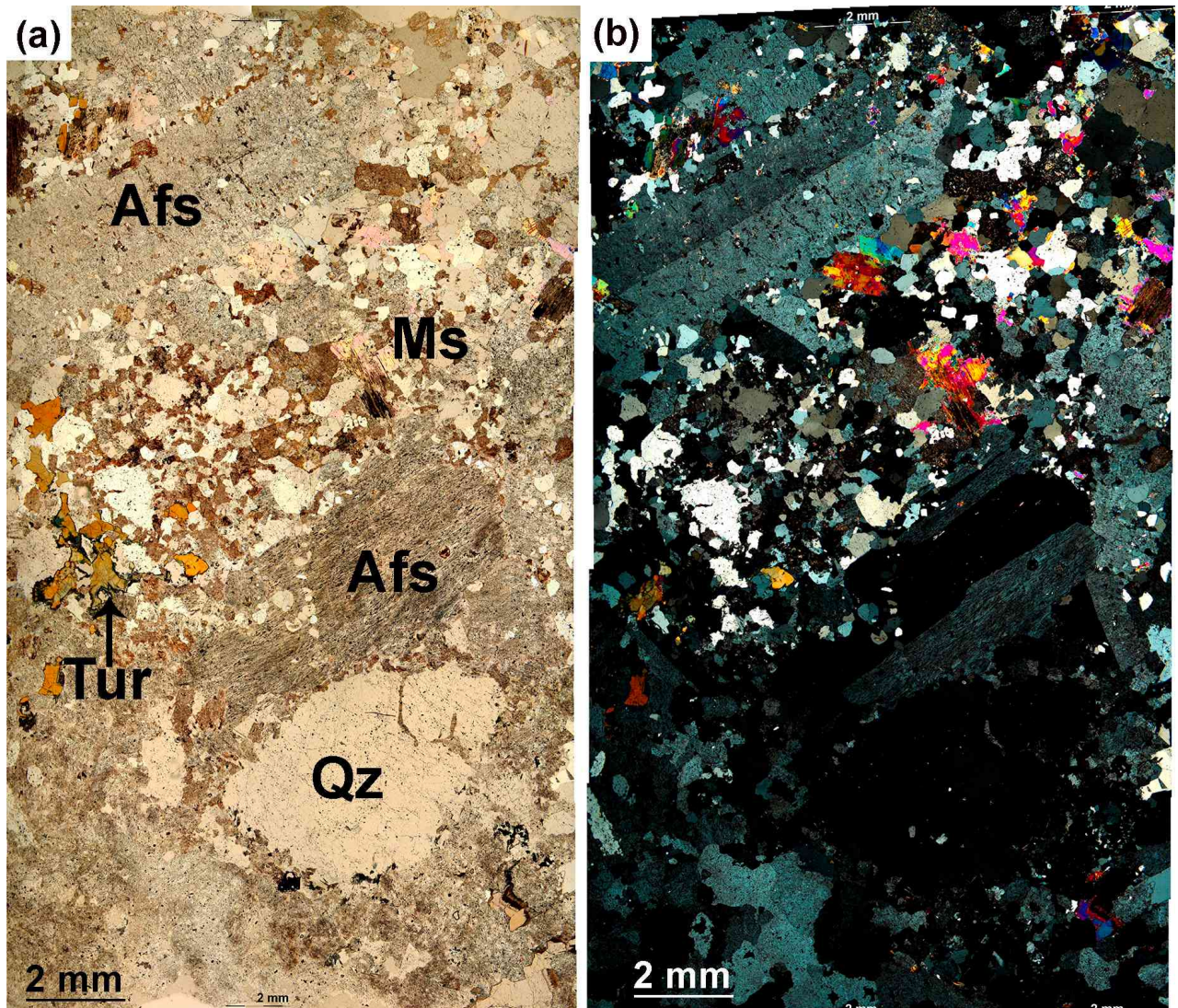


Figure 5.9: Microscope image showing the width of type A distally from the vein (ME02V-A). Note the transition from feldspar-rich and quartz poor assemblage with quartz phenocryst, to a more fine-grained matrix of quartz, feldspar, muscovite and tourmaline, where the fine-grained feldspars are dusty with a brown-red colour. a) Plane-polarized light view. (b) Crossed polarized light view.

5.2.1. Quartz

Quartz occurs as both fine-grained (0.2-0.5 mm) interstitial and as subhedral phenocrysts (max 9 mm). The fine-grained quartz is anhedral and bimodally distributed as fine- and medium grained grains. In samples of Type B and C, the fine-grained quartz is abundant, often occurring as inclusions in feldspar, less often in tourmaline, biotite and muscovite. Many show undulatory extinction, and their grain boundaries are usually straight. The phenocrysts are cracked and cloudy, often containing lines of fluid inclusions trapped on annealed fractures. They display undulatory extinction, uneven grain boundaries and often bulging recrystallization. Fluid inclusions are present in all the quartz crystals. The quartz vein in ME01V show elongated quartz crystals, oriented perpendicular to the vein walls. CL-images (Figure 5.11, Figure 5.12) show growth zonation in quartz in the vein and different CL in quartz phenocryst and crystals comprising the vein.

ME02V, Type A, contains much less quartz than the other samples. Closest to the vein, in ME02V-B, quartz only occur as 2-3 mm sized aggregates, showing little to no undulating extinction, and is often poikilitic, containing inclusions of other minerals. Blue-brown needle-shaped tourmaline is growing radially as inclusions in quartz phenocrysts. Inclusions of fine-grained, anhedral feldspar, rutile and needle-shaped tourmaline is also common (Figure 5.10) Figure 5.9 depicts a quartz phenocryst and fine-grained matrix, and the transition from the quartz-poor inner zone of ME02V, to the more quartz-rich content seen in Type B, C and in the granite.

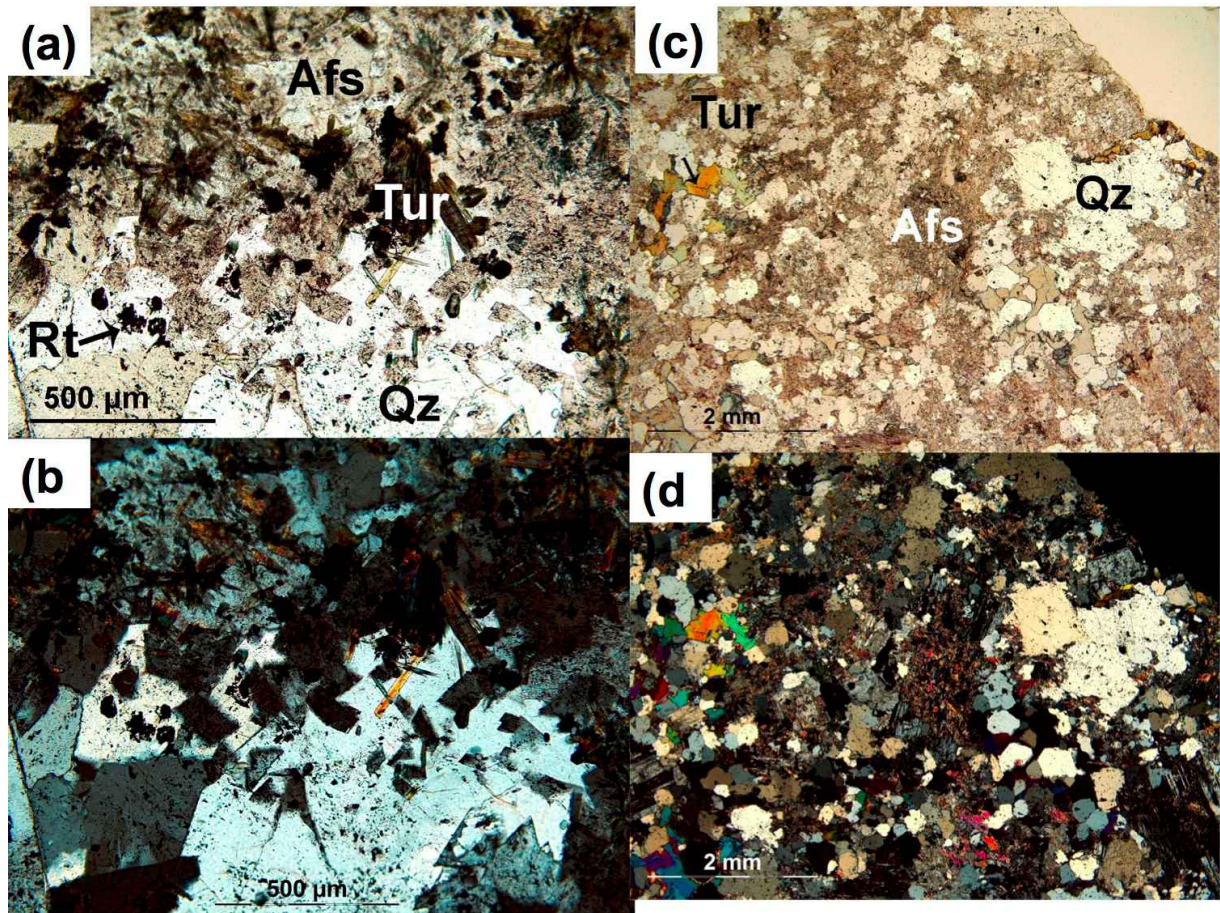


Figure 5.10: (a) and (b): Inclusions of feldspar, rutile and needle-shaped tourmaline in quartz, and rutile and radiating needle-shaped tourmaline in feldspar, in ME02V-B, type A proximal to the vein. (c) and (d): Fine –grained quartz , quartz phenocryst, interstitial feldspar undergoing sericitization and yellow tourmaline in ME04V-B, type B proximal to the vein. Plane-polarized light view on top and crossed polarized light view beneath.

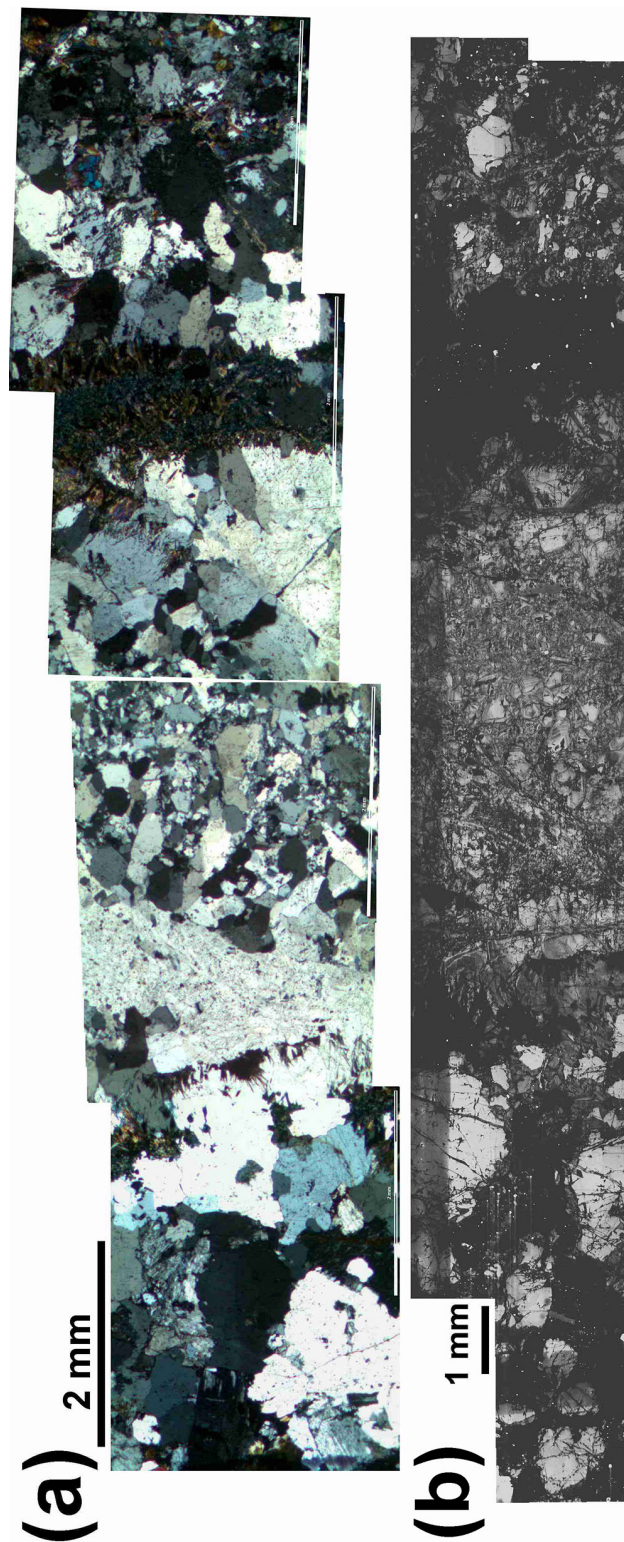


Figure 5.11: Traverse of the quartz-tourmaline vein in ME01V, type B tourmaline vein with a core zone of quartz: (a) Microscopic image (crossed-polarized light view) (b) SEM-CL image, showing difference in CL signal from different generations of quartz.

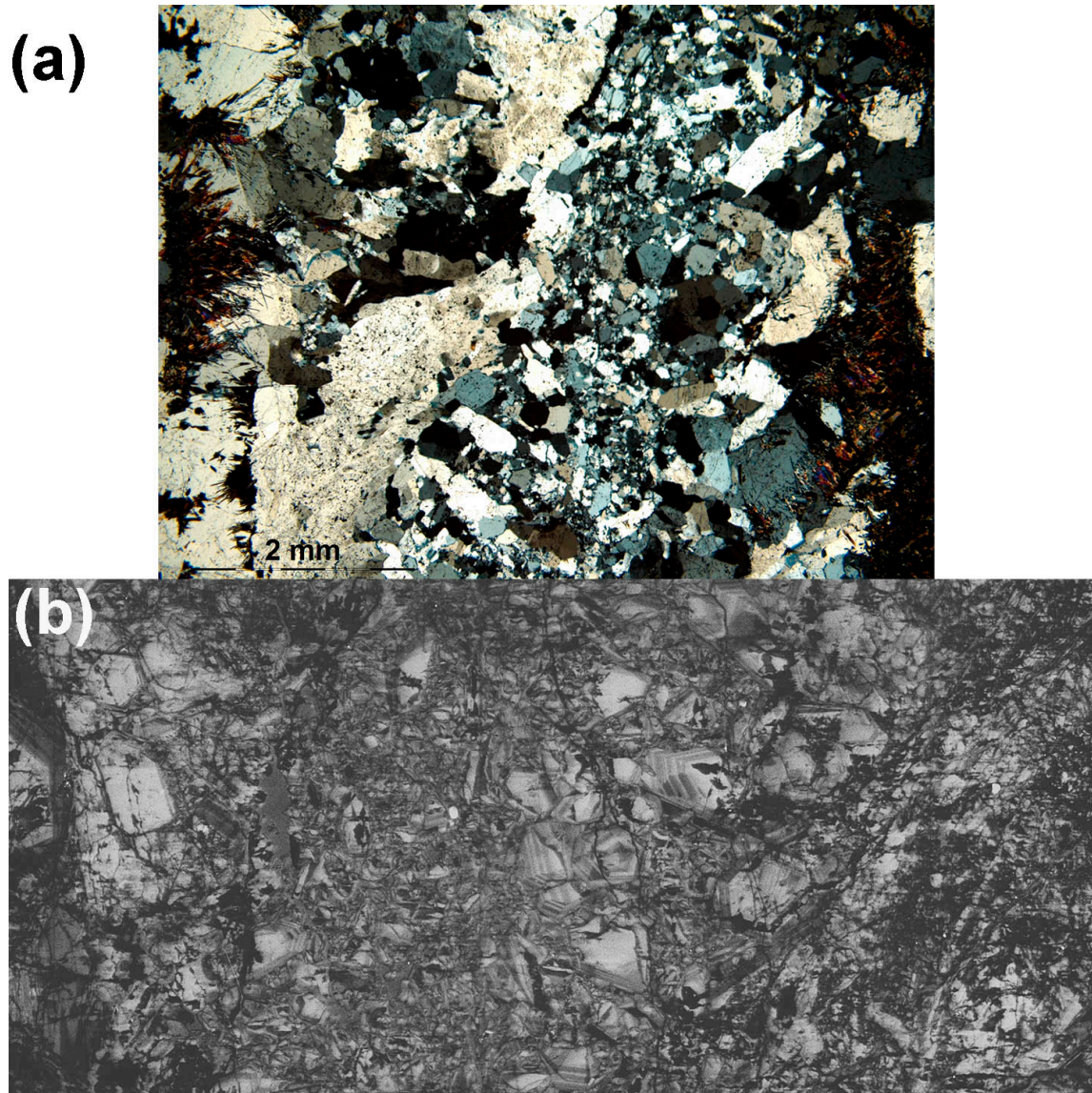


Figure 5.12: Traverse of the quartz-tourmaline vein in ME01V, zoomed in on the quartz core zone: (a) Microscopic image, crossed polarized light view.. (b) SEM-CL image, showing the growth zonation in quartz.

5.2.2. Feldspars

Two feldspars are present in the samples. K- feldspar (microcline and microperthite) is present as subhedral megacrysts (max 6 mm) and as interstitial grains. The microperthite, detected in XRD, is not always visible. Megacrysts of microcline often show carlsbad twinning. Plagioclase is subhedral or anhedral, showing albite twinning. XRD analysis of single feldspar grains revealed that the cream coloured K- feldspar crystals consisted of microcline, while the intense red coloured K- feldspar consists of microperthite.

In Type B, C and the granite, both K- feldspar and plagioclase are mostly anhedral and poikilitic, containing inclusions of quartz concentrated near and at the grain boundaries. Inclusions of muscovite and rutile also occur. All feldspars have a dusty, opaque amorphous appearance. They are often being replaced by variable amounts of sericite. Type B with tourmaline-vein (ME04V) has the most pervasive sericitization, where entire crystals are completely replaced by sericite (Figure 5.15 B). The sericite appears to be more coarse-grained in proximity to the vein. In Type B with quartz core-zone (ME01V), the megacrysts have more sericite than the groundmass and plagioclases. Overall, K- feldspar and plagioclases are equally sericitized. Type B with quartz core-zone (ME01V) has overall very little sericitization.

In ME02V-B, type A proximal to the tourmaline vein, sericite is absent. Distally the vein, In ME02V-A, there is a transition from unaltered feldspar to feldspars replaced by fine-grained sericite (Figure 5.16).

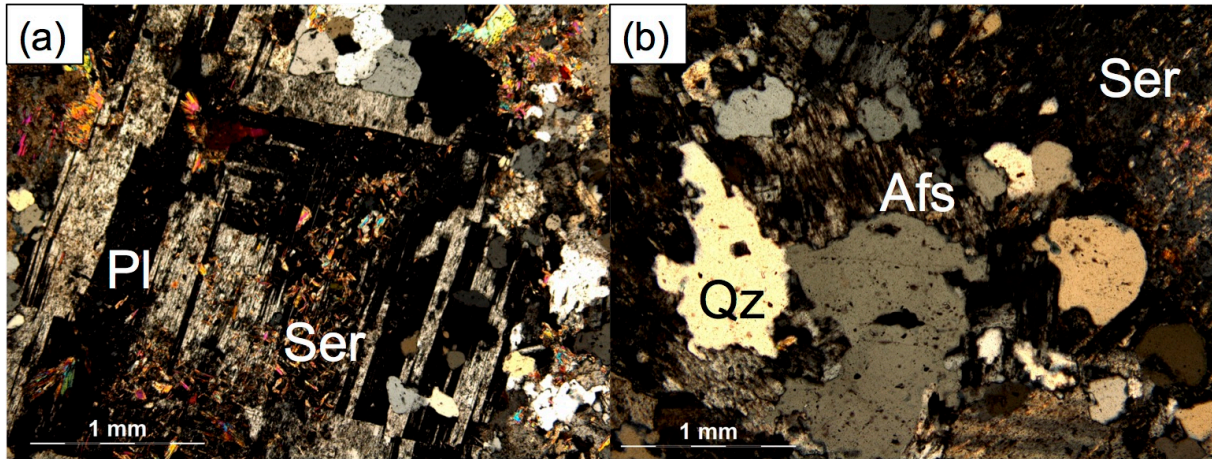


Figure 5.13: (A) Plagioclase with sericitization in ME04V-B, type B proximal to the vein. (b) Interstitial K- feldspar with microperthite in type C, ME05V. Both images in crossed polarized light view.

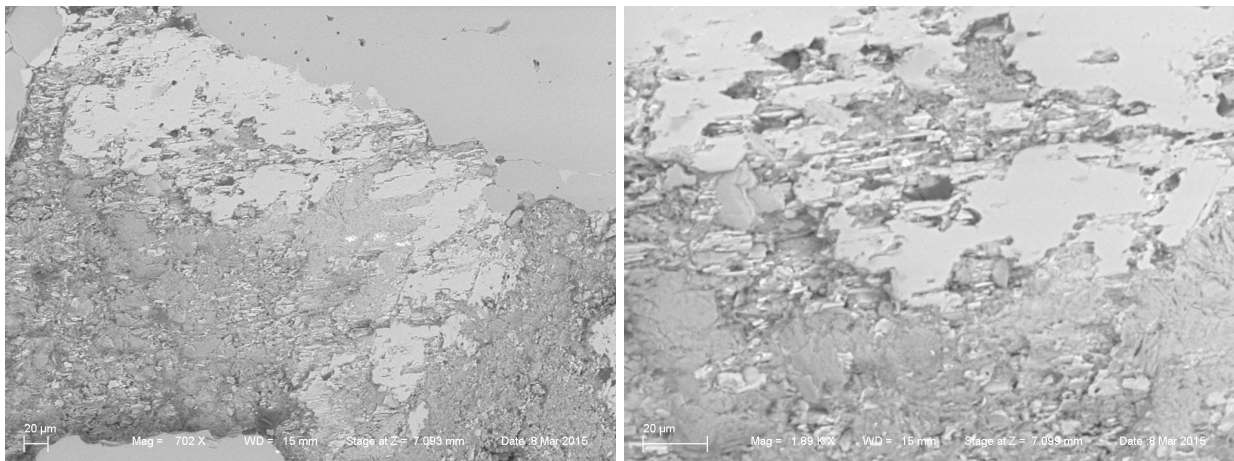


Figure 5.14: K- feldspar with rough pitted surface textures in a polished hand section of Type A, ME02V (slab four, C3-C4 Figure 5.8).

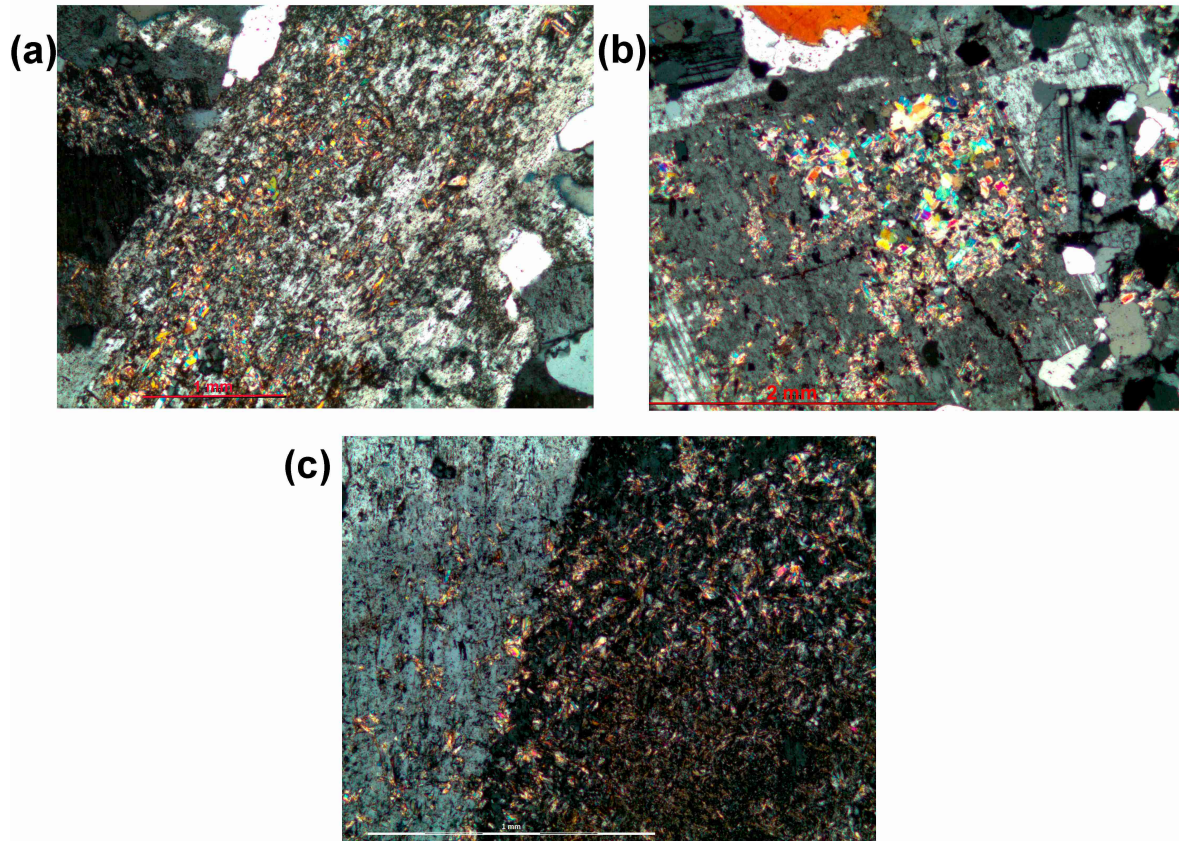


Figure 5.15: K- feldspars showing varying degrees of sericitization. (a) Sericite replacing feldspar in type B (ME01V). (b) More coarse-grained sericite replacing parts of an K- feldspar crystal in type B proximal to the vein (ME04V-B). (c) Sericitization of K- feldspar with Carlsbad twinning, Type C (ME05V). All images in crossed-polarised light view.

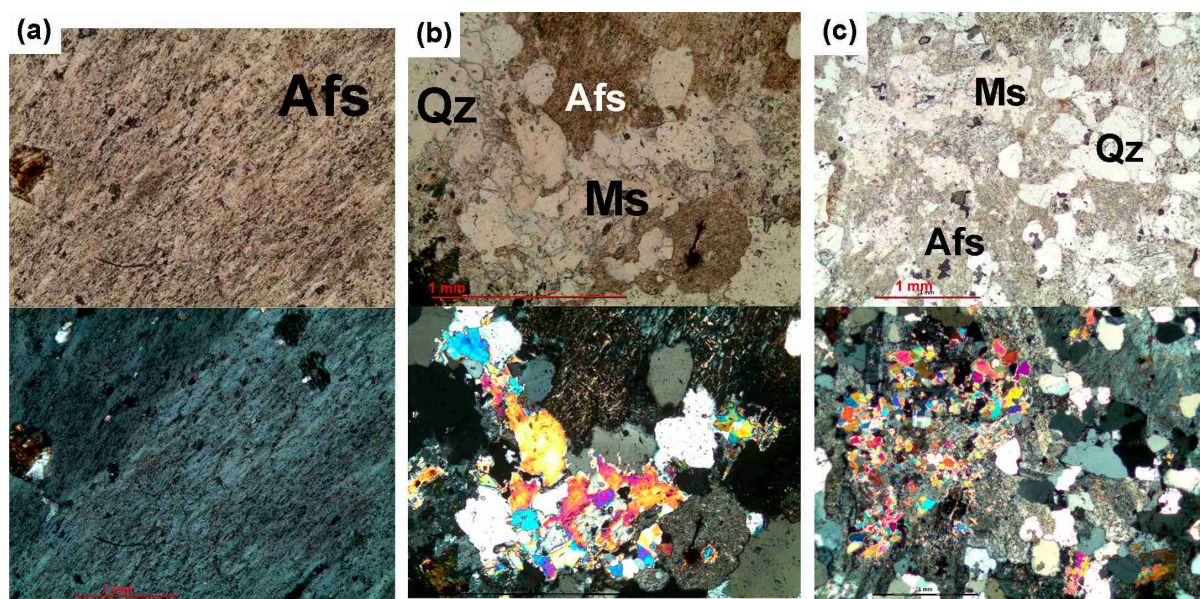


Figure 5.16: (a) Surface texture of K- feldspar in type A, distally to the vein (ME02V-A). (b) K- feldspar with sericitization and muscovite in type A, distally to the vein (ME02V-A). (c) K- feldspar with coarse-grained sericitization and muscovite in the granite (ME03V). All images are plane-polarized light view on top and crossed polarized light view beneath.

5.2.3. Mica

The mica content in the samples varies. In biotite- granite from Pordenack point (KDC granite) and granite from Nanjizal, both biotite and muscovite is present (Figure 5.17A). Biotite occurs as interstitial sub-to anhedral grains, brown in colour and with inclusions of rutile, apatite, zircon and monazite, usually with a pleochroic halo. In KDC granite, the biotite is partly chloritized. In granite (ME03V), chloritization and partly replacement by muscovite is evident. Muscovite is interstitial and fine-to medium-grained anhedral, replacing biotite (Figure 5.20).

Fresh biotite is absent in the rest of the samples, except for one grain at the edge of type A and B distally from the vein (ME02V-A and ME04V-B) (Figure 5.18). Elsewhere, biotite is present as strongly altered aggregates, mostly consisting of rutile (Figure 5.19 and Figure 5.21). Muscovite occurs as anhedral, interstitial fine-to medium- grained in Type B (ME04V), Type A distally from the vein (ME02V-A) and Type C. The muscovite in Type C is more coarse- grained, often occurring in association with altered biotite and sericitization of

feldspars. In Type A proximal to the vein (ME02V-B) and Type B with quartz infill (ME01V), muscovite is absent.

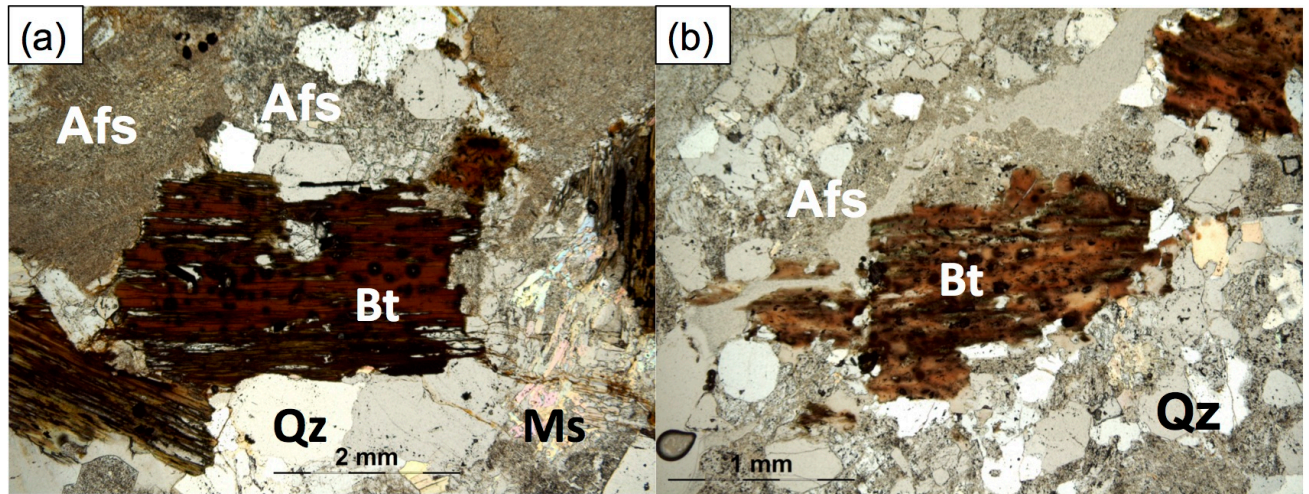


Figure 5.17: Biotite with minor green chloritization and inclusions of rutile, Plane-polarized light view. (a) Biotite-granite from Pordenack point (KDC granite). (b) Biotite-granite at Nanjizal (ME03V).

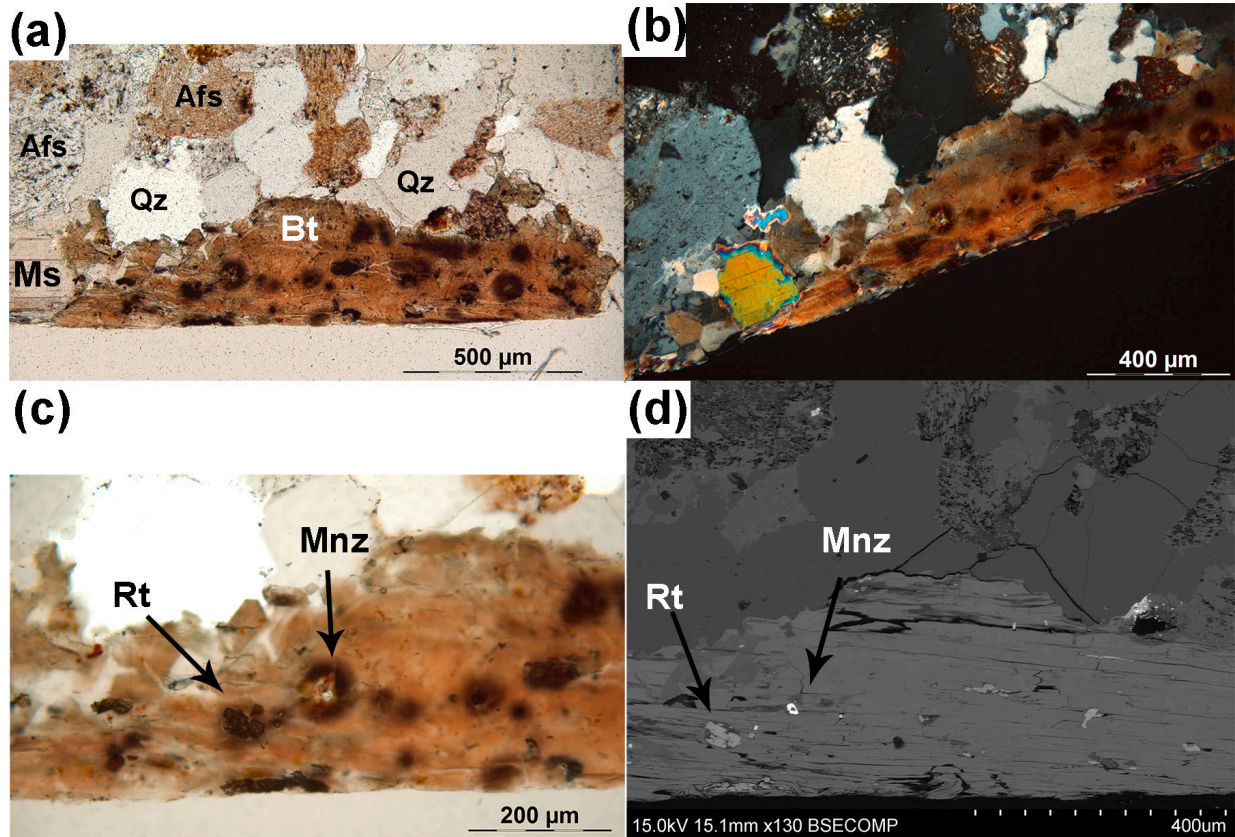


Figure 5.18: Biotite with inclusions of rutile and monazite with pleochroic halo, type A distally from the vein (ME02V-A). (a) Plane-polarized view, with dusty red K- feldspars, quartz and muscovite (b) cross-polarized light view, showing strong reddish brown absorption colour suggesting a high Ti-content (Deer et al., 1992) (c) plane-polarized light view, zoomed in on rutile and monazite with pleochroic halo. (d) BSE-image of the same area as (c).

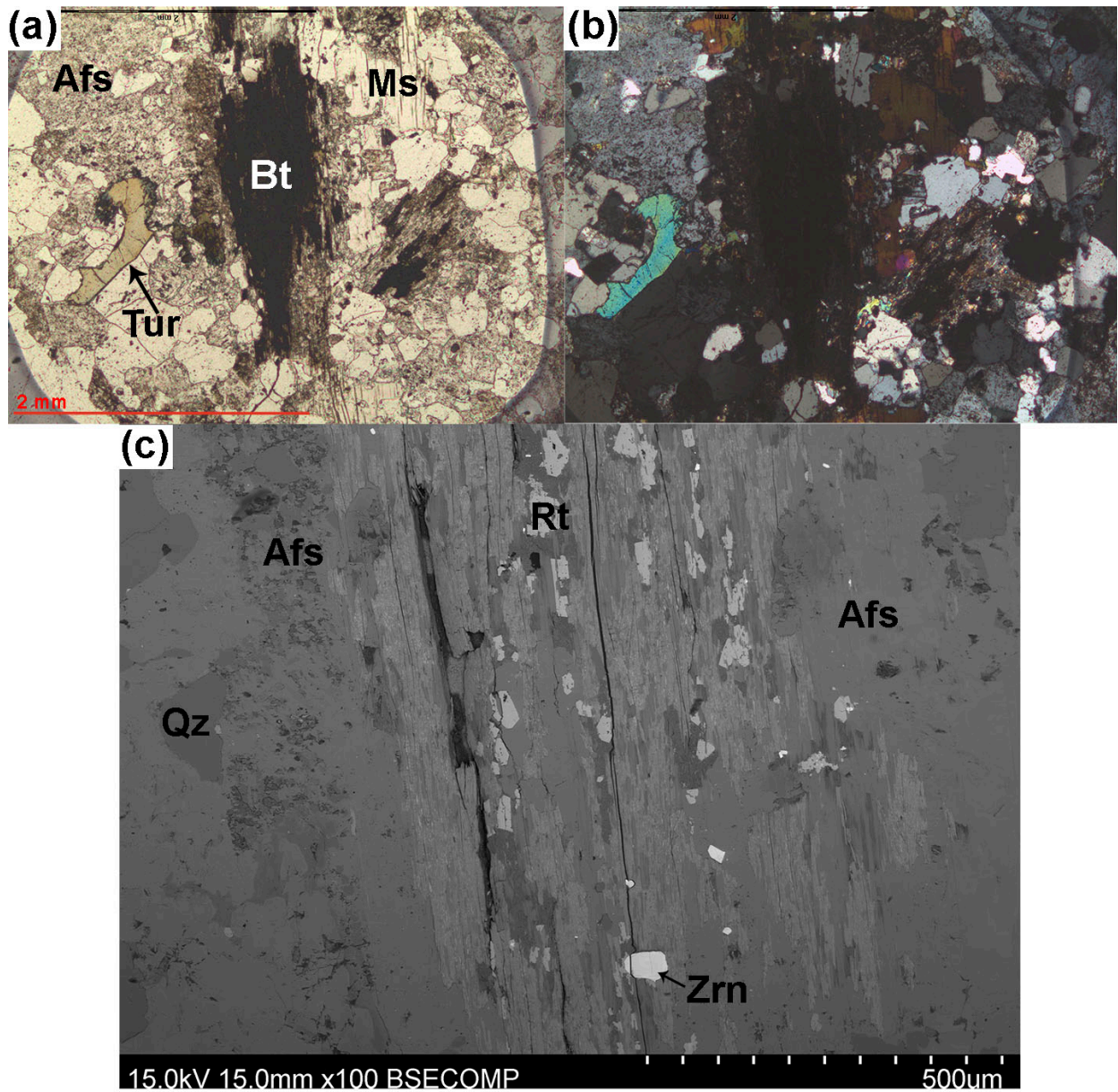


Figure 5.19: (a) plane-polarized and (b) crossed-polarized light view light view of altered biotite consisting of opaque aggregates in type C (ME05V). (c) BSE-image, showing inclusions of zircon and rutile located along the cleavage planes.

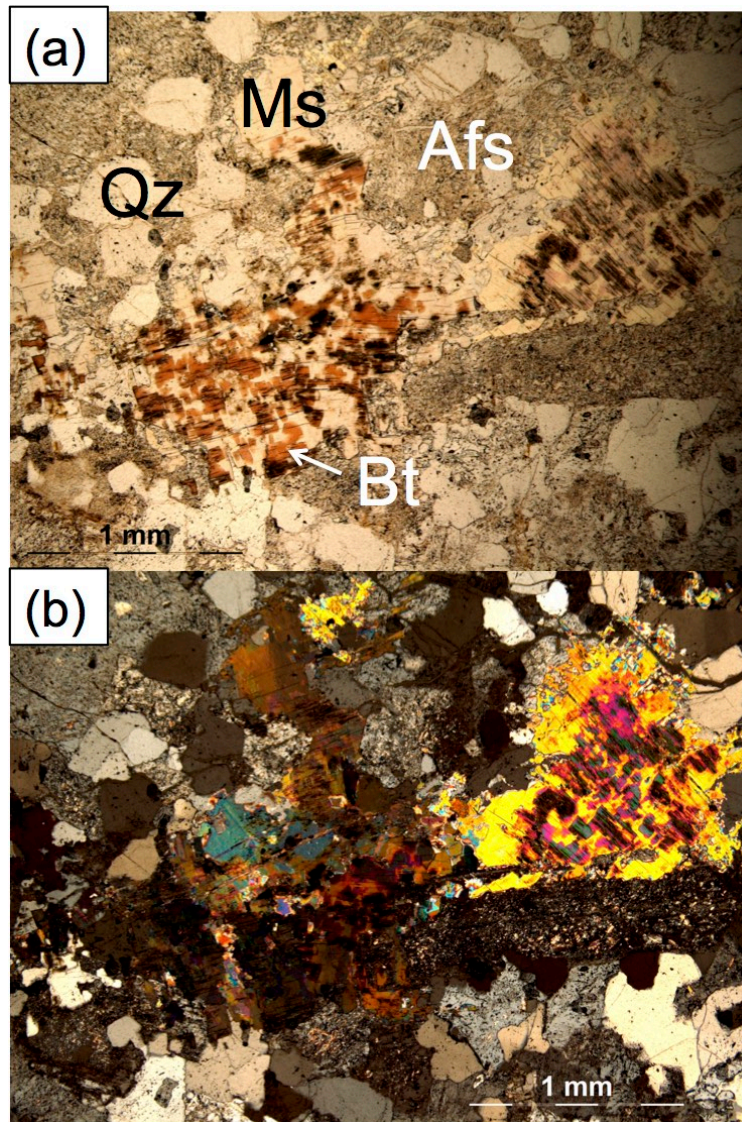


Figure 5.20: Muscovite replacing biotite in the granite, and sericitization of the K- feldspars (ME03V). (a) Plane-polarized light view. (b) Crossed polarized light view.

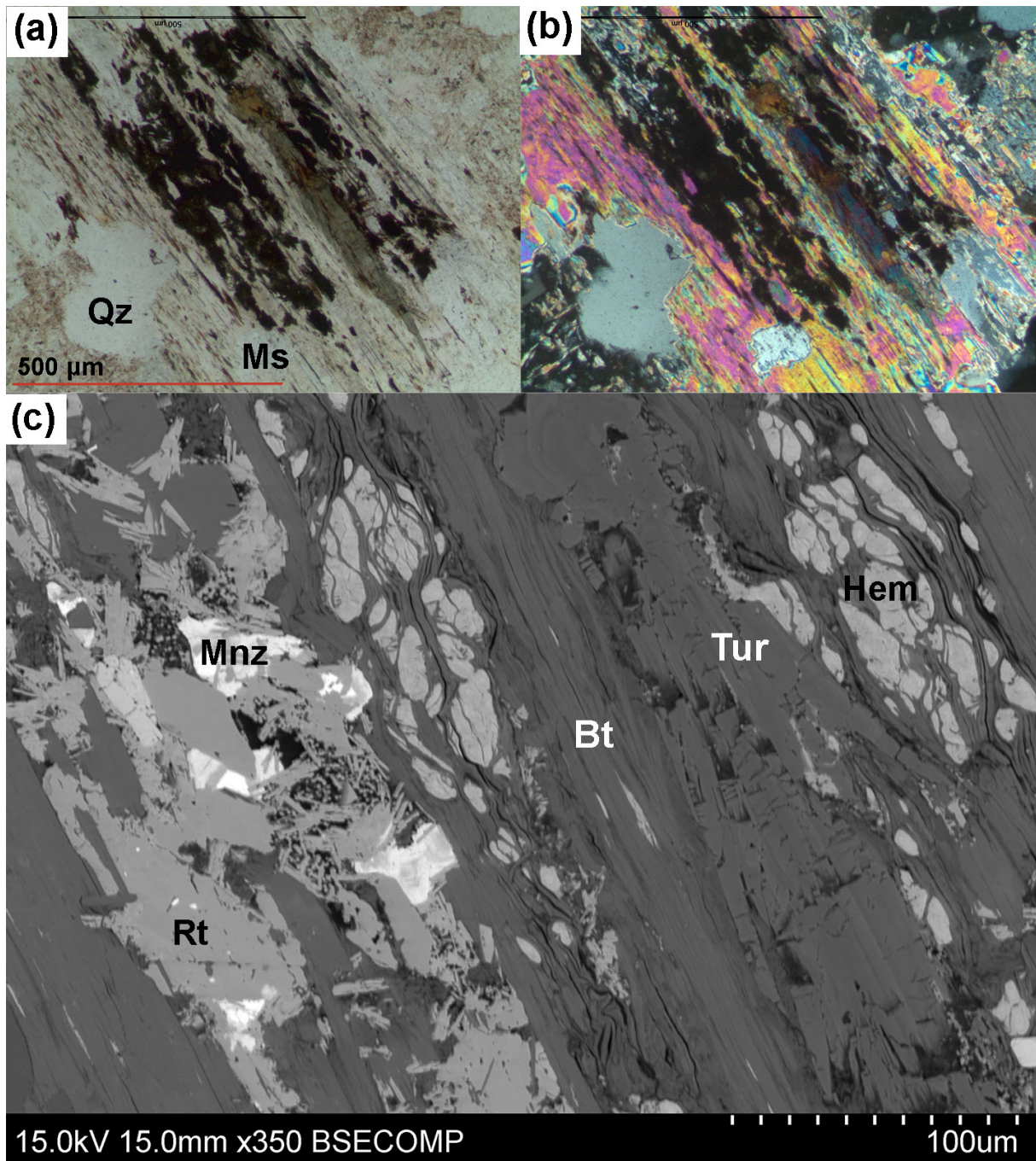


Figure 5.21: Altered biotite in type A distally from the vein (ME02V-A). (a) Plane-polarized and (b) crossed polarized light view, showing aggregates of opaque minerals and tourmaline within secondary muscovite. (c) Zoomed in BSE-image showing tourmaline, lath-shaped rutile, monazite and hematite forming within the cleavage planes of the altered biotite.

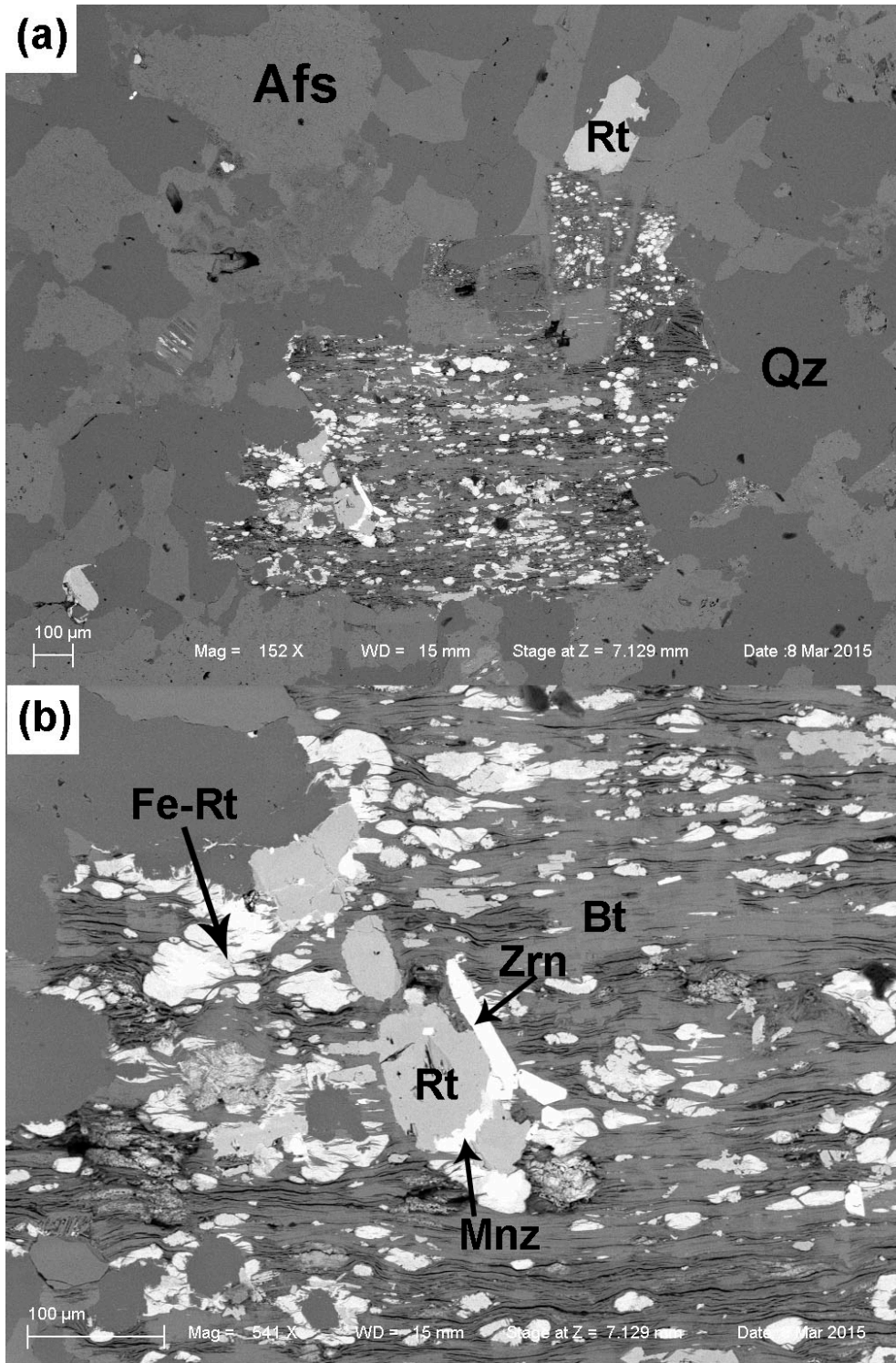


Figure 5.22: (a) Altered biotite with aggregates of rutile located along the cleavage planes, polished hand section of type A, ME02V (slab four, C3-C4 Figure 5.8). (b) Zoomed area showing rutile, Fe-rich rutile and monazite growing in the biotite foliation.

5.2.4. Tourmaline

Tourmaline is present as primary yellow crystals, blue-brown overgrowths and blue-brown needle-like lath shaped crystals in the veins or as clots. The yellow tourmaline, roughly 2 mm, is subhedral to anhedral with sharp contacts towards quartz and K-feldspar. It is sometimes poikilitic with quartz inclusions, and occasionally with yellow-orange to colourless pleochroism. Blue and brown tourmalines have dark to pale blue and/or brown-colourless pleochroism, forming as needle-shaped laths and are often fine-grained. They possess zonation between dark and near colourless (Figure 5.25, Figure 5.26). The colour in the tourmalines in the vein varies from type of vein (Figure 5.24), where Type A have more brown and green-blue tourmaline, Type B with quartz and Type C are more deep blue, and Type B with only tourmaline is more light -blue. The brown-blue tourmaline in Type A is more fine-grained.

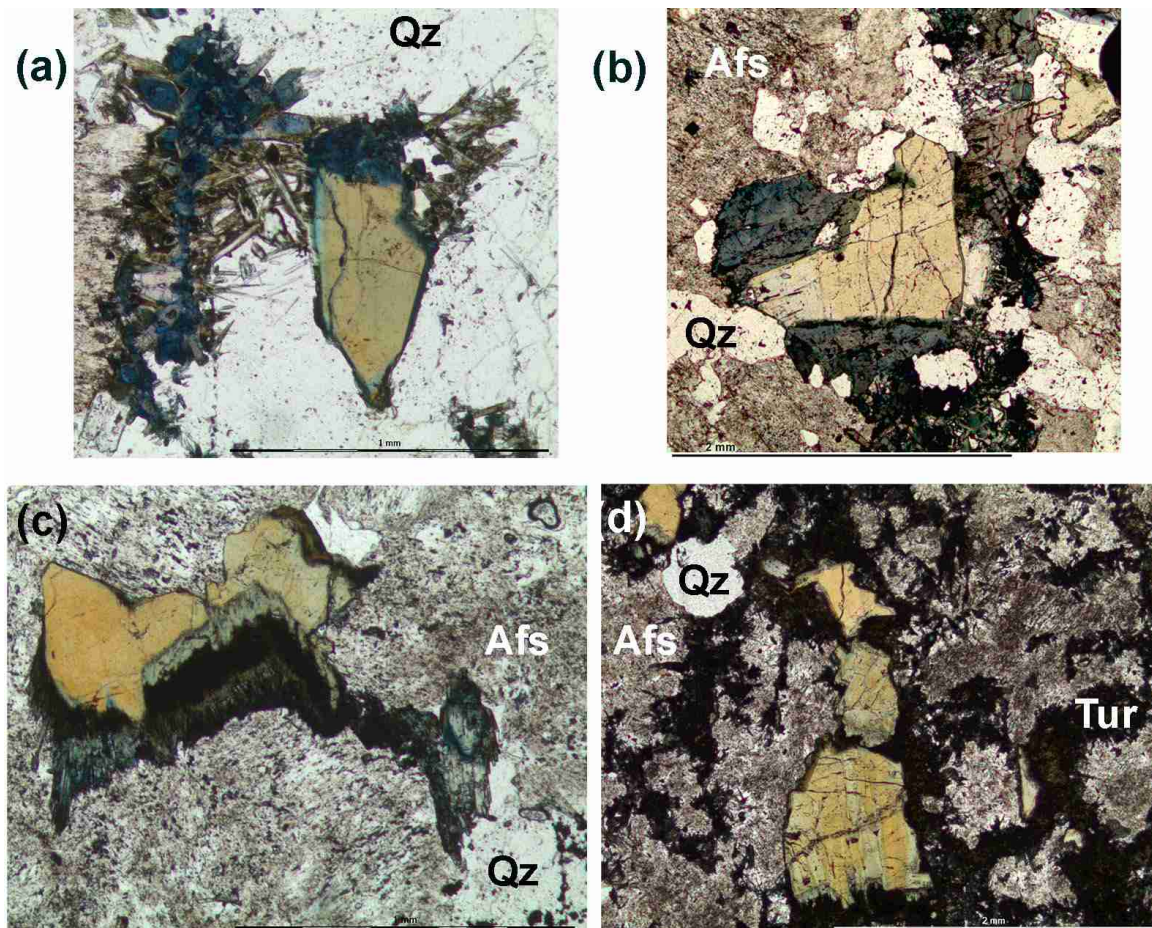
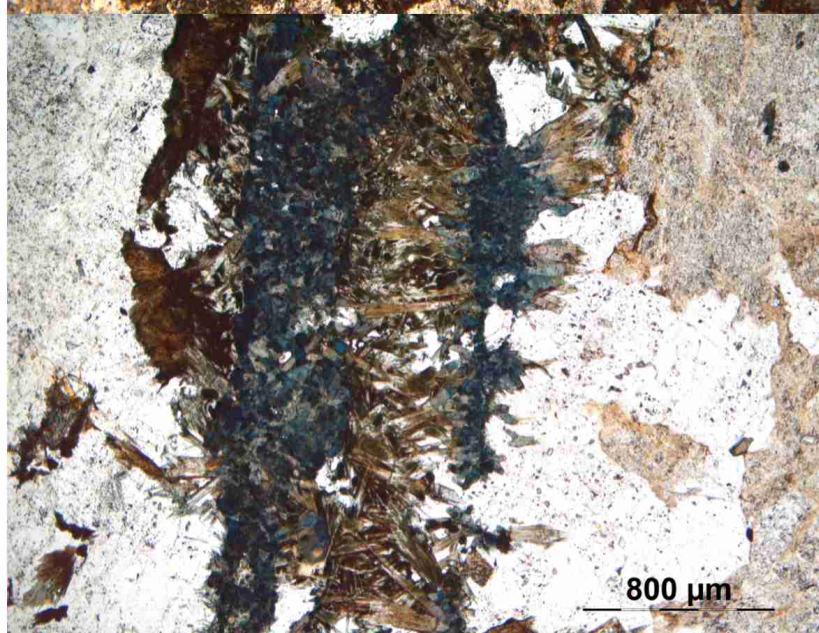


Figure 5.23: Yellow tourmaline with blue-brown overgrowths, plane-polarized light view. (a) Type B (ME01V). (b) Type C (ME05V). (c) Type A distal (ME02V-A). (d) Type A proximal (ME02V-B).

(a)



(b)



(c)

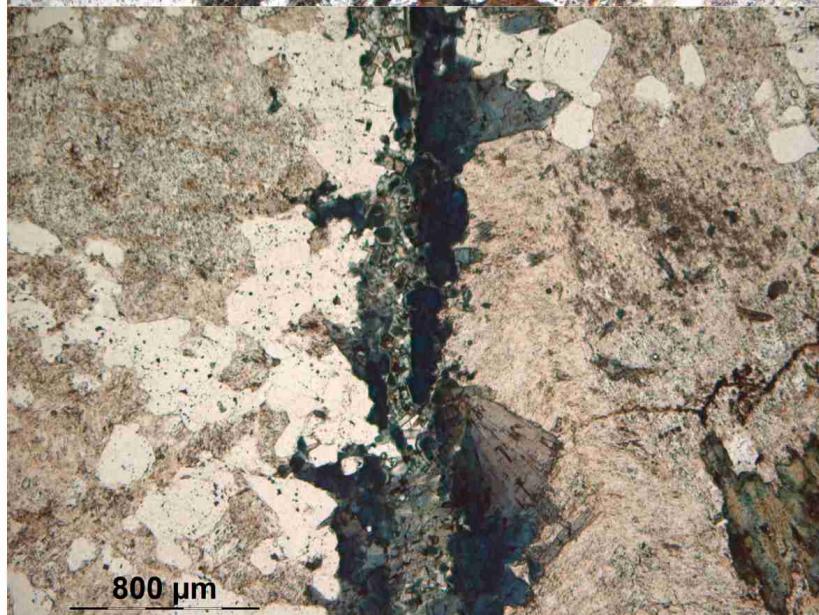


Figure 5.24: Brown and pale blue tourmaline comprising the veins in the three different vein types, in plane-polarized light view. (a) Vein type A, showing tourmalinization enveloping and replacing feldspar (b) vein type B, showing blue and brown tourmaline growth normal to the walls of the fracture (c) Vein type C consisting of blue tourmaline.

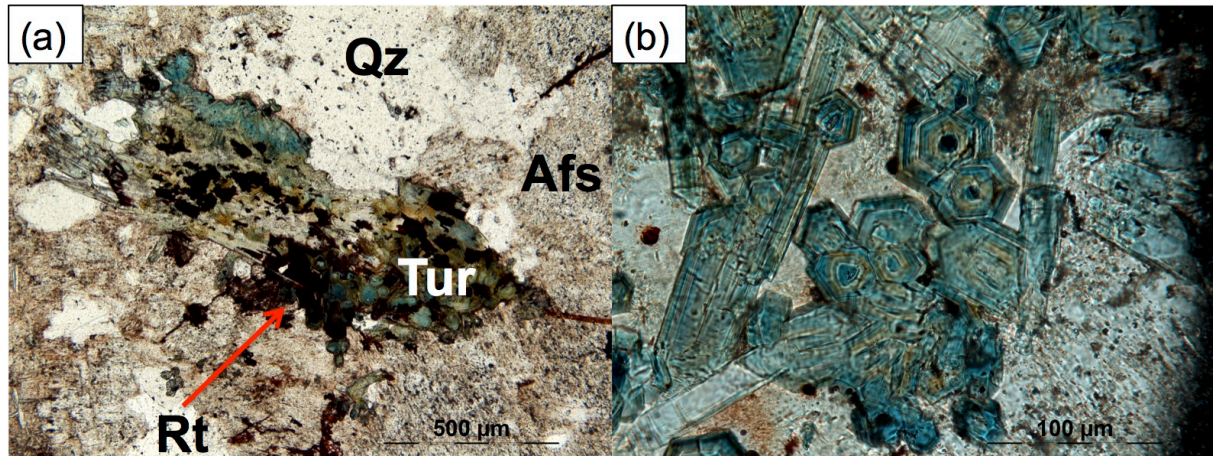


Figure 5.25: (a) Blue tourmaline with rutile inclusions, with sharp grain boundaries towards quartz and K- feldspar. Tourmaline is possibly replacing biotite (b) Finely zoned blue tourmaline. Both in type B (ME04V-B), plane-polarized light view.

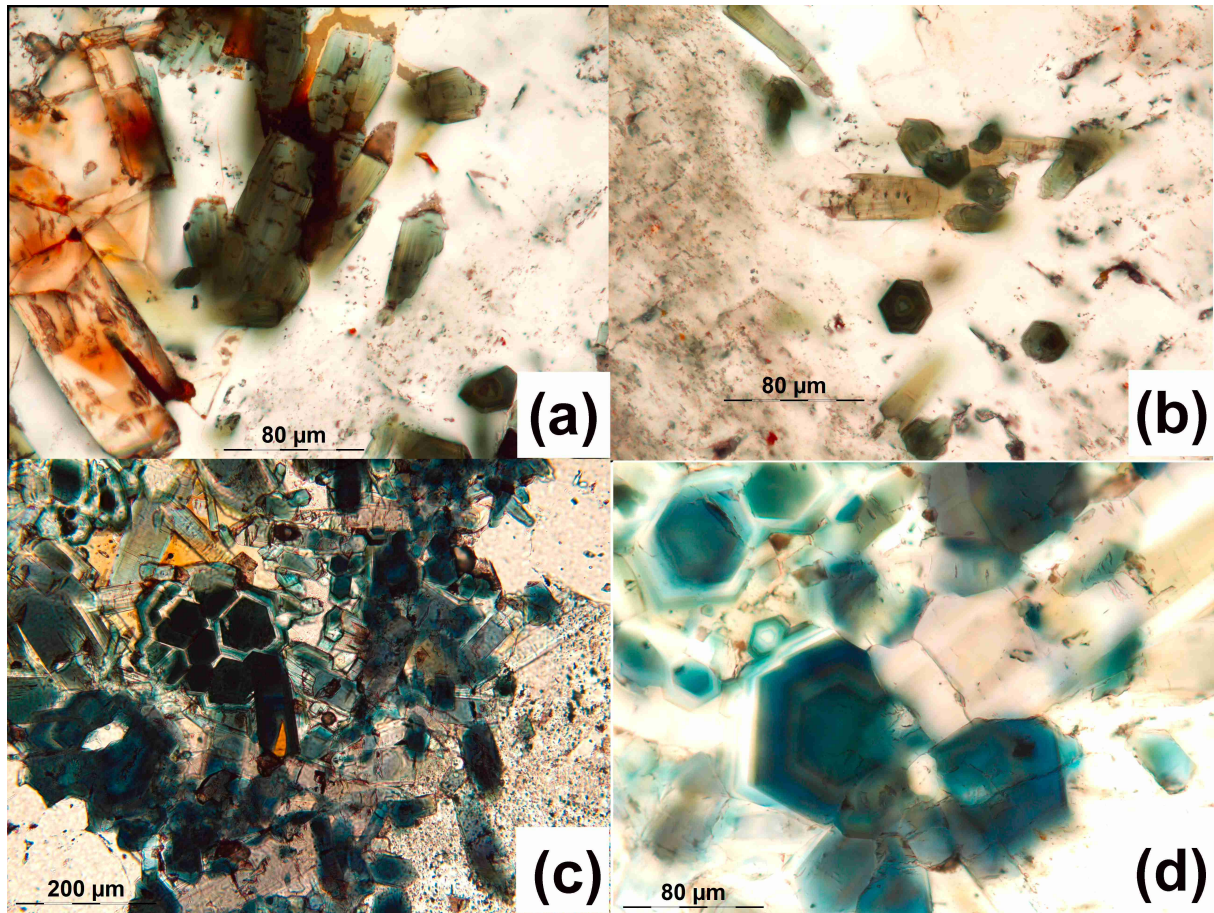


Figure 5.26: Finely zoned blue-brown tourmaline. (a): Zoned, pale blue tourmaline in type A distal associated with cassiterite (ME02V-A). (b): Fine-grained, hexagonal tourmaline cut perpendicular to the c-axis, type A distal (ME02VA). (c) and (d): blue, hexagonal zoned tourmaline cut perpendicular to the c-axis, with dark blue core zones in type C (ME05V). All in plane-polarized light view, (a), (b) and (d) with top lens inserted.

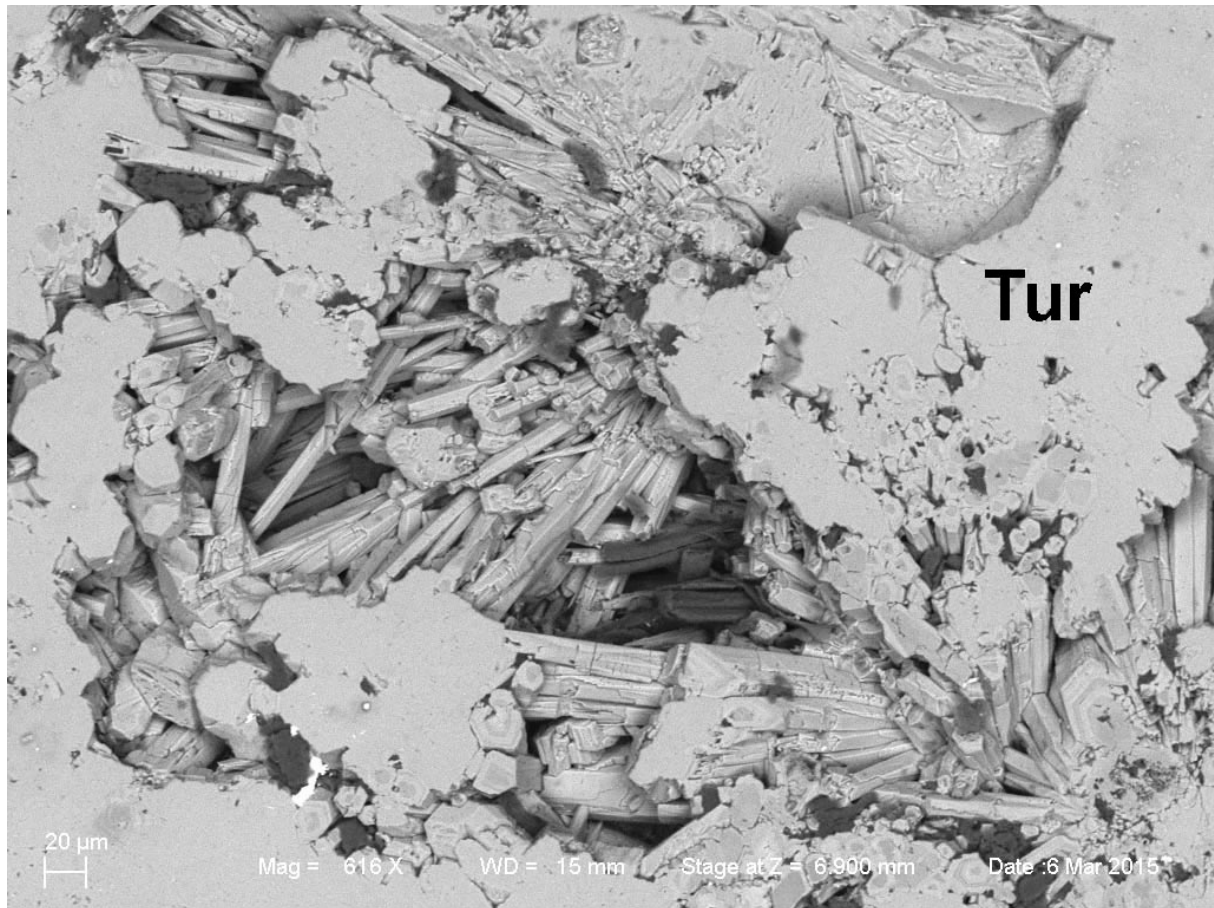


Figure 5.27: BSE-image from the polished sample of type A, ME02V (slab four, C3-C4 Figure 5.8), showing prismatic laths of tourmaline growing in cavities.

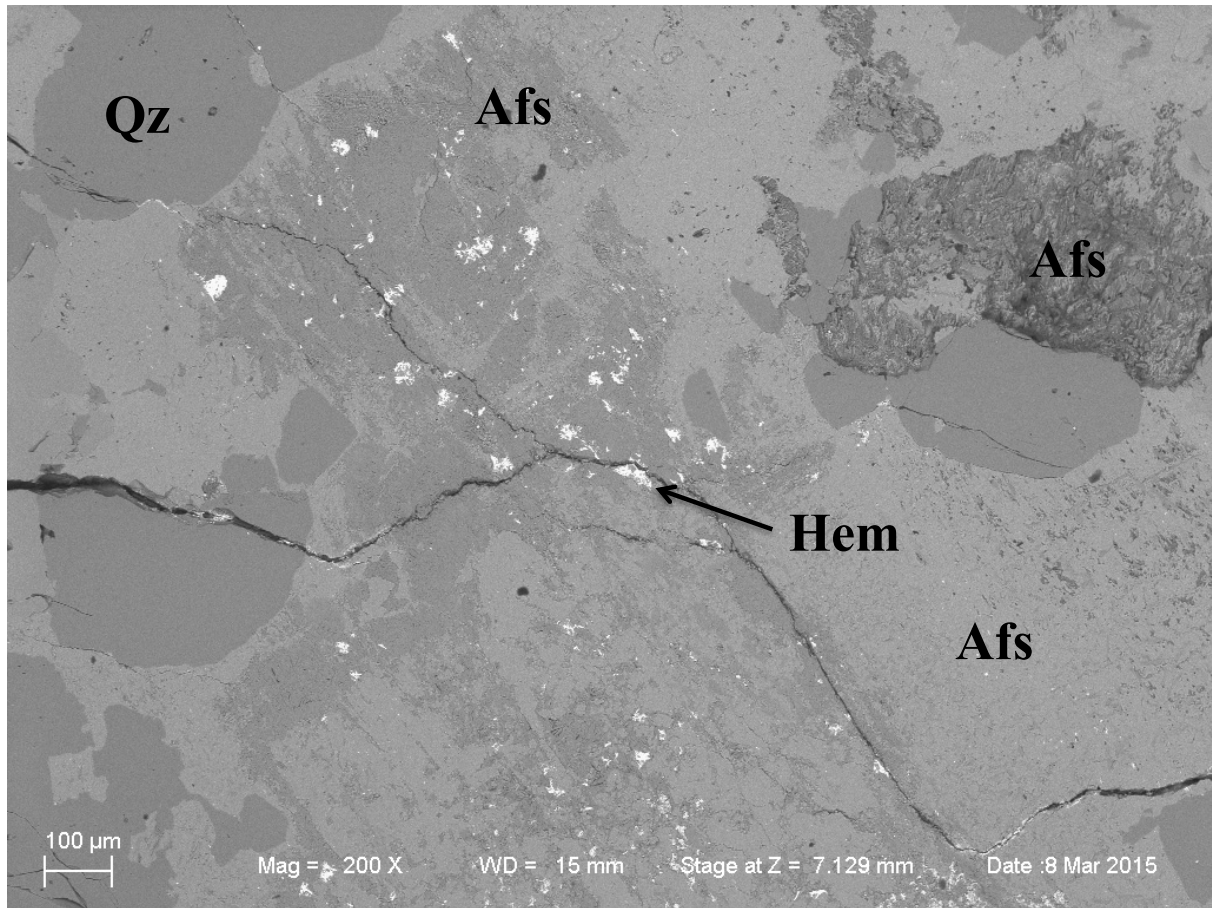


Figure 5.28: Hematite as disseminations and veinlets, in the polished sample of type A, ME02V (slab four, C3-C4 Figure 5.8)

5.2.5. Accessory minerals

The accessory minerals identified in the Nanjizal samples are rutile, zircon, apatite, monazite, cassiterite and hematite. Rutile, zircon, apatite and monazite occur together; most often as inclusions in altered biotite (Figure 5.19, Figure 5.21 and Figure 5.22). *Monazite* is rare, < 50 µm, anhedral and is associated with rutile. *Zircon* forms euhedral, zoned crystals of 50-100 µm, associated with rutile and as inclusions in fresh and altered biotite. *Apatite* is rare, euhedral <100 µm and is associated with rutile. *Hematite* is rare, occurring in type A and B (ME04V) and is associated with rutile in altered biotite (Figure 5.21) and as disseminations and veinlets within type A (Figure 5.28). The main accessory phase is *rutile*, consisting of lath-shaped or anhedral crystals up to 200 µm. It occurs as inclusions in biotite, altered biotite and K- feldspar. Different domains, with highly variable amounts of Sn, Nb, W and Fe, were distinguished by BSE-images. See Figure 5.37 for domain classification. Sn- and W-rich rutile was identified in type A and B, and was absent in type C

Cassiterite occurs mostly in Type A, but is also found in type B. It appears as fine-grained (150 µm) euhedral crystals in association with feldspar and as prismatic laths in Type A distally from the tourmaline vein (Figure 5.30). It also occurs as anhedral grains enclosed within rutile in type A and B, in association with zircon and often monazite (Figure 5.29). Minute inclusions of cassiterite also occur close to the vein in type C.

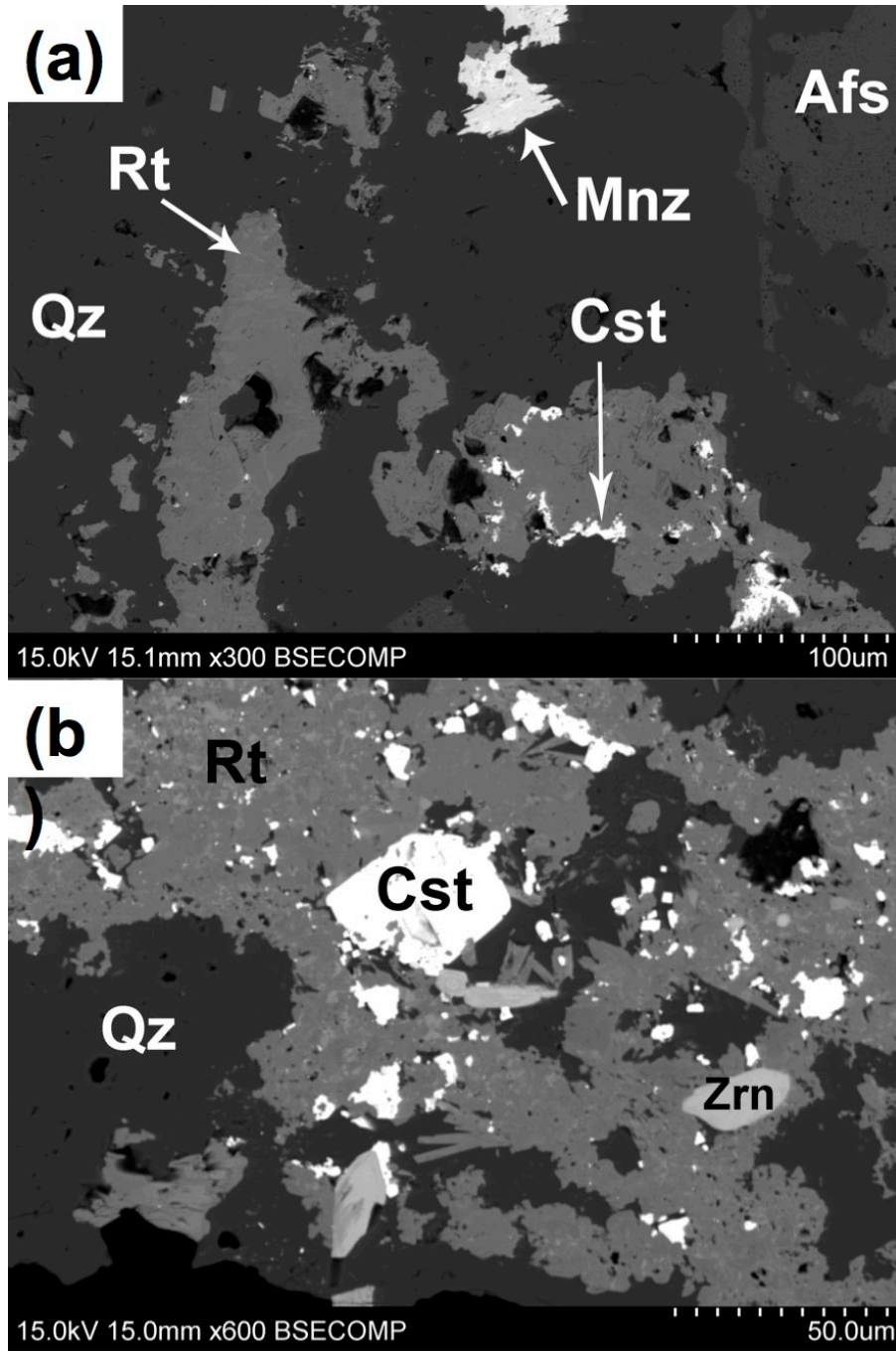


Figure 5.29: Cassiterite in rutile. (a) Cassiterite as fine-grained, anhedral inclusions within rutile, type A distally to the vein (ME02V-A). (b) Euhedral and fine-grained anhedral cassiterite inclusions within rutile, type A proximal to the vein (ME02V-B).

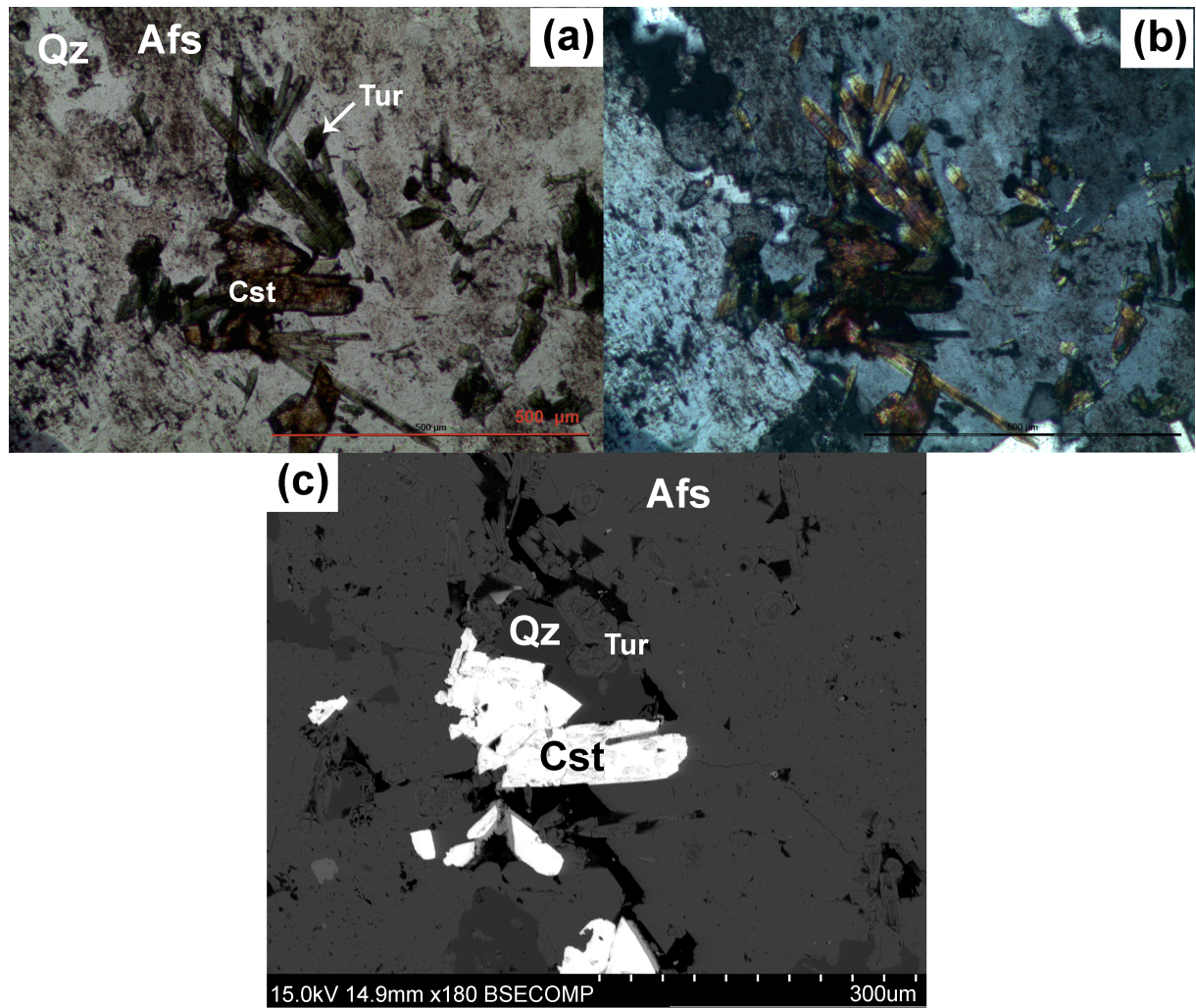


Figure 5.30: Cassiterite associated with pale blue needle-shaped tourmaline, as inclusions within K- feldspar, Type A distally from the vein (ME02V-A). (a) Plane-polarized light view. (b) crossed-polarized light view, (c) BSE-image.

5.3. Geochemical results

5.3.1. Whole rock chemistry and trace element content

Whole-rock chemistry and trace element content is presented in Figure 5.31 as harker diagrams, showing the geochemical variation. Original data is found in Appendix C. Loss of Ignition in these samples is roughly 1 %, indicating loss of H₂O and lightweight elements such as B and Li. Vein type B and C are similar, and compared to KDC granite contains slightly elevated levels in SiO₂, Al₂O₃ and K₂O, and contain slightly less of in the remaining oxides. The higher levels of SiO₂ and K₂O are due to increased amount of Quartz and feldspar

compared to unaltered granite, confirmed by modal mineralogy by XRD. The lower amount of the remaining oxides is probably due a dilution effect because of the changed modal mineralogy.

Sample ME02V, Type A, is different from the other samples geochemically. It has very elevated amounts in K_2O , with 11,71 wt.% compared to 5-6 % in the other samples, due to it containing roughly 70 % K- feldspar, 20 % more than the other samples.

It has a higher percentage of Al_2O_3 , MgO and Fe_2O_3 compared to type B and C, explained by the higher amounts of tourmaline. The lower content of in SiO_2 corresponds to the low amount of quartz (17%), and the low content of Na_2O is likely due to the absence of albite.

In terms of trace elements, the same tendencies are present, where type A (ME02V) displays the greatest differences. Most noticeably is the amount of Sn, where the concentration of 1000 ppm is prominent compared to <100 ppm in the other samples, and 6 -7 ppm in the granite. The amount of W is 12 ppm, and though it is slightly higher in Type A compared to the other samples, it does not display the same trend as Sn.

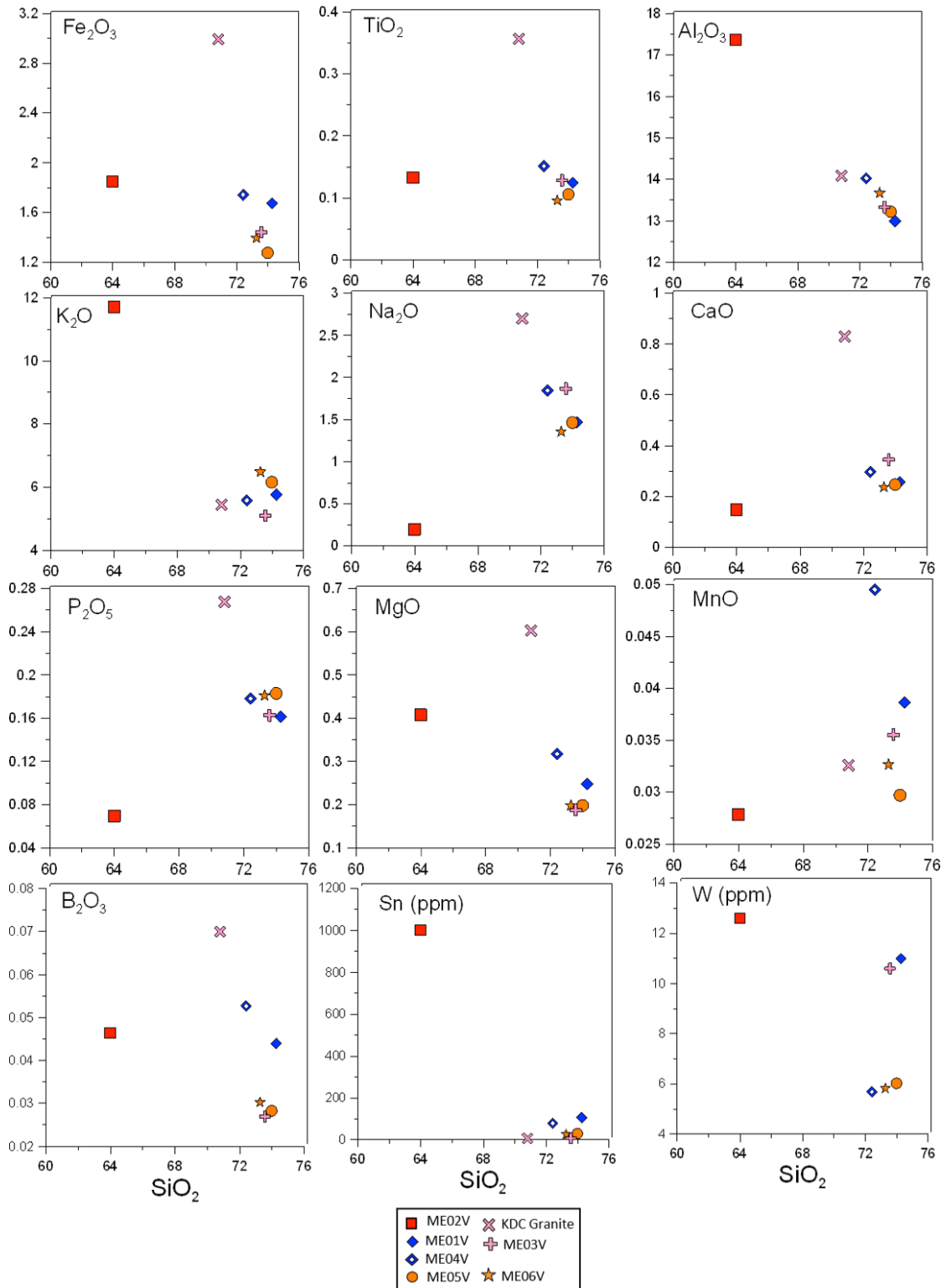


Figure 5.31: Harker diagrams of whole rock chemistry and trace element content of Sn and W plotted against SiO_2 . Red corresponds to Type A, blue is Type B, Orange is Type C and pink is granite. All values in wt.%, except Sn (ppm) and W (ppm). Type A stands out, with elevated levels of Sn, K_2O and Al_2O_3 .

5.3.2. ME02V: Chemical variations across Type A tourmaline vein and alteration zone

Based on the distinctive character of ME02V in terms of macroscopic and microscopic descriptions, as well as enrichment in Sn, it was analysed in more detail. Modal percentages, whole-rock chemistry and trace element content of various zones were analysed, and polished sections were analysed in SEM. Thin sections were not made due to limited time. Figure 5.32 and Figure 5.33 illustrate the petrographic and geochemical variation within a hand section containing a red alteration zone and two tourmaline veins, presented and compared with the data from the Nanjizal granite (ME03V). Geochemical data are found in Appendix C. Within the alteration zone, the amount of quartz and albite is low or decreasing. Coherent is a decrease in SiO_2 and Na_2O , with a minimum in zone C3 containing a tourmaline vein. Middle zones have elevated amounts of microcline, reflected on a relative increase in K_2O and Al_2O_3 . The microperthite amount is mostly constant, with a slight increase in zones C2 and C3, and a decrease in zone 4. Na_2O displays the same trend. Quartz and SiO_2 increases in zone C4, thus making the relative microperthite lower. The tourmaline-content is understandably increased in the areas containing tourmaline veins, reflected by a relative increase in Fe_2O_3 , MgO and B.

Considering the alteration zone and tourmaline veins in terms of metal enrichment, there appears to be no mutual trend. Sn content is high (ca. 1000 ppm) throughout the alteration zone, with increasing amounts in zone C3 associated with a tourmaline vein. There is little enrichment of other metals (<30 ppm). Cu shows very little variation (<10 ppm), Ni is slightly elevated within the alteration zone, and Zn increases towards the transition between alteration zone and granite. The content of W is low (15-30 ppm) and erratic, with a minimum in zone C3 and the granite, and a maximum in zone C5 and C1. Element mapping of the polished slabs shows the distribution of elements within the observable minerals of ME02V (Figure 5.34). BSE image shows similar grey-scale, due to similar densities. Elevated amounts of Si displays quartz, clearly illustrating the geochemical variation presented in Figure 5.32. The amount of K is constant within the feldspar. Al is constant within the feldspar, and is enriched within some of the tourmaline. Mg and Fe is somewhat enriched in tourmaline. The distribution of Sn is illustrated in blue, appearing to be associated with the tourmaline- veins, with a higher amount Sn detected near the tourmaline vein in C3, correlating with the geochemical trend in Sn.

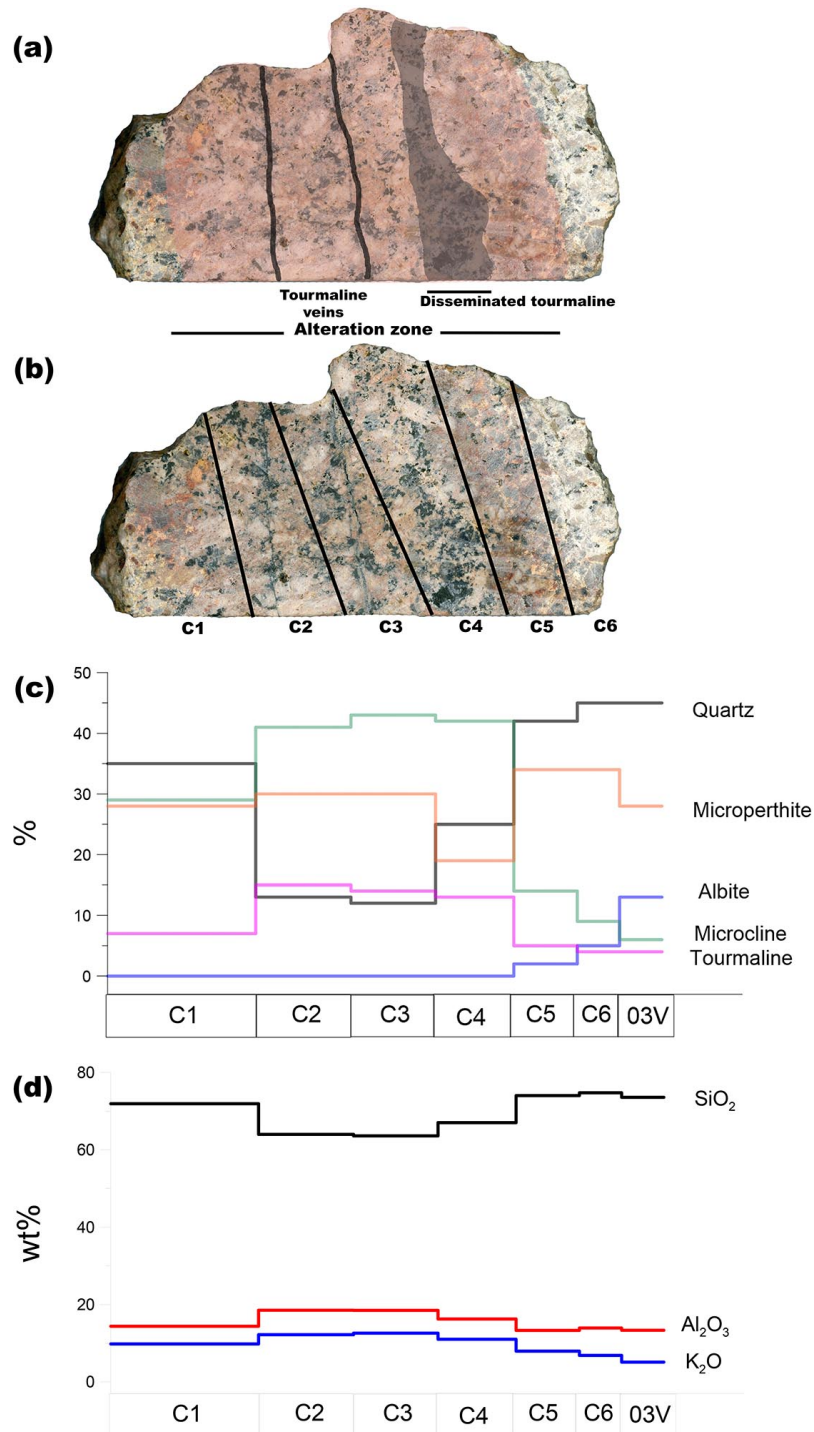


Figure 5.32: Plots showing the distribution of elements across a vein zone in ME02V. (a) Hand section of ME02V, consisting of red alteration zone, two tourmaline veins and a zone of disseminated tourmaline. (b) The division of ME02V into six zones (C1-C6), based on the observed features in a. (c) Plot showing the modal mineralogy distribution of Quartz, Microperthite, Albite, Microcline and Tourmaline within the six zones, compared with the granite (ME03V). (d) Whole rock chemistry distribution of SiO_2 , Al_2O_3 and K_2O within the six zones, compared with the granite (ME03V).

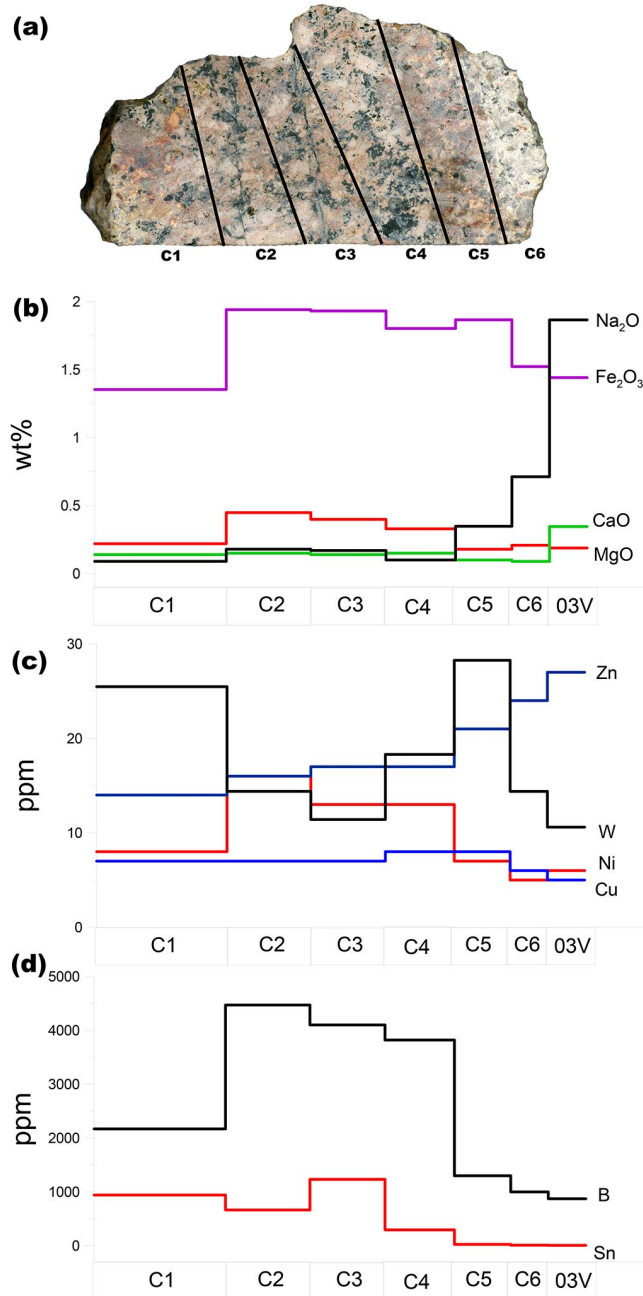


Figure 5.33: Plots showing the distribution of elements across a within the six zones in ME02V, compared with the granite (ME03V). (a) The division of ME02V into six zones (C1-C6). (b) Whole rock chemistry (wt.%) distribution of Na_2O , Fe_2O_3 , CaO and MgO within the six zones, compared with the granite (ME03V). (c) Trace element distribution (ppm) of the metals Zn, Ni, W and Cu within the six zones, compared with the granite (ME03V). (d) Trace element distribution (ppm) of B and Sn within the six zones, compared with the granite (ME03V).

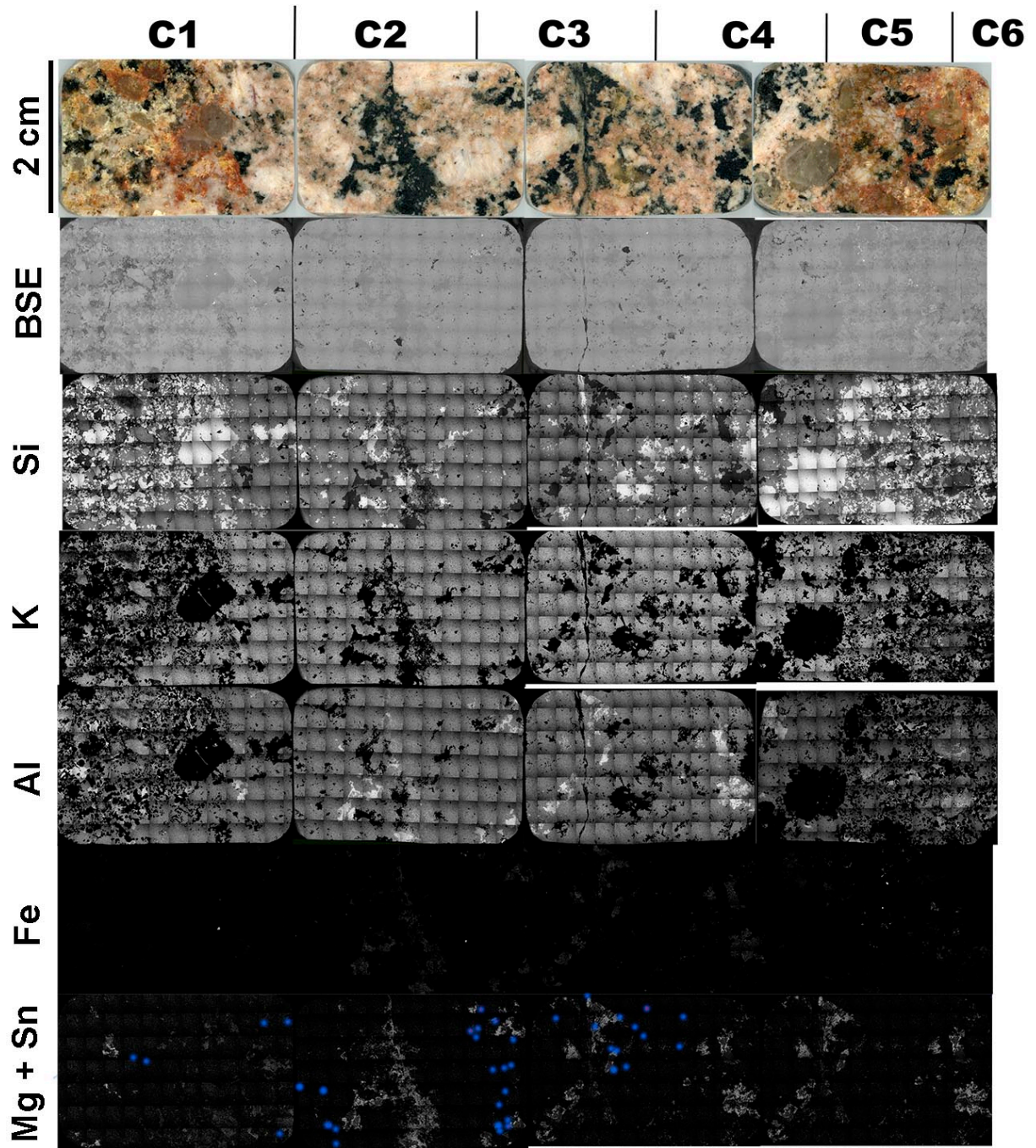


Figure 5.34: SEM Element mapping of the polished slabs of ME02V. Shown from top to bottom are the divisions corresponding to the hand section of ME02V, the polished sections used, BSE-image and the element distribution of Si, K, Al, Fe and Mg. White colour represent enrichment, black represent depletion. Shown in blue is the distribution of Sn, marked in red within the blue are the size of pixels that responded for Sn during the element mapping.

5.3.3. Isocon diagram

Isocon diagrams were made to display the mass change between zones C3 and C6, assuming that TiO_2 and Zr remained essentially immobile during the alteration. The results of the isocon calculations are shown in Figure 5.35. The most striking feature is the very high gain of Sn (1295 ppm), verifying that Sn enrichment is a feature of the alteration zone. The gain in K_2O and loss of Na_2O is likely a feature of potassic alteration. Gain in Al_2O_3 , MgO , Fe_2O_3 , CaO and B is likely due to higher amount of tourmaline. Gain in the large ion lithophile elements (LILEs) Ba, Rb, Sr are related to high mobility of these elements during alteration processes, and the large gain in Ba relative to Rb and Sr could be explained by the increased amount of K- feldspar, and Sr. V, Zr and Nd presents immobile behaviour.

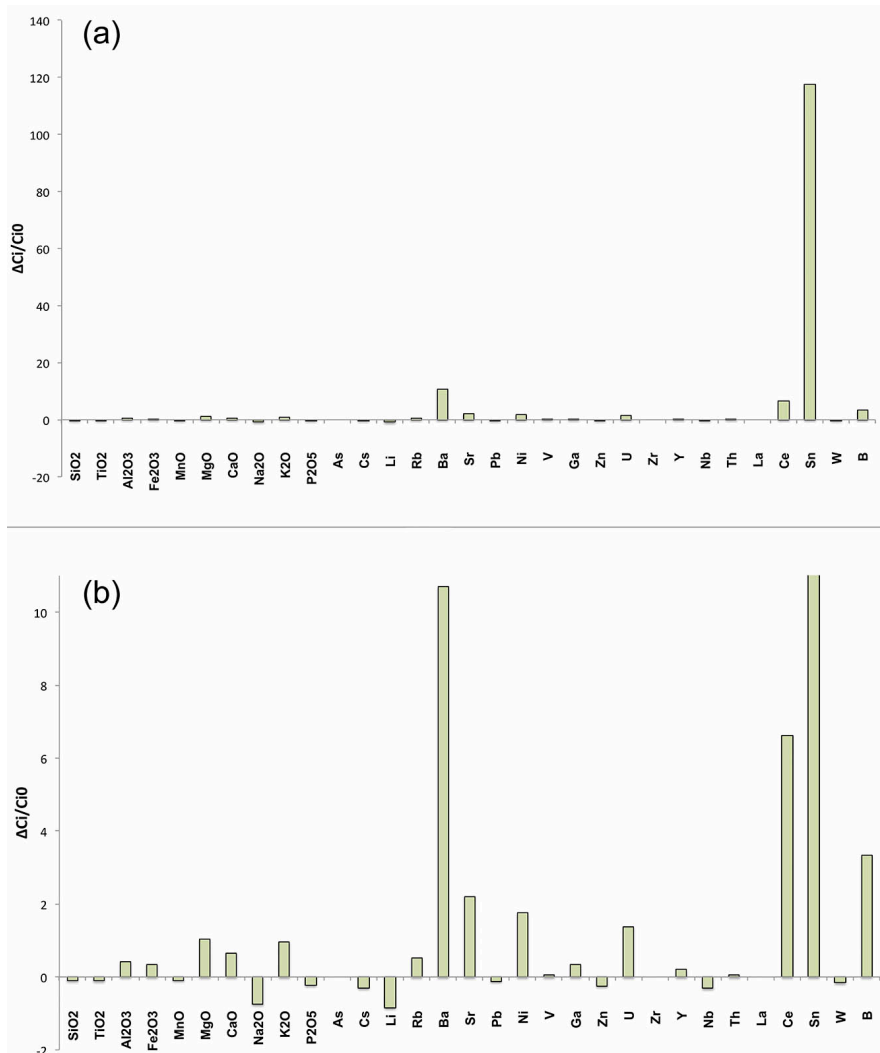


Figure 5.35: Isocon mass balance calculations for the alteration of ME02V, type A. The isocon diagram compares the middle zone of the alteration with tourmaline vein (C3) with the least altered zone (C6). The results are plotted as loss/gain relative to the least altered sample ($\Delta C_i/C_i^0$). The absolute gain/loss (ΔC_i) in wt% or ppm are reported in Appendix C.

5.3.4. Feldspar

The feldspar ternary diagram in Figure 5.36 displays the composition of feldspars in unaltered feldspar from biotite-granites in the Land's End granite (KD) and the altered samples from Nanjizal. The feldspars consist of K- feldspars, plotting between Or₉₅ and Or₁₀₀, with perthite lamellae. Compared to unaltered granite, anorthite is absent in the Nanjizal samples. There appear to be no chemical distinction and small variations among the megacrystic and interstitial K- feldspar, and core and rim. One measurement of the K- feldspar interstitial rim is consisting of a larger albite-component (Ab₃₉, Or₆₁) and plots as an outlier. The accompanying core measurement has a much smaller albite component (Ab₆), and there is no visible zonation in thin section. Given the high amount of microperthite (32%), it can be assumed that an albitic microperthite contributed to the abnormal measurement.

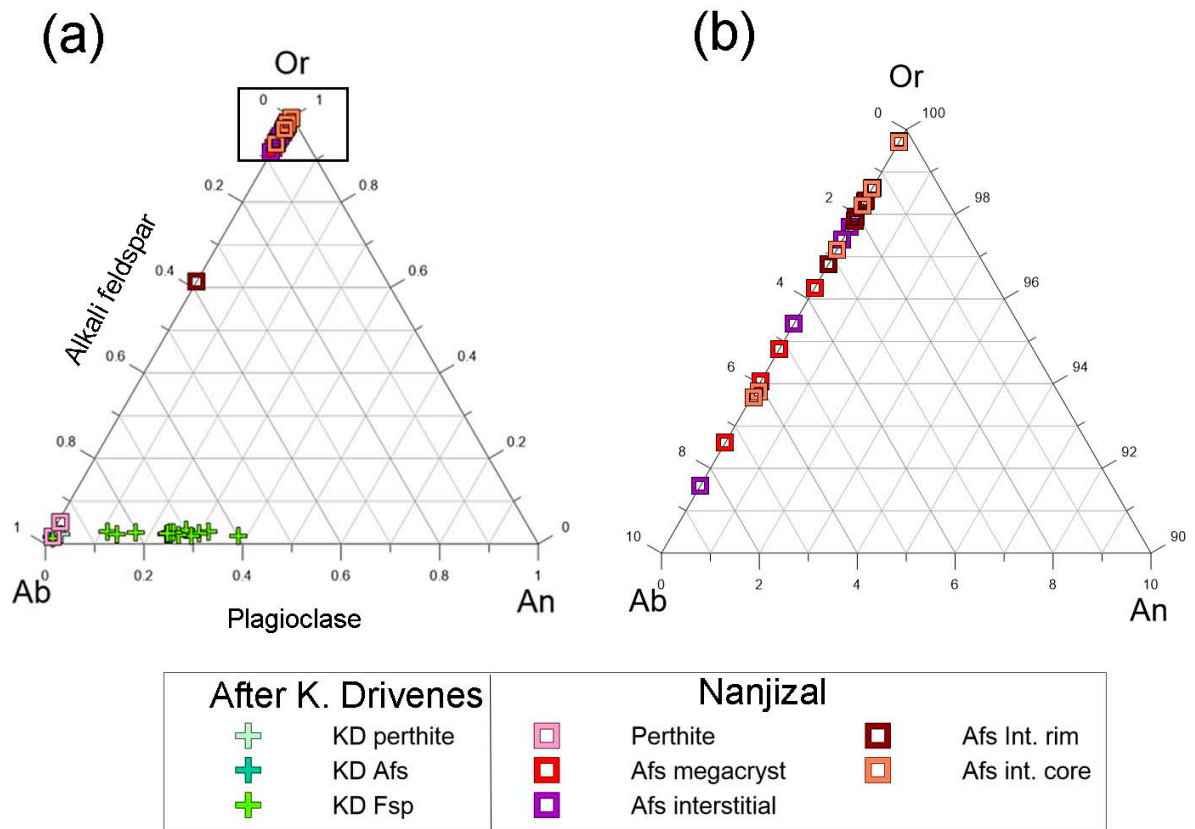


Figure 5.36: Feldspar ternary diagrams. (a) Nanjizal samples and granite data from the southern parts of the Land's End granite, sampled and analysed by PhD-candidate Kristian Drivenes. (b) Zoomed in on area marked in 7a, showing no anorthite component in the feldspars and no apparent trends between analysis of the rim, core, megacrystic and interstitial K-feldspars.

5.3.5. Rutile

Four different domains in a rutile grain in type A were distinguished based on physical appearance and grey scale on BSE-imaging (Figure 5.37): (1) Dark and homogeneous, (2) Light grey homogeneous along the edge (3) Bright grey and (4) Highly homogeneous. The Paragenetic sequence of domains is unclear, although domain 2 must be youngest as it is situated at the outer rim. Trace element contents of Sn, W, Nb, Fe, Si, V and Al were done by microprobe analysis, and the variations in Sn, W, Fe and Nb is plotted in Figure 5.38. Plotted in blue are data by Müller and Halls (2005), where four different domains within a rutile grain have been distinguished. The rutile in type A contains highly variable amounts of S, W, Fe and Nb, shown by the contrast of the BSE signal.

Domain 1 has a highly variable amount of Fe (6000-25 000 ppm) and Nb (1400 -15 800) and W (200-12 000), and contains relatively low Sn (2000-7000 ppm). *Domain 2* contains relatively low Fe (6000-13 800) and W (1000 -18 600 ppm), and has highly variable amounts of Sn (3000-50 000 ppm) and Nb (3500- 46 000 ppm). *Domain 3* is enriched in Nb (20 000-48 500 ppm), Fe (18 000-42 000 ppm) and W (12 300-38 500 ppm), and contains highly variable amounts of Sn (2800- 50 700 ppm). *Domain 4* is somewhat enriched in Nb (8400-20 600 ppm), contains relatively low Fe (1900-7000 ppm), W (3000-8200 ppm) and Sn (457-31ppm).

The most enriched domain in terms of Sn and W is Domain 3, corresponding to the brightness of rutile in BSE, followed by domain 2. The enrichment of W appears to be associated with the amount of Fe (Figure 5.38D), while the enrichment of Sn does not exhibit such a trend (Figure 5.38C)

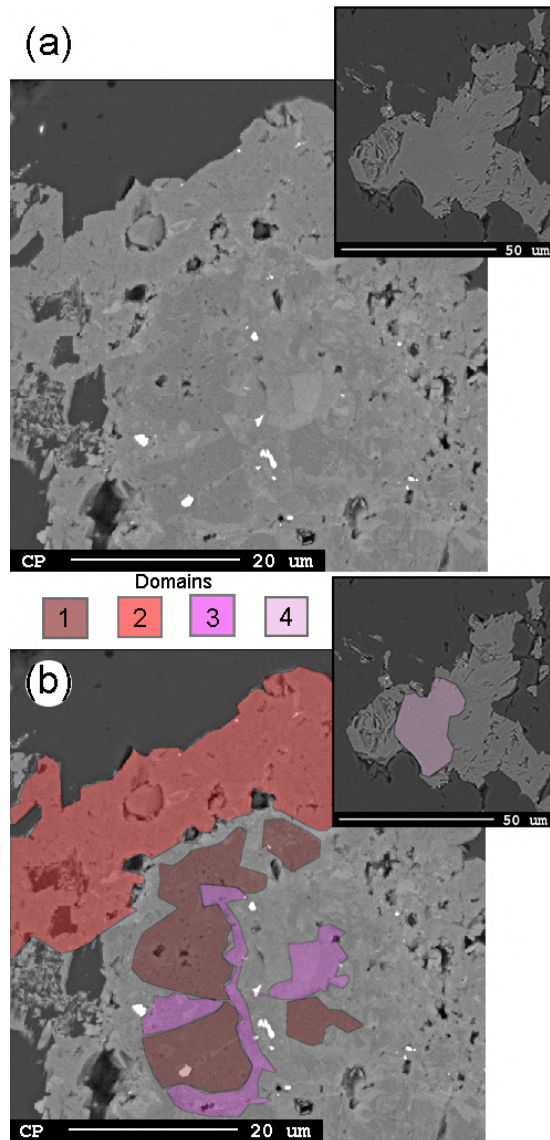


Figure 5.37: (a) BSE image of rutile in type A in proximity to the tourmaline vein. The rutile contains different textures and domains contrasted by BSE within the crystals. (b) Distribution map of four different domains within the rutile shown in (a). The bright white phases are cassiterite. See Figure 5.29B for the rutile association with cassiterite in the same rutile grain.

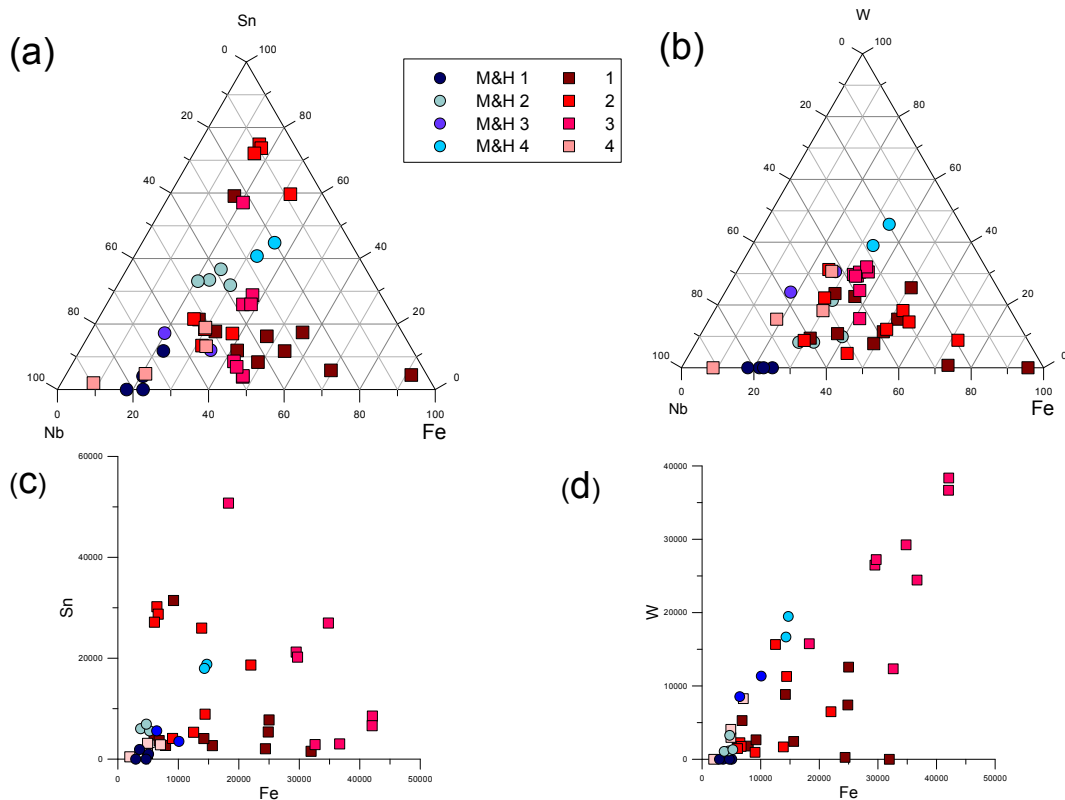


Figure 5.38: Rutile composition diagrams showing analysis from ME02V-B compared to analysis done by Müller and Halls (2005) in Wheal Remfry, each divided into four domains seen in Figure 5.37. (a) Sn-Fe-Nb. (b) W-Fe-Nb. (c) Fe vs Sn, showing no direct correlation (d) Fe vs W, showing correlation in both the Wheal Remfry and Nanjizal analyses.

5.3.6. Tourmaline chemistry

Quantitative analysis of the tourmalines and structural formulae and site allocation calculations are listed Appendix D. Tourmaline is grouped based on colour in plane-polarized light and sample name, and the nomenclature are after Henry et al. (2011). The categorization of colour in the brown, blue and pale blue tourmaline was difficult (Figure 5.39), as most of the tourmalines display a brown-blue to translucent pleochroism, and fine-grained crystals in proximity would often show a variation in colour.

Tourmalines classify as Schorl and dravite in the alkali and vacancy groups (Figure 5.40 A), with the majority plotting within the schorl field. Yellow tourmaline plots exclusively within the schorl field (Figure 5.40 B), with $Mg/(Mg+Fe)$ from 0.02 to 0.17 and X-site vacancies between 0.26 and 0.49. The dark blue tourmaline plot in a similar trend in terms of X-site vacancies (0.0-0.46), but with a larger variation in $Mg/(Mg+Fe)$ from 0.0 to 0.72, with the

majority plotting close to zero. The brown and pale blue tourmaline plot in a similar fashion both lying within the schorl and dravite field. The brown have $Mg/Mg+Fe$ from 0.0 to 0.79 and x-site vacancies from 0.0 to 0.24, while the pale blue have $Mg/Mg+Fe$ from 0.05 to 0.93 and X-site vacancies from 0.07 to 0.16 (Figure 5.40 C).

Pale blue tourmalines in Type A distal and all tourmalines in type B and C plot along the $FeMg_{-1}$ -vector (Figure 5.41 A), where the yellow tourmaline and dark blue tourmaline are more Fe-rich and close to stoichiometric schorl, while the pale blue show a wide distribution and a higher Mg towards stoichiometric dravite. Some of the pale blue tourmaline in type A distal also plot along the $Fe^{2+}Fe^{3+}(Mg,Al)_{-1}$.

The values of $\sum(Fe+Mg) < 3$ a.p.f.u in Figure 5.41 A reveal the presence of Al in the Y site within much of the blue and pale blue tourmaline (Pesquera et al., 2012). Substantial amounts of Al may be accommodated by a combination of two exchange vectors, foitite $(Na,R^{2+}(Xvac,Al)_{-1})$ and olenite $[Al,O(R^{2+},OH)_{-1}]$, where $R^{2+} = \sum^Y Fe + \sum^Y Mg + \sum^Y Mn$. The relative importance of these substitutions can be established by using the Xvac vs Al diagram (Figure 5.42 A) and Xvac vs $\sum^Y R^{2+}$ (Figure 5.42 B), where deviations from the $Al,Xvac(R^{2+},Na)_{-1}$ exchange vector are observed in the brown tourmalines, which have a Al deficiency. This means that other substitutions contribute in the brown tourmalines in type A vein. By removing the influence of the substitution $Al,Xvac(R^{2+},Na)_{-1}$, the contribution by the exchange vector $Al^Y O(R^{2+}OH)_{-1}$ can be tested (Figure 5.42 C). However, some data still deviate significantly from the exchange vector line. The compositional variability is therefore controlled mainly by a combination of the $Al,Xvac(R^{2+},Na)_{-1}$, $Al^Y O(R^{2+}OH)_{-1}$ and $FeMg_{-1}$ exchange vectors.

The brown and blue tourmaline in Type A in the vein contains high Fe (>3 a.p.f.u) and low Mg ($<0,5$ a.p.f.u), and lies above the schorl-dravite vector. They also display a negative correlation between Fe and Al (Figure 5.41B), where several have Al <5 a.p.f.u. They appear to plot along the vector $(Fe^{2+} Fe^{3+}(Mg,Al)_{-1})$ (Figure 5.41 B), indicating that there are more exchange vectors controlling the composition in tourmaline. The Y site also has a maximum occupancy of 3 a.p.f.u Fe +Mg, so tourmalines containing >3 a.p.f.u must have an involvement of the uvite substitution, $Ca,Mg(Na,Al)_{-1}$, or the ferric substitution, $Fe^{3+}Al_{-1}$, where “excess” Fe is contained within a different site than Y (London and Manning, 1995). These tourmalines do not plot along the uvite substitution vector (Figure 5.42D), indicating a

substitution of “excess” Fe most likely as Fe^{3+} in Z because of the substitution vector $\text{Fe}^{3+}\text{Al}_1$. This is supported by a negative correlation between Fe and Al (Figure 5.41B), indicating a “deficit” of Al in Z allowing the substitution of Fe^{3+} . This is further supported by the fact that depletion of Al less than 5 a.p.f.u in tourmaline cannot be balanced on the basis of uvite substitution, and the more likely substitution is ${}^Z\text{Al}^{3+} \rightarrow {}^Z\text{Fe}^{3+}$ (Bačík et al., 2008).

The uvite substitution Ca,Mg(Na,Al)_1 is necessary to explain the variation in Ca, mainly in Type C, where the blue tourmalines hold the highest amounts, and the amount of Ca is decreasing in the blue, brown and pale blue tourmalines as Al increases slightly (Figure 5.42 D). The yellow tourmalines have less than 6 a.p.f.u Si in the T-site, where Al is substituted in accordance with the exchange vector $\text{R}^{2+}\text{SiAl}_2$ (Figure 5.42 E).

The blue, brown and pale blue tourmaline in Type A distal is associated with cassiterite. It is most affected by the FeMg_1 vector, as well as showing some influence from the $\text{Fe}^{2+}\text{Fe}^{3+}(\text{Mg,Al})_1$ vector. Sn measured within tourmaline structure appears to have a correlation with Mg in type A (Figure 5.42F), with the highest enrichment (6033 ppm) within the vein in Type A, with high levels (2161 ppm). In type A distally from the vein Sn is relatively depleted low the other samples (<1268 ppm). There appear to be some correlation between Fe^{3+} and Sn accommodated in the tourmaline structure in type A in the vein, but there is an equally high enrichment where no Fe^{3+} is evident.

Table 5.3: Summation of the identified exchange vectors in tourmalines in type A, B and C, categorized by colour in plane polarized light view (see Figure 5.39 for legend).

	Type A distal	Type A vein	Type B	Type C
Primary Yellow		Na,R ²⁺ (Xvac,Al) ₋₁ Al ₃ O(R ²⁺ ,OH) ₋₁ R ²⁺ SiAl ₂		Na,R ²⁺ (Xvac,Al) ₋₁ Al ₃ O(R ²⁺ ,OH) ₋₁ R ²⁺ SiAl ₂
Blue	Fe ²⁺ Fe ³⁺ (Mg,Al) ₋₁ . Na,R ²⁺ (Xvac,Al) ₋₁ Al ₃ O(R ²⁺ ,OH) ₋₁		FeMg ₋₁ Na,R ²⁺ (Xvac,Al) ₋₁ 1 Al ₃ O(R ²⁺ ,OH) ₋₁	FeMg ₋₁ Na,R ²⁺ (Xvac,Al) ₋₁ Al ₃ O(R ²⁺ ,OH) ₋₁ Ca,Mg(Na,Al) ₋₁ R ²⁺ SiAl ₂
Pale blue	FeMg ₋₁ Fe ²⁺ Fe ³⁺ (Mg,Al) ₋₁ . R ²⁺ SiAl ₂	Fe ²⁺ Fe ³⁺ (Mg,Al) ₋₁ .		FeMg ₋₁ Na,R ²⁺ (Xvac,Al) ₋₁ Al ₃ O(R ²⁺ ,OH) ₋₁ Ca,Mg(Na,Al) ₋₁ R ²⁺ SiAl ₂
Brown	FeMg ₋₁ Fe ²⁺ Fe ³⁺ (Mg,Al) ₋₁ .	Fe ²⁺ Fe ³⁺ (Mg,Al) ₋₁ . Fe ³⁺ Al ₁ Al ₃ O(Mg,OH) ₋₁		


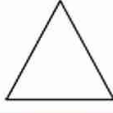
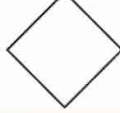
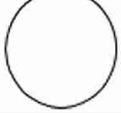
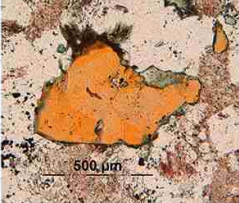
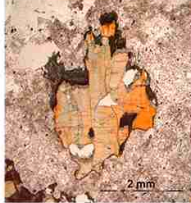

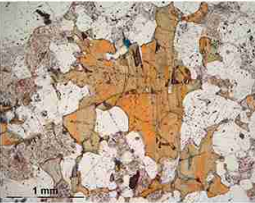
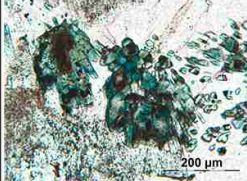

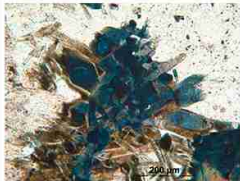
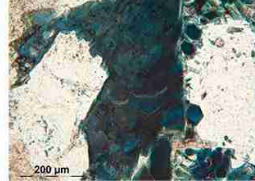
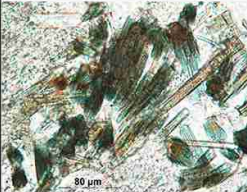
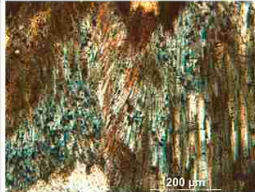

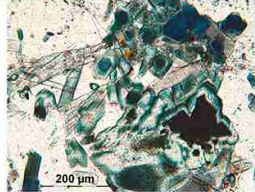
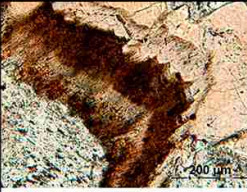


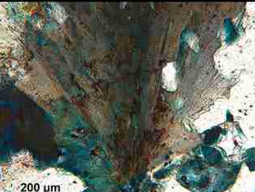
	Type A distal 	Type A Vein 	Type B 	Type C 
Primary Yellow	 500 µm	 2 mm	 800 µm	 1 mm
Blue	 200 µm	 200 µm	 200 µm	 200 µm
Pale Blue	 80 µm	 200 µm	 200 µm	 200 µm
Brown	 200 µm	 500 µm	 200 µm	 200 µm

Figure 5.39: Legend for the following tourmaline plots, showing the defined vein type colour and symbol classification used. Images are captured in plane-polarized light view, with minerals displaying maximum absorption colour.

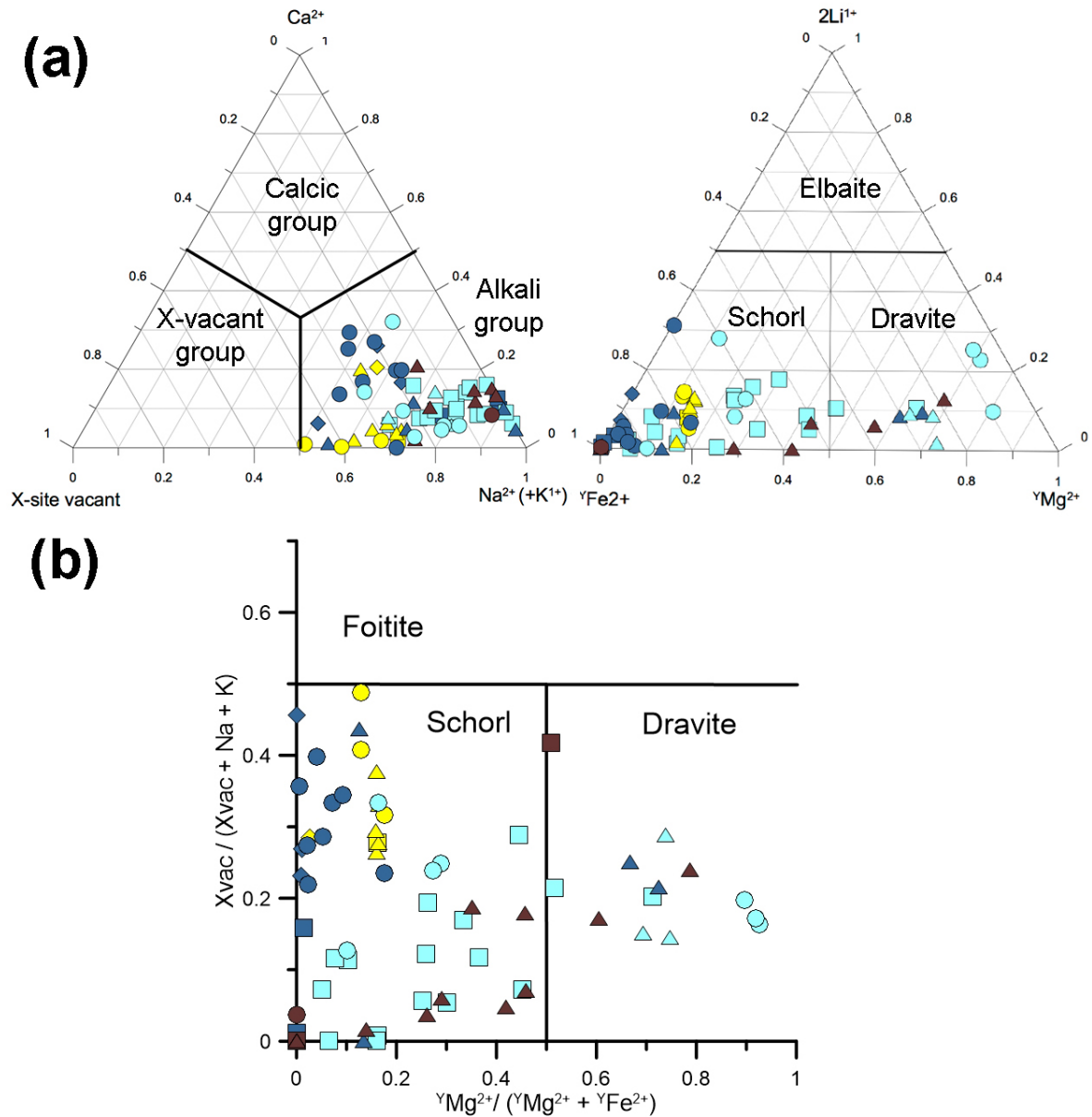


Figure 5.40: (a) Binary plot of cation occupancies in analysed tourmaline with common exchange vectors, showing Mg vs Fe. Stoichiometric schorl and dravite are marked by dots. Substitution of Al in the Y-site is indicated by $\Sigma Fe+Mg+Mn+Ti < 3$. All values are a.p.f.u. (b) Classification diagrams of analysed tourmaline based on X-site occupancy (left) and the dravite-schorl-elbaite subsystem of the alkali group (right). Tourmaline plot within the schorl and dravite fields. (c) Diagram of tourmaline based on Mg-content and vacancies in the X-site. See Figure 5.39 for legend.

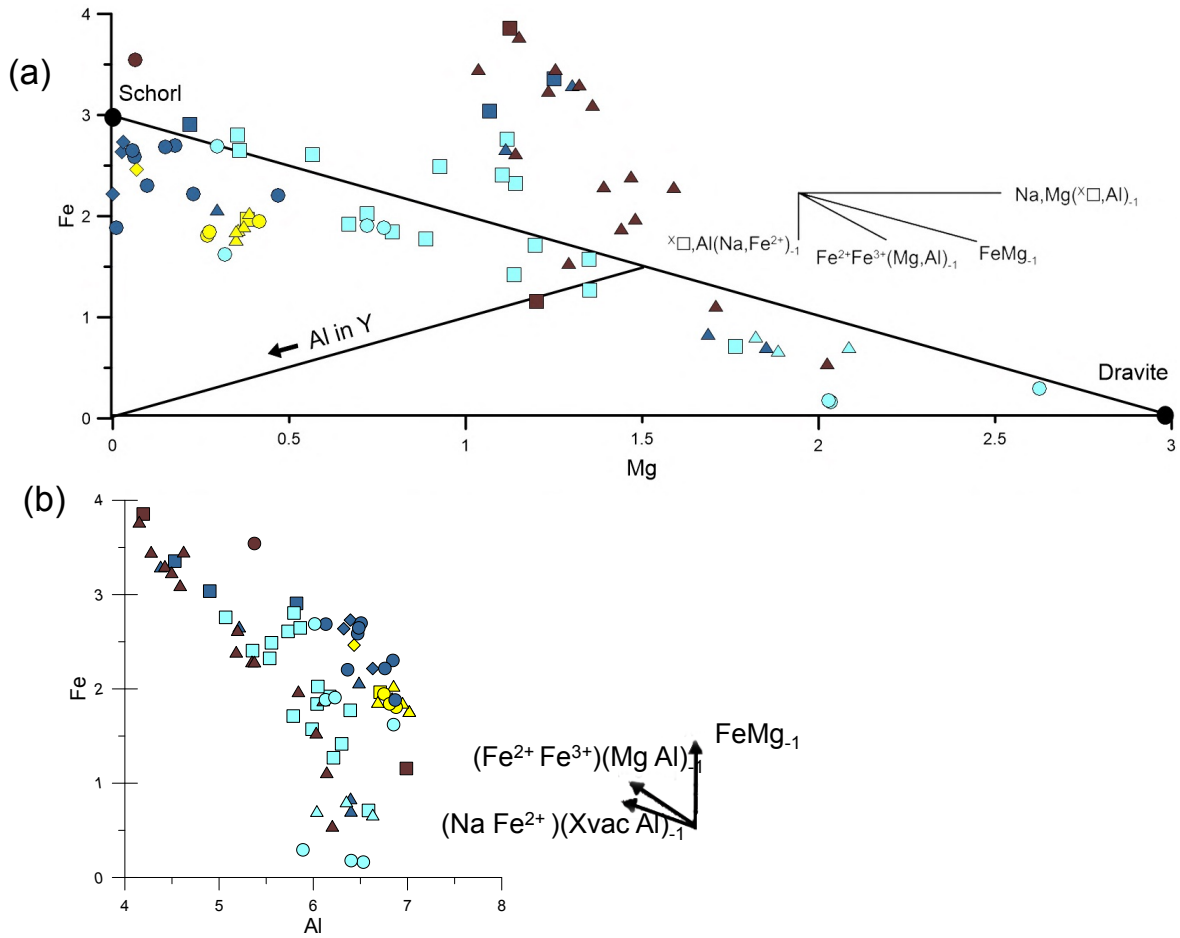


Figure 5.41: Binary plots of cation occupancies in analysed tourmaline with common exchange vectors. All values are a.p.f.u. (a) Plot of Mg vs Fe. Stoichiometric schorl and dravite are marked by dots. Substitution of Al in the Y-site is indicated by $\Sigma\text{Fe}+\text{Mg}+\text{Mn}+\text{Ti} < 3$. Tourmaline plot along the FeMg_{-1} and $(\text{Fe}^{2+}\text{Fe}^{3+})(\text{Mg},\text{Al})_{-1}$ substitution vectors. (b) Plot of Al vs Fe. Tourmaline plot along the FeMg_{-1} and $(\text{Fe}^{2+}\text{Fe}^{3+})(\text{Mg},\text{Al})_{-1}$ substitution vectors. See Figure 5.39 for legend.

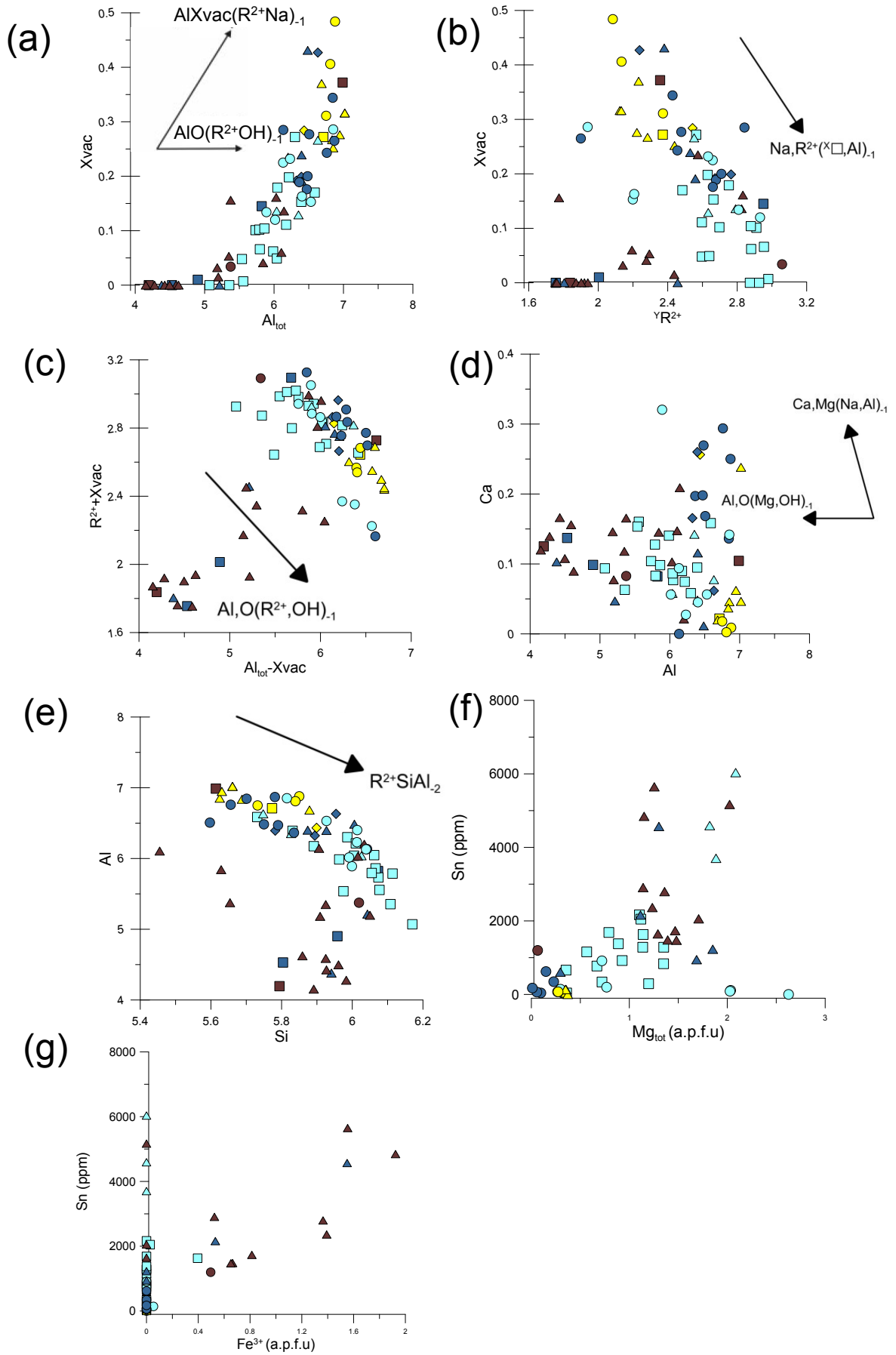


Figure 5.42: Binary plots of cation occupancies in analysed tourmaline with common exchange vectors. All values except Sn are a.p.f.u. (a) plot of Al_{tot} vs. X_{vac} . (b) Plot of ${}^Y R^{2+}$ vs. X_{vac} . ($R^2 = \sum {}^Y Fe + {}^Y Mg + {}^Y Mn$). (c) Plot of $Al_{tot} - X_{vac}$ vs. $R^2 + X_{vac}$. (d) Plot of Al vs. Ca. (e) Plot of Si vs. Al. (f) Plot of Mg vs. Sn (ppm) within the tourmaline structure. (g) Fe^{3+} (a.p.f.u) vs. Sn (ppm). See Figure 5.39 for legend.

5.3.7. Traverses of zoned tourmaline

Three microprobe traverses were carried out across tourmaline crystals. Traverse 1 contains the transition from yellow, primary tourmaline to the light blue and brown overgrowths, subdivided into four zones (Figure 5.45). Traverse 2 (Figure 5.46) were carried out across a pale blue tourmaline crystal, parallel to the c-axis, and traverse 3 (Figure 5.47) were carried out across a blue tourmaline crystal, perpendicular to the c-axis. Traverse 10 consists of ten analysing points, and traverse 2 and 3 consists of six points each. The low number of analysis points is due to the crystals being very fine grained (<50 μm), and each zone was close to the microprobe spot size. To obtain data of the very finely compositionally zoned tourmalines, perpendicular to the c axis, element mapping was used to show the distribution and variation of elements (Figure 5.44). The crystals have a wide core zone, which are bright in BSE-image, while the colour of the core in plane-polarized light view varies between brown and pale blue. Compositionally, the core zone is lower in Al, Ca and Mg, and high in Fe. The crystals also show oscillatory zoning between light grey and slightly darker grey on BSE-image. The lightest, thin zonation is compositionally high in Al and Fe, while the darker zonation is compositionally high in Al, low in Fe and high in Mg. There is a slight enrichment of Ca towards the edge.

Traverse 1 from type A vein consists of the primary yellow tourmaline, zone 1 which is pale blue in plane-polarized light view and dark on BSE –image, zone 2 which is dark brown in plane-polarized light view and light grey in BSE-image and zone 3, which is light brown in plane-polarized light view and medium grey with oscillatory zonation on BSE-image. The primary zone has no chemical variation, containing no to little Sn (133 ppm). Zone 1 is enriched in Sn (4500 ppm), along with an increase in Mg and decrease in Fe. Decreasing Sn content in zone 2 to zone 3 is followed by a slight decrease in Mg, and elevated amounts of Fe, which is accommodated in the tourmaline structure as both Fe^{2+} and Fe^{3+} in zones 2 and 3. There is a peak in Sn in zone 3 (5600 ppm), where the Fe content is fluctuating (0.55-3.45 a.p.f.u), Fe^{3+} is peaking (1.55 a.p.f.u), while Al in Y is close to zero. The Al content is lower

in the overgrowths than in the primary tourmaline. In the Mg vs. Fe binary plot (Figure 5.43A), Traverse 1 appear to be dominated by a combination of the FeMg_{-1} and $\text{X}_{\text{vac,Al}}(\text{Na,Fe}^{2+})_{-1}$ vectors, where zone 1 (pale blue tourmaline) is dominated by Mg-substitution and zone 2 and 3 alternates between Mg- and Fe-substitution, where the light brown tourmaline are dominated by Fe, and the dark brown tourmaline are dominated by Mg. In the Al vs. Fe binary plot, Zone 1 and 2 clearly plot along the $(\text{Fe}^{2+}\text{Fe}^{3+})(\text{MgAl})_{-1}$, while zone 3 plot along both said vector and FeMg_{-1} .

Traverse 2 in type A distal consists of 6 points, plotting from the core to the rim, analysing the alternating oscillatory zoning within the tourmaline crystal. It appears to plot along the $\text{Fe}^{2+}\text{Fe}^{3+}(\text{Mg,Al})_{-1}$ substitution vector (Figure 5.43), with increasing $(\text{Fe}^{2+}\text{Fe}^{3+})$ substitution towards the rim. This is also seen in Figure 5.45, where the Fe content (as Fe^{2+}) is slightly alternating but overall high and increasing. Mg shows the inverse trend, and here is a complete loss of Al in the Y site from point 3 and outwards. Sn content is overall high (>700 ppm), with a peak in zone 5 (1630 ppm), corresponding to light grey colour on BSE-image with Mg substitution dominating over Fe. There is also a slight enrichment in Fe^{3+} and W (158 ppm) in peak 5.

Traverse 3 from type C also consists of 6 points. It appears to plot along the FeMg_{-1} vector in Figure 5.43. The dark grey tourmaline in the BSE-image has a greater influence of the Fe substitution than the light grey, which is dominated by Mg. There is a large compositional difference between tourmaline with the dark grey and light grey colour on BSE-image, with Mg contents from 0 a.p.f.u in the dark grey and 2.6 a.p.f.u in the light grey, with an opposite trend in Fe, with 1.8 a.p.f.u in the dark grey and 0.2 a.p.f.u in the light grey. The traverse in Figure 5.45 further illustrates this alternation between Fe (as Fe^{2+} exclusively) and Mg substitution, where point 3 and 4 have the same Fe-Mg content. Al in Y is increasing from point 2 and outwards, and W is only accommodated in tourmaline in point 6 with modest 47 ppm. The overall Sn content is low, averaging at 233 ppm and peaking at 913 ppm. The peak in Sn corresponds to the dark grey zone, where Fe dominates the FeMg_{-1} substitution. The amount of Sn is low (110 ppm) in point 4 where the Fe-Mg trend is the same as point 3.

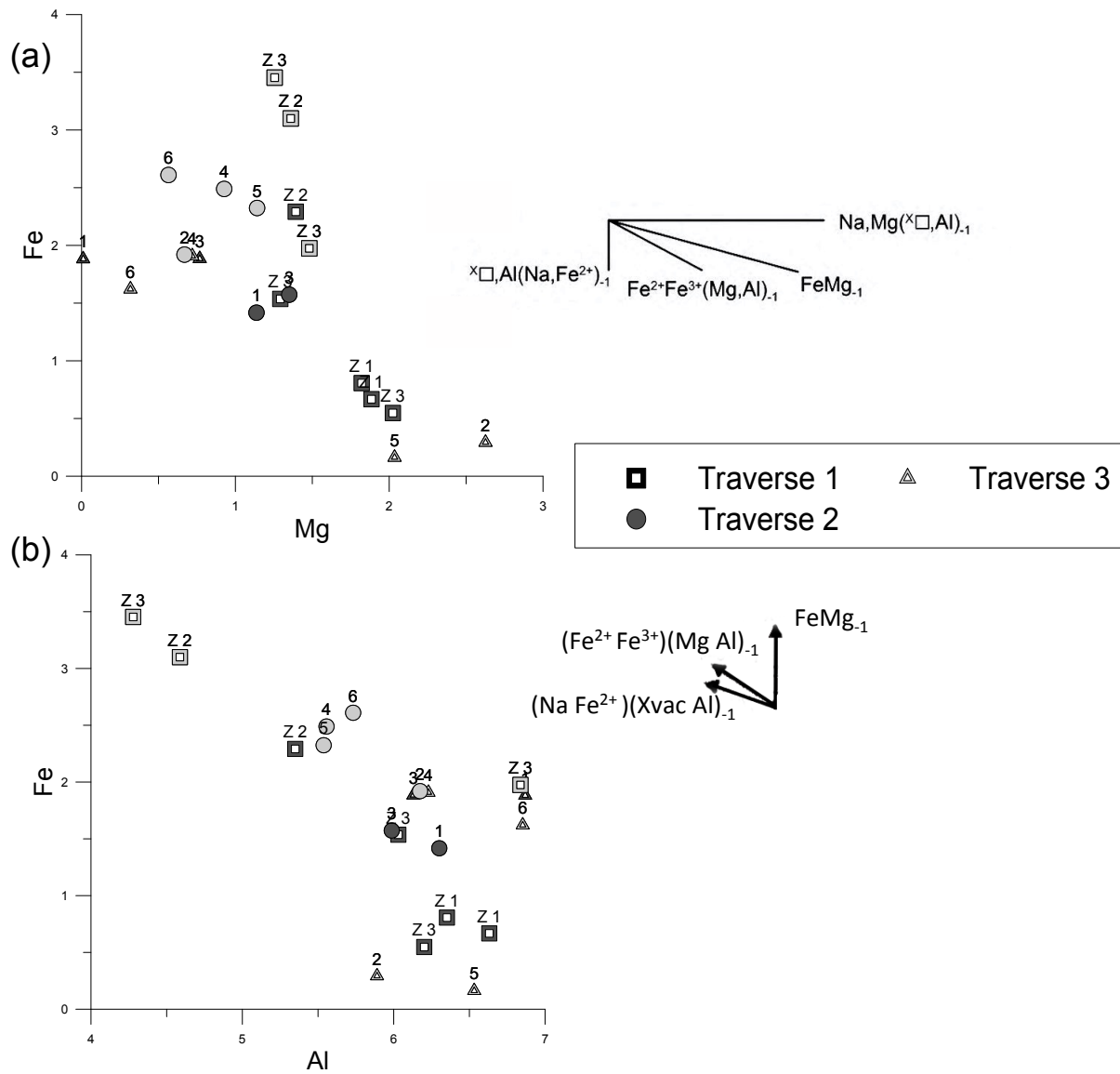


Figure 5.43: Binary plot of cation occupancies in analysed tourmaline traverses with common exchange vectors, showing (A) Mg vs. Fe and (B) Al vs. Fe. The labels are primary (P), zones (Zx) or analysing points (1-6). Black colour corresponds to primary tourmaline, light grey and dark grey is light grey and dark grey on BSE-images, respectively. Traverse 1 is Type A vein, traverse 2 is Type A distal and traverse 3 is type C.

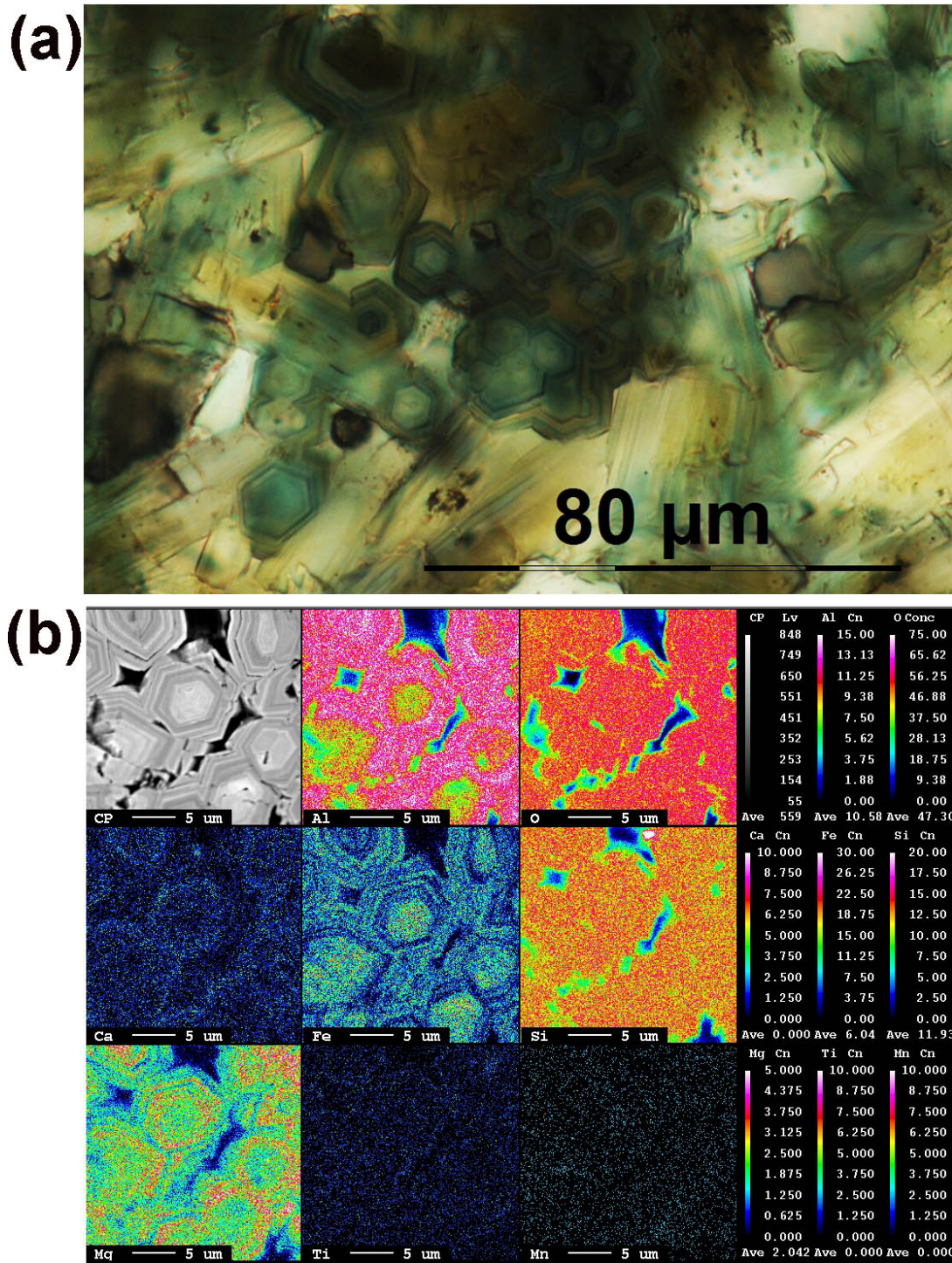


Figure 5.44: (a) Zoned pale blue tourmaline, plane-polarized light view with top lens inserted, ME05V (Type C). (b) Element map of pale blue tourmaline in type C (ME05V). Concentrations are represented as colours, showing the element distribution of Al, O, Ca, Fe, Si, Mg, Ti and Mn respectively.

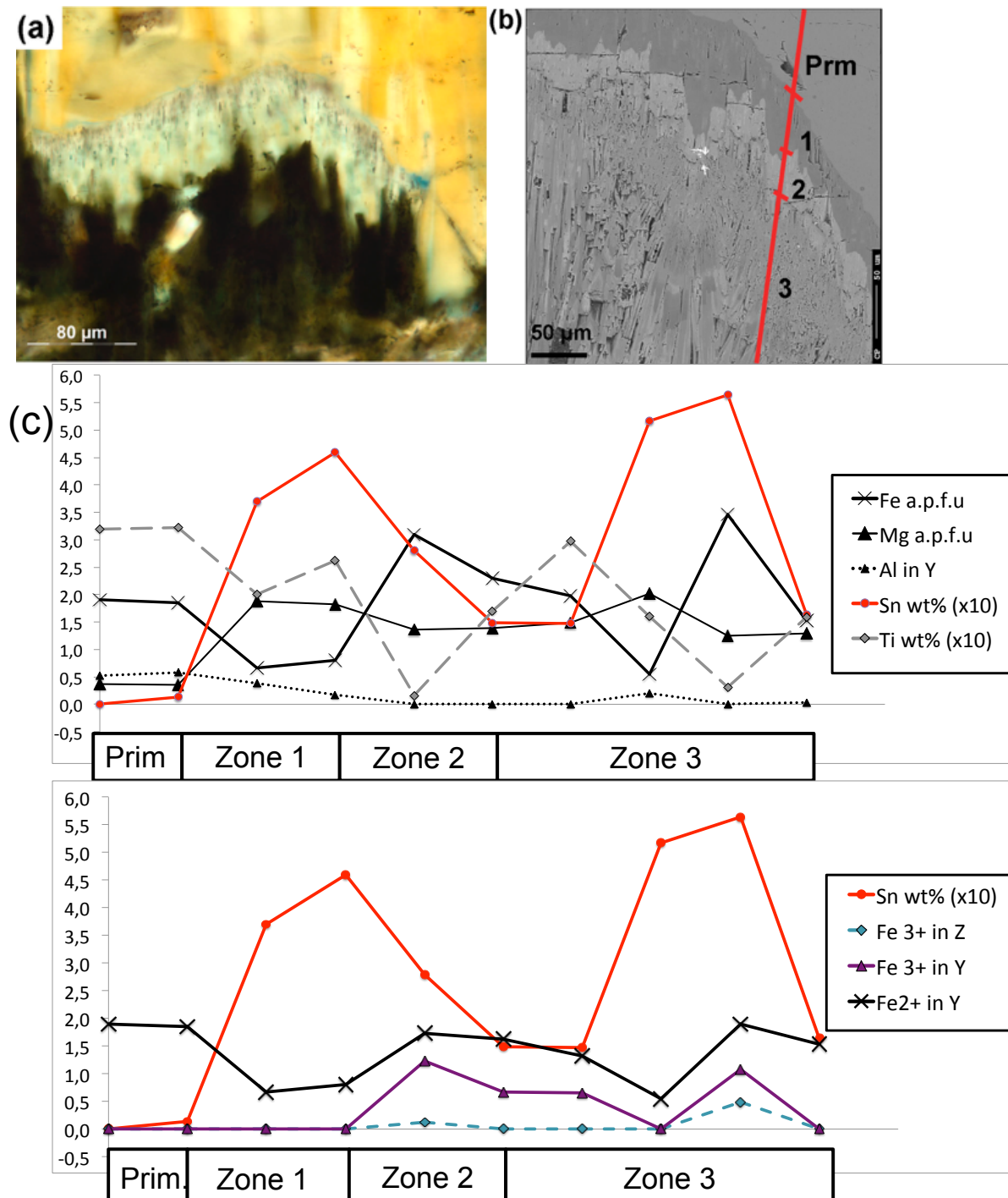


Figure 5.45: (a) Plane-polarized light view image of yellow tourmaline with pale blue and brown tourmaline overgrowths. (b) BSE-image with traverse location, including the subdivision of four zones based on grey scale signal. (c) Microprobe traverse 1 of tourmaline in type A proximal to the vein, showing the variations in Fe, Mg, Al, Sn and Ti. The units on the left hand axis are in a.p.f.u. Sn is enriched in zone 1 and zone 3, corresponding to the enrichments of Fe^{3+} .

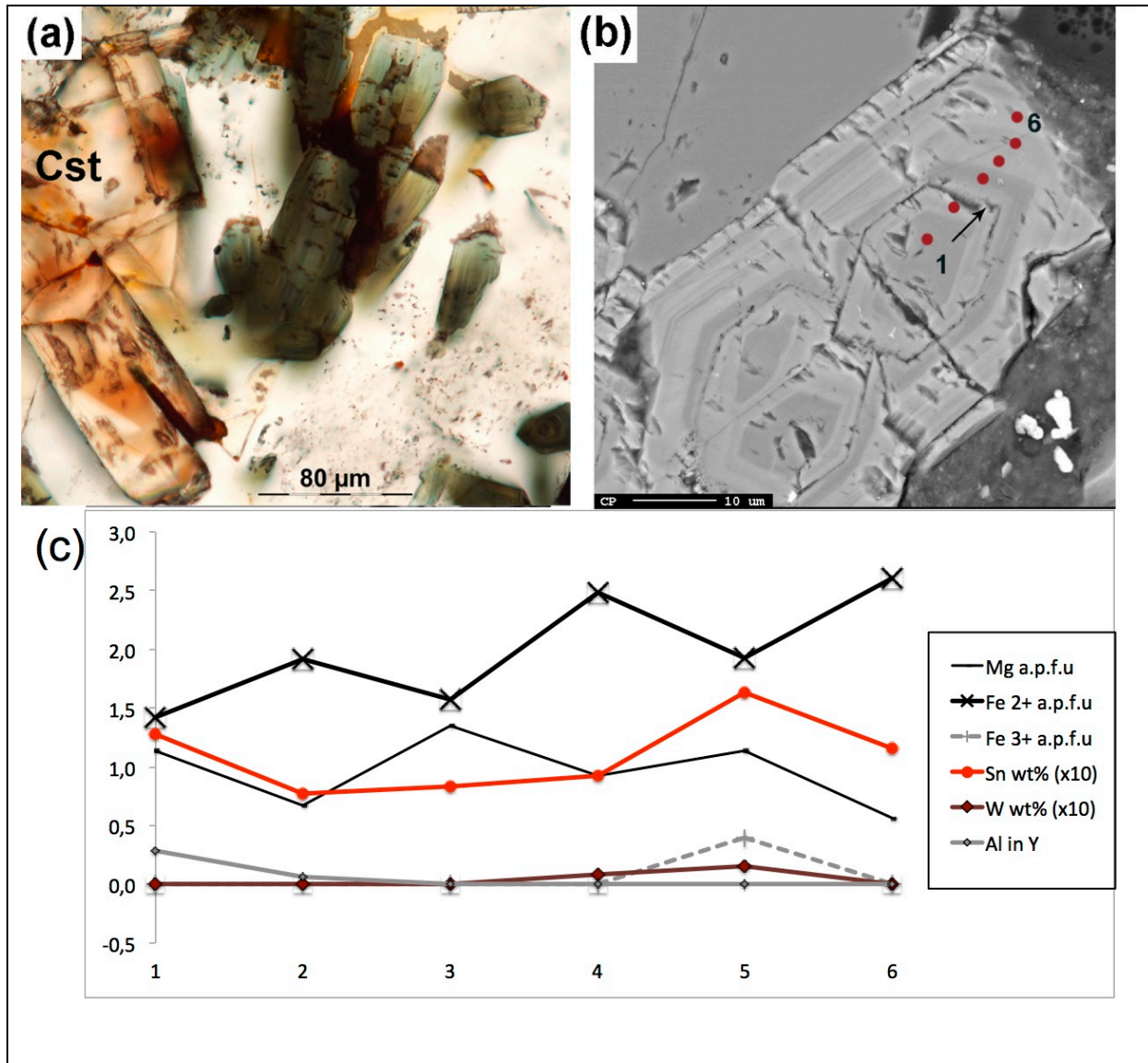


Figure 5.46 (a) Cassiterite and pale blue zoned tourmaline in type A distally to the vein, plane-polarized light view. (b) BSE-image showing the location of traverse analysing points. (c) Microprobe traverse 2 of tourmaline in type A distal, showing the variations in Fe, Mg, Al, Sn and W. The units on the left hand axis are in a.p.f.u. Sn is somewhat enriched in point 5 near the rim, corresponding with Fe³⁺.

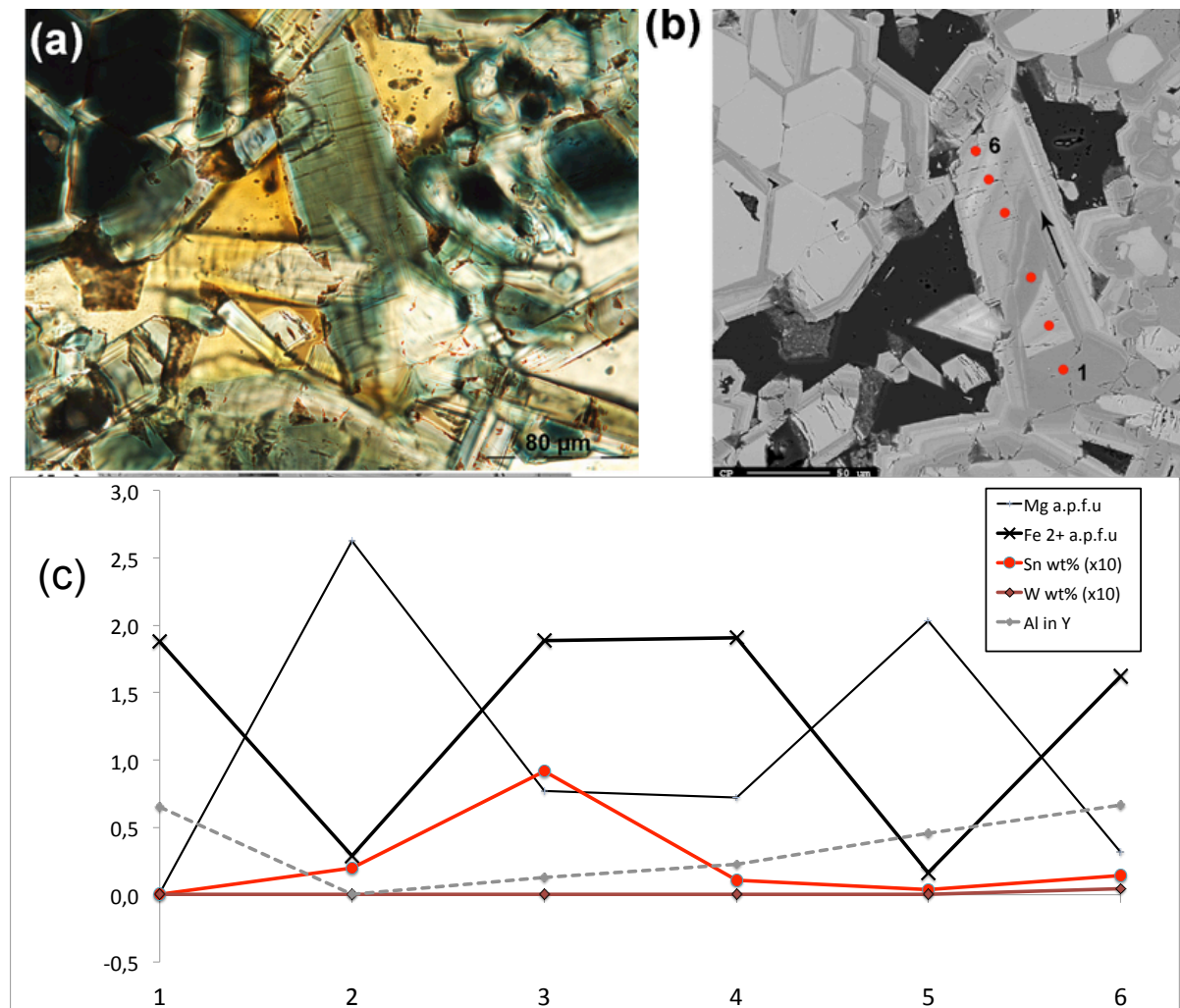


Figure 5.47: (a) Plane-polarized light view of zoned pale blue tourmaline in type C. The yellow colouration is carbon coating within cavities. (b) BSE-image showing the location of traverse analysing points. (c) Microprobe traverse 3 of tourmaline in type C (ME05V), showing the variations in Fe, Mg, Al, Sn and W. No Fe^{3+} is present. The units on the left hand axis are in a.p.f.u. Sn is somewhat enriched in point 3, corresponding to a Fe^{2+} rich zone.

Chapter 6. Discussion

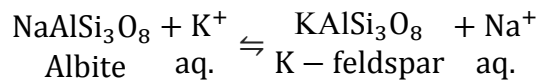
Potassic alteration associated with cassiterite mineralization is not previously reported from the Cornubian batholith, Cornwall, and this study describe the formation of cassiterite from high temperature, magmatic fluids as a function of changing oxygen fugacities. This contradicts with previously described episodes of cassiterite formation where mixing of magmatic-hydrothermal and oxidising Fe-rich fluids of meteoric origin is implied. Detailed characterization of the alteration assemblage is reported. Temperature and fluid compositions are inferred by discussing the alteration assemblage, tourmaline compositions and rutile trace element content. Finally, origin of the veins and mineralizing fluids are discussed, as well as the processes responsible for cassiterite formation.

Type A tourmaline veins with characteristic red alteration zone consists of tourmaline–K-Feldspar assemblage in a 3 cm wide zone from the tourmaline (\pm quartz) vein. The vein itself is disseminated into the wall rock, enclosing feldspar grains. The vein and alteration zone is enriched in Sn (1000 ppm), and cassiterite is identified as euhedral crystals associated with blue tourmaline as prismatic laths and as anhedral crystals enclosed within rutile. It differs chemically from type B and C, with higher levels of K_2O and Al_2O_3 . Type B and C consist of a quartz-K-feldspar-muscovite assemblage, commonly with sericitization of the feldspars. The tourmaline vein is massive and is intersecting the wall rock. Type B tourmaline vein often contains a core zone of quartz. Cassiterite is rare, with Sn levels <100 ppm in type B and <30 ppm in type C. Geochemically, they are close to granite, with elevated levels of SiO_2 and depletion in Na_2O . Tourmaline occurs as yellow, interstitial sub-to anhedral grains and as blue and brown overgrowths and prismatic, needle-shaped laths radiating from the vein or forming clots. They are classified as schorl and dravite, mostly plotting along the $FeMg_{-1}$ substitution vector. Tourmaline in type A is also dominated by the $Fe^{3+}Al_{-1}$ substitution component. Oscillatory zonation within these tourmaline grains contains Sn-rich zones corresponding to the variations in Fe^{3+} , but is slightly offset.

6.1. Type A: Potassic alteration and tourmalinization

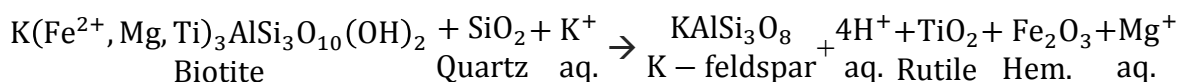
The mineral assemblage found in the alteration zone proximal to the vein is typical for potassic alteration, characterized by a newly formed the K-feldspar—quartz assemblage. Sericite, muscovite and biotite are absent in proximity to the vein, but gradually appear in the distal parts of the alteration zone due to descending temperatures and ratios of aK^+/aH^+ (Pirajno, 2009). This potassic alteration assemblage is a result of K^+ -metasomatism from high temperature volatile fluids. The granophyric texture indicate “pressure-quenched” intergrowth of newly formed quartz-K-feldspar formed in a system opened by rapid decompression (Pirajno, 2013).

Albite is absent, indicating a base cation exchange of K^+ from the volatile fluids to the wall rock during microclinisation:



Despite containing 32% microperthite as identified by XRD, no albite lamellae was observed on SEM. This indicates that the alteration has led to a net loss of albite, producing lamellae altered to regular microcline, strengthened by the fact that type A consists 32% microcline compared to 6 % microcline in the granite. The progressive replacement of plagioclase by K-feldspar has been demonstrated to be very rapid during hydrothermal conditions (Putnis et al., 2007). In the context of fluid flow, reactive fluids can pass through individual crystals by interface-coupled dissolution-precipitation, generating microporosity (Putnis and Austrheim, 2010). This porosity is supported by the rough and pitted surfaces of the K-feldspar in type A (Figure 5.14).

The amount of quartz is low within the alteration zone, and biotite is absent. Aggregates of rutile with associated hematite (Figure 5.21) is an indication of breakdown of biotite and quartz to form K-feldspar, rutile and hematite in the following, unbalanced equation.



The amount of MgO is higher within the alteration zone (Figure 5.35), and Mg^+ released into the fluids from the equation could be incorporated in tourmaline, which is shown to form within the altered biotite (Figure 5.21) and possibly replacing the biotite (Figure 5.25A).

Quartz is a reactant, supported by the SEM-element mapping showing the amount of quartz decreasing closer to the tourmaline veins. Quartz saturation occurred at high temperatures, with sufficiently high aK^+/aH^+ to stabilize K-feldspar.

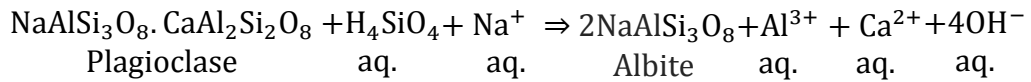
The formation of hematite is an indication of iron present as Fe^{3+} in the fluids, thus making it likely that the characteristic reddish colour and cloudy texture in thin section is due to hematite within pores of the K- feldspar, precipitated as a sub-solidus fluid-rock interaction. The brick red feldspars in type A consist of microcline-microperthite, indicating recrystallization at high temperature, where rapid pseudomorphic recrystallization yielded microporosity to accommodate hematite as minute inclusions (Putnis et al., 2007). The occurrence of ferric iron implies oxidising conditions and a high oxygen fugacity above the magnetite=hematite equilibria (Frost, 1991).

Pervasive K^+ -metasomatism is supported by geochemical data, with the enrichment in K_2O and increased amounts of microcline. The width of the alteration zone and the pervasive nature of the alteration indicate a high fluid/rock ratio. The temperature was likely 500-600 °C, typical for potassic alteration (Robb, 2005). The first exsolved magmatic volatile fluids, would be enriched in K, resulting to the transfer of K^+ from fluids to the wall rocks and forming of a potassic mineral assemblage (Pirajno, 2013).

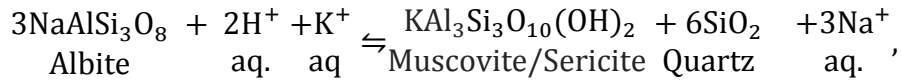
The increase of B and a modal mineralogy of 15 % tourmaline within the alteration zone (Figure 5.32, Figure 5.33) is an indication of tourmalinization, caused by B^{3+} -metasomatism. Tourmaline occurs not as a massive vein, but is instead forming clots and disseminated zones associated with the veins (Figure 5.24A). The vein consists of dispersed fine-grained prismatic laths of tourmaline, often enclosing K-feldspar crystals. This can be interpreted as the initial replacement of feldspar by tourmaline. Fe^{3+} accommodated in the vein-forming tourmaline (Figure 5.41) indicates crystallization during oxidizing conditions. Fe^{2+} in needle-shaped tourmaline distally from the vein indicates reducing conditions. These occur as inclusions in the newly formed K-feldspar (Figure 5.10AB), and was likely crystallized simultaneous as the potassic alteration. Formation of K-feldspar during potassic alteration is independent of the high oxygen fugacity inferred from the vein-forming tourmaline, and it is likely that the potassic alteration predates tourmalinization comprising the vein. This is supported by the change in oxygen fugacity recorded in the distal tourmaline and the vein-comprising tourmaline.

6.2. Type B and C: Sericitization and tourmalinization

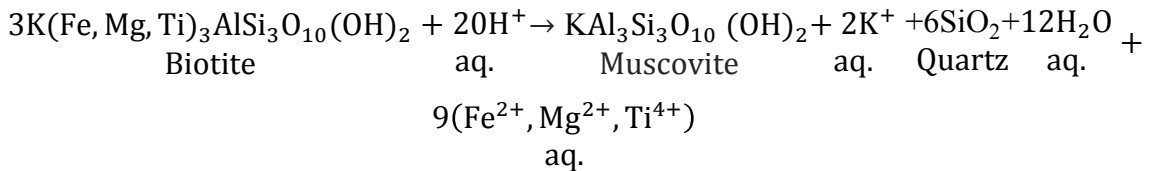
Type B and C consists of a mineral assemblage mostly identical to the granite, with the exception of alteration of the feldspars to form sericite, as fine-grained muscovite, and secondary muscovite. Muscovite is observed to replace biotite. Textural and compositional evidence indicate that the altered domains of plagioclase and K-feldspar reacted with the fluids in two ways. Firstly, the identification of albite by XRD and the complete lack of anorthite component in the feldspar ternary diagram (Figure 5.36) indicate replacement of Ca^{2+} by Na^{2+} in plagioclase to form albite. The following reaction of albite replacing oligoclase is suggested by Putnis and Austrheim (2013):



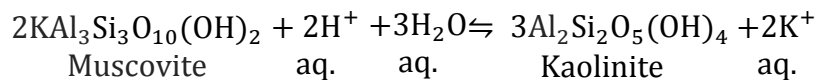
Secondly, the formation of sericite and secondary quartz due to replacement of plagioclase and selective K- feldspar is illustrated by the following equilibria (Pirajno, 2009):



Biotite is being replaced by muscovite by the following reaction (assuming Al to be immobile)(Pirajno, 2009):



It is evident from the equilibria that hydrolysis by H^+ -metasomatism is imperative. The detection of kaolinite in XRD is an indication of the muscovite continuing to react with H^+ and large fluid-rock ratios, indicating a transition to intermediate argillic alteration below 300°C (Pirajno, 2009). The formation of kaolinite can be expressed by the following equilibria (Pirajno, 2009):



B-metasomatism and tourmalinization is evident by the formation of tourmaline clots in proximity to the veins. Another indicator is the apparent replacement of biotite by tourmaline, where rutile has remained incompatible and exists as inclusions in the tourmaline in Figure 5.25. The reddish colouration seen in vein type A is also seen to a lesser degree in type B, which could indicate similar oxidizing conditions during the formation of the veins.

6.3. Insights into hydrothermal processes

6.3.1. Tourmaline as a recorder of fluid composition and redox state

Hydrothermal tourmaline chemistry reflect both the host rock and fluid characteristics, but will in high fluid-flux systems such as veins be generally buffered by the fluid phase (Slack and Trumbull, 2011). Common cation-exchange vectors will be used to constrain the fluid composition, especially in terms of variations in the redox state.

The yellow tourmaline is interpreted to be of magmatic origin. It predates the blue and brown tourmaline, which is present as overgrowths. It is randomly disseminated within the samples, and mostly geochemically uniform in composition. Compositionally they plot as schorl, in the same fashion as magmatic tourmaline in biotite-granite rocks in Cornwall as described by London and Manning (1995). The blue and brown tourmaline can safely be classified as hydrothermal, as they comprise the vein. Prismatic laths of tourmaline radiating from cavities also support a hydrothermal origin (Figure 5.27). Accordingly, brown, blue and pale blue tourmaline crystallized in the veins from B-rich low-density (e.g. aqueous) fluids.

Tourmaline associated within potassic alteration in vein type A show evidence of changing fluid composition in terms of redox state and oxygen fugacity. The tourmaline composition is dominated by more than one exchange vector, involving substitution of Fe as both Fe^{2+} and Fe^{3+} (Figure 5.41A). The substitution of Fe^{3+} is a strong indicator of an oxidising event, and the progressive negative correlation of Fe and Al in type A from distal to proximal tourmaline is an indicator of a $\text{Fe}^{3+}\text{Al}_1$ substitution. From looking at traverse 1 and 2 (Figure 5.45 and Figure 5.46), there appears to be a negative correlation between Fe^{2+} and Sn incorporated into the tourmaline, and a slightly offset positive correlation between Fe^{3+} and Sn. Sn within tourmaline also correlates well with Mg. The presence of Fe^{3+} indicates oxidising conditions, and Sn would be accommodated in the tourmaline as Sn^{4+} , with an ionic radius of 0.069 nm in

six-coordination, which can readily substitute in a variety of coupled substitutions, probably in the Y-site (Williamson et al., 2000, Mlynarczyk and Williams-Jones, 2006).

Tourmaline associated with sericitic alteration in type C is mostly dominated by the FeMg_{-1} and $\text{Na,R}^{2+}(\text{Xvac,Al})_{-1}$ exchange vectors, and shows no evidence for substitutions involving Fe^{+3} (Figure 5.41, Figure 5.43). Thus the volatile fluids from which the tourmaline crystallized must have been reducing in character. The substitution $\text{Ca,Mg}(\text{Na,Al})_{-1}$ in type C tourmaline might be a result of the replacement of plagioclase to albite, releasing Ca^{2+} in the fluid phase.

The Sn content in the sericite-associated tourmaline is low (<0,1 wt.%) compared to the potassic-associated tourmaline (0,6 wt.%), and a peak in traverse 3 (Figure 5.47) show no influence of Fe^{3+} . Sn was probably contained in the reducing hydrothermal fluid as Sn^{2+} . It can enter the tourmaline structure, but is not accommodated as easily within the tourmaline structure as its oxidised form Sn^{4+} . Sn^{2+} with the large ionic radius of 0,122 nm in eight coordination could substitute within the X site, usually occupied by Ca (0,100 nm), minor K (0,138) or is vacant (Williamson et al., 2000).

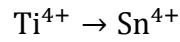
6.3.2. Rutile as a Sn-W host

The main accessory phase in all of the three vein types is rutile, which in type A in proximity to the vein contains inclusions of cassiterite. Much of the rutile is inferred as hydrothermal, as the rutile consists of multiple growth domains (Figure 5.37) and hosts a number of trace elements (Sn, W, Fe, Nb, V, Ta) up to percent level (Rice et al., 1998). The likely source of Ti and Fe from the breakdown of Ti-rich biotite, supported by the textures seen in Figure 5.21 and Figure 5.22 where rutile preferentially occurs in the cleavage planes.

The likely ions to enter the structure (W^{6+} , Nb^{5+} , Al^{3+} , Fe^{3+}) have similar ionic radii, but charge variation would also require additional substitutions to maintain charge balance (Rice et al., 1998). W-bearing rutile has previously been associated within the oxidation zone of altered phenocrysts of biotite, and numerous studies of iron in rutile indicate that iron is mostly present as Fe^{3+} in the Ti site (Rice et al., 1998). A clear association between Fe and W (Figure 5.38D) is an indication of double substitutions;



Where the charge is balanced by vacancies in Ti sites or loss of oxygen by a gas (Rice et al., 1998). Fe^{3+} substitution is likely in type A, as tourmaline indicate oxidizing conditions. Sn is accommodated into rutile by the homovalent substitution:



These metals have ionic radius of 0,060 nm and 0,069 nm for Ti^{4+} and Sn^{4+} respectively in six co-ordination (Shannon, 1976). No Sn was found within rutile in type C, further indicating oxidising conditions in type A and reducing conditions in type C. This also indicates that W is incorporated in rutile only by the double substitution involving Fe^{3+} . The presence of W in rutile in type B will thus indicate oxidizing conditions during rutile formation.

The least enriched domain is the homogenous domain 4, indicating that the spongy texture in domain 1-3 could be due to hydrothermal alteration. The brightness of zones in Figure 5.37 corresponds to enrichment of Sn, W and Fe. The latest growth, domain 2, is enriched in both Fe (2,1 wt.%) W (1,5 wt.%) and Sn (3 wt.%), while the older domain 3 is the most enriched with 3,8 wt.% W, 5 wt.% Sn and 4 wt.% Fe. W was only found as inclusions in Rutile and rarely in tourmaline, possibly indicating too low amounts of W or too high temperatures to form wolframite or scheelite as a separate phase. Wolframite precipitation proceeds over a relatively narrow cooling interval through 350 °C to 300°C (Heinrich, 1990), indicating higher temperatures during cassiterite formation.

The erratic enrichment could indicate fluctuations in the fluids properties, in contrast to Sn-W bearing rutile at Wheal Remfry, which is progressively enriched in the latest domains with increasing contributions from relatively oxidizing formation waters (Müller and Halls, 2005).

6.4. Origin of the veins and mineralizing fluids

The following scenario is envisioned: The land's end pluton was emplaced, and a solidified shell crystallized at the roof zone, chambering a H₂O-saturated melt (Figure 2.1). As H₂O-oversaturation was reached in a process of "second boiling", hydrothermal volatiles were exsolved, where the volume expansion caused overpressurization of the chamber interior. This led to hydrofracturing taking place in the direction of least principle stress. The magmatic hydrothermal fluids exsolved from the Land's End pluton must have been relatively reducing, as the granites from which they were derived have been classified as ilmenite (S-type) series (Ishihara, 1981). Fluid inclusion studies have inferred homogenization temperatures at ca. 480-570 °C with average salinity of 17,3 mass% NaCl for the early fluids (Drivenes, In review).

6.4.1. First hydrothermal episode: Type A

This first episode of fracturing led to formation of vein type A. It consists of NE-SW striking (Figure 5.4A) steeply dipping tourmaline (\pm quartz)-veins, consistent with having developed in the regional NNW-SSE extensional regime following the variscan convergence. Structurally, the veins correlate well with the first hydrothermal episode identified in Nanjizal, dated 274,5 \pm 1,4 Ma (LeBoutillier et al., 2002). The first episode of tourmaline \pm quartz veins identified in Nanjizal by LeBoutillier et al. (2002) were associated with little to no metalliferous mineralization, no alteration is described. The veins were interpreted to being precipitated from magmatic-hydrothermal fluids from the immediately surrounding granite. Cassiterite was associated with the latter stages of the second hydrothermal episode, and was formed during the transition from purely magmatic hydrothermal fluids (high Mg) to comprising progressively more meteoric groundwater (High Fe, oxidizing) (LeBoutillier et al., 2002). What is previously described at Nanjizal is highly contrasting to what is observed for this locality in this study, indicating different processes involved in the formation of cassiterite.

In the oldest tourmaline-veins, type A, the surrounding potassic alteration mineral assemblage indicates high temperature alteration at 500-600 °C. The assemblage formed due to H⁺-, K⁺- and B³⁺- metasomatism from the first magmatic hydrothermal fluids, which would have been reducing, acidic and enriched in K and B (Pirajno, 2009). The pervasiveness of alteration

indicates a high fluid/rock ratio. The FeMg_{-1} exchange vector mostly dominates the pale blue hydrothermal tourmaline in the distal parts of the alteration zone, indicating Fe present as Fe^{2+} in reducing conditions. The tourmaline also shows evidence of increasingly oxidizing conditions, as seen by the influence of substitution vector $\text{Fe}^{2+} \text{Fe}^{3+}(\text{MgAl})_{-1}$ (Figure 5.41) and the appearance of Fe^{3+} together with increasing Sn accommodated in the tourmaline structure towards the rim in traverse 2 (Figure 5.46). The $\text{Fe}^{3+}\text{Al}_{-1}$ dominates the tourmaline comprising the vein and tourmalinization alteration, indicating high oxygen fugacities during the main stage of vein formation. The alteration zone holds cassiterite mineralization (0,1wt. % Sn), most likely precipitated due to more oxidizing conditions (see 6.5). The crystallization of rutile and hematite together in type A (Figure 5.21) indicates high oxygen fugacities and high temperatures. Rutile + hematite is stable at oxygen fugacities $\text{Log } f_{\text{O}_2}$ of -18 ($T=600^\circ\text{C}$ and $P=1$ kbar) (Rumble III, 1973) and iron in hematite is stable at $-\text{Log } f_{\text{O}_2}$ of -18, $T=400^\circ\text{C}$ (Frost, 1991). Boiling would cause a separation of the fluid into a high salinity (>29 equivalent wt.% NaCl) and a low salinity (<12 equivalent wt% NaCl) CO_2 -enriched components at temperatures 500-600 °C, and lithostatic pressures (1-2 kbar) (Jackson et al., 1989).

Increasing oxygen fugacities and subsequent cassiterite precipitation could have been caused by mixing with cooler oxidizing fluids or boiling (phase separation). The former has been described as the cause of main-stage cassiterite mineralization in Cornwall (Scrivener and Shepherd, 1998), and schorl-cassiterite mineralization in Nanjizal ((LeBoutillier et al., 2002). The mixing of Fe-rich, oxidizing meteoric waters has also been inferred as the cause of Sn in tourmaline at Roche rock (Williamson et al., 2000) and Sn-W hosted rutile from Wheal Remfry (Müller and Halls, 2005). Boiling would lead to separation of the fluid into a high salinity fluid phase (>29 equivalent wt.% NaCl) and a low salinity CO_2 -enriched phase (<12 equivalent wt.% NaCl) at temperatures 500-600 °C, and lithostatic pressures (1-2 Kbar) (Jackson et al., 1989).

In this case, the most likely cause of oxidizing conditions is phase separation by boiling of the magmatic hydrothermal fluid. Strike-slip fault formation, associated with the extensional regime following the variscan convergence, is a likely cause of rupture-related dilation (Robb, 2005). This would instantaneously reduce pressure to such an extent that a fluid could move from supercritical to a high density fluid and a vapour phase (Robb, 2005). Mineral

solubilities are influenced by boiling due to preferential fractionation of components between a high-density fluid and a vapour phase. Heavier saline species (KCl, NaCl, K₂BO₃ etc.) will concentrate in the former, while lighter species (HCl, HF) will partition into the vapour phase (Pirajno, 2009). Oxidation is a result of preferential loss of the main reducing species, e.g. H₂ (see 2.1.2). Formation of cassiterite and absence of wolframite indicate temperatures above the wolframite precipitation temperature at 350°C (Heinrich, 1990), making it unlikely that the oxidizing conditions is due to mixing with cooler meteoric fluids.

The veins have been interpreted as early veins fracturing within the granite roof zone. Convecting meteoric fluids within the granite is unlikely at that early stage in granite emplacement. The high temperature alteration assemblage also contradicts mixing with cooler fluids, as the meteoric fluids are often associated with greisen alteration at moderately lower temperatures. This is also supported by the decrease of F in tourmalines in type A, as HF would have partitioned into the vapour phase. An explanation for the difference in style between potassic–tourmaline-associated and greisen-associated cassiterite deposits has been suggested to be the separation of a magmatic fluid into a denser fraction giving rise to tourmaline veins, and a lighter, F- and CO₂-rich fraction giving greisen alteration (Shepherd et al., 1985). Partitioning of Boron into the fluid phase could also have initiated B-metasomatism and tourmalinization in the vein, supported by brown tourmaline in the vein, which are dominated by Fe³⁺Al₁ substitution. Small scale oscillatory zoning between Fe- and Mg rich zones in the tourmalines (Figure 5.46) could be due to rapid disequilibrium growth of the tourmaline or changes in P or T, and dravitic compositions are usually associated with magmatic, Mg-rich fluids (London and Manning, 1995).

6.4.2. Second and third hydrothermal episodes: Type B and C

A second episode of mineralization, type B, is hosted by N-S and NE-SW striking, steeply dipping veins, characterized by sericitic alteration of the feldspars. Vein type B is N-S striking and consists of schorl-veins and quartz core zone, where both quartz and tourmaline is showing syntaxial fibers and growth normal to the walls of the veins (Figure 5.12, Figure 5.24B). The textures show that the mineral growth took place at a greater rate than fracture opening, and the two-coloured tourmaline within the vein (Figure 5.24) could indicate more than one phase of opening due to renewed extension (LeBoutillier, 2002).

Type B tourmaline vein (ME04V) displays the same NE-SW strike as type A, indicating formation during the same structural domain. The narrower alteration zone and the less intense red colouration could possibly be due to lower fluid/rock ratio from initially oxidising fluids, precipitating hematite in pores as in type A, and as disseminations and veinlets. The following fluids was probably reducing, with low oxygen fugacity and low pH, where H⁺-metasomatism led to the formation of sericite replacing the feldspars. In the mentioned sample of type B, the sericitization is more pervasive, and microcline is absent. This could support an initial potassic alteration, creating the porosity mentioned previously which enables the fluids to gain access to the minerals, leading to pervasive sericitization.

The occurrence of albite in type B would indicate less pervasive potassic alteration compared to type A where albite was absent, and/or later Na-rich fluids causing replacement of microcline by albite. It is likely that there was a transition from early potassic to a main-stage sericitic alteration, due to increasing H⁺-metasomatism and/or decreasing temperature (Figure 2.3). This could be caused by a decrease in temperature, but not necessarily as formation of sericite can occur over wide temperature range, and sericitization at 400 °C have been reported (Que and Allen, 1996, Robb, 2005). This decrease in temperature and/or decreasing aK⁺/aH⁺ of the fluid led to sericite becoming the predominant K-silicate phase during the subsequent veining events. Tourmaline vein with quartz core zone in type B (Figure 5.7) indicate reactivation of the vein, also evident by euhedral crystals with growth zoning (Figure 5.12)(Taylor, 2010). It is likely that the later fluids in type B were magmatic-hydrothermal, exsolved at a later stage and thus more Na-rich, reducing, high temperature and acidic (Pirajno, 2009). Due to the formation of sericitic alteration, it is unlikely that boiling took place at this later stage. Sn was probably contained in the fluid as Sn(II)Cl_x^{2-x}, and was precipitated in small amounts in Sn-hosted rutile and as cassiterite inclusions in rutile in the oldest generation of type B veins. The Type B veins are only containing 100 ppm SN, 1/10 of type A (Figure 5.31). Cassiterite could have precipitated due to acid neutralization by feldspathic host rocks through hydrolysis to form the sericitic assemblage, which can effectively extract tin but in limited amounts (Heinrich, 1990). Cassiterite could also have formed during the later stages of boiling in when most of the Sn in the fluids already had been precipitated during the first stages of boiling in type A.

Type C consists of two sets of vertical N-S and NE-SW striking veins, consisting of zoned hydrothermal tourmaline classified as mostly schorl, but with zones of dravite. Unlike zoned

tourmaline in type A and B, these tourmalines have a larger, Fe-rich core zone (Figure 5.44), and very fine zonation towards the rim, alternating between Fe and Mg according to the FeMg_{-1} substitution. Due to the reducing character of Fe in tourmaline, with no substitutions involving Fe^{3+} , a meteoric source of Fe is unlikely. Another more likely source of Fe is from the breakdown of biotite by muscovite, releasing Fe. This is indicated by the bleached rims around the veins in both type B and C (Figure 5.7, indicating the granite itself being the source of Fe needed to make tourmaline (London and Manning, 1995). The oscillatory zoning could be due to rapid disequilibrium growths, but this cannot be determined. The overall Sn content is low (30 ppm). Sn is not hosted by rutile, and Sn in tourmaline is probably contained as Sn^{2+} .

6.5. Formation of cassiterite

In type A distally to the tourmaline vein, cassiterite occurs as euhedral crystals in association with tourmaline (Figure 5.30), and as euhedral crystals and smaller anhedral phases interstitial within rutile (Figure 5.29). The latter is also observed in the oldest generation of type B veins. Cassiterite is absent in type C.

Sn^{2+} was likely transported in the first exsolved reducing, acidic high temperature magmatic fluids as Sn(II)Cl_x^{2-x} at temperatures at ca. 480-570 °C with average salinity 17,3 mass% NaCl (Drivenes, In review). These ligands can transport high tin concentrations to any low temperature (<400°C) deposition, provided that chemical buffering by the wall rocks were prevented by relatively rapid fluid flow through the veins (Heinrich, 1990). Vapour separation at ca. 400°C led to effective cassiterite mineralization through the oxidizing effect of H_2 loss, making the Sn-ligand complexes unstable and thus precipitating SnO_2 . Disseminated cassiterite was formed 1-1,5 cm from the tourmaline vein (Figure 5.34) in type A. The pervasive potassic alteration and high fluid/rock ratio probably formed porosity in which the fluids could migrate. After the initial boiling, tin solubility increased again due to rising concentrations of Cl^- and H^+ due to the loss of solvent (Heinrich, 1990), and Sn entered the sites available in rutile and tourmaline instead of cassiterite precipitation. Vapour loss without concomitant rock reaction is a moderately efficient cassiterite precipitation mechanism at 400°C where the fluid is already close to saturation prior to boiling. With decreasing

temperature it becomes less efficient because of increasing H^+ activity (Heinrich, 1990). Sn was largely deposited in the first 10-20 percent boiling (Drummond and Ohmoto, 1985).

The Sn content for type A vein and alteration zone is 1000 ppm, or 0,1 g/t. This grade could be economically viable in large amounts of material, but due to the small grain size of cassiterite, as well as the small outcrop area, this deposit is not economically viable.

Chapter 7. Conclusions

Three hydrothermal episodes are recognized. The first episode comprises NE-SW striking tourmaline (\pm quartz)-veins intersecting the biotite-granite, surrounded by a red zone of potassic alteration and tourmalinization, characterized by a newly formed K-feldspar-quartz assemblage. This assemblage is likely to have resulted from K^+ - B^{3+} - and H^+ - metasomatism from high temperature magmatic- hydrothermal fluids released from the pluton in a process of second boiling, causing hydrofracturing in the crystallized roof zone of the granite. The red colouration is probably due to hematite precipitating in microporosity formed during rapid replacement of plagioclase. The breakdown of biotite formed aggregates of rutile and hematite, and their coexistence indicate high temperatures and high oxygen fugacities. The latter is also recorded in tourmaline comprising the vein and tourmalinization alteration and, as $Fe^{3+}Al_1$ substitution. Log f_{O_2} of -18 and temperatures at 400-500 °C are inferred from the mineral assemblage and the absence of wolframite. The likely cause of oxidizing conditions is phase separation due to rupture-related pressure changes, causing prolonged boiling of the magmatic-hydrothermal fluid that resulted in to formation of 0,1 wt.% cassiterite.

The second hydrothermal episode comprises N-S and NE-SW striking tourmaline (\pm quartz) veins, characterized by sericitic alteration of the feldspars and tourmalinization formed by H^+ - and B^{3+} -metasomatism. Veins formed in the same structural domain as the first episode show evidence of early potassic alteration and oxidizing conditions, possibly due to the late stages of boiling, suggested by locally red alteration zones and formation of hematite and small amounts of cassiterite (100 ppm Sn). This was later overprinted by sericitic alteration due to influx of later, reducing and acidic magmatic-hydrothermal fluids, with a higher aK^+/ aH^+ -ratio and/or having lower temperatures. The third hydrothermal episode comprises two sets of N-S and NE-SW striking tourmaline-veins, respectively, and is characterized by not showing visible alteration zones. Sericite alteration of the feldspars and tourmalinization is evident on thin section scale. Bleached rims surrounding the tourmaline vein indicate a depletion of Fe and Mg from the breakdown of biotite. Tourmaline analyses show no evidence of Fe^{3+} , indicating reducing conditions.

Formation of cassiterite during oxidizing conditions is explained by boiling and phase separation at high temperature, from saline magmatic-hydrothermal fluids. None of the three hydrothermal episodes show evidence of mixing with cooler, oxidizing meteoric fluids that otherwise would have yielded the greisen-associated cassiterite deposits seen elsewhere in the Cornubian ore-field. A proposed temperature of the fluids is 400-500 °C, at 1-2 kbar, on the basis of the high-temperature potassic alteration and the absence of temperature-dependant wolframite deposition.

7.1. Suggestions for future work

In order to confirm the proposed temperature, oxygen fugacities and chronology, more data is needed. Fluid inclusion studies, with hydrogen and oxygen isotope studies, can be used to estimate temperatures and salinities. It can also be used to confirm if the hydrothermal fluids were truly magmatic or have a meteoric component. Boron isotope studies can be used to confirm that the source of boron was magmatic, and not from meteoric waters. Monazite U-Pb age determination can be used for geochronology of the different mineralizing episodes. It could also be of interest to expand the study area, as there are a number of other vein systems in the Nanjizal area.

- CEPURITIS, R., JACOBSEN, S., GARBOCZI, E. J., FERRARIS, C. F. & SØRENSEN, B. E. In review. Particle size distribution and specific surface determination of crushed concrete aggregate fines. submitted to CCC (Cement and Concrete Composites): Department of Structural Engineering, Norwegian University of Science and Technology.
- CHAPPELL, B. W. & HINE, R. 2006. The Cornubian Batholith: an example of magmatic fractionation on a crustal scale. *Resource Geology*, 56, 203-244.
- CHEN, Y., CLARK, A., FARRAR, E., WASTENEYS, H., HODGSON, M. & BROMLEY, A. 1993. Diachronous and independent histories of plutonism and mineralization in the Cornubian Batholith, southwest England. *Journal of the Geological Society*, 150, 1183-1191.
- CLARK, C. M. 2007. Tourmaline: Structural formula calculations. *The Canadian Mineralogist*, 45, 229-237.
- CLARKE, D. B. 1992. *Granitoid rocks*, London, Chapman & Hall.
- COLLINS, A. C. 2010. *Mineralogy and geochemistry of tourmaline in contrasting hydrothermal systems: Copiapó area, Northern Chile*. University of Arizona.
- DARBYSHIRE, D. & SHEPHERD, T. 1985. Chronology of granite magmatism and associated mineralization, SW England. *Journal of the Geological Society*, 142, 1159-1177.
- DEER, W. A., HOWIE, R. A. & ZUSSMAN, J. 1992. *An introduction to the rock-forming minerals*, Longman London.
- DRIVENES, K., LARSEN, R.B., MÜLLER, A., SØRENSEN, B.E. In review. Crystallization and uplift path of late Variscan granites evidenced by quartz chemistry and fluid inclusions: Example from the Land's End granite, SW England.
- DRUMMOND, S. & OHMOTO, H. 1985. Chemical evolution and mineral deposition in boiling hydrothermal systems. *Economic Geology*, 80, 126-147.
- EVANS, A. M. & EVANS, A. M. 1993. *Ore geology and industrial minerals*, Oxford, Blackwell Scientific Publications.
- EXLEY, C., STONE, M. & FLOYD, P. 1983. Composition and petrogenesis of the Cornubian granite batholith and post-orogenic volcanic rocks in southwest England. *The Variscan fold belt in the British Isles*. Adam Hilger Ltd.

- EXLEY, C. S. & STONE, M. Petrology of the granites and minor intrusions. *In: SUTHERLAND, D. S., ed. Igneous rocks of the British Isles, 1982. John Wiley & Sons, Chichester, United Kingdom, 293-302.*
- FROST, B. R. 1991. Introduction to oxygen fugacity and its petrologic importance. *Reviews in Mineralogy and Geochemistry, 25, 1-9.*
- GOLDSTEIN, J. I. 2003. *Scanning electron microscopy and X-ray microanalysis*, New York, Kluwer Academic/Plenum Publishers.
- GRANSETH, A. U. 2015. *Deformation, phyllonitization and associated element mobilization of granitoid rocks: A geochemical study of the Fagervika granitoid, Norway*. Master of science, Norwegian University of Science and Technology.
- GRANT, J. A. 1986. The isocon diagram; a simple solution to Gresens' equation for metasomatic alteration. *Economic Geology, 81, 1976-1982.*
- GRANT, J. A. 2005. Isocon analysis: a brief review of the method and applications. *Physics and Chemistry of the Earth, Parts A/B/C, 30, 997-1004.*
- HAWTHORNE, F. C. & DIRLAM, D. M. 2011. Tourmaline the indicator mineral: From atomic arrangement to Viking navigation. *Elements, 7, 307-312.*
- HAWTHORNE, F. C. & HENRY, D. J. 1999. Classification of the minerals of the tourmaline group. *EUROPEAN JOURNAL OF MINERALOGY-STUTTGART-, 11, 201-216.*
- HEINRICH, C. A. 1990. The chemistry of hydrothermal tin (-tungsten) ore deposition. *Economic Geology, 85, 457-481.*
- HENRY, D. J. & DUTROW, B. L. 1996. Metamorphic tourmaline and its petrologic applications. *Reviews in Mineralogy and Geochemistry, 33, 503-557.*
- HENRY, D. J. & GUIDOTTI, C. V. 1985. Tourmaline as a petrogenetic indicator mineral- An example from the staurolite-grade metapelites of NW Maine. *American mineralogist, 70, 1-15.*
- HENRY, D. J., NOVÁK, M., HAWTHORNE, F. C., ERTL, A., DUTROW, B. L., UHER, P. & PEZZOTTA, F. 2011. Nomenclature of the tourmaline-supergroup minerals. *American Mineralogist, 96, 895-913.*
- ISHIHARA, S. 1981. The granitoid series and mineralization. *Econ. Geol. 75th Anniv. Vol., 458-484.*
- JACKSON, N. J., WILLIS-RICHARDS, J., MANNING, D. A. & SAMS, M. S. 1989. Evolution of the Cornubian ore field, Southwest England; Part II, Mineral deposits and ore-forming processes. *Economic Geology, 84, 1101-1133.*

- KINNAIRD, J. A., BOWDEN, P., IXER, R. A. & ODLING, N. W. A. 1985. Mineralogy, geochemistry and mineralization of the Ririwai complex, northern Nigeria. *Journal of African Earth Sciences (1983)*, 3, 185-222.
- KRONER, U. & ROMER, R. L. 2013. Two plates — Many subduction zones: The Variscan orogeny reconsidered. *Gondwana Research*, 24, 298-329.
- LEBOUTILLIER, N., SHAIL, R. & JEWSON, C. 2003. Monazite in polymetallic chlorite-(tourmaline)-quartz-(fluorite)-cassiterite-sulphide lodes and its potential for constraining the chronology of magmatic hydrothermal mineralisation in Cornwall.
- LEBOUTILLIER, N. G. 2002. *The Tectoics of Variscan Magmatism and Mineralisation in South West England*. Doctor of philosophy in Mining Geology PhD, University of Exter.
- LEBOUTILLIER, N. G., CAMM, G. S., SHAIL, R. K., BROMLEY, A. V., JEWSON, C. & HOPPE, N. 2002. Tourmaline-quartz-cassiterite mineralization of the Land's End granite at Nanjizal, West Cornwall. *Proceedings of the Ussher Society*, 10, Part 3, 312-318.
- LEVERIDGE, B., HOLDER, M., GOODE, A., SCRIVENER, R., JONES, N. & MERRIMAN, R. 2002. Geology of the Plymouth and south-east Cornwall area. *Memoir of the British Geological Survey, Sheet*, 348.
- LONDON, D. & MANNING, D. A. C. 1995. Chemical variation and significance of tourmaline from Southwest England. *Economic Geology and the Bulletin of the Society of Economic Geologists*, 90, 495-519.
- LÓPEZ-MORO, F. J. 2012. EASYGRESGRANT—A Microsoft Excel spreadsheet to quantify volume changes and to perform mass-balance modeling in metasomatic systems. *Computers & Geosciences*, 39, 191-196.
- MANNING, D. 1998. Granites and associated igneous activity. *The geology of Cornwall*, 120-135.
- MATTSON, S. M. & ROSSMAN, G. R. 1987. Fe²⁺-Fe³⁺ interactions in tourmaline. *Physics and Chemistry of Minerals*, 14, 163-171.
- MEHTA, R. 2012. *Interactions, Imaging and Spectra in SEM*, INTECH Open Access Publisher.
- MEYER, C. & HEMLEY, J. J. 1967. Wall rock alteration. *Geochemistry of hydrothermal ore deposits*, 1, 166.

- MLYNARCZYK, M. S. J. & WILLIAMS-JONES, A. E. 2006. Zoned tourmaline associated with cassiterite; implications for fluid evolution and tin mineralization in the San Rafael Sn-Cu deposit, southeastern Peru. *The Canadian Mineralogist*, 44, Part 2, 347-365.
- MUKHERJEE, P. & GUPTA, P. 2008. Arbitrary scaling in ISOCON method of geochemical mass balance: An evaluation of the graphical approach. *Geochemical Journal*, 42, 247-253.
- MÜLLER, A. & HALLS, C. Rutile—the tin-tungsten host in the intrusive tourmaline breccia at Wheal Remfry, SW England. *Mineral Deposit Research: Meeting the Global Challenge*, 2005. Springer, 441-444.
- MÜLLER, A., SELTMANN, R., HALLS, C., SIEBEL, W., DULSKI, P., JEFFRIES, T., SPRATT, J. & KRONZ, A. 2006. The magmatic evolution of the Land's End pluton, Cornwall, and associated pre-enrichment of metals. *Ore Geology Reviews*, 28, 329-367.
- ORVILLE, P. M. 1962. Alkali metasomatism and feldspars. *Norsk Geologisk Tidsskrift*, 42, e316.
- PESQUERA, A., TORRES-RUIZ, J., GARCÍA-CASCO, A. & GIL-CRESPO, P. P. 2012. Evaluating the controls on tourmaline formation in granitic systems: a case study on peraluminous granites from the Central Iberian Zone (CIZ), Western Spain. *Journal of Petrology*, egs080.
- PETFORD, N., CRUDEN, A. R., MCCAFFREY, K. J. W. & VIGNERESSE, J. L. 2000. Granite magma formation, transport and emplacement in the Earth's crust. *Nature*, 408, 669-73.
- PIRAJNO, F. 2009. *Hydrothermal Processes and Mineral Systems*, Dordrecht, Springer Science+Business Media B.V.
- PIRAJNO, F. 2013. Effects of metasomatism on mineral systems and their host rocks: alkali metasomatism, skarns, greisens, tourmalinites, rodingites, black-wall alteration and listvenites. *Metasomatism and the Chemical Transformation of Rock*. Springer.
- POWNALL, J. M., WATERS, D. J., SEARLE, M. P., SHAIL, R. K. & ROBB, L. J. 2012. Shallow laccolithic emplacement of the Land's End and Tregonning granites, Cornwall, UK: Evidence from aureole field relations and PT modeling of cordierite-anthophyllite hornfels. *Geosphere*, 8, 1467-1504.

- PUTNIS, A. 2002. Mineral replacement reactions: from macroscopic observations to microscopic mechanisms. *Mineralogical Magazine*, 66, 689-708.
- PUTNIS, A. & AUSTRHEIM, H. 2010. Fluid - induced processes: metasomatism and metamorphism. *Geofluids*, 10, 254-269.
- PUTNIS, A. & AUSTRHEIM, H. 2013. Mechanisms of metasomatism and metamorphism on the local mineral scale: the role of dissolution-reprecipitation during mineral re-equilibration. *Metasomatism and the Chemical Transformation of Rock*. Springer.
- PUTNIS, A., HINRICHS, R., PUTNIS, C. V., GOLLA-SCHINDLER, U. & COLLINS, L. G. 2007. Hematite in porous red-clouded feldspars: evidence of large-scale crustal fluid-rock interaction. *Lithos*, 95, 10-18.
- QUE, M. & ALLEN, A. R. 1996. Sericitization of plagioclase in the Rosses granite complex, Co. Donegal, Ireland. *Mineralogical Magazine*, 60, 927-936.
- RAMIK, R. A., ORGAN, R. M. & MANDARINO, J. A. 2003. On type romarchite and hydroromarchite from Boundary Falls, Ontario, and notes on other occurrences. *Canadian Mineralogist*, 41, 649-657.
- REED, S. J. B. 2005. *Electron microprobe analysis and scanning electron microscopy in geology*, Cambridge, Cambridge University Press.
- RICE, C., DARKE, K., STILL, J. & LACHOWSKI, E. 1998. Tungsten-bearing rutile from the Kori Kollo gold mine, Bolivia. *Mineralogical Magazine*, 62, 421-429.
- ROBB, L. 2005. *Introduction to ore-forming processes*, Malden, Mass., Blackwell.
- RUMBLE III, D. 1973. Fe-Ti oxide minerals from regionally metamorphosed quartzites of western New Hampshire. *Contributions to Mineralogy and Petrology*, 42, 181-195.
- SCRIVENER, R. C. & SHEPHERD, T. 1998. Mineralization. *The geology of Cornwall: and the Isles of Scilly*. Univ of Exeter Pr.
- SHANNON, R. T. 1976. Revised effective ionic radii and systematic studies of interatomic distances in halides and chalcogenides. *Acta Crystallographica Section A: Crystal Physics, Diffraction, Theoretical and General Crystallography*, 32, 751-767.
- SHEPHERD, T., MILLER, M., SCRIVENER, R. & DARBYSHIRE, D. 1985. Hydrothermal fluid evolution in relation to mineralization in southwest England with special reference to the Dartmoor-Bodmin area. *High Heat Production (HHP) Granites, hydrothermal circulation and ore genesis*, 345-364.

- SLACK, J. F. & TRUMBULL, R. B. 2011. Tourmaline as a recorder of ore-forming processes. *Elements*, 7, 321-326.
- STOCK, S. & CULLITY, B. 2001. Elements of X-ray diffraction. *Prentice Hall, Upper Saddle River, New Jersey*.
- TAYLOR, B. E. & SLACK, J. F. 1984. Tourmalines from Appalachian-Caledonian massive sulfide deposits; textural, chemical, and isotopic relationships. *Economic Geology*, 79, 1703-1726.
- TAYLOR, R. 2010. *Ore textures: recognition and interpretation*, Springer Science & Business Media.
- THOMAS, R. 2008. *Practical guide to ICP-MS: a tutorial for beginners*, Boca Raton, CRC Press.
- TINDLE, A. G., BREAKS, F. W. & SELWAY, J. B. 2002. Tourmaline in petalite-subtype granitic pegmatites: evidence of fractionation and contamination from the Pakeagama Lake and Separation Lake areas of northwestern Ontario, Canada. *The Canadian Mineralogist*, 40, 753-788.
- TISCHENDORF, G., FÖRSTER, H.-J. & GOTTESMANN, B. 2001. Minor-and trace-element composition of trioctahedral micas: a review. *Mineralogical Magazine*, 65, 249-276.
- WILL, G. 2006. *Powder diffraction: The Rietveld method and the two stage method to determine and refine crystal structures from powder diffraction data*, Springer.
- WILLIAMSON, B., SPRATT, J., ADAMS, J., TINDLE, A. & STANLEY, C. 2000. Geochemical constraints from zoned hydrothermal tourmalines on fluid evolution and Sn mineralization: An example from fault breccias at Roche, SW England. *Journal of Petrology*, 41, 1439-1453.
- WINTER, J. D. 2010. *An introduction to igneous and metamorphic petrology*, New York, Prentice Hall.
- YARDLEY, B. W. 2013. The chemical composition of metasomatic fluids in the crust. *Metasomatism and the Chemical Transformation of Rock*. Springer.
- ZHARIKOV, V. P. N., RUSINOV VL, CALLEGARI E, FETTES DJ 2007. *Metasomatism and metasomatic rocks. Recommendations by the IUGS subcommission on the systematics of metamorphic rocks*, 9 [Online]. Available: http://www.bgs.ac.uk/scmr/docs/papers/paper_9.pdf.

Appendices

Appendix A	Mineral abbreviations
Appendix B	Thin section images
Appendix C	Geochemical data
Appendix D	Tourmaline structure calculations
Appendix E	XRD spectra

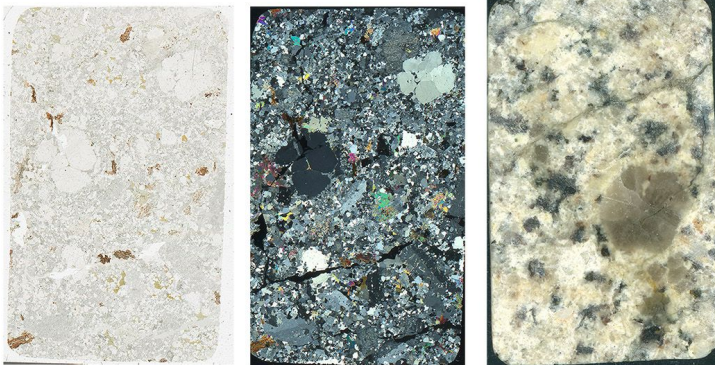
Digital appendix can also be found at <http://daim.idi.ntnu.no/>.

Appendix A Mineral Abbreviations

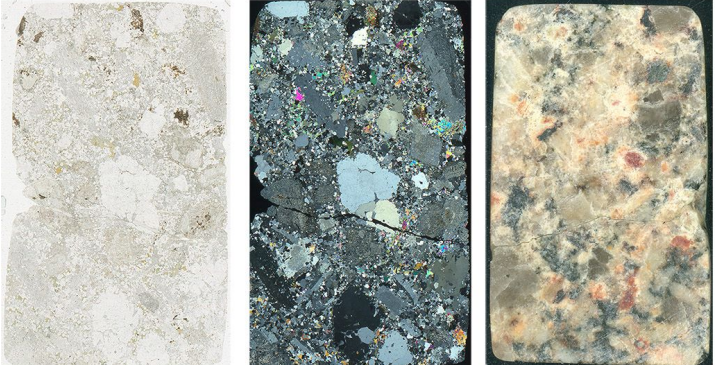
Symbol	Mineral name
Afs	Alkali feldspar
Bt	Biotite
Cst	Cassiterite
Hem	Hematite
Mnz	Monazite
Ms	Muscovite
Pl	Plagioclase
Qz	Quartz
Rt	Rutile
Ser	Sericite
Tur	Tourmaline
Zrm	Zircon

Appendix B Thin sections images

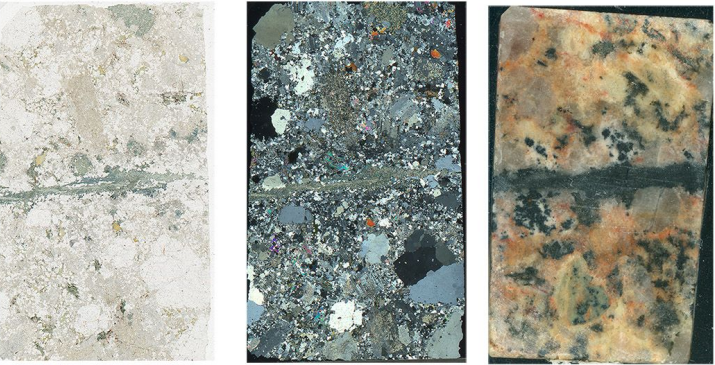
ME03V



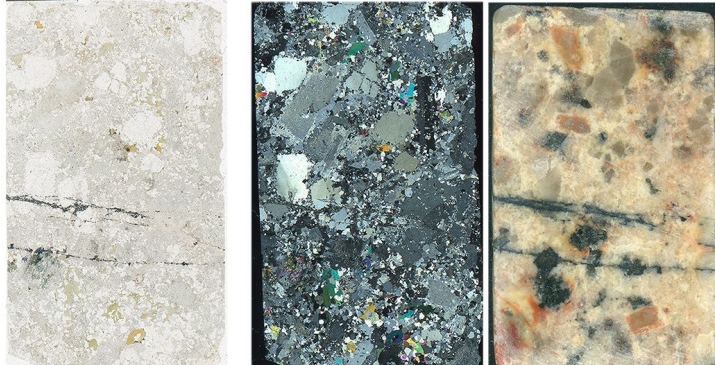
ME04V-A



ME04V-B



ME05V



Appendix C Geochemical data

Table C.1: Geochemical results of samples from XRD whole rock analysis (wt%), XRD trace elements (ppm) and ICP-MS (ppm) (in italic).

	ME 01 V	ME 02 V	ME 03 V	ME 04 V	ME 05 V	ME 06 V	KDC Granite 1103
Type of Vein	B	A		B	C	C	
Fe ₂ O ₃ (%)	1,68	1,85	1,44	1,74	1,28	1,39	2,99
TiO ₂ (%)	0,12	0,13	0,13	0,15	0,11	0,10	0,36
CaO (%)	0,26	0,15	0,35	0,30	0,25	0,24	0,83
K ₂ O (%)	5,76	11,71	5,10	5,58	6,16	6,48	5,44
P ₂ O ₅ (%)	0,16	0,07	0,16	0,18	0,18	0,18	0,27
SiO ₂ (%)	74,26	63,98	73,57	72,40	73,98	73,26	70,80
Al ₂ O ₃ (%)	12,99	17,37	13,33	14,03	13,22	13,67	14,09
MgO (%)	0,25	0,41	0,19	0,32	0,20	0,20	0,60
Na ₂ O (%)	1,47	0,20	1,87	1,84	1,46	1,36	2,70
MnO (%)	0,04	0,03	0,04	0,05	0,03	0,03	0,03
LOI (%) 1000°C	0,88	0,60	1,32	0,94	1,05	1,08	1,22
B ₂ O ₃	0,04	0,05	0,03	0,05	0,03	0,03	0,07
Sum (%)	97,91	96,54	97,51	97,58	97,93	98,01	99,39
Element							
Sc	3	3	2	2	1	2	3
V	7	5	7	8	5	7	24
Cr						1	12
Co		2					
Ni	7	15	6	8	6	6	9
Cu	5	8	5	7	9	11	7
Zn	22	17	27	23	20	22	45
Ga	23	29	23	24	20	22	23
As	5	25		7	2		11
Rb	432	801	599	403	494	529	455
Sr	46	95	30	46	45	43	78
Y	17	19	17	14	19	20	25
Zr	52	58	53	68	55	50	153
Nb	18	17	19	19	18	17	20
Mo	1		1	1		1	
Sn	107	1001	8	80	30	26	7
Sb	5	4	6	6	8	4	5
Cs	16	17	38	19	21	15	35
Ba	180	959	44	173	151	111	181
La	2	14		1			39
Ce		19	5			2	78
Pb	9	11	16	10	13	13	23
Th	6	6	6	9	7	5	24
U	3	7	4	3	3	2	8
Li	47,2	26,4	364	101	69,7	76,4	152
Be	1,76	1,39	2,46	1,84	0,96	1,69	< 20
Ge	1,90	3,15	2,66	2,09	2,15	2,18	< 30
Te	3,14	4,59	< 0.02	< 0.02	5,74	4,12	
Cs	3,16	5,39	8,33	6,06	5,91	4,34	15,6
Hf	1,52	1,49	1,62	2,13	1,71	1,69	4,51
Ta	4,07	4,54	4,53	4,47	4,50	4,71	2,27
W	11,0	12,6	10,6	5,69	6,03	5,83	< 6
Tl	2,41	5,54	3,01	2,28	2,70	2,92	2,67

Table C.2: Geochemical results of sample ME02V from XRD whole rock analysis (wt%), XRD trace elements (ppm) and ICP-MS (ppm) (in italic).

	ME02V-C1	ME02V-C2	ME02V-C3	ME02V-C4	ME02V-C5	ME02V-C6
Type of Vein	A	A	A	A	A	A
Fe₂O₃ (%)	1,35	1,94	1,93	1,80	1,87	1,52
TiO₂ (%)	0,11	0,15	0,10	0,10	0,10	0,12
CaO (%)	0,14	0,15	0,14	0,15	0,10	0,09
K₂O (%)	9,79	12,19	12,59	11,01	7,93	6,83
P₂O₅ (%)	0,09	0,07	0,07	0,09	0,10	0,10
SiO₂ (%)	71,91	63,99	63,60	67,01	74,01	74,74
Al₂O₃ (%)	14,35	18,52	18,48	16,24	13,30	13,91
MgO (%)	0,22	0,45	0,40	0,33	0,18	0,21
Na₂O (%)	0,09	0,18	0,17	0,10	0,35	0,71
MnO (%)	0,03	0,03	0,03	0,03	0,04	0,04
LOI (%) 1000°C	0,52	0,50	0,47	0,44	0,76	1,18
B₂O₃	0,03	0,07	0,06	0,07	0,08	0,06
Sum (%)	98,63	98,23	98,05	97,38	98,81	99,51
Element						
Sc		3	2			2
V	5	6	6	6	6	6
Cr						
Co		3	1	1		
Ni	8	16	13	13	7	5
Cu	7	7	7	8	8	6
Zn	14	16	17	17	21	24
Ga	22	29	28	24	22	22
As	9	22	22	15	3	
Rb	687	868	898	824	608	626
Sr	64	105	109	84	41	36
Y	16	17	17	15	13	15
Zr	57	55	51	53	54	54
Nb	17	18	13	14	16	20
Mo				1	1	1
Sn	942	665	1233	295	26	11
Sb		4	3	4	5	4
Cs	18	18	19	14	20	29
Ba	602	1149	1116	743	230	101
La	3	10	29	6		
Ce		12	36	8		5
Pb	15	13	15	16	15	18
Th	7	7	7	6	6	7
U	3	5	9	7	7	4
<i>Li</i>	62,6	36,4	30,2	33,5	119	206
<i>Be</i>	< 10	< 10	< 10	< 10	< 10	< 10
<i>Ge</i>	< 8	< 8	< 8	< 8	< 8	< 8
<i>Te</i>						
<i>Cs</i>	8,03	7,53	9,98	5,51	7,60	8,34
<i>Hf</i>	< 4	< 4	< 4	< 4	< 4	< 4
<i>Ta</i>	4,55	5,53	3,45	4,15	3,95	4,89
<i>W</i>	25,5	14,4	11,4	18,3	28,3	14,4
<i>Tl</i>	4,59	6,16	6,12	5,43	2,82	2,30

Table C.3: Mass balance Isocon diagram. Zr and TiO₂ are assumed immobile.

	Unaltered	Altered	Gain/Loss relative to C _i ⁰
	ME02V-C6	ME02V-C3	$\Delta C_i/C_i^0$
SiO ₂	74,74	63,60	-0,10
TiO ₂	0,12	0,10	-0,11
Al ₂ O ₃	13,91	18,48	0,41
Fe ₂ O ₃	1,52	1,93	0,34
MnO	0,04	0,03	-0,09
MgO	0,21	0,40	1,03
CaO	0,09	0,14	0,66
Na ₂ O	0,71	0,17	-0,75
K ₂ O	6,83	12,59	0,95
P ₂ O ₅	0,10	0,07	-0,23
As		22,00	
Cs	29,00	19,00	-0,31
Li	205,94	30,17	-0,84
Rb	626,00	898,00	0,52
Ba	101,00	1116,00	10,70
Sr	36,00	109,00	2,21
Pb	18,00	15,00	-0,12
Ni	5,00	13,00	1,75
V	6,00	6,00	0,06
Ga	22,00	28,00	0,35
Zn	24,00	17,00	-0,25
U	4,00	9,00	1,38
Zr	54,00	51,00	0,00
Y	15,00	17,00	0,20
Nb	20,00	13,00	-0,31
Th	7,00	7,00	0,06
La		29,00	
Ce	5,00	36,00	6,62
Sn	11,00	1233,00	117,68
W	14,38	11,41	-0,16
B	1000,00	4100,00	3,34
Overall volume change (%)	Overall mass change (%)	Slope	
4,67	5,88	0,94	

Na ₂ O	F	Cl	MnO	Al ₂ O ₃	MgO	P ₂ O ₅	FeO	SiO ₂	K ₂ O	CaO	TiO ₂	BaO	Total	Analysis	Vein type
0,20	0,10	0,01	0,01	19,01	0,00	0,00	0,01	69,90	12,90	0,00	0,00	0,00	102,10	01V.4.4	B
4,99	0,00	0,00	0,00	19,96	0,00	0,05	0,02	71,79	0,13	0,06	0,00	0,03	97,02	01V.4.5	B
0,34	0,00	0,00	0,02	18,02	0,03	0,02	0,07	65,19	15,55	0,00	0,03	0,15	99,42	01V.5.1	B
0,15	0,00	0,10	0,00	17,99	0,00	0,04	0,00	65,11	15,91	0,00	0,03	0,07	99,37	01V.5.2	B
0,66	0,09	0,00	0,00	17,99	0,00	0,18	0,05	64,38	15,46	0,02	0,03	0,00	98,83	02VA.1.3	A distal
4,19	0,01	0,02	0,01	17,90	0,00	0,25	0,02	64,63	10,10	0,01	0,02	0,00	97,15	02VA.1.4	A distal
0,18	0,03	0,00	0,01	17,86	0,01	0,00	0,10	64,73	15,62	0,00	0,00	0,12	98,65	02VA.4.1	A distal
0,18	0,02	0,00	0,01	17,77	0,00	0,01	0,03	64,46	15,88	0,00	0,00	0,27	98,62	02VA.4.2	A distal
0,38	0,00	0,02	0,00	17,75	0,00	0,07	0,00	63,77	14,95	0,00	0,00	0,09	97,03	02VA.8.7	A proximal
0,56	0,00	0,01	0,00	18,16	0,00	0,13	0,00	63,22	15,43	0,00	0,03	0,13	97,66	02VA.8.8	A proximal
0,80	0,00	0,00	0,00	18,24	0,00	0,16	0,04	63,50	15,21	0,00	0,02	0,05	98,01	02VA.8.9	A proximal
0,64	0,05	0,00	0,00	18,09	0,00	0,23	0,00	63,06	15,46	0,00	0,02	0,05	97,57	02VA.8.10	A proximal
0,50	0,09	0,00	0,00	18,04	0,00	0,21	0,01	63,22	15,73	0,00	0,03	0,08	97,86	02VA.8.11	A proximal
0,90	0,06	0,01	0,03	18,30	0,00	0,25	0,00	63,06	14,90	0,00	0,04	0,00	97,52	02VA.8.12	A proximal
0,03	0,05	0,00	0,00	17,64	0,00	0,00	0,07	64,57	14,92	0,00	0,00	0,00	97,25	02VA.8.13	A proximal
0,03	0,02	0,00	0,00	17,86	0,01	0,00	0,09	64,28	15,55	0,00	0,04	0,00	97,86	02VA.8.14	A proximal
0,68	0,03	0,00	0,03	18,13	0,00	0,23	0,00	64,46	15,35	0,01	0,00	0,00	98,90	02VB.1.6	A proximal
0,21	0,00	0,00	0,02	17,89	0,00	0,00	0,05	64,69	15,49	0,00	0,03	0,16	98,54	02VB.1.7	A proximal
0,14	0,00	0,00	0,00	18,27	0,03	0,00	0,36	65,67	15,81	0,00	0,00	0,03	100,32	02VB.3.1	A proximal
0,19	0,00	0,00	0,00	18,11	0,00	0,00	0,04	65,86	15,70	0,00	0,04	0,15	100,09	02VB.3.2	A proximal
0,23	0,00	0,00	0,00	17,89	0,02	0,17	0,00	64,53	16,15	0,01	0,03	0,00	99,04	05V.2.1	C
0,31	0,00	0,00	0,00	18,20	0,00	0,17	0,05	65,10	15,87	0,00	0,00	0,00	99,70	05V.2.2	C
0,28	0,00	0,02	0,00	18,07	0,00	0,01	0,01	66,28	16,03	0,00	0,00	0,06	100,76	05V.4.4	C
10,97	0,09	0,00	0,00	18,97	0,00	0,00	0,02	68,62	0,88	0,11	0,00	0,00	99,62	05V.4.5	C

Table C.5: Microprobe analysis of feldspar, in (%)

Table C.6: Trace element content in Rutile, from microprobe analysis. All values are in ppm.

Domain	Ca	Al	Fe	Si	Nb	V	W	Sn
1	0	1651	5068	0	18511	5781	0	1000
1	1730	1080	3583	0	10688	4128	0	1906
1	0	1403	4656	0	15889	5299	0	0
1	0	1392	2954	0	13177	5702	0	0
1	1122	386	7882	3576	6075	4957	1808	2710
1	279	111	24400	1641	8668	4797	262	2056
1	679	360	15624	2655	13659	4821	2434	2678
1	1408	381	9203	3328	12576	5829	2656	31443
1	172	95	24998	1744	11751	4889	12569	7766
1	93	196	24866	2281	15575	4852	7406	5380
1	236	196	14217	3300	15875	4914	8842	4080
1	79	333	5985	3034	11597	5565	1832	4781
1	172	413	6825	3188	10220	5165	5281	3670
1	393	159	31947	3599	1440	5055	0	1552
2	572	1313	4539	0	8319	1692	1142	6467
2	0	1133	3762	0	8437	2403	1078	6033
2	629	1043	5239	1800	6732	2818	1316	5600
2	658	1191	4703	2608	7242	2000	3266	6931
2	3831	2159	6452	12032	3684	5884	2260	30206
2	3102	1699	6669	10620	3586	6025	1752	28733
2	3109	1212	6047	8218	4453	5786	1467	27142
2	1079	460	9040	3978	10807	4901	952	4096
2	1222	577	13859	6745	3712	6050	1689	25969
2	186	677	14419	7311	25033	4514	11292	8908
2	71	318	12522	2749	21831	5331	15653	5325
2	393	625	21990	8391	45990	4379	6487	18652
3	1051	1371	10089	0	15617	1132	11345	3514
3	0	900	6421	1449	20489	829	8546	5600
3	1551	1138	18290	5072	19853	5245	15757	50748
3	565	286	36673	2562	38203	4471	24440	3017
3	536	191	42084	2837	48576	4195	38356	8538
3	815	513	29483	4347	30947	4422	26478	21219
3	865	312	34808	3702	31764	4416	29245	26977
3	422	318	32608	2837	33861	4379	12339	2883
3	3238	1365	29709	9008	27787	4502	27231	20219
3	622	370	42045	3225	46934	4084	36683	6624
4	250	619	14707	0	8430	1798	19479	18801
4	300	1148	14310	0	11828	1619	16673	17982
4	193	212	7035	5118	11611	5454	8271	2843
4	14	90	1974	6161	20664	5024	0	457
4	86	164	4913	4693	8493	5479	2982	3127
4	71	95	4897	4039	17413	5239	4084	1126

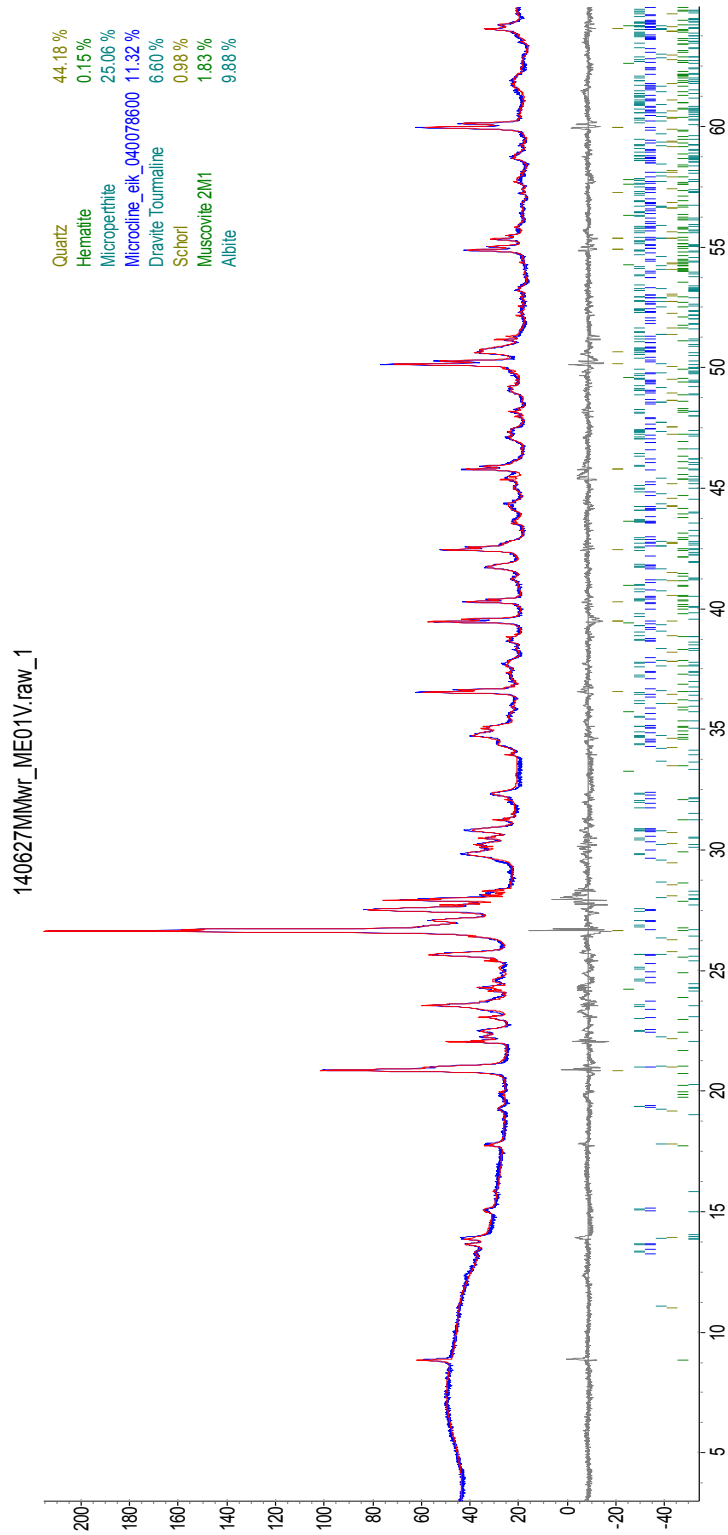
Geochemical data

Table C.7: Microprobe analysis results of tourmaline (%).

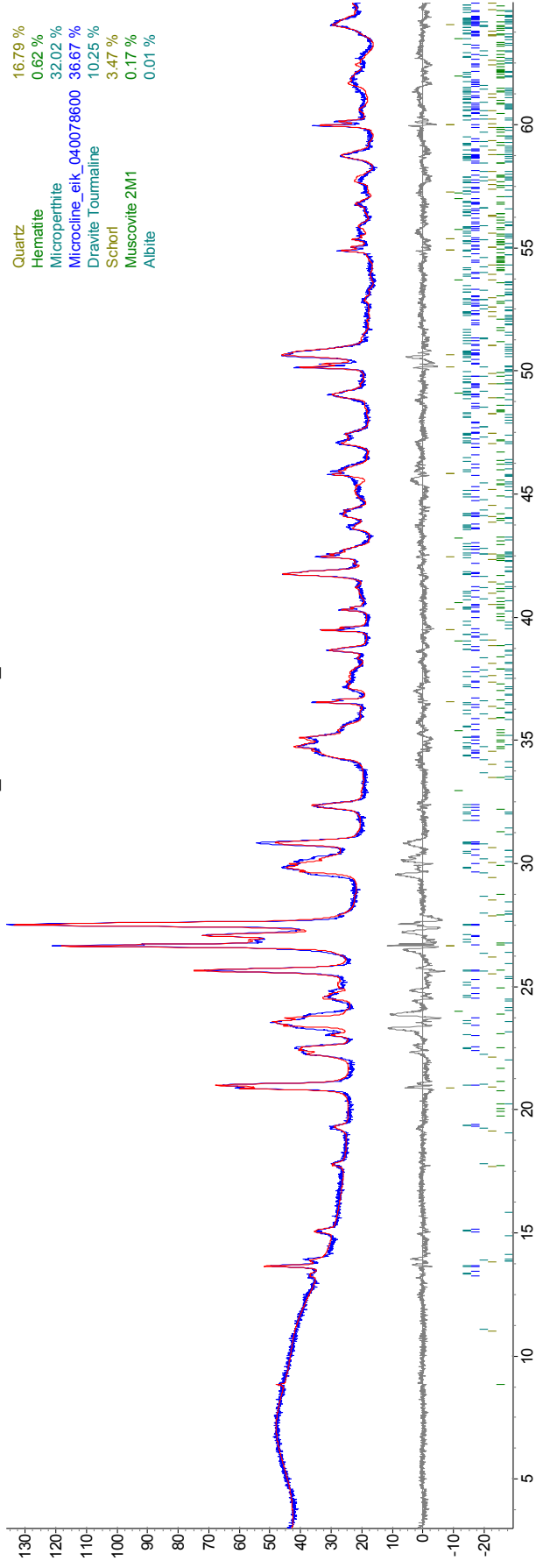
Al ₂ O ₃	F	Cl	MnO	SiO ₂	Na ₂ O	K ₂ O	FeO	MgO	CaO	P ₂ O ₅	TiO ₂	BaO	SnO ₂	WO ₃	Total	Comment	Vein type
32,17	0,08	0,02	0,07	36,02	2,07	0,01	10,20	4,59	0,33	0,00	0,24	0,00	0,16	0,00	85,91	02VA.4.1	A distal
27,13	0,24	0,25	0,06	30,51	2,04	0,14	11,89	2,32	0,44	0,04	0,92	0,00	0,10	0,00	75,93	02VA.4.2	A distal
30,10	0,24	0,03	0,05	35,34	2,40	0,06	11,14	5,37	0,78	0,01	0,34	0,00	0,11	0,00	85,84	02VA.4.3	A distal
26,84	0,12	0,00	0,05	34,60	2,41	0,04	16,95	3,54	0,85	0,02	0,00	0,02	0,12	0,01	85,53	02VA.4.4	A distal
27,24	0,16	0,00	0,05	34,64	2,35	0,05	16,11	4,44	0,83	0,03	0,07	0,00	0,21	0,02	86,13	02VA.4.5	A distal
28,09	0,10	0,03	0,10	35,09	2,32	0,06	18,03	2,19	0,56	0,00	0,11	0,04	0,15	0,00	86,82	02VA.4.6	A distal
30,54	0,10	0,00	0,02	34,81	2,05	0,18	8,80	5,25	0,40	0,00	0,07	0,05	0,16	0,00	82,39	02VA.4.7	A distal
30,11	0,10	0,01	0,06	35,56	2,11	0,22	14,21	2,84	0,42	0,00	0,01	0,00	0,04	0,00	85,64	02VA.4.8	A distal
28,87	0,15	0,00	0,04	35,95	2,20	0,21	12,03	4,72	0,70	0,02	0,08	0,00	0,04	0,00	84,93	02VA.4.9	A distal
28,67	0,02	0,00	0,01	34,97	2,23	0,19	18,25	1,39	0,53	0,04	0,02	0,07	0,01	0,00	86,38	02VA.4.10	A distal
28,15	0,04	0,00	0,07	34,66	2,37	0,22	19,20	1,36	0,44	0,05	0,02	0,00	0,08	0,00	86,65	02VA.4.11	A distal
25,95	0,22	0,00	0,00	34,88	2,69	0,22	16,43	4,23	0,34	0,00	0,65	0,00	0,28	0,00	85,79	02VA.4.12	A distal
29,60	0,15	0,02	0,06	34,69	2,45	0,20	12,71	3,07	0,47	0,00	0,57	0,00	0,21	0,00	84,11	02VA.4.13	A distal
31,55	0,20	0,02	0,06	33,93	2,11	0,21	12,33	3,47	0,52	0,02	0,28	0,04	0,18	0,00	84,83	02VA.4.14	A distal
24,24	0,02	0,01	0,05	34,76	2,62	0,21	18,58	4,23	0,49	0,01	0,34	0,00	0,26	0,00	85,81	02VA.4.15	A distal
29,40	0,16	0,03	0,02	36,14	2,34	0,06	20,69	0,88	0,46	0,01	0,00	0,00	0,06	-	90,22	02VA.4.4	A distal
23,30	0,16	0,02	0,00	33,39	2,52	0,08	20,35	4,01	0,52	0,00	0,25	0,00	0,24	-	84,84	02VA.4.5	A distal
1,28	0,03	0,30	0,00	69,78	0,16	0,23	0,78	0,09	0,09	0,00	0,00	0,06	0,02	-	72,82	02VA.4.6	A distal
33,69	0,53	0,00	0,18	34,16	2,13	0,04	13,90	1,51	0,12	0,01	0,37	0,00	0,00	-	86,64	02VA.5.1	A distal
32,70	0,15	0,01	0,02	33,53	2,03	0,00	4,97	6,93	0,87	0,01	0,44	0,00	0,35	-	81,99	02VA.5.2	A distal
20,06	0,00	0,00	0,17	32,65	2,65	0,06	25,98	4,26	0,66	0,02	0,00	0,00	0,30	-	86,81	02VA.5.3	A distal
34,14	0,06	0,00	0,00	32,32	1,54	0,00	7,96	4,63	0,56	0,00	0,23	0,06	0,25	-	81,75	02VA.5.4	A distal
21,56	0,00	0,01	0,29	32,55	2,70	0,07	22,50	4,70	0,72	0,00	0,03	0,00	0,32	-	85,46	02VA.5.5	A distal
34,56	0,44	0,00	0,11	33,45	1,96	0,05	13,01	1,38	0,31	0,15	0,49	0,00	0,02	0,00	85,74	02VB.3.1	A proximal
35,34	0,42	0,01	0,13	33,59	1,92	0,05	12,52	1,39	0,26	0,10	0,31	0,01	0,01	0,00	85,86	02VB.3.2	A proximal
33,60	0,14	0,01	0,10	34,83	1,85	0,03	13,19	1,42	0,11	0,12	0,29	0,00	0,02	0,00	85,64	02VB.3.3	A proximal
30,74	0,00	0,00	0,00	36,15	2,49	0,00	5,06	8,39	0,32	0,00	0,29	0,02	0,77	0,00	84,24	02VB.3.4	A proximal
19,79	0,00	0,01	0,16	33,08	2,62	0,00	25,33	4,34	0,63	0,02	0,00	0,03	0,62	0,00	86,62	02VB.3.5	A proximal
25,30	0,01	0,00	0,02	34,00	2,42	0,03	16,47	5,66	0,78	0,01	0,30	0,00	0,22	0,00	85,21	02VB.3.6	A proximal
21,45	0,07	0,02	0,38	33,51	2,74	0,08	21,76	4,66	0,57	0,04	0,06	0,00	0,30	0,00	85,58	02VB.3.7	A proximal
20,83	0,00	0,01	0,37	33,30	2,67	0,01	22,10	4,89	0,54	0,03	0,17	0,07	0,58	0,00	85,57	02VB.3.8	A proximal
32,56	0,19	0,02	0,00	35,21	2,13	0,02	5,07	7,45	0,65	0,02	0,25	0,00	0,16	0,00	83,63	02VB.3.9	A proximal
32,64	0,04	0,00	0,03	35,64	2,17	0,05	6,04	6,80	0,27	0,01	0,24	0,02	0,12	0,00	84,04	02VB.3.10	A proximal
32,64	0,04	0,00	0,11	35,63	1,59	0,18	14,67	1,18	0,06	0,00	0,12	0,00	0,08	0,00	86,28	02VB.3.11	A proximal
25,11	0,00	0,00	0,00	34,30	2,71	0,18	18,06	4,24	0,25	0,00	0,08	0,01	0,27	0,00	85,22	02VB.3.12	A proximal
34,17	0,49	0,00	0,08	33,50	2,08	0,04	13,40	1,47	0,20	0,13	0,53	0,03	0,00	0,00	85,90	02VB.1.1	A proximal
34,85	0,49	0,01	0,14	33,29	2,00	0,04	13,10	1,38	0,34	0,16	0,54	0,00	0,02	0,00	86,14	02VB.1.2	A proximal
32,84	0,14	0,00	0,00	33,54	1,98	0,00	4,66	7,38	0,42	0,00	0,34	0,00	0,47	0,00	81,70	02VB.1.3	A proximal
31,69	0,13	0,00	0,04	34,26	2,20	0,01	5,67	7,18	0,78	0,00	0,44	0,03	0,58	0,00	82,95	02VB.1.4	A proximal
21,78	0,00	0,01	0,12	33,15	2,52	0,01	20,74	5,11	0,82	0,03	0,03	0,10	0,36	0,00	84,76	02VB.1.5	A proximal
26,13	0,09	0,00	0,01	34,10	2,45	0,02	15,77	5,38	0,63	0,01	0,28	0,02	0,19	0,00	85,05	02VB.1.6	A proximal
26,68	0,06	0,05	0,02	30,30	2,19	0,07	12,71	5,35	0,73	0,02	0,50	0,10	0,19	0,00	78,90	02VB.1.7	A proximal
31,59	0,01	0,00	0,01	36,22	2,30	0,00	3,93	8,15	0,12	0,02	0,27	0,00	0,66	0,00	83,27	02VB.1.8	A proximal
20,15	0,00	0,01	0,13	33,20	2,57	0,03	22,92	4,67	0,72	0,01	0,05	0,05	0,72	0,00	85,23	02VB.1.9	A proximal
30,06	0,27	0,01	0,03	35,33	2,23	0,00	10,79	5,09	0,56	0,00	0,26	0,01	0,21	0,00	84,74	02VB.1.10	A proximal
30,68	0,17	0,03	0,01	34,76	1,99	0,00	7,86	6,74	0,15	0,04	0,26	0,00	0,26	0,00	83,86	02VB.1.11	A proximal
25,19	0,03	0,05	0,00	34,56	2,65	0,03	17,93	4,37	0,41	0,00	0,14	0,02	0,37	0,00	85,72	02VB.1.12	A proximal
34,09	0,39	0,00	0,13	32,98	2,09	0,04	14,25	1,52	0,25	0,05	0,48	0,04	0,00	-	86,32	02VB.1.1	A proximal
20,26	0,00	0,02	0,07	31,98	2,34	0,02	21,32	4,78	0,84	0,03	0,01	0,00	0,39	-	82,04	02VB.1.2	A proximal
28,66	0,14	0,01	0,07	30,17	2,23	0,03	12,42	5,35	0,76	0,00	0,76	0,05	0,17	-	80,81	02VB.1.3	A proximal
23,62	0,15	0,01	0,07	29,28	1,77	0,06	14,18	5,52	0,80	0,03	0,56	0,00	0,24	-	76,28	02VB.1.4	A proximal
22,17	0,02	0,02	0,03	33,11	2,75	0,02	23,35	3,93	0,47	0,00	0,07	0,03	0,35	-	86,31	02VB.1.5	A proximal

Al ₂ O ₃	F	Cl	MnO	SiO ₂	Na ₂ O	K ₂ O	FeO	MgO	CaO	P ₂ O ₅	TiO ₂	BaO	SnO ₂	WO ₃	Total	Comment	Vein type
32,13	0,48	0,00	0,08	34,73	2,16	0,01	17,34	0,27	0,01	0,00	0,46	0,04	0,00	-	87,69	01V.4.1	B
30,84	0,29	0,02	0,07	33,87	1,90	0,00	18,13	0,10	0,89	0,02	0,06	0,04	0,06	-	86,27	01V.4.2	B
33,34	0,21	0,02	0,15	35,28	1,54	0,02	15,70	0,00	0,34	0,00	0,00	0,05	0,00	-	86,66	01V.4.3	B
30,93	0,22	0,04	0,04	32,97	1,59	0,01	18,62	0,11	1,38	0,00	0,10	0,00	0,05	-	86,05	01V.4.8	B
34,57	0,43	0,00	0,08	34,65	1,53	0,03	12,79	1,06	0,05	0,00	0,22	0,00	0,01	0,00	85,23	05V.4.1	C
34,39	0,54	0,00	0,08	34,76	1,79	0,04	13,10	1,09	0,01	0,00	0,37	0,00	0,01	0,00	85,96	05V.4.2	C
25,62	0,13	0,08	0,08	33,81	2,53	0,01	23,79	0,24	0,43	0,01	0,01	0,10	0,15	0,00	86,93	05V.4.3	C
33,20	0,19	0,00	0,06	32,58	1,53	0,01	15,73	0,37	0,73	0,01	0,02	0,00	0,01	0,00	84,34	05V.4.4	C
33,17	0,20	0,01	0,05	32,71	1,37	0,01	15,33	0,89	1,59	0,00	0,03	0,00	0,04	0,00	85,31	05V.4.5	C
31,23	0,03	0,02	0,08	32,65	1,55	0,01	17,97	0,22	1,43	0,00	0,00	0,00	0,01	0,04	85,22	05V.4.6	C
34,35	0,28	0,02	0,20	34,08	1,44	0,02	13,27	0,04	1,38	0,00	0,02	0,10	0,02	0,00	85,10	05V.4.7	C
30,52	0,69	0,01	0,00	36,64	1,70	0,03	2,14	10,76	1,83	0,00	0,32	0,03	0,00	0,00	84,35	05V.4.8	C
30,61	0,02	0,00	0,04	35,54	2,06	0,01	13,26	3,03	0,52	0,03	0,15	0,00	0,03	0,00	85,28	05V.4.9	C
31,41	0,00	0,00	0,03	35,73	2,26	0,00	13,56	2,87	0,15	0,05	0,15	0,04	0,12	0,00	86,38	05V.4.10	C
34,57	0,27	0,00	0,01	36,97	2,53	0,01	1,22	8,51	0,33	0,00	0,14	0,05	0,01	0,00	84,50	05V.4.11	C
34,47	0,18	0,03	0,00	34,47	1,73	0,03	11,49	1,26	0,79	0,09	0,15	0,00	0,01	0,00	84,60	05V.4.12	C
29,18	0,07	0,00	0,00	34,25	2,42	0,02	18,38	1,14	0,30	0,00	0,06	0,00	0,02	0,01	85,80	05V.4.13	C
30,02	0,00	0,00	0,04	34,													

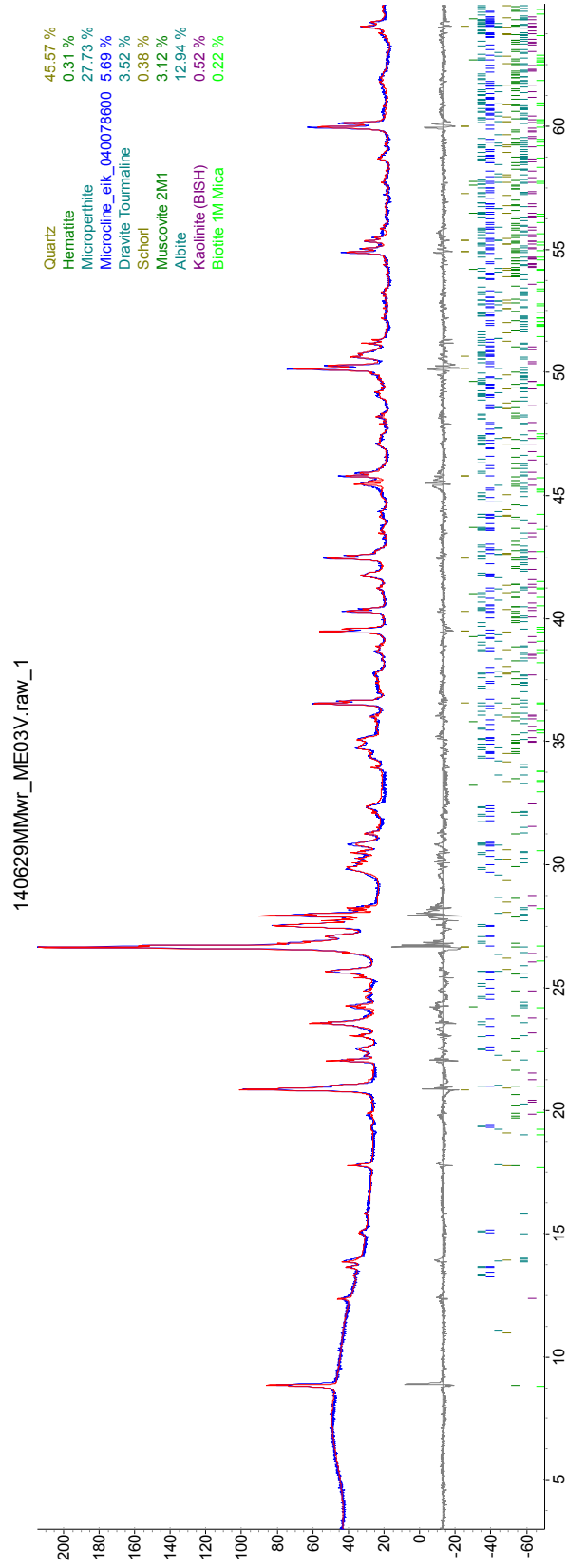
Appendix E XRD spectra



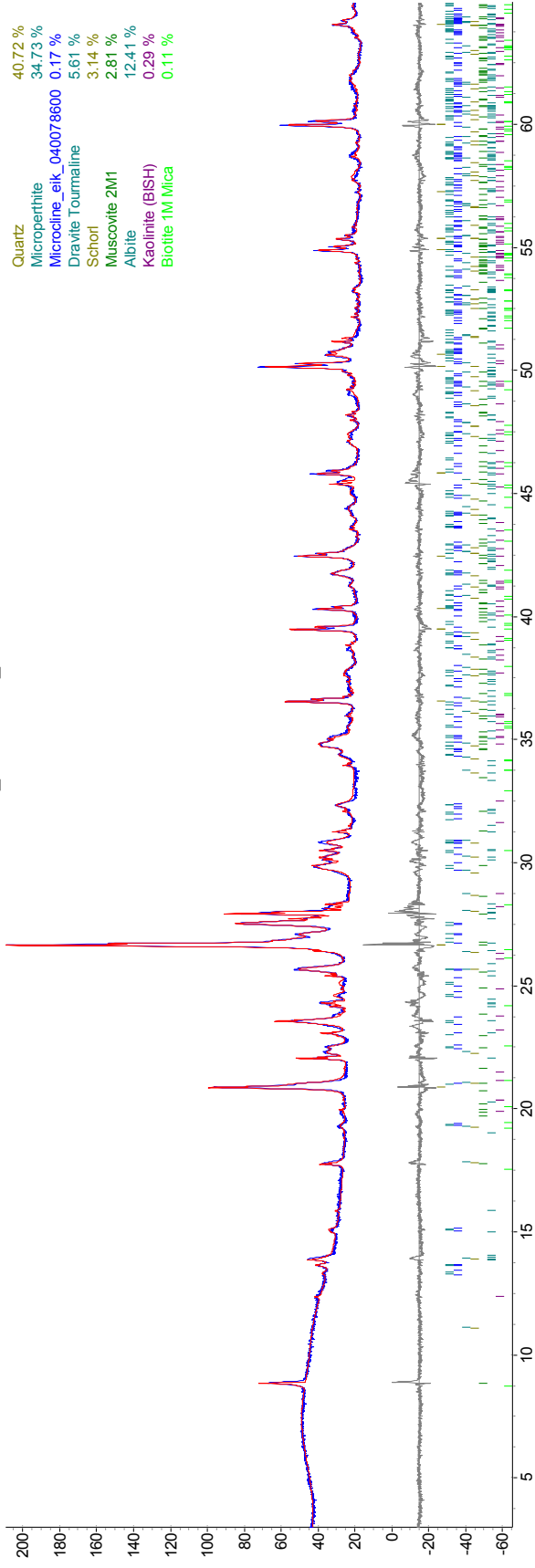
140628MIMwr_ME02V.raw_1

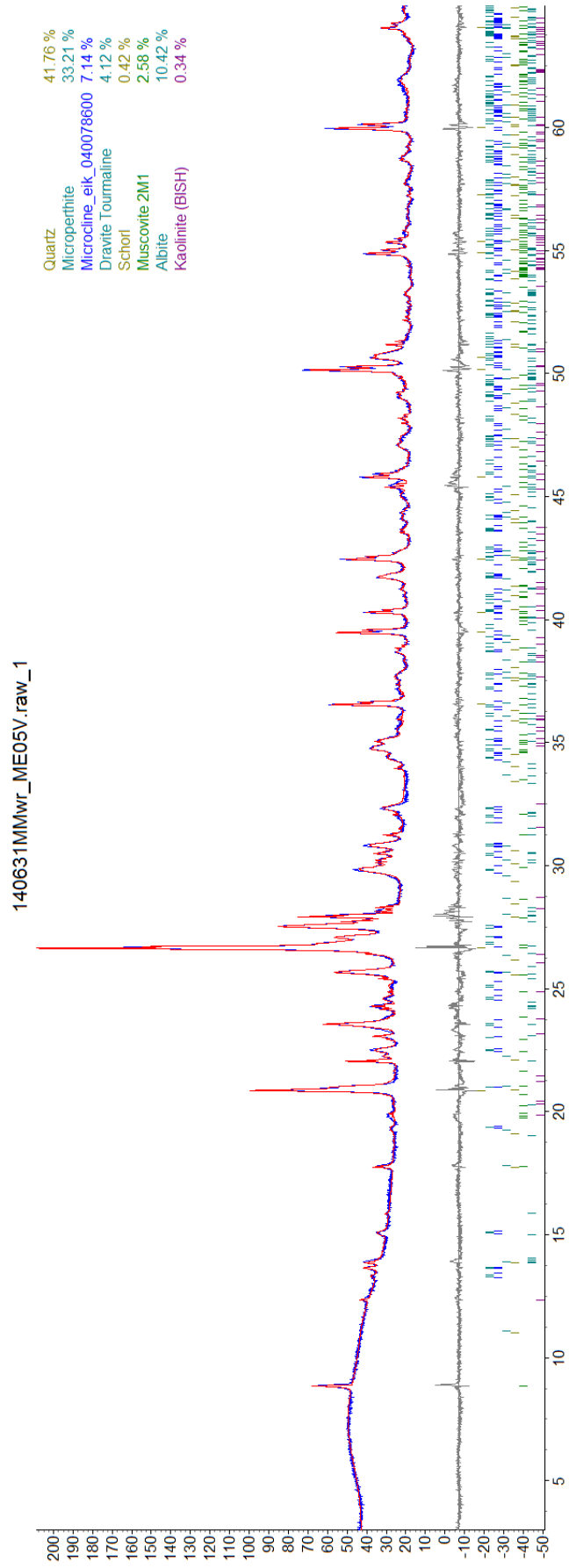


XRD spectra

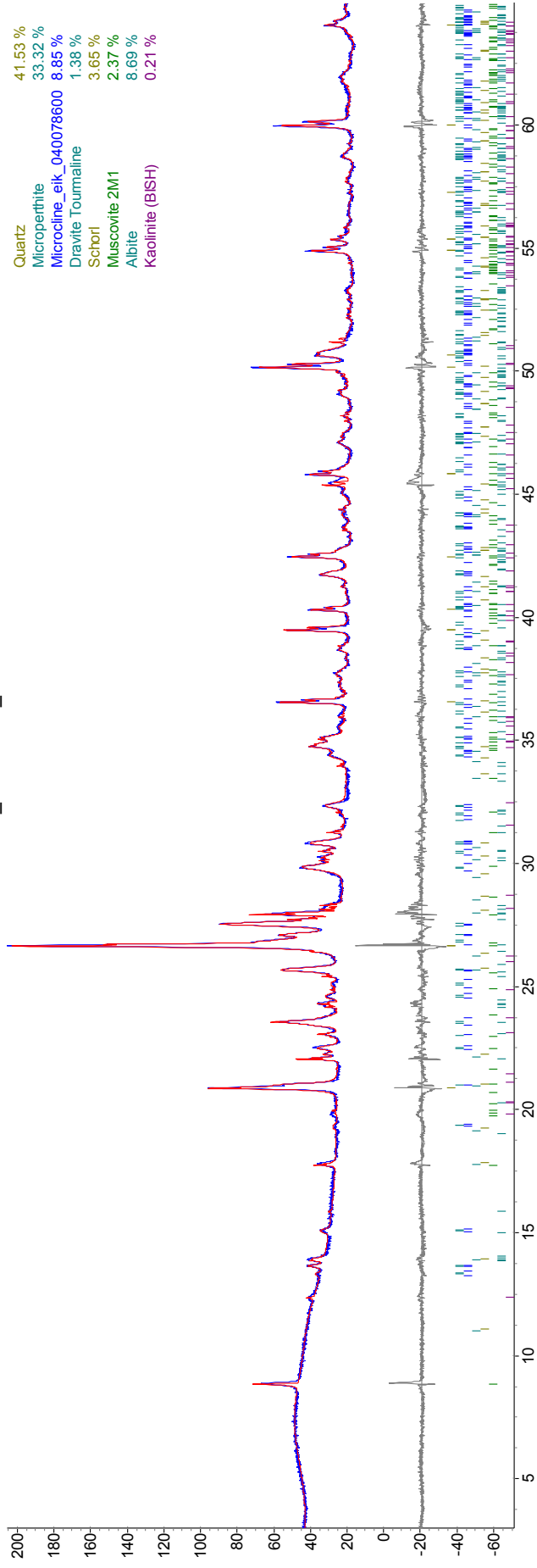


140630MMwr_ME04V.raw_1





140632_me06v.raw_1



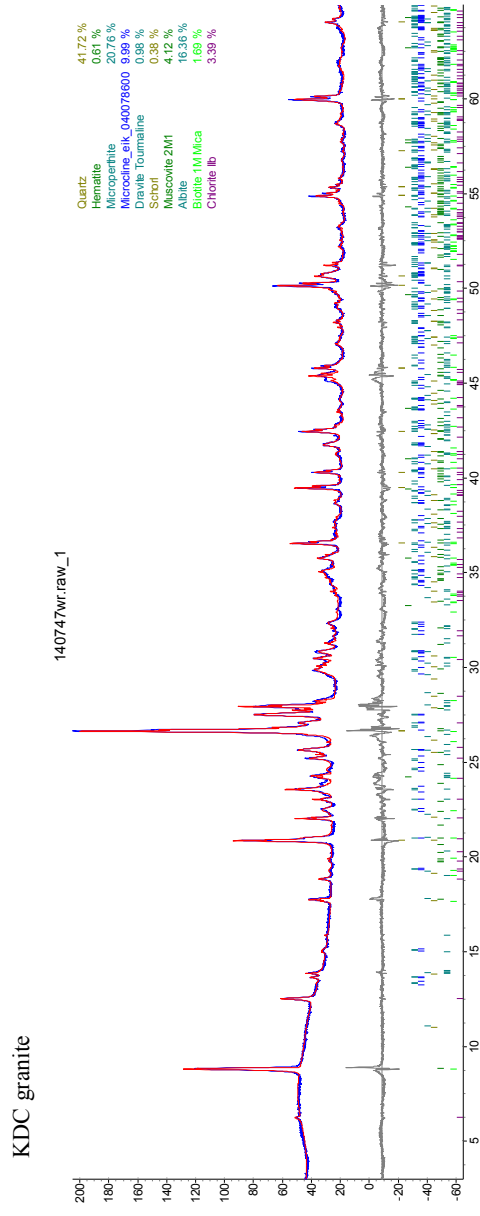
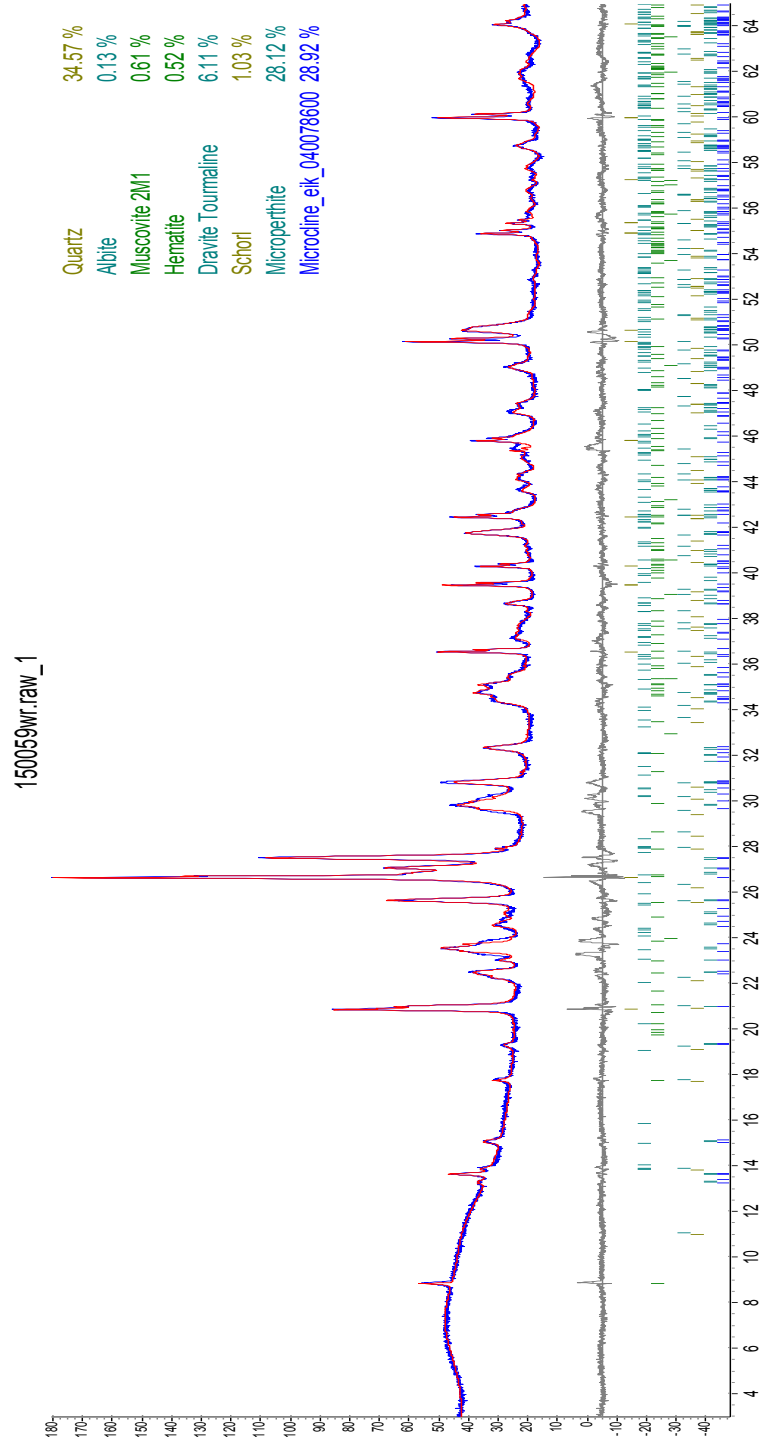
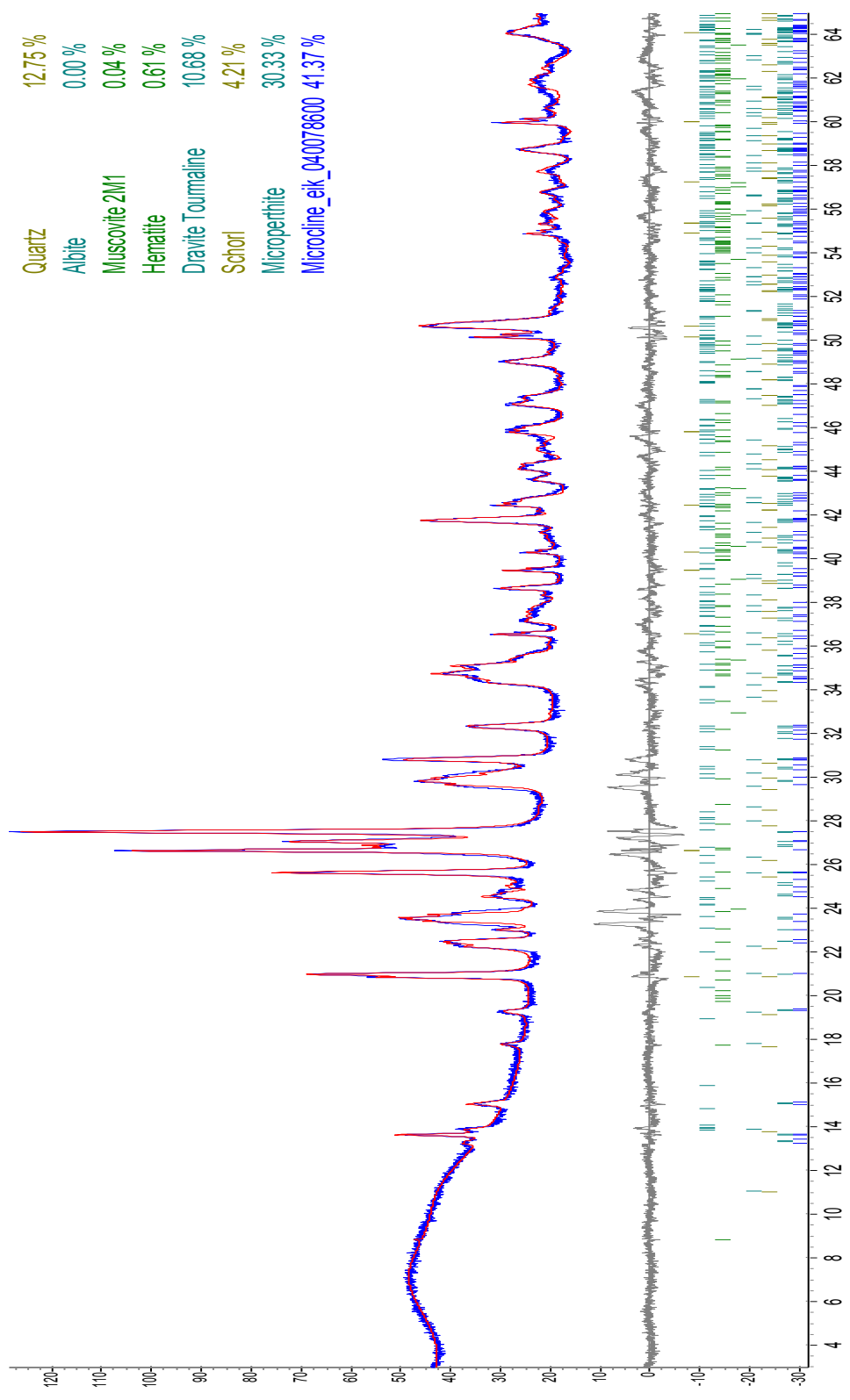


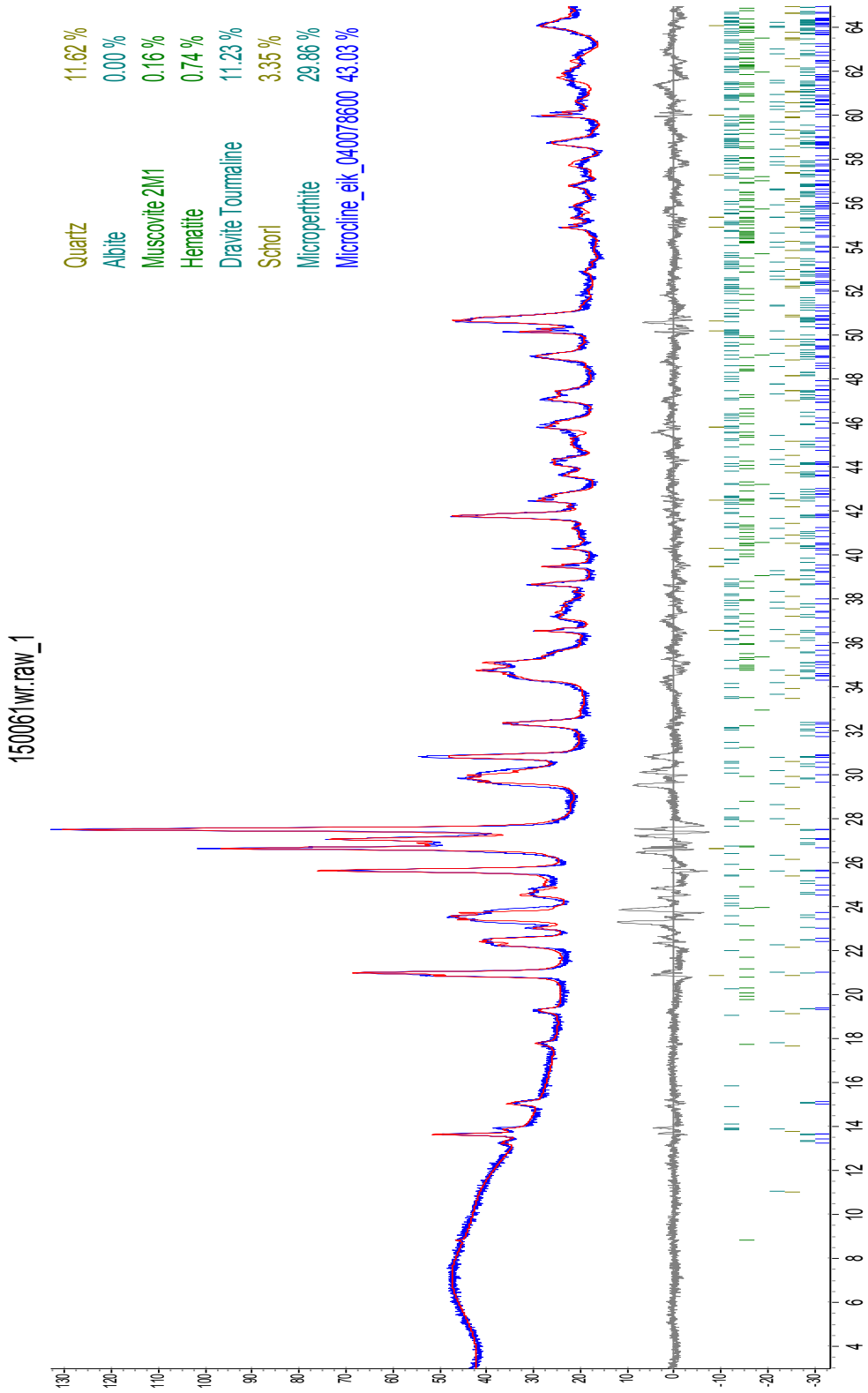
Table E.1: XRD journal number corresponding to following XRD spectra of the six sections of type A ME02V

Sample	Number
ME02V-C1	150059
ME02V-C2	150060
ME02V-C3	150061
ME02V-C4	150062
ME02V-C5	150063
ME02V-C6	150064

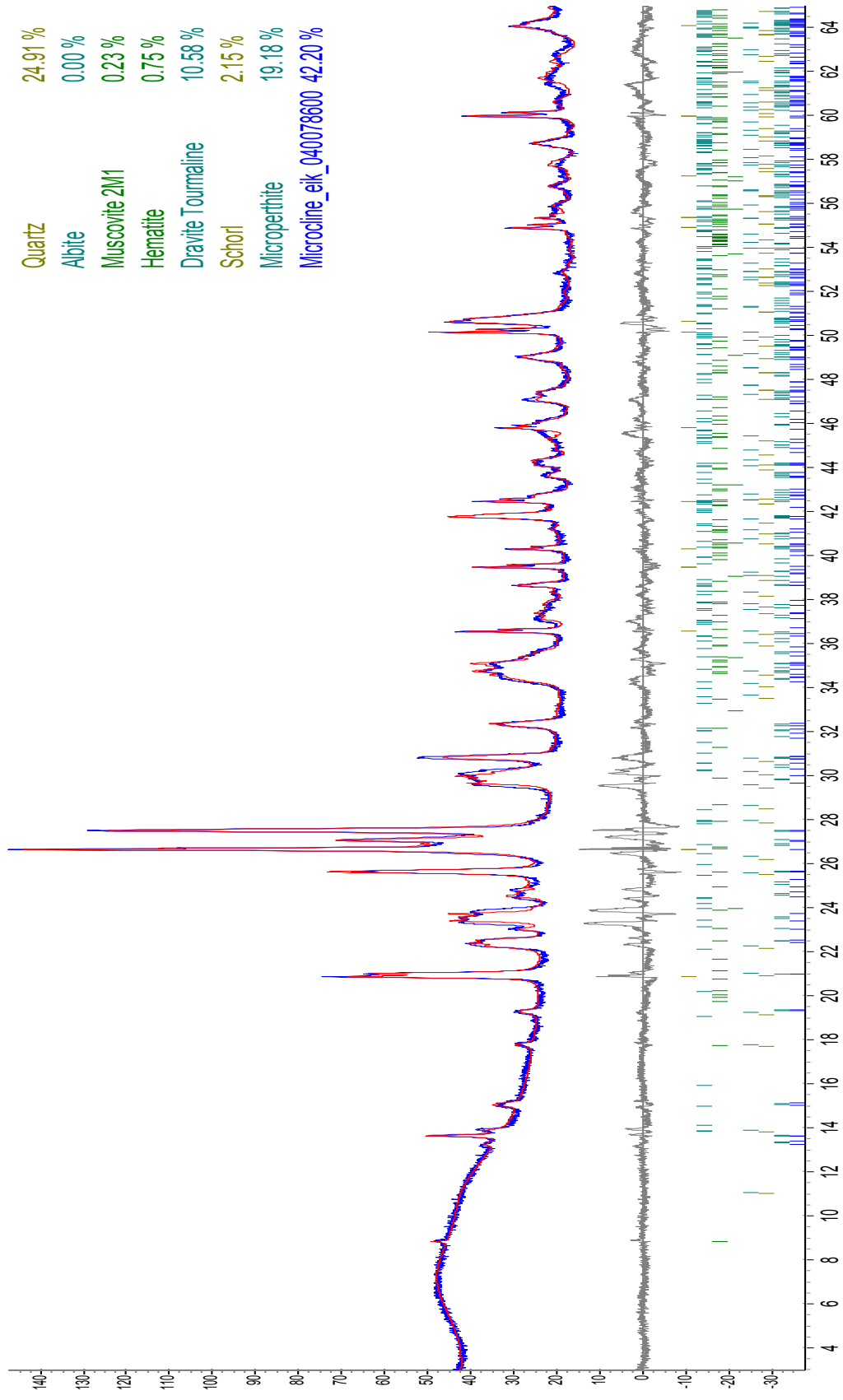


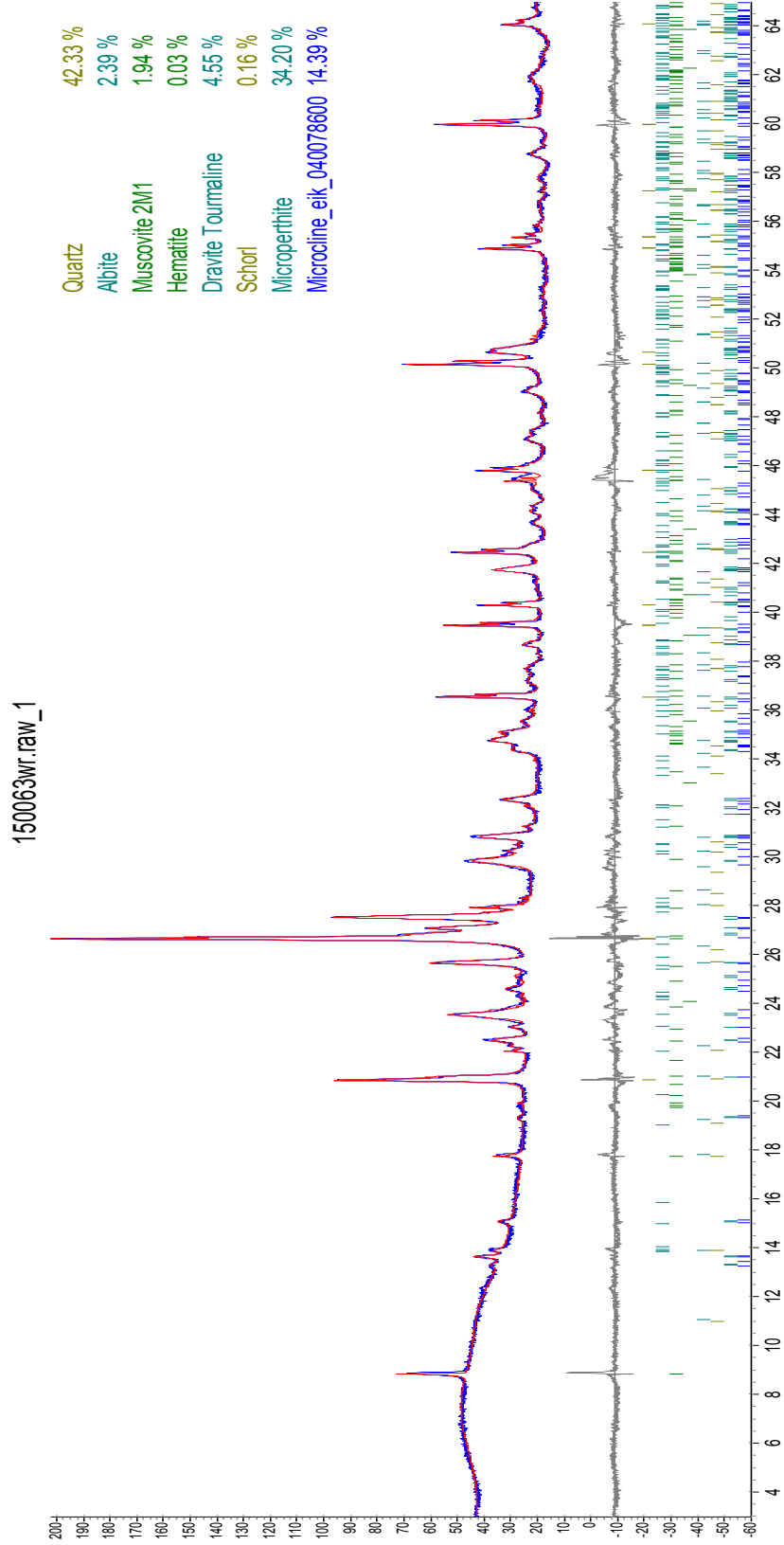
150060wr.raw_1





150062mr.raw_1





150064wr raw_1

